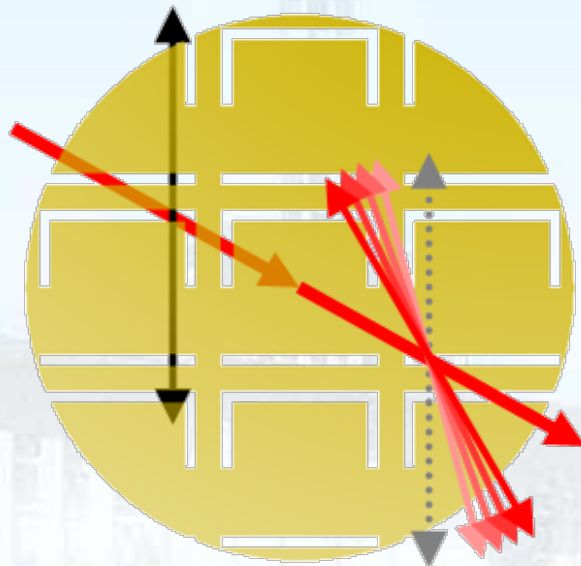


The Key Laboratory of Weak Light Nonlinear Photonics,
Ministry of Education

Annual Report 2012



南开大学弱光非线性光子学
教育部重点实验室

Annual Report 2012

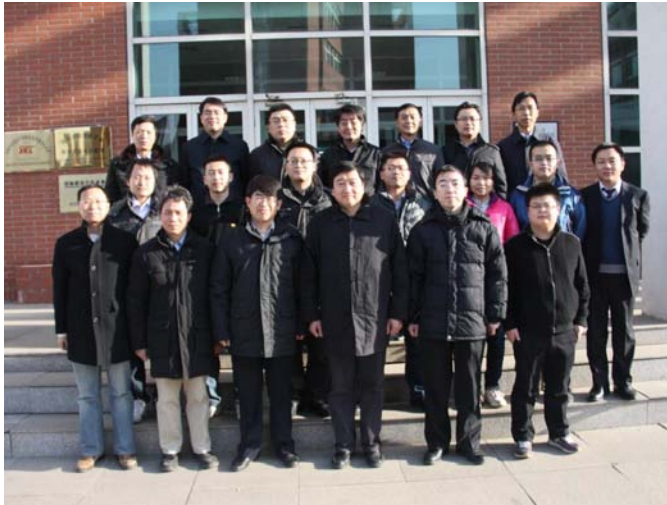
The Key Laboratory of Weak Light Nonlinear Photonics,
Ministry of Education



南开大学弱光非线性光子学
教育部重点实验室

▼ 弱光非线性光子学教育部重点实验室学术年会在泰达应用物理学院召开。

(2012.1.3)



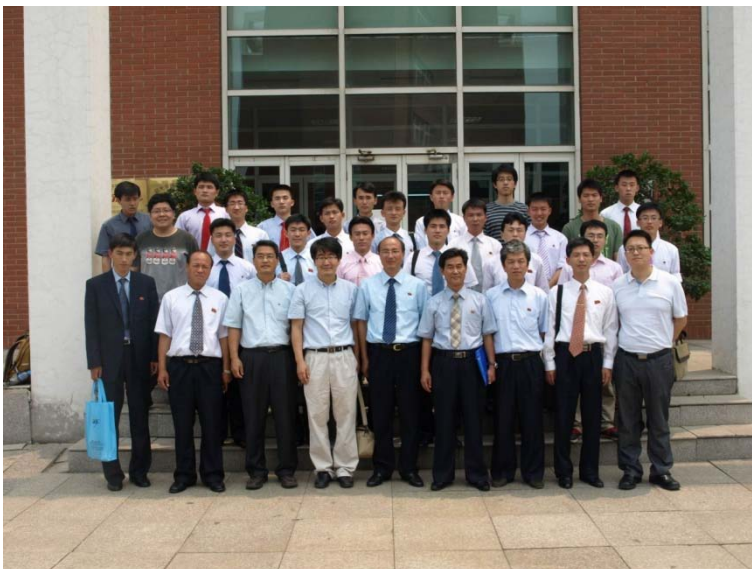
▼ 教育部海外名师、德国奥斯纳布吕克大学(University Osnabrück)前副校长 Peter Hertel 教授来华工作，在泰达应用物理学院和物理科学学院分别为研究生讲授了物理课程。

(2012.3.25-5.6; 10.25-12.9)



▼ 朝鲜平壤科技大学一行 20 余师生来弱光非线性光子学教育部重点实验室交流访问。

(2012.6.5)



▼ 南安普顿大学副校长 Perk Spearing 教授、国际处处长 Jo Doyle 女士和当代中国研究中心执行主任 Mark Cranshaw 先生参观了弱光非线性光子学教育部重点实验室。

(2012.6.19)



▼ 教育部重点实验室特聘教授、卢布雅尔娜大学&斯特藩研究所 Irena Olenik 副教授来弱光非线性光子学教育部重点实验室进行合作研究。

(2012.8.20-2013.2.20)



▼ 日本电气通信大学 Yasuo Tomita 教授来弱光非线性光子学教育部重点实验室进行交流访问，并在泰达应用物理学院做了精彩报告。

(2012.8.21-8.27)



- ▼ 乌克兰切尔诺维茨国立大学校长 MelnychukStepan 教授、先进光学中心主任 Mokhun Igor 教授访问南开大学期间来弱光非线性光子学教育部重点实验室参观访问并签订了合作协议，Rupp 院长、孔勇发副院长及张心正教授陪同会见，Mokhun Igor 教授在泰达应用物理学院为实验室师生做了精彩报告。



(2012.8.22-8.23)

- ▶ 维也纳大学研究生 Meingabner Michael 来弱光非线性光子学教育部重点实验室进行科研工作，作为第一个来实验室长期工作的留学生，标志着实验室教育国际化进入新阶段。（2011.9.21）



- ▼ 韩国首尔大学 Guicy Scalia 来弱光非线性光子学教育部重点实验室进行交流访问并做了精彩的学术报告。



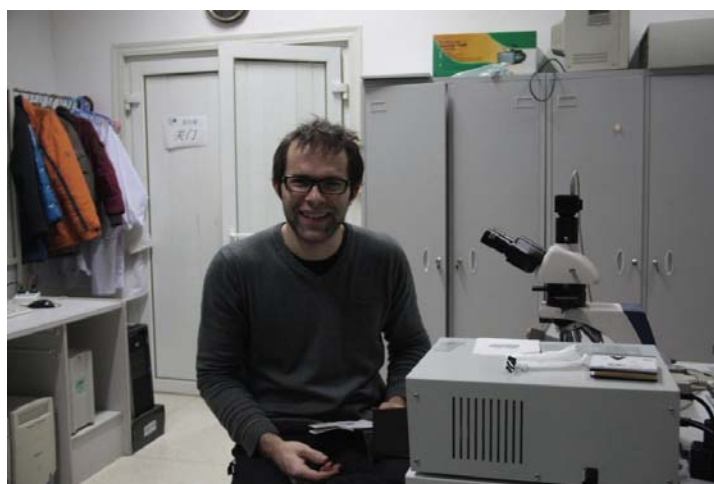
(2012.11.28-12.1)

▼ 台湾长庚大学廖骏伟教授来弱光非线性光子学教育部重点实验室进行参观访问并做了精彩的学术报告。



(2012.11.30)

▼ 卢布尔雅纳大学 Blaž Tašič 作为留学生来弱光非线性光子学教育部重点实验室开展科研工作。



(2012.12.3)

▼ 南安普顿大学的 Kevin. F. MacDonald 和 Eric Plum 来弱光非线性光子学教育部重点实验室进行参观访问并做了精彩的学术报告。



(2012.12.10)

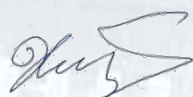
前 言/Preface

In 2012, the work at our lab was mainly focused on optical nonlinearities of new functional materials and their microstructure systems, also nonlinear optical manipulation of light and its application. Especially we achieved some fruitful results in the nonlinear optical effects and their applications of the micro-structure optical systems and meta-materials, and the manipulation of optical field. In this report, we present a short summary of our research progress in each line of activity of 2012.

All the activities summarized here have been done in the frame of international projects, cooperation agreements, and contracts with NSFC, MOE, MOST and Tianjin Municipal government. We also benefit a lot from our colleagues from other units all over world, who provide us advices and supports. Many thanks for their kind supports. In addition, our staff and students worked hard in order to make our research better and faster. Thanks a lot for their indispensable contributions and wonderful research works.

Hereby I would also like to stress that our lab is a big happy family for all of us. We should keep our own excellent tradition and develop our research well in the next year.

Prof. Dr. Jingjun Xu



Director,

The Key laboratory of Weak-Light Nonlinear Photonics

目 录/Contents

人员结构/Organization	1
承担课题/Projects under Researching.....	4
仪器设备平台/Facilities	12
研究工作报告/Scientific Report.....	13
发表论文/Publications in Journal.....	53
专利/Patents	59
国际合作与交流/International Cooperation and Exchange.....	60
国内、国际会议报告/Talks at Conferences	65
学术组织与期刊任职/Academic Service	69
获奖情况/Awards & Honors.....	71
学位论文/Dissertations.....	72

人员结构/Organization

实验室主任/Director

许京军 教授

实验室副主任/Deputy Directors

张国权 教授

孙 骞 教授

学术秘书/Academical Secretary

禹宣伊 副教授

研究方向负责人/Research Group Leaders

弱光非线性及量子相干光学 许京军 教授

非线性物理与光子技术 田建国 教授

光子学材料及先进制备技术 孔勇发 教授

光谱表征及传感技术 宋 峰 教授

光场调控及其应用 王慧田 教授

学术委员会/Academic Committee

主 任/Chairman

李树深 院 士 (中国科学院半导体研究所)

委 员/Committee Members

薛其坤 院 士 (清华大学)

孙昌璞 院 士 (中国科学院理论物理研究所)

许宁生 院 士 (中山大学)

龚旗煌 教 授 (北京大学)

陆 卫 研究员 (中国科学院上海技术物理研究所)

徐现刚 教 授 (山东大学)

资 剑 教 授 (复旦大学)

申德振 研究员 (中国科学院长春光学精密机械与物理研究所)

曾和平 教 授 (华东师范大学)

田建国 教 授 (南开大学)

王慧田 教 授 (南开大学)

许京军 教 授 (南开大学)

外籍学术顾问委员

D. Kip 教 授 德国 Clausthal 工业大学

L. Hessenlink 教 授 美国斯坦福大学物理系

R. A. Rupp 教 授 奥地利维也纳大学实验物理所

T. Volk 教 授 俄罗斯国家晶体研究所

Y. Tomita 教 授 日本电气通信大学

K. A. Nelson 教 授 美国麻省理工学院

杰出人才/Intelligent Staff

教育部“长江奖励计划”特聘教授

许京军（1999） 王慧田（1999） 陈志刚（2006）

国家杰出青年基金获得者

许京军（1998） 田建国（2001） 王慧田（2003） 李宝会（2009）

教育部“优秀青年教师资助计划”入选者

张国权（2002） 宋 峰（2003）

教育部“跨世纪优秀人才培养计划”入选者

许京军（1998） 田建国（2000） 孙 骞（2001） 孔勇发（2002）

教育部“新世纪优秀人才支持计划”入选者

张国权（2004） 宋 峰（2004） 宋 智（2004） 臧维平（2005）
李宝会（2005） 孙甲明（2007） 张心正（2008） 刘智波（2009）
陈 璟（2009） 顾 兵（2010） 楼慈波（2010） 张天浩（2011）
武 莉（2011）

首批新世纪百千万人才工程国家级人选

田建国（2004）

国家海外青年学者合作研究基金获得者

陈志刚（2005）

“天津市授衔专家”称号获得者

许京军（2005） 田建国（2005）

教育部“长江学者和创新团队发展计划”创新团队基金资助

弱光非线性光子学重点实验室人员名录/Name List

研究人员/Scientific Staff (49人)

许亚军 王慧田 田建国 Romano A. Rupp 陈志刚 张国权 孔勇发 孙 骞 宋 智
 宋 峰 臧维平 李宝会 舒永春 姚江宏 赵丽娟 曹亚安 孙甲明 张天浩 李玉栋
 徐晓轩 张心正 周文远 邢晓东 禹宣伊 余 华 吴 强 孙同庆 武 莉 楼慈波
 高 峰 刘智波 李祖斌 薄 方 齐继伟 叶 青 潘雷霆 蔡 卫 陈树琪 宋道红
 孙 军 张 玲(兼) 刘士国(兼) 李 威(兼) 陈 璟 李勇男 刘宏德 王 斌
 皮 彪 任梦昕 涂成厚

技术人员/Technical Staff (4人)

陈绍林 马玉祥 张 玲 刘士国

行政人员/administrative Staff (3人)

梁 建 李 威 唐柏权

博士生/Ph.D Students (95人)

郑超逸 李 毅 郜向阳 刘 欣 陈旭东 赵 欣 孔翔天 应翠凤 王 槿 闫卫国
 李健雄 姚 筠 李志莉 杨 阳 赵子宇 徐 建 杨 熹 王午登 吴玉娥 张 斌
 王 萌 潘崇佩 李存波 罗维维 辛非非 叶卓艺 张学智 任梦昕 石 凡 窦宜领
 翟召辉 张文定 徐 雷 洪佩龙 韩 彬 陈宗强 谢 楠 郝志强 谭信辉 吴 限
 向吟啸 梁 毅 刘鹏翊 杨 明 陈战东 王丕东 王 垒 石 彬 潘玉松 邱文娟
 赵明天 侯琼琼 赵丹丹 刘富才 曹 雪 程 辉 裴子栋 田 甜 葛新宇 刘 悦
 诸 玲 李燕丽 王 朗 徐纪华 张荣纯 彭勇进 于彦龙 王景声 杨荣巧 迟 鹏
 董江舟 张新星 刘 敏 张 鹏 郭丽梅 曹丽萍 龚 亮 王 蒙 潘 岳 娄 凯
 李思甬 钱升霞 任志成 董 校 叶 帆 康 明 王凤箫 施曙东 刘家东 李 伟
 刘艳玲 赵红艳 于 音 韦 晨 王立超

硕士生/M.S. Students (176人)

高承敏 杨 娜 晏 敏 赵连云 孙骥文 陈春晖 陈伦杰 刘 楠 李秀霞 蔚浩义
 赵 芳 刘瑞雪 曾欢欢 董 斌 杨 涛 郭燕磊 尹鹏飞 辛建康 石伟科 张光子
 李 莉 马 强 周 开 丁芳媛 闫 峥 赵明铎 周玉波 门双仁 杨 阳 马 跃
 高 赫 马晨欣 高 原 张 阳 王秋明 彭秋明 于 萍 辛 巍 王 鹏 王 群
 李文华 雷 琴 蒋文帅 邓志超 姜美玲 聂 伟 冀志超 廖宏艳 王世彪 左一平
 赵 丽 蒋鹏翀 李利明 杨 浩 李 莹 孟 涛 李 斌 赵 飞 潘 登 孔凡磊
 王莲莲 云志强 易三铭 马寅星 陈庆全 李文华 崔 伟 曹天祥 刘 颖 杨淑英
 殷 毅 张永哲 王 杰 王晓杰 李志向 黄礼刚 孙 哲 马腾飞 彭景阳 要佳莹
 张心铭 张冠南 单 排 宋亚婷 陈艳红 谭庆志 郝金龙 韩中兴 高 飞 兰子鉴
 刘 犇 刘晓芳 王雄龙 栗瑜梅 司元春 王文庆 张勇军 武丽伟 常丽芬 李清连
 刘文波 张建峰 郑先明 张 铭 张 盼 王亚洲 孟凡杰 闫艳花 王云峰 栾 星
 胡永能 王 俊 樊文博 孟 楠 赵建彬 李广平 张 宇 朱美玲 郑守君 黄 明
 张逍遥 郑大怀 解雅洁 崔 娇 乔晓龙 秦娇夷 史更新 甄彦赞 谢桂娟 黎 莎
 武 迪 唐 悦 闫亚斌 刘 艳 罗师强 吴婷婷 戈 进 王肖珩 靳亚粉 卢旭岑
 郝冰雪 张会平 刘 畅 韩凌云 张 华 徐海霞 黄绍龙 杨金凤 李 芳 张芳馨
 易 欢 李小静 王力伟 郭 辉 张 荣 高玲玲 吴学谦 郭廷柯 赵春兰 董职福
 田万辉 周 亮 孙希鹏 司 宇 孔令军 李 琼 韩迎东 王文艳 杜 鹏 王 芳
 张 超 张 功 张 俊 王津津 陈贵阳 郜慧斌

承担课题/Projects under Researching

序号	项目名称	项目来源	起止时间	负责人
1	纳/微结构非线性光学、光调控与器件应用研究	973 项目	2007.5-2012.8	许京军
2	硅基发光材料与光互联的基础研究(南开部分)	973 项目	2007.7-2012.12	孙甲明
3	空间结构光场与微结构的线性和非线性耦合效应	973 项目	2012.1-2016.12	田建国
4	光子束超衍射纳米加工基本原理基础研究	973 项目	2010.1-2014.12	张心正
5	超快激光与硅表面相互作用机理研究	973 项目	2012.1-2014.8	姚江宏
6	空间飞行器长寿命关键构件制备与服役中的基础问题	973 项目子课题	2010.01-2013.12	陈璟 李勇男
7	新颖动量和角动量光场与微结构相互作用的量子效应	973 项目子课题	2012.1-2013.6	宋智
8	减反与广谱吸收的黑硅材料研究	973 项目子课题	2012.1-2013.12	吴强
9	纳米器件制备工艺创新与应用基础研究	973 项目子课题	2012.1-2014.12	李威
10	关联光子学微结构的非线性光学特性与调控机理研究	国家重大科学研究计划	2010.1-2014.12	田建国

11	空间结构光场的调控机理、生成技术和新颖性质	国家重点基础研究发展计划子课题	2012.01-2016.08	王慧田
12	带电聚合物链构象与静电作用的耦合机制	国家自然科学基金重大项目(南开部分)	2010.1-2013.12	李宝会
13	铈酸锂晶体的紫外带边缺陷结构和非线性光学性质研究	国家自然科学基金重大研究计划培育项目	2010.1-2012.12	张国权
14	稀土掺杂光学材料中金属纳米微结构的制造及其对发光的影响	国家自然科学基金重大研究计划培育项目	2010.1-2012.12	宋峰
15	多相聚合物溶液体系受限于软膜内的自组装行为研究	国家自然科学基金重大研究计划培育项目	2013.1-2015.12	李宝会
16	纳米切削基础理论及相关关键技术研究	国家自然科学基金重大研究计划子课题	2010.1-2013.12	徐晓轩
17	矢量光场的动态调控:新方法、新效应和应用	国家自然科学基金重点项目	2010.1-2013.12	王慧田
18	大功率 DUV-DPL 热效应研究	国家自然科学基金重点项目子课题	2012.1-2015.12	宋峰
19	氧化锌铝纳米粉体及靶材中试技术研究	863 计划	2012.1-2014.12	舒永春
20	高分子物理与高分子物理化学	国家自然科学基金杰出青年科学基金	2010.1-2013.12	李宝会
21	XXX	科技部	2012.7-2015.7	宋峰
22	弱光非线性光子学科学与技术创新引智基地	111 计划	2012.1-2016.12	许京军

23	新型聚合物纳米复合材料及其光子学微结构研究	国家国际科技合作专项	2012.1-2014.12	张心正
24	新型乳腺癌早期预警系统的建立及防治方法的合作研究	国家国际科技合作专项	2012.6.1-2015.5.31	田建国
25	Peter Hertel (MS2010NKDX023)	教育部“海外名师”项目	2010.1-2014.12	许京军
26	碳结构及其杂化材料的光学非线性与超快特性研究	国家自然科学基金	2010.1-2012.12	田建国
27	三维磁光光子晶体飞秒激光直写技术研究	国家自然科学基金	2010.1-2012.12	李玉栋
28	缺陷光子晶格中的光动力学研究	国家自然科学基金	2010.1-2012.12	楼慈波
29	稀土离子掺杂的硅基紫外纳米层状结构发光器件	国家自然科学基金	2010.1-2012.12	孙甲明
30	高灵敏度快响应 InP 和 InN 胶体量子点近红外光探测器	国家自然科学基金	2010.1-2012.12	徐章程
31	新型碱金属碱土金属硼酸盐材料结构与荧光性质研究	国家自然科学基金	2010.1-2012.12	武 莉
32	利用法珀腔共振效应提高有机材料中慢光的相对延迟	国家自然科学基金	2010.1-2012.12	薄 方
33	各向异性介质亚波长结构的光学异常透射及其应用研究	国家自然科学基金	2010.1-2012.12	陈 璟
34	稀土掺杂光学材料中金属纳米微结构的制造及其对发光的影响	国家自然科学基金	2010.1-2012.12	宋 峰
35	Airy 光束的传输特性及在光学微粒操控中的应用研究	国家自然科学基金	2011.1-2013.12	臧维平

36	光折变表面孤子及其应用研究	国家自然科学基金	2011.1-2013.12	张天浩
37	有序与无序金属亚波长微纳结构的表面增强非线性	国家自然科学基金	2011.1-2013.12	李祖斌
38	微结构光纤表面等离子体谐振和局域场增强及其应用研究	国家自然科学基金	2011.1-2013.12	陈树琪
39	电子显微镜在等离激元光学中应用的理论研究	国家自然科学基金	2011.1-2013.12	蔡卫
40	双掺杂 TiO ₂ 基可见光催化剂二元离子协同作用的研究	国家自然科学基金	2011.1-2013.12	曹亚安
41	超快激光构造黑硅材料的光电性能优化及微观机理研究	国家自然科学基金	2011.1-2013.12	姚江宏
42	基于非线性光学表面波的可调谐长程传播表面等离子激元及其应用研究	国家自然科学基金	2012.1-2015.12	张天浩
43	碳基纳米材料超快光学非线性及其非线性光学显微成像研究	国家自然科学基金	2012.1-2015.12	刘智波
44	高增益光子晶体自发辐射增强效应及其生物传感应用	国家自然科学基金	2012.1-2015.12	周文远
45	通过非均匀随机介质体系的图像传输与成像研究	国家自然科学基金	2012.1-2015.12	张国权
46	介电纳米波导/金属纳米微结构复合体系光传输性能及其应用	国家自然科学基金	2012.1-2015.12	孙骞
47	无序非线性增益介质中光子局域化及上转换随机激光的研究	国家自然科学基金	2012.1-2015.12	张心正
48	可见光催化剂微观表面光生载流子特性的原位定量研究	国家自然科学基金	2012.1-2015.12	曹亚安

49	基于特异介质的矢量光场生成与调控	国家自然科学基金	2012.1-2015.12	陈璟
50	锂在铈酸锂晶体中的扩散行为及其应用研究	国家自然科学基金	2012.1-2014.12	孙 军
51	中俄 2012 年激光物理研讨会	国家自然科学基金	2012.1-2012.12	宋 峰
52	有机杂化结构光学非线性及其应用研究	教育部新世纪优秀人才支持计划	2010.1-2012.12	刘智波
53	Airy 光束的传播动力学调控及其应用	教育部新世纪优秀人才支持计划	2011.1-2013.12	楼慈波
54		教育部新世纪优秀人才支持计划	2012.1—2014.12	张天浩
55	光折变表面孤子及其应用研究	教育部高等学校博士点基金（博导类）	2011.1-2013.12	张天浩
56	铈酸锂晶体热释电性能改进的研究	教育部高等学校博士点新教师基金	2010.1-2012.12	孙 军
57	基于微结构光纤的表面等离子体谐振和局域场增强及其应用研究	教育部高等学校博士点新教师基金	2011.1-2013.12	陈树琪
58	基于光刻技术的细胞图案化控制及其数值仿真研究	教育部高等学校博士点新教师基金	2012.1-2014.12	潘雷霆
59	荧光增强空间分辨生物传感技术	天津市国际合作项目	2010.10-2013.9	周文远
60	基于聚合物-纳米颗粒复合材料的光子学微结构研究	天津市科技支撑计划 国际科技合作专项	2011.10-2013.9	张心正
61	基于聚合物-纳米颗粒复合材料的光子学微结构研究（9-17）	中国与斯洛文尼亚政府间科技合作项目	2011.7-2013.6	张心正

62	激发态电子超快能量传输过程研究	中德合作科研项目	2011.1-2012.12	赵丽娟
63	低成本床旁快速诊断系统的研究与开发	天津市科技支撑计划 重点项目	2011.04-2013.09	田建国
64	基于近红外光谱的油料农作物品质快速检测的全固定式仪器研发和应用	天津市科技支撑计划 重点项目	2012.4-2015.3	徐晓轩
65	新型无机液体激光介质-掺稀土氟化物纳米晶溶胶	天津市自然科学基金 重点基金	2009.4-2012.3	赵丽娟
66	基于微结构光纤的空间分辨免疫传感技术研究	天津市自然科学基金 基础重点项目	2011.03-2013.03	周文远
67	基于物联网的近海多参数水质分析仪及监测网络	天津市科技兴海项目	2012.1-2014.12	徐晓轩
68	云计算模式下基于手机信令的智能交通指挥与突发事件感知平台	天津市信息化项目	2012.1-2013.12	徐晓轩
69	电磁波与微结构的瞬态相互作用	天津市自然科学基金	2009.4-2012.3	吴 强
70	碳基材料复合物光学非线性及其应用研究	天津市自然科学基金	2009.4-2012.3	刘智波
71	碱金属碱土金属硼酸盐基发光材料结构与性能研究	天津市自然科学基金	2009.4-2012.3	武 莉
72	亚波长微结构异常光学性质及其应用的研究	天津市自然科学基金	2009.4-2012.3	李祖斌
73	近化学计量比掺铈铈酸锂晶体生长及铁电畴性能优化研究	天津市自然科学基金	2010.4-2013.3	刘宏德
74	楔形超声角锥驱动的光纤结构的滤波色散特性及其应用	天津市自然科学基金	2012.4-2015.3	高峰

75	矢量光场下的表面等离子共振及表面增强拉曼研究	天津市自然科学基金	2012.4-2015.3	齐继伟
76	GF 项目 (XXX 晶体)	国防科工局 GF 项目	2010.1-2012.12	孙 军
77	XXX	国防基础科研计划	2012.1-2013.6	宋 峰
78	电光晶体研制	中电 27 所军工配套	2010.10-2012.12	孙 军
79	拉曼表面增强传感器	精密测试技术及仪器 国家重点实验室开放 基金	2009.9-2012.9	徐晓轩
80	GaAs、Si 材料纳米切削基础理论及相关技术研究	中科院半导体所重点 实验室开放课题	2011.1-2012.12	王 斌
81	局域等离子激元微结构优化设计和表面增强应用研究	教育部重点实验室开 放课题	2012.7-2014.6	王斌
82	蓝宝石晶体用高纯氧化铝委托开发技术	横向课题	2011.10-2012.12	孙 军
83	电光晶体	中电 27 所	2012.3-2013.3	孙 军
84	基于 Zigbee 技术的温度传感物联网监控平台	天津大学	2012.10-2013.3	徐晓轩
85	ITO 用纳米 SnO ₂ 粉体制备方法	校企合作项目	2011.1-2013.12	舒永春
86	光功能晶体的缺陷调控与性能优化	中央高校基本科研业 务费专项基金重大培 育	2011.9-2013.6	孔勇发
87	新型稀土磷酸复盐光电功能材料的制备、结构与性质	中央高校基本科研业 务费专项资金平台重 大项目	2012.10-2013.9	孙同庆

88	电子显微镜高分辨成像表面等离子激元的理论研究	中央高校基本科研业务费专项基金	2010.6-2012.5	蔡 卫
89	紫外光折变材料及器件研究	中央高校基本科研业务费专项基金	2010.6-2012.5	李 威
90	利用快速显微荧光成像法对嗜中性粒细胞免疫信号转导过程中耗散现象的研究	中央高校基本科研业务费专项基金	2010.6-2012.5	潘雷霆
91	有序与无序金属亚波长微纳结构的表面增强非线性	中央高校基本科研业务费专项基金	2010.6-2012.5	李祖斌
92	微结构光纤表面等离子体谐振和局域场增强及其应用研究	中央高校基本科研业务费专项基金	2010.6-2012.5	陈树琪
93	粗糙表面效应对组织光学参数测定的影响及相关问题研究	中央高校基本科研业务费专项基金	2010.6-2012.5	叶 青
94	表面等离子激光磁光非线性效应的研究	中央高校基本科研业务费专项基金	2010.6-2012.5	齐继伟
95	非线性介质纳米波导阵列光学性质的研究	中央高校基本科研业务费专项基金	2010.6-2012.5	陈 靖
96	掺杂铌酸锂晶体热释电增强机理研究	中央高校基本科研业务费专项基金	2010.6-2012.5	孙 军
97	纳米颗粒的荧光量子剪裁调控及在生物近红外探测中的应用	中央高校基本科研业务费专项基金	2010.6-2012.5	余 华
98	抗紫外光损伤铌酸锂晶体设计及性能研究	中央高校基本科研业务费专项基金	2010.6-2012.5	刘宏德
99	复杂体系的光谱表征新方法研究	中央高校基本科研业务费专项基金	2010.6-2012.5	王 斌
100	类石墨烯型光子晶格的制备及其光传播特性研究	中央高校基本科研业务费专项基金	2011.10-2013.9	宋道红

仪器设备平台/Facilities

仪器设备名称	规格型号	购置时间
激光器工作站	899-29	2005.09
飞秒激光器	VF-T2S	2000.08
皮秒激光器	PY61	2003.11
纳秒激光器	Panther OPO	2003.11
光纤激光器	PLY-20-M	2003.11
可调频再生放大器	Spitfire F-1K	2000.04
时间分辨光谱及瞬态吸收光谱系统	Spectrapro.300i	2000.04
光谱分析仪	AQ6315A	2005.09
显微拉曼光谱仪	MKI2000	1998.09
分子速外延生长炉	Riber Compact 21T	2003.09
提拉法晶体生长炉	研制	2002.04
晶体切割研磨抛光系统	Logitech 系列	2001.06
扫描探针显微镜	Nanoscope IIIa	2006.08

注：除开放基金外，所有仪器设备均为有偿使用

sensors and biosensor devices, which are in high demand.

(2) 我们在近红外区域提出并且实验证明了一种偏振无关广角等离子激元诱导透明平面超材料，它可以很容易的制作在光纤端面。同时提出一种四能级等离子激元系统解释并且分析这种等离子激元诱导透明平面超材料的形成机制，四能级模型同数值模拟和实验结果符合的很好。我们的结果证明局域反对称是形成等离子激元诱导透明的关键因素，但是并不意味着等离子激元诱导透明不能通过对称结构产生。我们的结果推动了光调控领域的进一步发展。

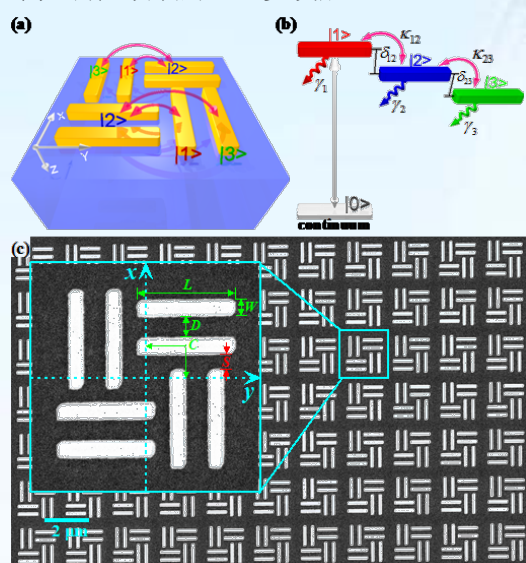


图 2 (a) 偏振无关广角等离子激元诱导透明平面超材料结构示意图；(b) 四能级等离子激元系统；(c) 外层结构和(d) 偏振无关广角等离子激元诱导透明平面超材料 SEM 图。

Fig. 2 (a) Unit cell of the PIT planar MM. The pink arrows indicate the near-field coupling between meta-atoms. (b) Coupled four-level plasmonic system for the PIT planar MM. (c) SEM of the sample with $S = 140$ nm. Inset: Amplified figure of the unit cell, showing the definitions of the geometrical parameters: $L = 900$ nm, $W = 150$ nm, $D = 200$ nm.

We present the design, characterization and experimental demonstration of a polarization-insensitive wide-angle plasmonically induced transparency (PIT) planar metamaterial (MM) in the near-infrared regime. A four-level plasmonic system is proposed to explain and analyze the forming mechanisms of the PIT planar MM, whose results agree closely with the simulated and

experimental results. This shows that the local asymmetrical nanostructure leading to the plasmon-assisted interaction is the key to producing PIT, but it does not mean that PIT cannot be achieved by the whole symmetrical nanostructure. This work offers a further step in developing optical modulation.

(3) 我们设计了一种双带的红外近完美超材料吸收器，它包含#型的金属微结构阵列以及一个金属层，中间由一个损耗的电介质隔开。不论 TE 还是 TM 偏振的电磁波，这个双带的吸收对于很大的入射角度仍然保持很高的吸收，因此，实现了广角的吸收器。同时由于结构的对称性，这个双带的吸收器是偏振无关的。所以，这个双带的超材料吸收器能够很好的应用到最大化吸收广角和任意偏振以及非偏振的电磁波。我们设计的这个双带近完美超材料吸收器的本质是在共振频率处激发了局域的电偶极共振和磁偶极共振。我们可以通过简单的调节一个元胞的尺寸大小，来使其中任意一个吸收带实现完美吸收，或者实现两个吸收带同时达到近完美吸收，这样可以灵活的应用到频率灵活的超材料。同时，这里设计的双带近完美超材料吸收器能够应用到局域表面等离子共振传感上。这个吸收器的广角和偏振无关特性，对于探测不同质量浓度溶液中的化学和生物分子，以及微纳环境下的化学反应都十分有利。

We first present the design, characterization, and experimental demonstration of a dual band MA in the infrared regime. The structure has single patterned top layer with #-shaped wires, which is simple and easy to fabricate. The two absorption resonances of the dual band MA are induced by the mixture of electric and magnetic Plasmon resonances, and are fundamental order resonance (at $6\mu\text{m}$) and higher order resonance (at $3.1\mu\text{m}$) of the #-shaped gold wires. The experimental peak absorptions of our fabricated infrared dual band MA reach 74% at $3.15\mu\text{m}$ and 96% at

5.86 μm . In addition, the absorption resonances are polarization insensitive due to the symmetry of the unit cell, and absorptions remain high even at large incident angles both for TE and TM polarizations. These are useful for applications as absorbing elements, since it can maximize absorption for wide-angle and arbitrarily polarized or incoherent incident light.

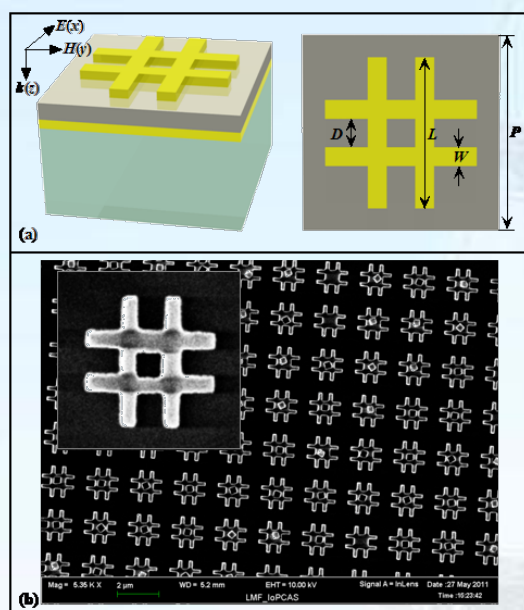


图 3 (a) 设计的双带近完美双带吸收器; (b) 制作的双带近完美双带吸收器俯视图。其中周期 $P=2.1 \mu\text{m}$, $L=1.5 \mu\text{m}$, $W=0.2 \mu\text{m}$, $D=0.3 \mu\text{m}$ 。

Fig.3. (a) Schematic diagram of the infrared dual band MA design and the incident light polarization configuration. The geometry parameters are as: unit cell length of $P=2.1 \mu\text{m}$, the bar length and width of $L=1.5 \mu\text{m}$ and $W=0.2 \mu\text{m}$, the interspace between two bars of $D=0.3 \mu\text{m}$. (b) Top-view scanning electron micrographs of the dual band MA. Inset: Enlarged view.

(4) 提出一种基于简易型空心微结构光纤结合使用光纤侧面探测方法的荧光检测技术方案。使用的空芯光子晶体光纤经选择性填充处理, 能在纤芯孔中填充荧光染料液。激光耦合入光纤, 经过交替填充的液柱段和空气段被束缚在纤芯中, 增大光和物质相互作用强度。探测装置设置在光纤侧面, 减小背景激光影响, 能够实时在线探测微弱荧光信号, 有效地降低了检测液体的极限浓度, 提高了荧光检测的灵敏度。该检测系统对若丹明溶液浓度极限值为 1 pM , 低浓度时出射荧光强度随染料浓度增大而升高。通过相

对移动探测装置来分别探测光纤侧面每一段液柱界面出射的荧光, 能实现空间分辨的分段荧光生物传感, 系统实现集成化, 微型化。

A high efficiency fluorescence measurement technology based on a simplified hollow-core microstructured optical fiber (SHMOF) and a charge-coupled device (CCD) lateral side detection approach is demonstrated. By selective injection of dye solutions into the hollow core, the input laser beam is transferred between the hollow core and the liquid core of the SHMOF, resulting in strong fluorescence stimulation. By using a CCD to detect fluorescence on the fiber's lateral side, highlighted sensitivity with dye concentrations down to 1 pM is achieved. It also provides a practical way to detect multiple signals simultaneously and distinguish between them in space.

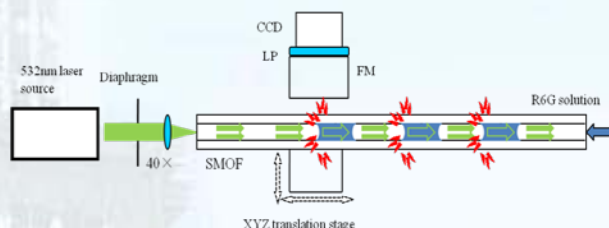


图 4 一种基于简易型微结构光纤以及光纤侧面设置检测系统的荧光检测装置。

Fig.4. Configuration of the fiber-based fluorescence sensing system; inset: the enlarged liquid column in the fiber core.

(5) 生物组织的折射率作为组织的重要光学参数之一收到广泛关注, 我们发现在利用全内反射法进行生物组织折射率测量过程中, 棱镜与样品存在的组织液是不可避免的, 会严重影响组织折射率的正确测量。在测量接触面上同时存在组织液和实际需要测量的生物组织。我们基于扩展微分全内反射的测量方法提出了一个新的模型, 用于揭示实际测量中被掩盖的信息。为了验证此模型, 我们测量了由甘油和甲基红组成的模拟样品。然后, 我们应用此模型测量了新鲜的猪肌肉组织, 鸡胸肌肉组织和鸡肝组织。我

们发现, 组织液在测量过程中是不可避免的, 对于存在的不同比例的组织液, 我们都可以用此模型进行生物组织折射率的精确测量。

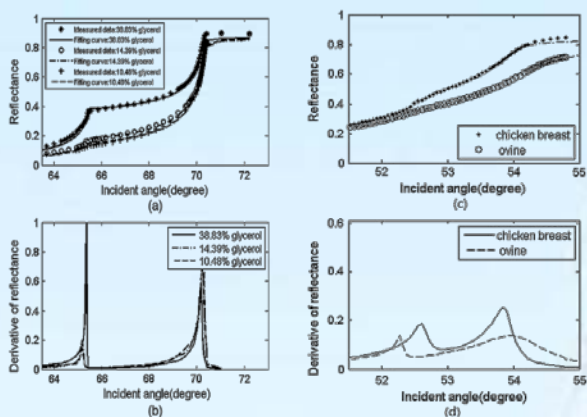


图 5 (a) 不同甘油比例的模拟样品的反射测量曲线和拟合曲线(TE 波) (b) b 图反射曲线的导数图 (c) 鸡胸肌肉组织和鸡肝组织的反射测量曲线和拟合曲线(TM 波) (d) (b) c 图反射曲线的导数图。

Fig. 5 (a) Measured reflectance data and fitting curves of the simulation sample with three different proportions of glycerol (TE wave). (b) The derivative of the reflectance curves. (c) Measured reflectance data and fitting curves of chicken breast and ovine tissue (TM wave). (d) The derivative of the reflectance curves.

We discover that the existence of the tissue fluid at the prism-sample interface is unavoidable in the measurement and has an important effect on the determination of RI of animal muscle tissue. The contacting area of the tissue sample consists of tissue fluid and muscle tissue. A new model based on EDTRM is proposed to explain the significant information revealed by the measured results. In order to verify the new model, a simulation sample made of glycerol and methyl-red-doped poly(methyl methacrylate) (MR-PMMA) is measured. Then we applied the new model for the measurement of fresh porcine, chicken breast, and ovine muscle tissues. During the laborious preparation and measurement of tissue samples, we find that a compromised pressure that is between eliminating partial tissue fluid and avoiding damage to the intrinsic properties of the tissue sample is needed in sample preparation. We also find that with a change of the proportion parameter of the tissue fluid, the RI

of muscle tissue can still be measured using the new model.

(6)我们研究了飞秒激光在磁光微结构写入中的应用。在磁光材料中通过飞秒激光直写技术可以引入正的折射率变化, 因此我们利用飞秒激光直写技术在磁光玻璃中写入了波导结构, 并测量了波导区域的 verdet 系数。实验结果表明, 在波导区域, 产生了光学损伤, verdet 系数降低。随着写入光强的增加, verdet 系数非线性的降低。利用合适的光强, 我们可以获得 verdet 系数保持在 80% 的单模波导。

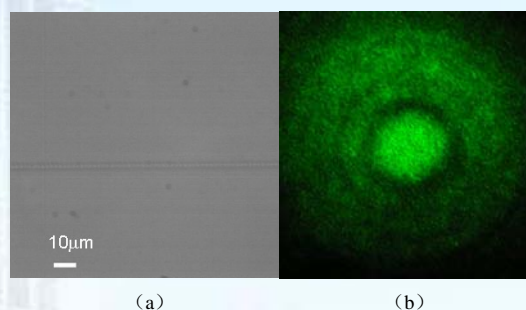


图 6 波导俯视图 (a) 和 近场导波图 (b)。

Fig. 6 (a) Top-view of the waveguide; (b) its beam guiding experiment result.

We investigated the application of femtosecond laser direct writing in the fabrication of magneto-optical (MO) microstructure. The experiments show that FDLW can introduce positive refractive index change in MO materials. With FDLW, we wrote successfully waveguides in MO glass. The Faraday rotation of the guided beam was measured. The results show that the core part of the waveguide, i.e. the optical damaged area, has lower Verdet constant. With the increase in the writing intensity of femtosecond laser pulses, refractive index change increases, whereas Verdet constant of the damaged area decreases nonlinearly. With suitable writing intensity, we get single mode waveguide of which Verdet constant is 80% of the bulk MO glass.

(7)在光学微操控研究方面: 利用矢势

和谱方法我们导出了 Airy 光束在介质分界面的电磁场分布情况。使用这些场表示和任意光束理论,我们对电解质表明的 Mie 粒子的光学力情况进行了理论研究。数值计算结果表明,光学力具有一个强的振荡特性,另外我们还分析了粒子形态相关共振情况。

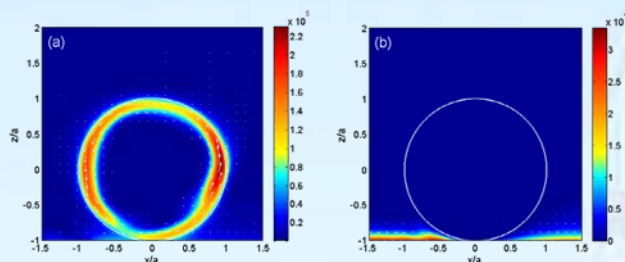


图 7 一个聚苯乙烯电介质球(a)和一个金属镍球(b)位于介质的分界面处引起的 Airy 消逝波的光强分布。

Fig.7. Plots of the source function of Airy evanescent field in the x-z plane with a dielectric spherical particle situating on the interface: (a) $n_3=1.59$, a polystyrene sphere, (b) $n_3=1.5+3.1i$, a nickel sphere. The arrows in plots represent power flow of Airy evanescent field. Particle radius $a=d/2$, $x_c=y_c=0$, $z_c=d+0.8\lambda$, $\theta_1=0.85$ rad.

Using vector potential and spectrum representation, we derive the expressions of the Airy evanescent field existed at the interface. Utilizing these expressions and the Arbitrary Beam Theory, the optical forces exerted on a Mie dielectric particle in the Airy evanescent field were theoretically investigated in detail. Numerical results show that the optical forces exhibit strong oscillations which are corresponding to the distributions of the evanescent field. With the increasing the size of particle radius, Morphology Dependent Resonance occurs for the particle with specific refractive index.

(8)在利用自组装聚苯乙烯小球为模板加工金属微纳结构的研究中,通过不断摸索改良加工技术,我们已经可以制备较大面积的周期金属结构。通过控制加工条件或引入其他控制,可以调控加工的金属结构的参数,也可以得到完全不同的金属结构。例如,利

用氧等离子体刻蚀机处理组装好的聚苯乙烯小球阵列,可以改变小球大小从而改变小球间距,然后镀金膜去除小球后,就可以得到间距不同金属三角结构,如图 1 所示。另外,在加工好的金属三角结构上再次镀银,我们得到了一种周期排布的针尖结构,如图 2 所示。针尖结构具有很强的近场增强特性,我们的方法可以通过简单的方法得到较大面积的周期排布的针尖,可以用于近场增强拉曼信号的探测等。

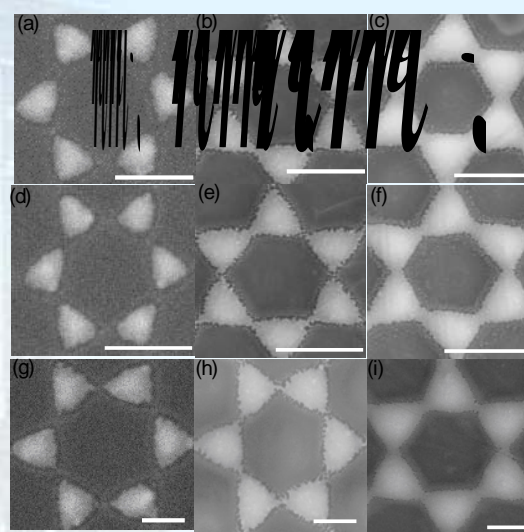


图 8. 不同大小(直径 500nm、750nm、1000nm)的聚苯乙烯小球模板经过 50 秒、20 秒、0 秒氧等离子处理后制备的金属微纳结构。

Fig. 8 Nano-pyramid structures fabricated by self-assembled nano-sphere templates (with diameters of 500nm, 750nm, 1000nm) after oxygen plasma treatment (50s, 20s, 0s).

By improving the fabricating technology, we now can make metal nano-structure with large area and periodic patterns by self-assembled nano-sphere lithography method. We can tune the geometric parameters of the metal nano-structures by modulating the fabricating factors, or obtain new structures different to the original ones. For example, an oxygen plasma etching process can reduce the diameter of the polystyrene nano-sphere, and enlarged the interspace of the spheres. Then after the gold deposition and removing the nano-sphere, we obtained nano-pyramid

arrays structure with different interspace, as shown in figure 1. Only by deposition silver film on the gold nano-pyramid structure, we obtained periodic nano-tip structures, as shown in figure 2. Metal tip can enhance strongly the surface electromagnetic fields, and can be used for surface enhanced Raman scattering. Our method can fabricate large-area periodic nano-tips by a very simple way and may be useful for some nanoscale applications.

光子学材料及先进制备技术/ Photonics Materials and Advanced Fabrication Techniques

负责人: 孔勇发

本方向涉及多功能光学晶体、低维功能材料、软物质、硅基发光、微晶玻璃陶瓷、光子学微结构等方面。本年度发表论文22篇, 申请发明专利4项, 获得授权专利2项, 在研课题经费1483万元。取得的代表性成果如下:

In this field, we mainly focused on the multi-functional optical crystals, low-dimensional functional materials, soft matter, silicon based light emitting materials, nano-crystalline glass ceramics, and photonic microstructure. 22 papers were published in international academic journals, 4 invention patents applied, and 2 patent issued. The total researching funds are 14.83 millions. This year, we obtained some important results, they are mainly shown as following:

我们生长了不同掺杂不同极化条件的掺钼铌酸锂晶体, 与以往掺杂不同, 六价的钼离子更倾向于占铌位, 对晶体的性能也造成了不用以往的影响。掺镁铌酸锂晶体能够以很短的响应时间在紫外到可见实现全波段的全息存储。尤其是掺0.5 mol%钼的铌酸锂晶体, 使用351 nm激光写入, 在保持60%衍射效率的同时, 响应时间只有0.35 s。因此掺钼铌酸锂晶体是一种性能出众的全色存储材料。

Molybdenum doped lithium niobate crystals were grown under different polarization conditions and their holographic properties were investigated. In contrast to current dopants, hexavalent molybdenum prefers niobium sites. Thereby, holographic storage becomes possible from the ultraviolet to the visible with considerably lower response time. Especially the response time of 0.5 mol% Mo doped LiNbO_3 can be shortened to as small as 0.35 s with a still high saturation diffraction efficiency of about 60% at 351 nm. Molybdenum doped lithium niobate thus is a promising candidate for all-color holographic

storage applications

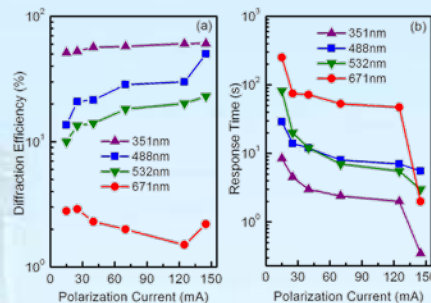


图1. 在不同极化电流下极化15分钟的LN:Mo0.5晶体的紫外-可见光折变性能。对于351、488、532和671 nm激光, 单束光的光强分别为320、400、400和3000 mW/cm²。

Fig.1 The UV-visible photorefractive characteristics of LN:Mo0.5 crystals polarized under various polarization currents for 15 min. The light intensity per beam is 320, 400, 400, and 3000 mW/cm² for 351, 488, 532, and 671 nm laser, respectively.

我们生长了一系列掺钒铌酸锂晶体, 研究了晶体在可见光范围的光折变性能。采用光强为471 mW/cm²的532 nm激光, 掺钒0.1 mol%铌酸锂晶体的响应时间可以缩短到0.57 s。光折变的主要机制为扩散, 而非光伏打场, 主导载流子为电子。这一研究结果与去年我们报道的掺钒铌酸锂晶体在紫外波段出色的性能表明掺钒铌酸锂晶体是一种出色的全息存储材料。

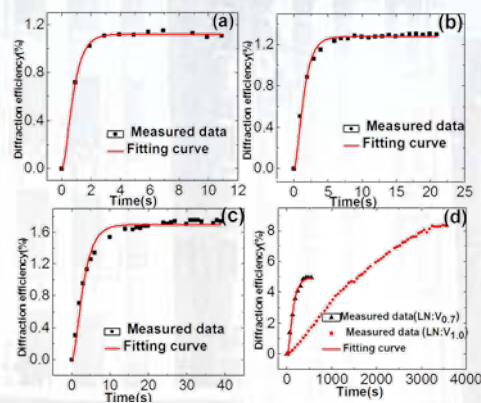


图2. 掺钒铌酸锂晶体的衍射效率随时间的变化。(a) LN:V_{0.1}, (b) LN:V_{0.3}, (c) LN:V_{0.5}, (d) LN:V_{0.7}和LN:V_{1.0}。

Fig.2 Time dependence of the diffraction efficiency of $\text{LiNbO}_3:\text{V}$ crystals. (a) LN:V_{0.1}, (b) LN:V_{0.3}, (c) LN:V_{0.5}, (d) LN:V_{0.7} and LN:V_{1.0}.

A series of vanadium doped lithium niobate crystals was grown and their photorefractive properties were investigated with a 532 nm laser. At a total light intensity of 471 mW/cm^2 a short response time of only 0.57 s was achieved for 0.1 mol% vanadium in LiNbO_3 . The photorefractive process is dominated by the diffusion field instead of the photovoltaic field. The dominant charge carriers are electrons. The overall scenarios in this work and the work published in 2011 indicate that V-doped LiNbO_3 may be a suitable material for holographic storage.

我们开发了一套实时探测光诱导铁电畴反转的成像系统,发现一个有趣的实验现象,即光辅助畴反转通常在辅助光关闭以后完成。对于 $6.6 \times 10^4 \text{ W/cm}^2$ 的 532 nm 激光,存在一个约 350 V/mm 的额外电场。我们提出这个额外电场来源于光照区的温度变化引起铌酸锂晶体的热释电效应。随后,我们计算出光照区的温度变化约有 $2.3 \text{ }^\circ\text{C}$,这个结果与文献报道一致。我们的研究表明,对于铌酸锂以及其它的铁电晶体,在强光照下,由于热释电效应导致的电场变化可能会在某些实验中起到重要作用。

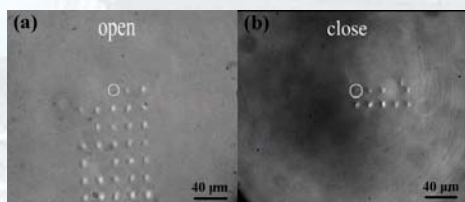


图 3. (a) 从动画中截取的 CCD 显示的单幅光辅助畴反转过程图,从该图可以清晰地看出,当施加一个 1.0 kV/mm 的电场,光辅助畴反转只有在光关闭后才发生; (b) 当施加一个 1.4 kV/mm 的电场,光辅助畴反转在光关闭前就已经发生。图中中间白色圆圈表示光斑的位置。图中的“close”和“open”分别表示光的关闭和打开。

Fig. 3. (a) Single frame excerpts from movie of light-induced domain reversal process on CCD. It is clear that laser-assisted domain reversal occurred just after light was turned off when applying a electric field of 1.0 kV/mm . (b) Laser-assisted domain reversal occurred before light was turned off when applying a higher electric field of 1.4 kV/mm . Centre of white circle is the position of laser spot. Words ‘close’ and ‘open’ on the

We developed a real-time imaging system to probe light-induced domain reversal

process of Mg-doped LiNbO_3 . An interesting phenomenon was observed that laser-assisted domain reversal occurred just after light was turned off. An exclusive electric field of about 350 V/mm was measured at 532 nm light of irradiation intensity of $6.6 \times 10^4 \text{ W/cm}^2$. The exclusive electric field was considered to be produced by pyroelectric effect owing to temperature change in the region of irradiation. Then, temperature change in the light-irradiated region was calculated as about $2.3 \text{ }^\circ\text{C}$. Our experimental results indicate that change of electric field caused by pyroelectric effect may play a significant role when LiNbO_3 or other ferroelectric crystals are used under strong light.

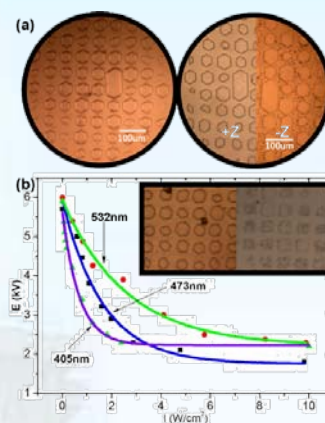


图 4. (a) 铌酸锂晶片上“光学印刷”的畴结构,左图为显微镜下图像,右图为湿法腐蚀后的±Z图像;(b)晶片反转电场和光强之间的关系,内图是不同条件下的畴结构,其光学掩模版均为方孔周期结构。

Fig.4 (a) "optical printing" domain structure on lithium niobate chip, left for microscope images, the right for wet etching of $\pm Z$ image; (b) the relationship between the reversal electric field of wafer and light intensity, the inner is the contrast of the domain structure with the different conditions, optical mask for square hole cycle structure.

利用可见光辅助方法实现了铁电晶片的畴结构的“光学印刷”(见图 Fig. 4(a))。该技术不仅大幅降低了晶片的反转电场(如图 Fig. 4(b)),使之适合较厚晶片的制备,而且通过反复实验研究寻找到了低光强阈值的晶片(其可见光强阈值与紫外光强阈值等同量级),可实现微米级畴结构的“无光刻”大幅制备。通过调节参数,可不再受制于晶格影响,实现精确复制光学模板结构(如图

Fig. 4(b)内图的正方形畴结构)。

The “optical printing” of domain structure on the ferroelectric wafer is achieved with visible light illumination (see Fig. 4(a)). This technology not only lowers the chip's reversal electric field (as shown in figure Fig. 4(b)), making suitable for thicker wafer preparation, but also realize the large area preparation of micron-order domain structure with “no lithography” by the repeated experiment research for the low light intensity threshold value of the chip (its visible light intensity threshold is of the same order magnitude as the ultraviolet ones). By adjusting the parameters, chips can no longer constrained by lattice effects, and achieves the accurate replication of optical mask(the square domain structure as shown in figure Fig. 4(b) inset).

随着激光二极管 (LD) 泵浦固体激光器的发展, 新型掺钕激光晶体材料的探索获得了广泛的关注。由于 LD 的输出波长会随着激光装置的运转温度升高而发生漂移, 因此激光晶体需具有大的吸收半峰宽。我们在对稀土磷酸盐研究工作的基础上, 获得一种具有宽吸收峰特征的 Nd:KGdP₄O₁₂ 晶体, 详细研究了其结构、热学和光谱性质。

With the development of the solid-state laser with diode laser pumped, research on more efficient Nd³⁺-doped crystal materials is gaining more interest. Since the output wavelength of diode laser is increased with the operating temperature of the laser device, the temperature stability of the output wavelength of the diode-laser is needed to be crucially controlled. Therefore, the absorption band of laser crystals close to the laser output of AlGaAs diode-laser needs to have a large full-width at half-maximum (FWHM). We have grown Nd³⁺ doped KGdP₄O₁₂ single crystal by the top seed solution growth method and studied its structure, heat characteristics and spectroscopic properties.

X 射线衍射单晶结构分析表明该晶体为单斜 C2/c 空间群, 粉末衍射数据与根据

晶体结构的模拟结果一致; 同时我们对该晶体进行了红外与拉曼光谱表征。晶体中 Nd³⁺ 离子的浓度通过 ICP-MS 确认, 其分凝系数基本接近 1。摇摆曲线的测量结果表明该晶体具有非常好的结晶完整性。Nd:KGdP₄O₁₂ 晶体具有非同成分熔融的特点, 在 919.5°C 才发生热分解, 其比热容为 0.485–0.799 J·g⁻¹·K⁻¹ (在 -10 至 500°C 温度范围内), 室温下沿 c* 方向的热导率为 1.66W/m·K。该晶体在 798nm 处表现出强和宽的吸收 ($\sigma_{\text{abs}} = 3.26 \times 10^{-20} \text{ cm}^2$, FWHM = 14 nm); ⁴F_{3/2}→⁴I_{11/2} 跃迁具有较宽的发射谱带, 发射截面为 $6.25 \times 10^{-20} \text{ cm}^2$ 。荧光衰减曲线测量结果表明其荧光寿命长 (300 μs); 同时, Nd³⁺ 在 KGdP₄O₁₂ 晶格中的 Starks 能级分裂情况被分析。综合 Nd:KGdP₄O₁₂ 晶体的性质表现, 我们认为该晶体是一种潜在的适合 LD 泵浦的固体激光材料。

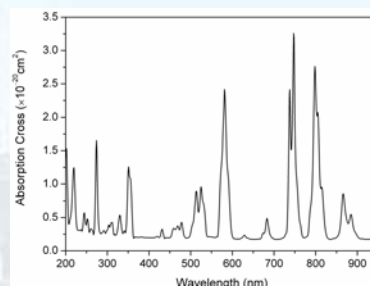


图 5. Nd:KGdP₄O₁₂ 晶体的吸收光谱。

Fig. 5. The absorption spectrum of the Nd:KGdP₄O₁₂ crystal.

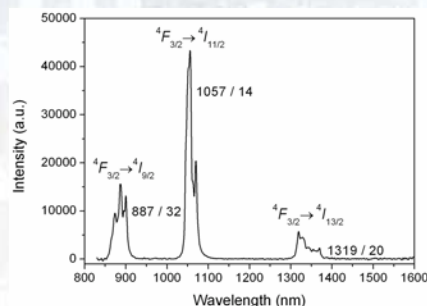


图 6. 808nm 光泵浦下的 Nd:KGdP₄O₁₂ 晶体的荧光光谱。

Fig. 6. The fluorescence spectrum of the Nd:KGdP₄O₁₂ crystal excited by the pumped light at 808nm.

The structure of the as-grown crystal determined by single crystal X-ray diffraction (XRD) is monoclinic crystal system, C2/c space group, which is characterized with cyclotetraphosphate anion [P₄O₁₂]⁴⁻. The

experimental pattern of power XRD coincided with the stimulated one according to the crystal structure. The results of IR and Raman confirmed that. The results of its rocking curve shows that the crystal have a very good crystallinity. The segregation coefficient of Nd^{3+} is equal to 1 approximately. $\text{Nd:KGdP}_4\text{O}_{12}$ crystal melts incongruently, and its specific heat varies from 0.485 to 0.799 $\text{J}\cdot\text{g}^{-1}\cdot\text{K}^{-1}$ with the temperature range from -10 to 500°C . The value of heat conductivity for $\text{Nd:KGdP}_4\text{O}_{12}$ along the c^* direction is $1.66\text{W}/\text{m}\cdot\text{K}$ at 28°C . There is a strong and wide absorption peak near 798nm ($\sigma_{\text{abs}} = 3.26 \times 10^{-20} \text{cm}^2$, $\text{FWHM} = 14 \text{nm}$). So the crystal can be pumped by AlGaAs diode-laser efficiently. The luminescence spectrum was measured, and the transition between ${}^4F_{3/2}$ and ${}^4I_{11/2}$ energy levels also has a wide emission band and the emission cross is $6.25 \times 10^{-20} \text{cm}^2$. The fluorescence lifetime is $300\mu\text{s}$. Then the Stark sublevels involved in laser operation of Nd^{3+} in $\text{KGdP}_4\text{O}_{12}$ crystal was analyzed. In summary, $\text{Nd:KGdP}_4\text{O}_{12}$ is suitable to be pumped by LD and is a promising solid state laser material.

本年度工作着重探索新的发光材料基质, 所选体系集中在碱金属、碱土金属及过渡族金属硼酸盐上。研究了 $\text{SrO-ZnO-B}_2\text{O}_3$ 和 $\text{K}_2\text{O-CaO/SrO/BaO-B}_2\text{O}_3$ 四个体系固相线下的相关关系, 并发现了两个新化合物, 其纯相正在制备中。研究了 $\text{KMgBO}_3:\text{Mn}^{2+}$ 的光致发光现象, 该样品可在蓝光激发下, 发射较高亮度及色纯度的红光。同时, 对 $\text{BaZn}_2\text{B}_2\text{O}_6:\text{Eu}^{3+}$ 的发射峰劈裂现象与掺杂浓度的关系进行了深入分析, 认为 Eu^{3+} 离子在低掺杂浓度时, 可选择性占据 Ba^{2+} 或 Zn^{2+} 的位置, 随掺杂浓度的增高, 会逐步占据第二种阳离子格位, 同时发射峰出现劈裂。研究了 $\text{NaSrBO}_3:\text{Eu}^{3+}$ 的发光现象及相变。该样品在近紫外光激发下发射红光。3% 以下的低掺杂时为 NaSrBO_3 的常温相, 在高掺杂时, XRD 谱线与在反应物中将 Na 含量增加 2 倍后的结果相同, 表明大量的 Na_2O 和少量的

Eu_2O_3 均可起到稳定相变的作用。同时, 由于猝灭浓度发生在相变之后, 因此该样品较好的发光性质应与相变后结构直接相关。

The work focuses on the investigation of new hosts for luminescence materials, and concentrates on the alkali metal-alkaline earth metal-transitional metal borate systems. Subsolidus phase relations of four systems $\text{SrO-ZnO-B}_2\text{O}_3$ 和 $\text{K}_2\text{O-CaO/SrO/BaO-B}_2\text{O}_3$ were studied by solid state reactions, and two new compounds were synthesized. The photoluminescence of $\text{KMgBO}_3:\text{Mn}^{2+}$ was studied, which could exhibit a red color with high color purity and brightness under the excitation of blue light. The splitting of the emission peaks of $\text{BaZn}_2\text{B}_2\text{O}_6:\text{Eu}^{3+}$ was investigated, and was believed to have close relationship with doping concentration. The Ba^{2+} or Zn^{2+} sites could be occupied as selected at low doping concentration, while the second cationic site would be taken up at high doping concentration with emission peaks splitting. The photoluminescence and phase transition of $\text{NaSrBO}_3:\text{Eu}^{3+}$ were studied. A red color emission with high quality could be obtained under a near UV excitation. The normal phase of NaSrBO_3 could be gotten when the doping concentration of Eu^{3+} was below 3%, while a new phase XRD was found at high doping concentration, which was same to the sample with two times Na concentration. It seemed that the new phase could be stabilized by a large amount of Na_2O or a small quantity of Eu_2O_3 . Because the quenching concentration was observed after the phase transition, it was believed that the good luminescence properties should have close relationship with the structure of new phase.

一直以来, 人们认为 Nd^{3+} 离子是用于产生激光输出的最高效的稀土离子之一, 尤其是它能用在不同的基质环境, 主要是晶体和玻璃之中以产生 $1.06\mu\text{m}$ 的近红外激光。尽管人们已经对稀土掺杂进入微晶这一过程进行了大量的研究工作, 然而相比于 Er^{3+} 、 Yb^{3+} 、

Tm³⁺、Eu³⁺等稀土离子而言,对于玻璃陶瓷中的 Nd³⁺离子的分布问题仍存在较多分歧,出现了一些不同的特殊结果,并对材料的荧光特性产生相应的影响。有别于文献中所选用的研究方法和测试手段,我们首先进行常规的掺 Nd³⁺离子玻璃陶瓷的实验制备。随后,通过氢氟酸腐蚀的办法将氧化物玻璃基质去除,使氟化物纳米微晶从基质中释放出来,进而对我们所关心的氟化物微晶进行直接的测试表征。这时再用 EDS 方法直接测量纳米微晶的化学成分组成,进一步提出了 Nd³⁺离子在玻璃陶瓷和纳米微晶中分布情况的物理模型。利用高分辨的扫描透射电子显微镜的高角度环形暗场像(HAADF-STEM)模式对关系的元素分布情况进行了 EDS 线扫描,并采用 Rietveld 方法全谱拟合 XRD 实验结果对玻璃陶瓷中 Nd³⁺离子分布的情况进行定量验证。我们认为在经过热处理得到的玻璃陶瓷材料中, Nd³⁺离子几乎没有进入到 β -PbF₂ 微晶相,而是完全留存与玻璃基质中

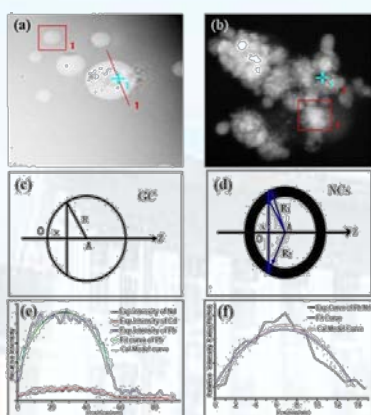


图 7. Nd 离子在玻璃陶瓷中的分布研究中 STEM 模式下的 EDS 线扫描图(a)和(b)、简化模型的 EDS 线扫描图(c)和(d)及相应的模型计算与实验测试结果(e)和(f)。

Fig. 7. EDS line scan graphs in HAADF mode (a,b). EDS line scans for the ideal models of (c) crystalline β -PbF₂ and (d) core-shell structure in NCs. (e) The relative element signal intensity of Pb, Nd, and Cd in GC; the fit curve; and the calculated model curve of element Pb are presented for comparison; (f) The fit curve of relative element intensity ratio Pb/Nd in NCs and the calculated core-shell model curve are also shown

It has been an open question whether Nd³⁺ ions are incorporated into the crystalline phase in oxyfluoride glass ceramics or not. Moreover, relative research has indicated that

spectra characters display minor differences between before and after heat treatment in oxyfluoride glass compared to similar Er³⁺-, Yb³⁺-, Tm³⁺-, Eu³⁺-, etc.-doped materials. Here, we have studied the distribution of Nd³⁺ ions in oxyfluoride glass ceramics by X-ray diffraction quantitative analysis and found that almost none of the Nd³⁺ ions can be incorporated into the crystalline phase. Transparent Nd³⁺-doped GCs were prepared and corrosion-treated to release NCs from the glass matrix for a direct study on their composition and structure information. Unlike the former results, β -PbF₂:RE crystalline phase was obtained, and pure β -PbF₂ crystalline phase was generated after thermal treatment. Especially after etching off the glass matrix, massive NdF₃ crystals simultaneously generate in free NCs. Through the XRD Rietveld refining method, almost the whole of Nd³⁺ ions reside in the glass matrix despite that the samples undergo the thermal treatment. For further demonstration, the models of Nd³⁺ ions existing in the glass matrix in GCs and the core-shell-like structure of pure β -PbF₂ surface absorbing NdF₃ crystals in NCs were built. Then, HRTEM, EDS line scan in HAADF mode, and conventional mathematical analysis were used to verify the models' rationality. The results of experimental characterization well coincide with those of the simulation. Our work explains the previous arguments about whether Nd³⁺ ions doped into the crystalline phase or not and removes the puzzle about minor differences on spectral properties. The study has paved a way to more comprehensively understand the properties of the Nd³⁺-doped oxyfluoride glass. The results here would benefit further research on the optical properties and applications of such materials.

采用红外, Raman, X 射线衍射测试分析方法,研究了 Al₂O₃ 对氟氧化物玻璃微结构和析晶的影响.结果表明,Al³⁺主要以[AIO₄]的形式与[SiO₄]以顶角相连的方式构成基本网

络骨架, Al_2O_3 含量的增加, 使氧化物玻璃基质的网络向单体和二聚体结构转变, 并使氟化物微晶尺寸有一个先变小后增大的趋势, 但不影响微晶结构。

The influence of Al_2O_3 on micro-structure and crystallization of oxyfluoride glass were investigated by Infrared spectra, Raman spectra and X-ray Diffraction analyses. The results showed that $[\text{AlO}_4]$ connected with $[\text{SiO}_4]$ units by means of angle connection, which formed the basic network of glass. When the content of Al_2O_3 increased, the structure of Monomer and Dimer increased in oxide glass matrix. Under the condition, the size of nanocrystals had minimum value, while the structure of nanocrystals was not affected.

硅基光子学和储能器件研究方向 2012 年度在原子层沉积光电薄膜和硅基光子学关键光源器件的研制方面取得了突破性的进展。主要体现的以下几个方面: (1) 我们利用原子层沉积方法制备出 $\text{ZnO}:\text{Al}$ 透明导电薄膜, 其薄膜电阻率为 $2.4 \times 10^{-3} \Omega \cdot \text{cm}$, 透过率达到 90% 以上, 主要技术指标达到国际上的最好水平。为进一步研制硅基光电子器件奠定了基础。(2) 为解决硅基 MOS 结构电致发光器件的稳定性问题, 我们提出了复合薄膜直流电致发光器件结构, 利用复合介质薄膜界面电位移矢量连续原理, 采用 high-k 介质薄膜来提高器件的耐压特性, 利用电压转移模型计算出了电稳定性好的器件结构。在此基础上, 利用原子层沉积技术从原子层精度 $\text{Al}_2\text{O}_3/\text{TiO}_2$ 纳米层状薄膜进行精确配比, 生长出介电常数和直流 I-V 特性都满足直流电致发光器件的 $\text{Al}_2\text{O}_3/\text{TiO}_2$ 复合高介电常数介质层, 为实现硅基 MOS 结构电致发光器件的稳定发光奠定了基础。(3) 我们首次利用原子层沉积方法生长稀土 Gd 离子掺杂的 $\text{SiO}_2:\text{Gd}$ 紫外硅基电致发光薄膜和稀土离子 Tb 掺杂的 $\text{SiO}_2:\text{Tb}$ 的绿色发光薄膜, 为研制硅基 MOS 结构光源提供了与微电子工艺兼容的发光层。(4) 最终

我们实验室完全自主地研制出完整的直流驱动的硅 MOS 结构电致发光器件, 器件关键薄膜的制备全部利用原子层沉积工艺来完成。这一进展得到德国同行的关注, 并与我们建立了材料生长合作关系。

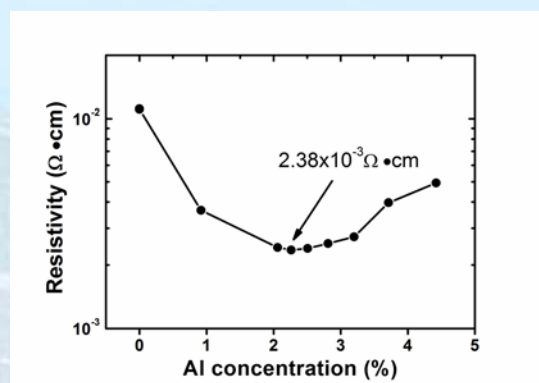


图 8. 掺铝氧化锌薄膜的电阻率随掺杂浓度的变化。

Fig. 8 Dependence of the resistivity on the Al doping content in the $\text{ZnO}:\text{Al}$ films.

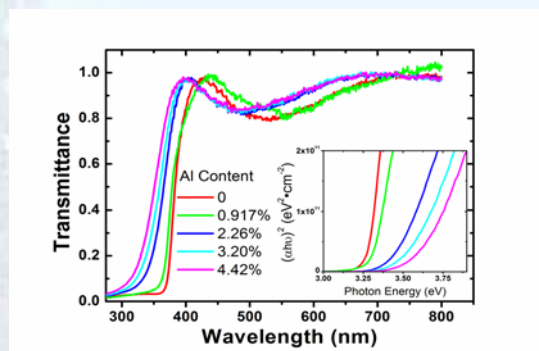


图 9. 不同铝掺杂浓度氧化锌的透射光谱。

Fig. 9 Transmission spectra of the $\text{ZnO}:\text{Al}$ films with different Al concentration.

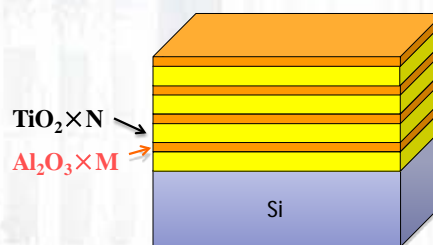


图 10. 原子层沉积的 $\text{Al}_2\text{O}_3/\text{TiO}_2$ 纳米层状结构示意图。

Fig. 10 Diagram of the $\text{Al}_2\text{O}_3/\text{TiO}_2$ nanolaminates by atomic layer deposition.

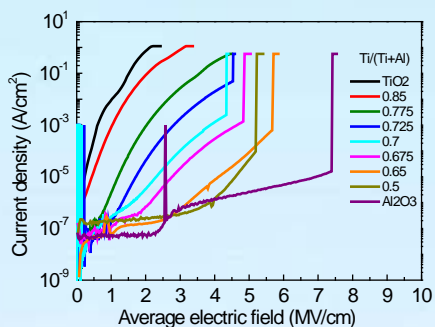


图 11. 不同组分的 Al₂O₃/TiO₂ 纳米层状结构 MOS 器件的电流-电压特性。

Fig. 11 I-V curves of the Al₂O₃/TiO₂ based MOS structure with different content of Ti.

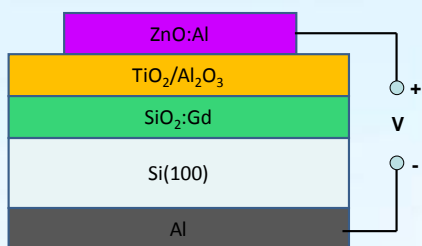


图 12(a) 硅 MOS 电致发光器件结构图。

Fig. 12. (a) Diagram of the Si MOSLED.

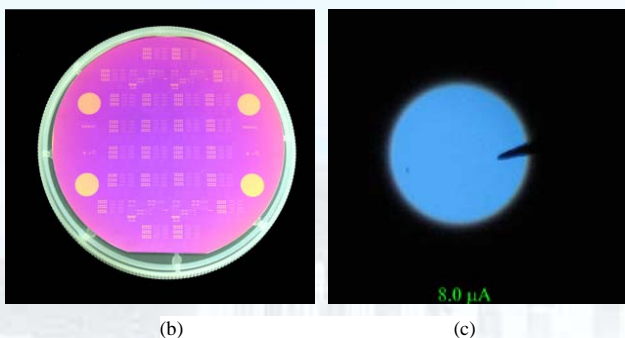


图 12. (b) 在 4 英寸硅片制备的薄膜电致发光器件；(c) 8 微安电流下电致发光器件的发光照片。

Fig. 12. (b) Photograph of the devices processed on 4-inch Si wafer. (c) Photograph of the EL device

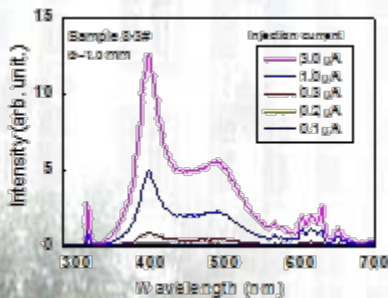


图 12. (d) 不同电流下 SiO₂:Gd MOS 电致发光器件的光谱。

Fig. 12 (d) EL spectra of the SiO₂:Gd MOS LED at different injection current

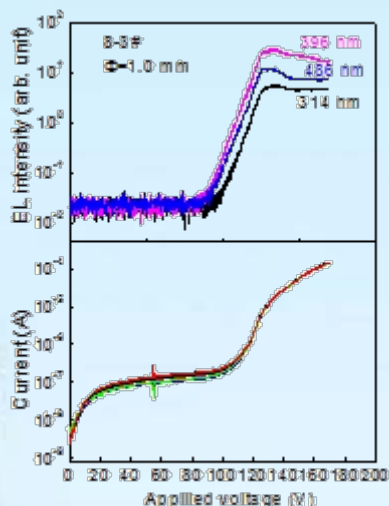


图 12. (e) 器件的电致发光强度-电流-电压特性。

Fig. 12 (e) EL-I-V characteristics of the SiO₂:Gd MOS LEDs

After four years construction of the laboratory, we are successful in the development of rare earth doped silicon dioxide metal-oxide-semiconductor light emitting devices (MOSLED) fully by atomic layer deposition technology. The MOSLED deposited on silicon substrate has a multiple layered structure of ZnO:Al/TiAlO_x/SiO₂:Gd/Si. For fully deposition of the multiple layered MOSLED on silicon substrate, the growth processes of four oxide layers of ZnO, Al₂O₃, TiO₂, SiO₂ and Gd₂O₃ were optimized concerning the overlap of ALD windows and the requirements of the optical and electrical transport properties for the direct-current operation of the EL devices. The transparent conductive ZnO:Al layer was deposited using DEZn, TMA and water process at low Al doping concentration from 0 to 4.42 % with the lowest resistivity of $2.38 \times 10^{-3} \Omega \cdot \text{cm}$ and transmittance above 80% in the violet and visible range, the high-k direct-current injection layers were prepared by alternative ALD deposition of the TiO₂/Al₂O₃ using TDMATi/TMA and ozone with dielectric constant of above 20, breakdown electric field above 4MV/cm, and injection current density up to 100 mA/cm², respectively. The Gd-doped SiO₂ light

emitting layer were deposited using 3DMAS/Gd(THD)₃ and ozone with Gd concentration of 2%. Efficient EL with peaks at 314 nm from Gd³⁺ ions and peaks at 375 and 460 nm from C impurities were observed in the EL spectra. The excitation mechanism of the EL was attributed to the impact excitation of the luminescent centers by hot electrons.

我们利用原子层沉积技术生长不同工艺条件下的 Tb₂O₃ 氧化物薄膜, 采用椭圆偏振仪测量了折射率和厚度, 优化了 ALD 生长稀土氧化物 Tb₂O₃ 薄膜的工艺条件; 利用原子层沉积技术生长制备了掺 Tb³⁺ 的硅基电致发光 Zn:Al/TiO₂+Al₂O₃/SiO₂:Tb/n-Si MOS 器件, 研究了电致发光光谱、电流-电压特性等, 获得了高发光效率的绿光硅基电致发光 MOS 器件。

The Tb₂O₃ nano film was grown by atomic layer deposition through the optimization of process conditions, and the refractive index and thickness was measured respectively. The efficient green electroluminescence was obtained from AZO/ATO/SiO₂:Tb/n-Si MOS devices fabricated wholly by ALD. The EL and Current vs electric field characteristics for MOS devices were researched.

采用溶胶-凝胶法, 并由不同的烧结温度制备出一组 InBO₃ 光催化剂。XRD、TEM 和吸收光谱研究了 InBO₃ 催化剂的结构、形貌和光物理性质, 对氯苯酚的光催化实验表明, InBO₃ 催化剂的光催化活性与它的烧结温度有关, 并高于 TiO₂, 这一结果能够由荧光光谱和 XPS 价带谱的结果加以解释。瞬态荧光光谱结果证明 InBO₃ 催化剂的光生电子的寿命长于 TiO₂, 表明对于治理环境污染 InBO₃ 是一种很有希望的光催化剂。

Indium borate has been prepared by a sol-gel method. The structure, morphology, and photophysics of the resultant photocatalysts have been studied via the techniques of X-ray diffraction (XRD), transmission electron microscopy (TEM), and

diffuse reflectance UV-visible light spectroscopy. These photocatalysts have been used to photodegrade 4-chlorophenol. The photocatalytic activity depends on the annealing temperature during preparation. It is found that borates can exhibit a high photodegradation activity under UV light irradiation, for which the efficiency can be higher than that of as-prepared TiO₂. This is explained according to the results of fluorescence spectra and valence band X-ray photoelectron spectroscopy (XPS). It is confirmed by the results of time-resolved photoluminescence decay spectra; i.e., the lifetime of electrons and holes involved in the radiative process can be longer for the borates than that for TiO₂. This implies that indium borate can be a promising photocatalyst for future applications in treatment of environment contaminants.

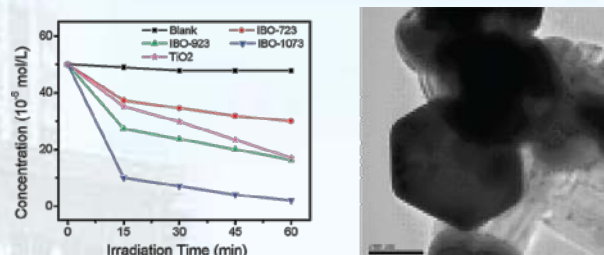


图 13 (左) 不同 InBO₃ 催化剂在紫外光照射下降解 4-CP 的浓度-时间曲线; (右) InBO₃-1073 催化剂 TEM 照片。

Fig.13 (Left) Concentration of 4-CP as a function of UV-light irradiation time during photodegradation with different catalysts. (Right) Images of TEM for InBO₃-1073 sample

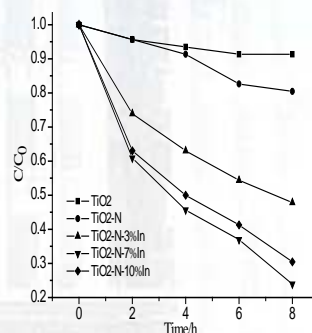


图 14 不同 In 离子浓度掺杂的 TiO₂-N-x%In 催化剂对对氯苯酚的光降解曲线。

Fig.14 Photodegradation of 4chlorophenol of TiO₂-N-x%In with different In-doping concentrations under visible light irradiation

采用溶胶-凝胶法制备出N和In修饰的TiO₂光催化剂(TiO₂-N-x%In)。在可见光照射下,该催化剂降解对氯苯酚的光催化活性高于纯TiO₂和N掺杂的TiO₂。利用XRD, BET, XPS, UV-vis DRS 和 PL技术确定TiO₂-N-x%In催化剂的结构和性质,结果发现两种特殊物种N-O and O-In-Clx (x 1 or 2)在TiO₂-N-x%In催化剂的表面。这两种物种的表面态能级分别靠近催化剂的价带和导带,使催化剂产生可见光吸收,而且促进了光生载流子的分离,所以N和In修饰改善了TiO₂催化剂的光催化活性。该研究证明,两种元素修饰TiO₂是研制高活性TiO₂基可见光催化剂的有效方法。

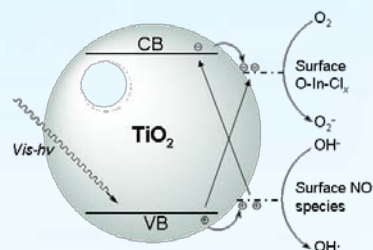


图 15 TiO₂-N-x%In 催化剂光催化机理示意图。

Fig. 15. Scheme of photocatalytic mechanism of TiO₂-N-x%In

Nitrogen and indium co-modified TiO₂ (TiO₂-N-x%In) was prepared by a simple sol-gel method. Under visible-light irradiation, the modified catalysts exhibited much higher photocatalytic activity for 4-chlorophenol photodegradation than both the as-prepared TiO₂ and nitrogen-doped TiO₂. The structure and properties of the resultant catalysts were characterized by XRD, BET, XPS, UV-vis DRS and PL techniques. It was found that unique chemical species, such as N-O and O-In-Clx (x 1 or 2), existed on the surface of the nitrogen and indium co-modified TiO₂. The surface-state energy levels introduced by these surface species were located close to the valence and conduction bands, respectively, which could lead to significant absorption in the visible-light region and facilitate the separation of photogenerated electrons and

holes. Thus, the visible-light photocatalytic activity of TiO₂ can be greatly improved by nitrogen and indium modification. We envision the opportunities for using such a method to develop TiO₂-based visible-light photocatalysts suitable for practical applications.

采用溶胶-凝胶法制备出偏硼酸锶(SrB₂O₄)光催化剂. 紫外光催化还原 CO₂ 合成 CH₄ (在液相水中) 的实验证明, SrB₂O₄ 催化剂的光催化活性略高于 TiO₂(P25). 利用 X 射线电子衍射谱 (XRD)、X 射线光电子能谱 (XPS), 透射电子显微镜(TEM),紫外-可见漫反射吸收光谱(UV-Vis) 和荧光光谱(PL)等技术,研究了 SrB₂O₄ 催化剂的晶体结构和能带结构,结果表明: SrB₂O₄ 的价带为 2.07 V(vs NHE), 低于 E^o_{redox}(H₂O/H⁺)氧化还原电位(0.82 V, vs NHE); 而导带-1.47 V(vs NHE), 高于 E^o_{redox}(CO₂/CH₄)氧化还原电位(-0.24 V, vs NHE). 因此, SrB₂O₄ 催化剂可以有效地光催化还原 CO₂ 生成 CH₄。

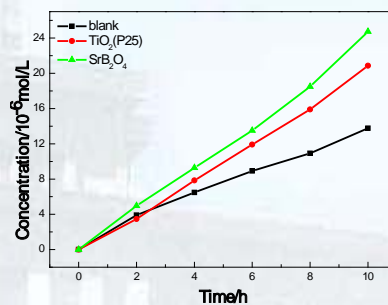


图 16 TiO₂(P25)和SrB₂O₄ 催化剂生成 CH₄(a)和 CO(b)的 c~t 曲线。

Fig. 16. c~t curves of photocatalytic reduction of CO₂ into CH₄(a) and CO(b) with TiO₂(P25) and SrB₂O₄ samples.

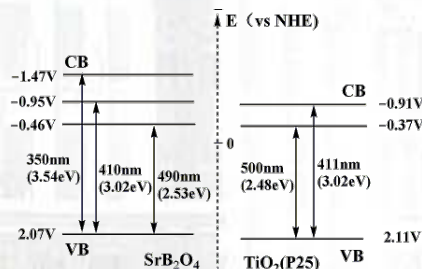


图 17 TiO₂(P25)和 SrB₂O₄ 样品的能带结构。

Fig.17 Schematic diagram for the alignment of energy levels of TiO₂(P25) and SrB₂O₄ samples.

Sample of pure SrB_2O_4 was obtained by sol-gel methods. The catalyst has been used to transform CO_2 into hydrocarbon fuel (CH_4) in the presence of water under UV-light. It is found that SrB_2O_4 can exhibit a high photocatalytic activity for which the efficiency can be higher than that of $\text{TiO}_2(\text{P}25)$. The structure and optoelectronic properties of the resultant photocatalyst have been studied via the techniques of XRD, FTIR, TEM, XPS, UV-Vis diffuse reflectance absorption spectra and photoluminescence. It was revealed that the edge of the valence band of SrB_2O_4 was determined to be 2.07 V(vs normal hydrogen electrode, NHE), which is more positive than that of $E_{\text{redox}}^{\circ}(\text{H}_2\text{O}/\text{H}^+)$ (0.82 V, vs NHE), and the edge of the conduction band was estimated to be -1.47 V(vs NHE), which is more negative than that of $E_{\text{redox}}^{\circ}(\text{CO}_2/\text{CH}_4)$ (-0.24 V, vs NHE). This indicates that SrB_2O_4 can exhibit a high photocatalytic activity toward reduction of CO_2 into CH_4 .

采用溶胶-凝胶法制备出 In 表面修饰的 TiO_2 ($\text{TiO}_2\text{-Inx}\%$) 纳米粒子, x% 代表在 In 掺杂的 TiO_2 样品中 In^{3+} 与 Ti^{4+} 离子摩尔百分含量. 利用二(四丁基铵)顺式-双(异硫氰基)双(2,2'-联吡啶-4,4'-二羧酸)钌(II) (N719) 作为敏化剂, 制备出 $\text{N719}/\text{TiO}_2/\text{FTO}$ (氟掺杂锡氧化物) 和 $\text{N719}/\text{TiO}_2\text{-Inx}\%/\text{FTO}$ 染料敏化薄膜电极. 光电转换效率实验表明, 在薄膜电极 $+0.5 \text{ mol}\cdot\text{L}^{-1} \text{ LiI} + 0.05 \text{ mol}\cdot\text{L}^{-1} \text{ I}_2$ 的三甲氧基丙腈 (MPN) 溶液 +Pt 光电池体系中, $\text{N719}/\text{TiO}_2\text{-Inx}\%/\text{FTO}$ 薄膜电极的光电转换效率均高于 $\text{N719}/\text{TiO}_2/\text{FTO}$, 其中 $\text{N719}/\text{TiO}_2\text{-In}0.1\%/\text{FTO}$ 的光电转换效率比 $\text{N719}/\text{TiO}_2/\text{FTO}$ 提高了 20%. 利用 X 射线衍射谱(XRD)、X 射线光电子能谱(XPS)、漫反射吸收光谱 (DRS)、荧光光谱(PL)和表面光电流作用谱确定了 $\text{TiO}_2\text{-Inx}\%$ 样品中 In 离子的存在方式和能带结构; 利用表面光电流作用谱研究了 $\text{N719}/\text{TiO}_2\text{-Inx}\%/\text{FTO}$ 薄膜

电极的光致界面电荷转移过程. 结果表明, In 离子在 TiO_2 表面形成 O-In-Cl_n ($n=1$ 或 2) 物种, 该物种的表面态能级在导带下 0.3 eV; 在光电流产生过程中, O-In-Cl_n ($n=1$ 或 2) 表面态能级有效地抑制了光生载流子在 $\text{TiO}_2\text{-Inx}\%$ 层的复合, 促进了阳极光电流的增加, 从而导致 $\text{N719}/\text{TiO}_2\text{-Inx}\%/\text{FTO}$ 薄膜电极的光电转化效率高于 $\text{N719}/\text{TiO}_2/\text{FTO}$, 并进一步讨论了光致界面电荷转移的机理.

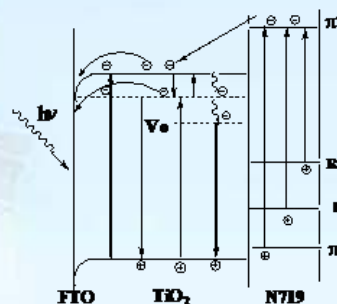


图 18 $\text{N719}/\text{TiO}_2\text{-Inx}\%/\text{FTO}$ 薄膜的能带结构示意图。

Fig.18 Schematic representation for energy band levels of the $\text{N719}/\text{TiO}_2\text{-Inx}\%/\text{FTO}$ film

We prepared surface-modified TiO_2 nanoparticle ($\text{TiO}_2\text{-Inx}\%$) by using sol-gel method, where x% represents the molar percentage content of In^{3+} ions in all metal ions (In^{3+} and Ti^{4+}) in TiO_2 . By using [NaRu(4,40-bis-(5-(hexylthio)thiophen-2-yl)-2,20-bipyridine) (4-carboxylic acid-40-carboxylate-2,20-bipyridine)(NCS) $_2$](N719) as the sensitizing agent, the $\text{N719}/\text{TiO}_2/\text{FTO}$ (fluorine-doped tin oxide) and $\text{N719}/\text{TiO}_2\text{-Inx}\%/\text{FTO}$ film electrodes were prepared. Under the solar cell structure of the thin film electrodes, $0.5 \text{ mol}\cdot\text{L}^{-1} \text{ LiI}$, $0.05 \text{ mol}\cdot\text{L}^{-1} \text{ I}_2$, MPN (Methoxypropionitrile) and Pt, the photoelectric conversion efficiency of all the $\text{N719}/\text{TiO}_2\text{-Inx}\%/\text{FTO}$ film electrodes were higher than that of $\text{N719}/\text{TiO}_2/\text{FTO}$, and the photoelectric conversion efficiency of the $\text{N719}/\text{TiO}_2\text{-In}0.1\%/\text{FTO}$ was enhanced by 20% than that of $\text{N719}/\text{TiO}_2/\text{FTO}$. We analyzed the band structure and presence of In ion in $\text{TiO}_2\text{-Inx}\%$ samples using X-ray diffraction (XRD) spectra, X-ray photoelectron

spectroscopy (XPS), optical diffuse-reflection spectra (DRS), photoluminescence (PL) spectra and surface photocurrent action spectra. The photo-induced charge transfer process of the N719/TiO₂-Inx%/FTO film electrodes were studied by surface photocurrent action spectra. The results show that the species O-In-Cl_n (n=1 or 2) are formed at the TiO₂ surface, and the surface state energy levels of the species locates at 0.3 eV below the conduction band of TiO₂. The surface state energy levels of the species can effectively inhibit the recombination of photo-generated carrier in the process of photocurrent generation, increase the anodic photocurrent, and improve the photoelectric conversion efficiency of N719/TiO₂-Inx%/FTO thin film electrode significantly. And the charge transfer mechanism in the light-induced interfacial is further discussed.

采用改性的 TiCl₄ 水解法制备出 TiO₂-5、TiO₂-10 和 TiO₂-20 (TiO₂-X) 三种不同表面性质的样品。利用 (1,10-邻菲咯啉)₂-(2-吡啶基)苯咪唑钌混配配合物(Rup₂P)作为敏化剂, 制备出 Rup₂P/ TiO₂-5/ITO、Rup₂P/ TiO₂-10/ITO 和 Rup₂P/ TiO₂-20/ITO 表面敏化薄膜电极。测试结果表明三种薄膜电极的光电转换效率为 Rup₂P/TiO₂-10/ITO > Rup₂P/TiO₂-20/ITO > Rup₂P/ TiO₂-5/ITO。利用吸收光谱、表面光电压谱(SPS)、荧光光谱和表面光电流作用谱等分析了 Rup₂P 和三种 TiO₂ 的能带结构和表面性质; 利用光致循环伏安和表面光电流作用谱研究了三种 Rup₂P/TiO₂-X/ITO 薄膜电极的光致界面电荷转移过程。结果证明, 在光致界面电荷转移过程中, TiO₂ 层表面氧空位对 Rup₂P/TiO₂-X/ITO 薄膜电极光致电荷转移产生重要影响, 并进一步讨论了 Rup₂P/TiO₂/ITO 薄膜电极的光电流产生机理。

TiO₂-5、TiO₂-10 and TiO₂-20 (TiO₂-X) sample prepared by modified TiCl₄ hydrolyzed, have different properties on

surface. Then they were further surface-sensitized with the Ru(phen)₂(PIBH) complex (Rup₂P) for Surface sensitization film electrode of Rup₂P/TiO₂-5/ITO、Rup₂P/ TiO₂-10/ITO and Rup₂P/ TiO₂-20/ITO. The measured results of photovoltaic properties of the three films revealed that Rup₂P/ TiO₂-10/ITO > Rup₂P/ TiO₂-20/ITO > Rup₂P/ TiO₂-5/ITO. We analyzed the energy band structures、properties on surface of Rup₂P and the three TiO₂ samples using Absorption spectrum、Surface photovoltage spectrum、Photoluminescence spectra and Photocurrent action spectra; studied the photo-induced charge transfer process with Cyclic voltammograms under irradiation and Photocurrent action spectra. The results revealed the oxygen vacancy at the TiO₂ surface was very important for the photo-induced charge transfer process of Rup₂P/ TiO₂/ITO, and further more we discussed the photocurrent mechanism of Rup₂P/ TiO₂/ITO.

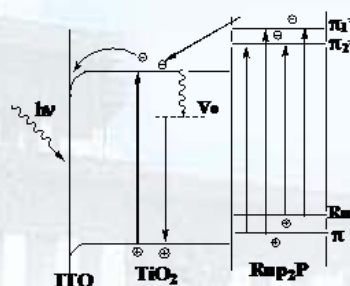


图 19 Rup₂P/ TiO₂-X/ITO 薄膜的能带结构示意图。

Fig.19 Schematic representation for energy band levels of the Rup₂P/ TiO₂-X/ITO film

采用低温可控的化学浴沉积法制备了 ZnO 纳米材料。利用 X 射线衍射仪、扫描电子显微镜、拉曼光谱、光致发光谱等对样品进行表征, 分析了衬底材料对 ZnO 结构和光学特性的影响, 结合溶胶-凝胶技术, 可以在硅衬底、蓝宝石和玻璃衬底上生长排列整齐、均匀一致的 ZnO 纳米棒阵列。在黑硅衬底及蓝宝石衬底上分别生长出树状结构的 ZnO 纳米材料和片状结构的 ZnO, 研究了这种新颖的 ZnO 结构的生长机理和

光电特性。

Among all the methods of preparing ZnO nanorods, chemical bath deposition is more attractive because of its excellent characteristics. It is simple, cost-effective, can be controlled easily and could be carried out at low temperature. In this paper, the simple CBD method was used to obtain the ZnO nanofilm. The structural and optical properties of as-grown ZnO nanomaterials on different substrates were investigated by XRD, SEM, PL and Raman spectrum. We analyzed the effect of substrates on the structural and optical properties of as-prepared ZnO. The ZnO nanorods grown on Si, Sapphire and glass substrates by chemical bath deposition combining sol-gel method were hexagonal wurtzite structure and preferentially oriented along the c-axis (002) and grown vertically to the substrates. However, we have synthesized tree-like ZnO nanostructure on black silicon substrate and ZnO nanopieces on GaN/Sapphire substrates. The growth mechanism of these novel ZnO nanostructures need further study.

利用纳米 Ag 颗粒的表面等离子体共振使周围局域场增强的特性, 制备了 Ag/ZnO 复合纳米薄膜, 分析了 Zn^{2+} 和 Ag^+ 的浓度比和水浴时间对复合纳米材料的光学性质的影响, 表明这种复合材料的紫外发光峰比纯 ZnO 的紫外发光峰强度增加很多, 从而可以改善 ZnO 在紫外器件方面的应用。

What's more, because of the surface plasmon resonance of Ag nanoparticles which can enhance the local crystalline field quickly, we prepared the Ag-ZnO composite nanofilms and studied the influence of the concentration of reactants and the growth time on the optical properties of Ag-ZnO nanofilms. The results shows that the intensity of the NBE emission peak increases while that of the blue emission peak decreases which was attributed to the surface Ag nanoparticles plasmon resonance.

在 ITO 用纳米 SnO_2 粉体制备方法方面, 获得了制备 10~30nm SnO_2 粉体

新型制备方法, 并进行了小批量试制试验。在纳米 ZnO 粉体制备方法方面, 获得了制备 10~30nm ZnO 粉体新型制备方法, 并进行了小批量试制试验, 为 863 项目 AZO 靶材制备奠定了基础。在注浆成型技术方面, 采用新型注浆成型技术, 获得了相对密度达到 68% 的 AZO 靶材生坯, 达到了等静压技术成型的同等水平, 增加了工艺的可控性, 为 863 项目 AZO 靶材制备奠定了基础。

Manufacturing methods of nano SnO_2 powders for ITO targets materials: The new preparation method of preparation 10~30nm SnO_2 powders under small batch production test. Preparation of nano ZnO powder method: The new preparation method of 10~30nm ZnO powders under small batch production test. Laid the foundations for the AZO targets materials. Slurry forming technology: Using new slurry forming technology acquired a relative density of up to 68% of AZO green, and reached the same level of isostatic pressing technology. Increases the controllability of technology, Laid the foundations for the AZO targets materials.

对典型软物质——嵌段共聚物体系进行了计算模拟研究。嵌段共聚物体系是典型的软物质, 具有软物质的最引人注目的特征, 即通过自组装形成纳米尺度的有序结构。这些结构在许多领域有着重要应用和广阔的应用前景。嵌段共聚物体系的自组装结构主要由单体-单体间的相互作用、嵌段共聚物的组成和嵌段共聚物的分子结

构控制。除了这些本征参数，将嵌段共聚物受限可引入多个外部因素，包括结构受挫程度和表面与嵌段共聚物间的相互作用。这些外部因素也可以强烈地影响嵌段共聚物的自组装结构。因此，嵌段共聚物受限提供了一种强而有力的操纵其自组装纳米结构的途径。在我们的综述中，我们讨论了受限条件和所形成的纳米结构之间的关系，聚焦于二维和三维受限的两嵌段共聚物体系的结构形成原理。特别是讨论了匹配条件、表面与嵌段共聚物间的相互作用和受限几何对自组装结构的影响。

We mainly focused on computational and simulation studies of typical soft matter, block copolymers. The typical result we obtained this year is shown as following: Block copolymers are a class of soft matter that self-assemble to form ordered morphologies at nanometer scales, making them ideal materials for various applications. The self-assembly of block copolymers is mainly controlled by the

monomer–monomer interactions, block compositions and molecular architectures. Besides intrinsic parameters, placing block copolymers under confinement introduces a number of extrinsic factors, including the degree of structural frustration and surface–polymer interactions, which can strongly influence the self-assembled morphologies. Therefore confinement of block copolymers provides a powerful route to manipulate their self-assembled nanostructures. In this review, we discuss the relationship between confining conditions and the resulting structures, focusing on principles governing structural formation of diblock copolymers under two-dimensional and three-dimensional confinement. In particular, the effects of commensurability condition, surface–polymer interactions, and confining geometries on the self-assembled morphologies are discussed.

弱光非线性及量子相干光学/ Weak Light Nonlinear Optics and Quantum Coherent Optics

负责人: 许京军

本方向主要开展纳微结构制备及其光学性质、非线性光调控与应用、量子非线性光学、飞秒超快探测技术以及光折变材料与新效应等方面的研究。2012 年度本方向共发表论文 31 篇, 主要取得如下进展:

The main research topics in this group are fabrication and optic properties of nano/micro-structure, nonlinear optical manipulation and its applications, quantum nonlinear optics, ultrafast detection and analysis by using fs technology and photorefractive materials and nonlinear optics. We published 31 papers in various academic journals. The main research progresses in 2012 are as follows.

基于爱因斯坦振子模型和 Urbach 带尾吸收规律, 我们研究了掺镁铌酸锂晶体的电声相互作用和带边缺陷结构。结果表明, 掺镁铌酸锂晶体的爱因斯坦振子、电声相互作用、吸收带边以及光致空穴小极化子 O^- 随掺镁浓度的增加均呈现浓度阈值效应, 与晶体的抗光损伤掺镁浓度阈值一致。这一结果给出了掺镁铌酸锂晶体吸收带边光学性质和光激发载流子输运过程阈值行为的基本微观机制, 对于优化铌酸锂晶体在非线性光学方面的应用有重要的意义。

Based on the Einstein oscillator model and the Urbach rule, we study the electron-phonon interaction and the band-edge structure of $\text{LiNbO}_3:\text{Mg}$. We report on the concentration threshold behavior of the Einstein oscillator, the electron-phonon interaction, the band-edge absorption, and the light-induced small hole polarons O^- in $\text{LiNbO}_3:\text{Mg}$ crystals with increasing Mg-doping concentration, which is in accordance with the optical-damage resistance concentration threshold. The result gives a fundamental microscopic mechanism of the concentration threshold behavior related to the

band-edge optical properties and the light-induced charge transport of $\text{LiNbO}_3:\text{Mg}$ crystals, and is helpful to optimize LiNbO_3 for applications such as nonlinear optics.

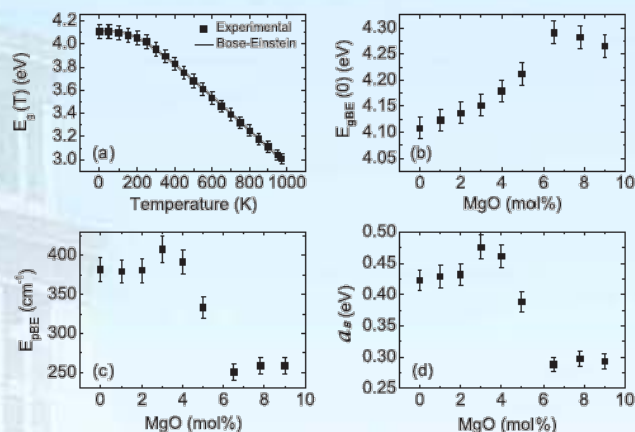


图 1. 名义纯同成分铌酸锂晶体的有效吸收带边的温度效应(a)、掺镁铌酸锂晶体的基本带隙(b)、爱因斯坦振子能量(c)、电声相互作用强度的掺镁浓度阈值效应。

Fig. 1 (a) The temperature dependence of the effective band energy gap of the pure congruent LiNbO_3 . The dependence of (b) the fundamental band gap at 0 K, (c) the average energy of the Einstein oscillator, and (d) the strength of the electron-phonon interaction on the Mg-doping concentration, respectively.

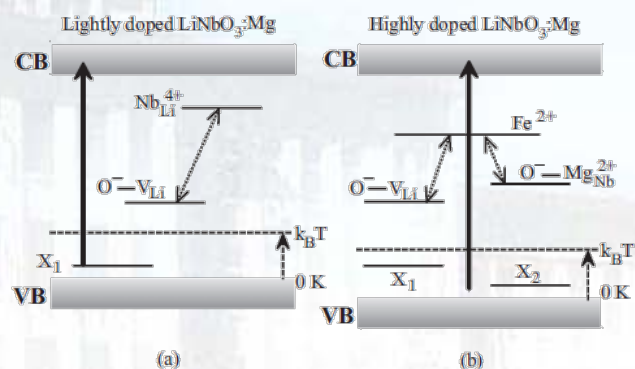


图 2. 掺镁浓度低于阈值(a)和高于阈值(b)的铌酸锂晶体的带边缺陷结构示意图。

Fig. 2 Schematic diagrams of the band structure and energy levels of various effective defect centers in the lightly (a) and highly (b) doped $\text{LiNbO}_3:\text{Mg}$ crystals, respectively.

基于多路径双光子相长干涉, 我们实现了经典热光的双光子超聚束效应, 显示了在线性系统中调控热光聚束性质的可能性。通过在传统的 HBT 干涉仪中串联地插入 n 对

一阶非相干的光学通道，热光的双光子聚束比可达到 2×1.5^n ，远远超过传统 HBT 干涉仪热光双光子聚束比的理论极限值 2。当在传统的 HBT 干涉仪中插入 1 对一阶非相干的光学通道时，实验测得的热光双光子聚束比为 2.4 ± 0.1 。这种插入了 n 对一阶非相干光学通道的 HBT 干涉仪可以看成是一个双光子光栅。

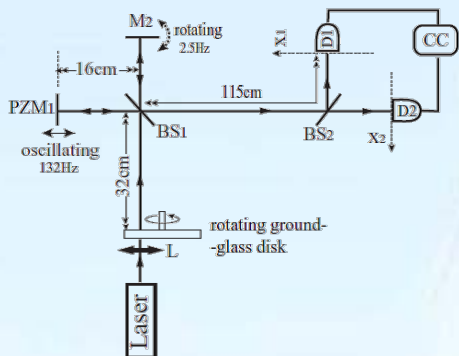


图 3. 热光的双光子超聚束效应实验装置图。

Fig. 3 Experimental scheme for the two-photon superbunching of thermal light..

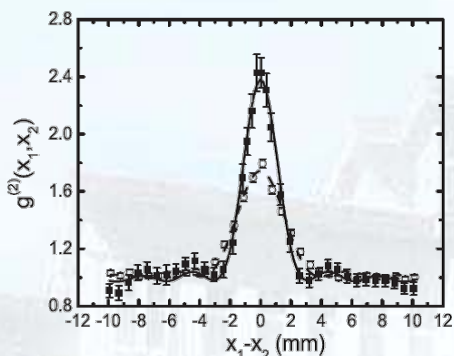


图 4. 热光的双光子聚束效应。

Fig. 4 Two-photon superbunching effect of thermal light.

We demonstrate the two-photon superbunching effect of thermal light via constructive multiple two-photon path interference, showing the possibility of controlling the bunching property of thermal light in a linear optical system. By inserting n -pairs of mutually first-order incoherent optical channels cascadingly into the traditional Hanbury Brown and Twiss (HBT) interferometer, the two-photon bunching peak-to-background ratio of thermal light can be increased by up to 2×1.5^n , surpassing the

theoretical upper limit of 2 for a traditional HBT interferometer. Experimentally, the ratio was measured to be 2.4 ± 0.1 when one pair of optical channels was inserted. Such a scheme can be viewed as a prototype of a two-photon grating.

通过声光可调谐滤波器 (AOTF) 的模式转换作用和锥形光纤的倏逝波导出效应，我们制作了快响应话路上下行转换器。该转换器继承了声光可调谐滤波器的特性，具备输出强度和中心工作波长可调的特点。工作插入损耗在 -5.1dB 。和类似的基于长周期光纤光栅的转换器相比，具有快速调谐的特性。这种结构可以广泛应用于粗波分复用结构中。

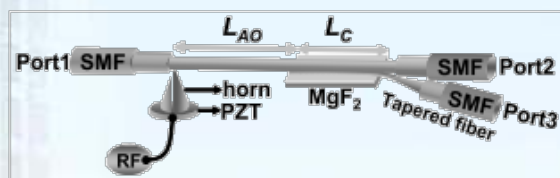


图 5. 基于 AOTF 的话路上行下行转换器配置。PZT 为压电驱动器， L_{AO} 为声光作用长度， L_C 为耦合长度，该区域浸在折射率匹配液中并置于 MgF_2 衬底之上。

Fig. 5 The experimental configuration of the tunable add/drop channel coupler. L_{AO} is the length of AO interaction region, L_C is the length of evanescent wave coupling region supported by a low-index MgF_2 substrate and dipped into a refractive-index-matched liquid.

We report a tunable add/drop channel coupler based on an acousto-optic tunable filter and a tapered fiber. The coupling efficiency and central wavelength of the add/drop channel coupler are tunable by simply tuning the power and frequency of the driving radio frequency signal. Further possible improvements on the configuration are also discussed. Compared with the structure based on long period fiber gratings, our configuration is of much faster tunability. Such add/drop couplers are very useful for coarse WDM applications.

基于非线性光学效应和法布里-珀罗腔的共振效应，我们有效提高了横向相位调制效应导致的慢光的延迟和快光的超前。作为

示例，我们计算了非线性介质为红宝石晶体的具体情况。计算表明，通过引入一个共振的法布里珀罗腔，慢光的相对延迟可以被提高几个数量级。慢光相对延迟共振增强技术可能在光信息处理和光通信等领域具有潜在的应用。

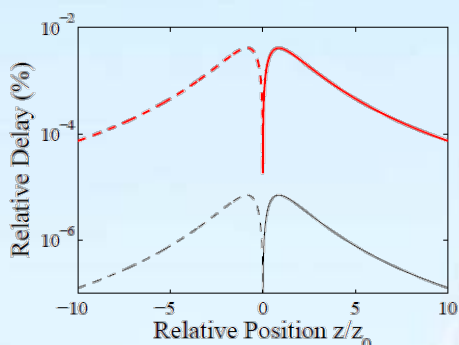


图 6. 有无共振腔两种情况下，信号光相对延迟（实线）或者超前（虚线）量与非线性介质位置之间的关系曲线。

Fig.6 The dependence of the relative delay (solid curve) or advance (dashed curve) on the position of the nonlinear medium with (red curves) and without (black curves) the resonant Fabry-Perot cavity.

A technique to improve the transverse-modulation-induced relative delay of light in nonlinear media through the combination of an optical nonlinearity and a resonant Fabry-Perot cavity was introduced and theoretically demonstrated in ruby as an example. The introduction of a resonant Fabry-Perot cavity can improve the relative delay by orders of magnitude. The techniques of resonant improvement of the group delay of light may have potential applications in optical information processing and optical communication network.

我们研究了一种基于耦合金属波导的新型多功能集成全光逻辑门，这个器件可以实现 AND, OR, XOR, 与 NOT 四种逻辑操作，超小尺寸的特点使得该器件成为高密度纳米集成器件的一种吸引人的候选。

A novel design of ultrasmall multifunctional Boolean logic gates is proposed in our work. This interferometric logic device is based on coupled metal

waveguides. This structure is theoretical analysis and logic performances are proved by using finite-difference time-domain (FDTD) method. The single device can perform individually four different kinds of basic functions: AND, OR, XOR, and NOT operations. The device with extremely small feature size is an attractive candidate for high density nano-photonic integrated circuits.

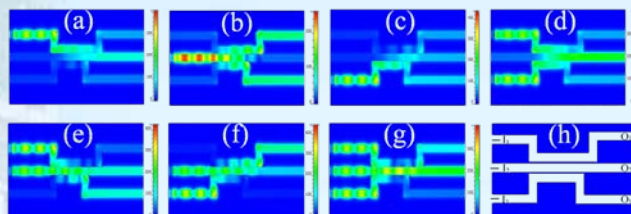


图 7. 全光逻辑门的磁场 y 方向的强度分布，(a) - (c) 只有一个波导有信号输入 (d) - (f) 有两个波导有信号输入 (g) 三个波导均有信号输入 (h) 逻辑门的结构图。

Fig.7 Simulated time-averaged intensity of Hy distributions in the logic device when optical signals are launched into one or more of the three MGWs.(a)-(c),only one waveguide is turned on; (d)-(f), only one waveguide is turned off; (g), all waveguides are turned on;(h) the structure of the logic gates.

TABLE I

The truth table of AND gate with $I_1 = 1$.

Input intensity		Output intensity	Output logic value of W_1
I_2	I_3	O_1	
0	0	0.10	0
0	1	0.10	0
1	0	0.035	0
1	1	0.26	1

表 I, 当 $I_1 = 1$ 时，AND 门的真值表。

TABLE II

The truth table of OR gate with $I_2 = 1$.

Input intensity		Output intensity	Output logic value of W_2
I_1	I_3	O_2	
0	0	0.014	0
0	1	0.18	1
1	0	0.41	1
1	1	1.01	1

表 II, 当 $I_2 = 1$ 时, OR 门的真值表。

TABLE III

The intensity and the truth table of XOR gate

with $I_1 = 0$.

Input intensity		Output intensity	Output logic value of W_3
I_2	I_3	O_3	
0	0	0	0
0	1	0.19	1
1	0	0.22	1
1	1	0.0030	0

表 III, 当 $I_1 = 0$ 时, XOR 门的真值表。

我们利用 AAO 模版, PDMS 作为基质, 用软印模的方法制作了大面积, 低成本的表面增强拉曼基底。我们研究了不同孔径 AAO 为模版制作的 SERS 基底的性能差异, 发现在我们的研究范围, 随着 AAO 孔径增大, 印模出来的纳米面条团簇中的纳米面条直径也随之增大, 同时 SERS 基底的拉曼增强因子也随之增大。实验测试结果表面, 我们的 SERS 基底, 具有均匀性好、面积大、超灵敏(增强因子大于 2×10^7) 等优点, 在定量、定性的化学、生物分析研究中具有巨

大的应用潜力。

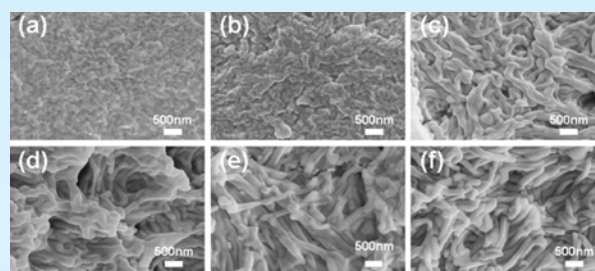


图 8. SERS 基底的顶视 SEM 图像, a-f 分别对应 AAO 孔径为 15nm, 25nm, 55nm, 90nm, 130nm, 180nm 为模版制作出的 SERS 基底。

Fig.8 The top viewed SEM images of nanonoodles clusters SERS substrates, (a) to (f) are the SEM images of Substrate1 to Substrate6, respectively.

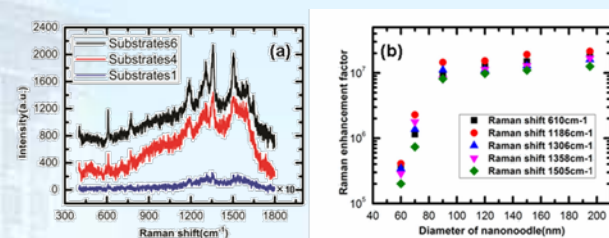


图 9 (a) 1×10^{-6} M R6G 的表面增强拉曼光谱; (b) 6 个 SERS 基底的拉曼增强因子, 25nm, 55nm, 90nm, 130nm, 180nm 为模版制作出的 SERS 基底。

Fig.9 (Color online) (a) SERS spectra of 1×10^{-6} M R6G solution on Substrate1, Substrate4 and Substrate6; (b) The enhancement factors of Substrate1 to Substrate6 for the characteristic Raman peaks of R6G, 610 cm^{-1} , 1186 cm^{-1} , 1306 cm^{-1} , 1358 cm^{-1} , and 1505 cm^{-1} , respectively.

A large-area low-cost and ultrasensitive surface-enhanced Raman scattering (SERS) substrate fabricated by soft-lithography and ion beam sputtering deposition is described. A batch nanofabrication method is developed to create ordered array PolyDiMethylSiloxane (PDMS) nanonoodles cluster structure by soft-lithography with bi-pass anodized aluminum oxide (AAO) membrane using as replication template. Depositing 50nm Au film onto the cluster template, ultrasensitive SERS substrate is fabricated. Raman enhancement factors of different diameter nanonoodles cluster substrates, which replicated from different pore diameter AAO, are measured. The results show that remarkable Raman enhancement is present for all the SERS substrates, the enhancement factor increases

with the increasing of the nanonoodle diameter dealt with in our experiments and a highest enhancement factor larger than 2.14×10^7 is obtained. The strong Raman enhancement is attributed to the existence of plenty nano-gaps constructed between the PDMS nanonoodles. This work provides a method to produce highly Raman-enhancing SERS substrates for potential applications.

我们研究了多层金属壳核结构的光激发性质。通过偶极子近似计算模拟研究，我们发现，由于对称性破缺，激发光谱对于光的偏振方向非常敏感。另外，由于壳层金属和金属核心的耦合作用，我们发现一个额外的表面等离子共振峰和比纳米杯结构更好的光谱可调性。通过改变几何结构，激发峰可以轻易地被调到近红外区域，激发峰对于环境介质的变化非常敏感，这些都为制作角度选择的灵敏生物传感器提供的有力的支持。并且，我们还在多层金属壳核纳米颗粒中引入了“二维”对称破缺（两个孔），并研究了其激发光谱特性。我们发现激发光谱对于两个孔的大小、相对位置等参数都非常敏感。

Symmetry breaking in gold nanoshell (or multilayer nanoshells) can supply many interesting optical properties, which has been studied in gold nanostructures such as nanocup, nanoegg, and core offset gold-silica-gold multilayer nanoshells. In this work, the optical extinction properties of the perforated gold-silica-gold multilayer nanoshells are studied by the discrete dipole approximation method simulations and plasmon hybridization theory. The extinction spectra of these particles are sensitive to the orientation of the particle with respect to polarization of the light due to the symmetry breaking. Because of the coupling of the plasmon resonance modes between the inner gold sphere and the outer nanocup structure, the perforated gold-silica-gold nanoshell provides the additional plasmon resonance peak and an even greater spectral tunability

comparing with the nanocup of similar dimensions. By changing the geometry of the particles, the extinction peaks of the particles can be easily tuned into the near-infrared region, which is favorable for biological applications. The local refractive index sensitivity of the particles is also investigated, and the multiple extinction peaks simultaneous shift is found as surrounding medium is altered. The perforated gold-silica-gold multilayer nanoshells may provide various applications ranging from angularly selective filters to biological sensors.

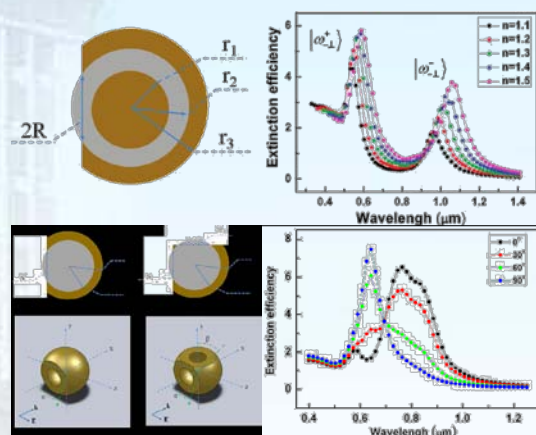


图 10. 多层壳核结构图以及相应的激发光谱图

Fig.10 Multilayer nanoshells structures and the corresponding extinction spectra

We also studied the optical extinction properties of Au nanoshell with two holes by the discrete-dipole approximation method. We found that the extinction spectra of the nanoparticles are sensitive to the angle between the polarization vector of the incident light and either symmetrical axis of the hole on nanoshell and also the sizes of two holes. The nanostructure we proposed provides the additional dimensional angularly selectivity of the optical properties and the plasmon resonances redshift comparing with the nanocup. In addition, the conception of the “two-dimensional” symmetry breaking of the nanoparticle is suggested which can induce the two-dimensional spatial asymmetry of optical

properties of nanoparticles.

在亚波长金属狭缝内嵌入凹槽后，狭缝的透射峰发生红移、蓝移，也可能不变。本文利用有限时域差分法，详细讨论了内嵌凹槽深度对狭缝透射光谱的影响。通过与腔共振模式理论对比，我们发现内嵌凹槽的亚波长金属狭缝透射峰变化一方面来自于共振腔长度的增长，另一方面来自于透射峰所对应的共振模式数的增加。透射峰蓝移等变化均为共振模式数改变和共振腔长度增长共同作用的结果。

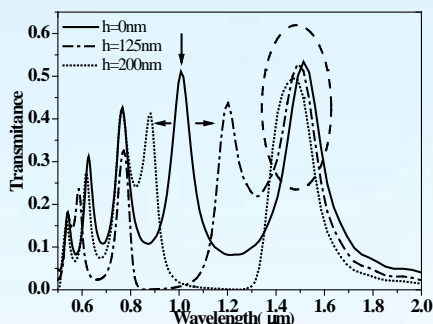


图 11. 凹槽狭缝透射谱，其中 $L=1\ \mu\text{m}$, $d=50\text{nm}$ 。图中实线、点划线和点线分别对应于内嵌凹槽高度 $h=0\text{nm}$, 125nm 和 200nm 的情形

Fig.11 Transmission spectrum of slit on the depth of the embedded groove, here $L=1\ \mu\text{m}$, $d=50\text{nm}$. The real line, dash-dot line and dot line show the transmission spectrum of slit when the height of the embedded grooves are 0nm , 125nm and 200nm

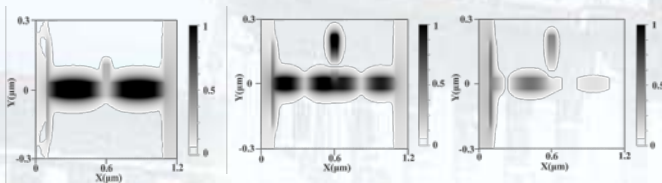


图 12 内嵌凹槽狭缝内磁场强度分量 H_z 分布示意图 (a) 入射波长 $\lambda=1510\text{nm}$, $h=75\text{nm}$ (b) 入射波长 $\lambda=900\text{nm}$ 时, $h=200\text{nm}$ (c) 入射波长 $\lambda=1100\text{nm}$, $h=200\text{nm}$

Fig.12 Schematic illustration of the distribution of the z component of the magnetic density in the slit embedded with a groove inside. (a) incident wavelength $\lambda=1510\text{nm}$, $h=75\text{nm}$; (b) incident wavelength $\lambda=900\text{nm}$, $h=200\text{nm}$; (c) incident wavelength $\lambda=1100\text{nm}$, $h=200\text{nm}$.

The subwavelength metal slit changes in its transmittance properties if embedded with a groove inside. Red-shift, blue-shift or no shift may happen. In this work, we study the dependence of the transmission spectrum of slit on the depth of the embedded groove by

using the Finite Difference Time Domain method. Comparing with the results from cavity resonance mode theory, we find that the shift situation of the subwavelength metal slit comes from two reasons, increase in the cavity length and the increase in the resonance mode number. The spectrum changes, such as blue-shift, are the hybrid results of the increase in both of the mode number and the cavity length.

研究了内嵌凹槽的狭缝阵列对光束的调控作用，结果显示通过改变内嵌凹槽的高度，可以控制透射场的相位，来实现光束的调控。我们设计了两种具有不同凹槽高度分布的狭缝阵列，在亚波长尺度内分别实现了光束的聚焦和偏转。

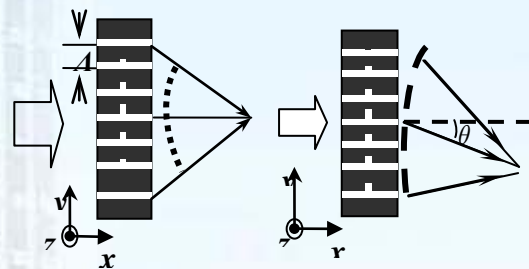


图 13. 纵切金属纳米狭缝阵列示意图。

Fig.13 Scheme of metallic nanoslit array with perpendicular cuts.

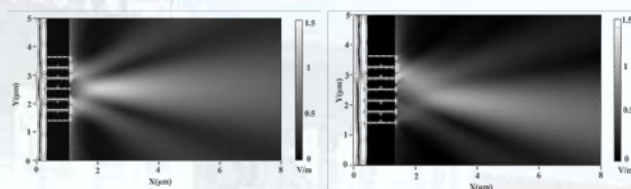


图 14. 透过纵切金属纳米狭缝阵列的光的电场分布图。

(a) 聚焦; (b) 偏向。

Fig. 14 Electric field of transmitted beam after slit array with cuts (a) focusing (b) deflection.

Beam manipulation by metallic nanoslit arrays with perpendicular cuts inside slits was investigated numerically. The simulated results performed by finite element method (FEM) show that perpendicular cuts with different heights can modulate phase retardation of the transmitted light through the slits. With the proper distribution of cuts height, a focused beam is achieved in our

metallic nanostructure with four-time amplitude at the focus point and half focal length compared to a slit array without cuts inside. By using asymmetric distribution of height amplitude, a beam deflection around 6° can be also realized in our design.

我们实验和理论研究了光束在六角光子晶格中的对称破缺线性衍射及非线性自陷的传播行为。我们发现条形的多涡旋光在线性条件下表现为非对称的线性衍射，而在自散焦非线性下会演化成能在光子晶格中横向移动的自陷态。而且我们也观察到椭圆形多涡旋光束也存在类似的对称破缺衍射行为。我们的结果提供了一种利用周期结构来控制光束传播的新方法。

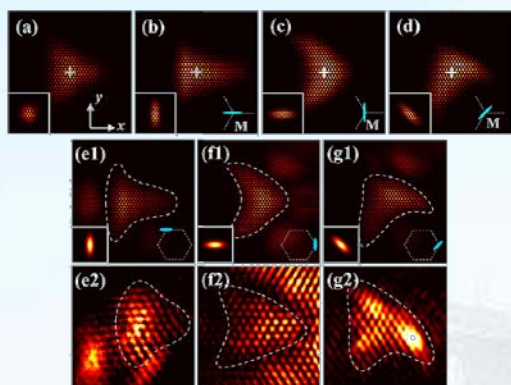


图 15 椭圆形的多涡旋光束在六角晶格中的对称破缺衍射的数值模拟 (a-d, e1-g1) 和实验结果图 (e2-g2). (a-d, e1-g1) 为传播距离 $z=400$ 处的出射光强分布, 其中的插图分别是入射光强分布及在空间频谱 M 点处的分布; (e2-g2) 为对应 2cm 传播长度上的出射光强分布.

Fig.15 Numerical (a-d,e1-g1) and experimental (e2-g2) results of symmetry-breaking diffraction of elliptical multivortex beams in a hexagonal lattice. (a-d,e1-g1) display the output intensity patterns at $z=400$ (about 5.3 cm in experimental condition) with the centers of the input beam marked by the white crosses, where the insets show the input beams and the distribution of the power spectra at the M point; (e2-g2) show the corresponding experimental output light intensity patterns after propagation in a 2cm-long SBN crystal.

We demonstrate both experimentally and numerically linear symmetry-breaking diffraction and nonlinear dynamic self-trapping of an optical beam in hexagonal photonic lattices. We show that a stripe multivortex beam undergoes asymmetric linear diffraction, but evolves into a moving

self-trapped beam under a self-defocusing nonlinearity. Fine features of symmetry-breaking in diffraction of elliptical multivortex beams are also observed and discussed. Our findings bring about an approach to control the flow of light with periodic photonic structures.

我们在六角光子晶格中实现了利用折射率结构的改变来调控布洛赫波的传播行为。其调控的原理是基于单个原胞格点折射率分布的不同从而导致带隙结构中某些高对称点附近衍射曲线变化。通过每个原胞格点的折射率取向的改变, 布洛赫模式的运动方向可以被控制。我们的理论结果和实验结果在光折变晶体中诱导的各向异性六角光子晶格中得到了验证。这种现象也能在其它具有相同对称性的周期系统中实现。

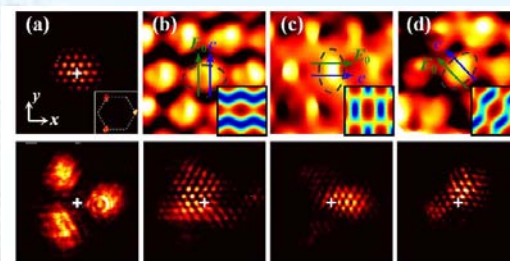


图 16. 光诱导六角晶格中由格点取向不同导致的布洛赫模式移动的实验结果图。(a) 入射光强分布 (上) 与没有晶格存在时候的线性衍射。(b) - (d) 在不同外加偏压方向下的各项异性六角晶格 (上) 与对应的出射光强分布 (下); 插图对应数值模拟的晶格折射率分布.

Fig 16. Experimental observation of the self-shifting Bloch modes in light-induced hexagonal lattices. (a) Input profile (top) and linear output without lattice (bottom); the inset shows the k-space spectrum. (b)-(d) Output beam profiles (bottom) in the anisotropic hexagonal lattices (top) under different bias conditions; insets depict the corresponding calculated lattice index profiles.

We study controllable self-shifting Bloch modes in anisotropic hexagonal photonic lattices. The shifting results from a deformed band structure due to deformation of the index distribution in each unit cell. By reconfiguration of the index profile of the unit cell, the direction in which the Bloch modes move can be controlled. Our theoretical predictions are experimentally demonstrated in hexagonal lattices optically induced in an

anisotropic nonlinear crystal. These wave phenomena are expected to occur in other periodic systems with similar symmetry.

我们理论和实验研究了有限大小的截断艾里光束在非线性光折变晶体中的改变其传播轨迹同时能够保持加速的传播行为。我们发现在这个过程中，其空间频谱相对于线性情形下发生了重整效应，具体来说，在自聚焦非线性下会频谱上产生一个负缺陷，而在自散焦非线性下会形成一个正缺陷。这种非线性对艾里光的调控也可以扩展到非傍轴的艾里光。

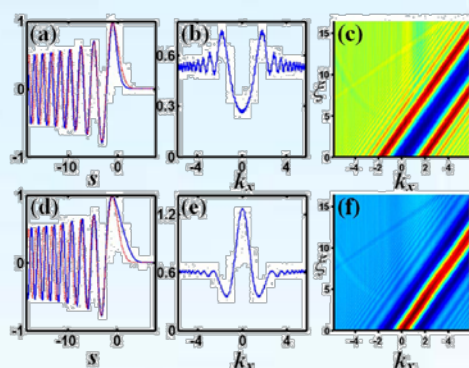


图 17 饱和非线性下的非线性自加速解。(a)和(d)分别是自聚焦和自散焦非线性下的自加速非线性模式。(红色的曲线对应的是线性的无限的艾里光束)。(b)和(e)分别是(a)和(d)对应的空间频谱。(c)和(f)分别是自加速模式(a)和(d)在非线性传播过程的空间频谱分布。

Fig.17 Nonlinear self-accelerating solutions under saturable nonlinearities. (a) and (d) Self-accelerating modes under self-focusing and -defocusing nonlinearities, respectively. (The red dashed curve corresponds to a linear infinite Airy beam). (b) and (e) Spectra corresponding to (a) and (d). (c) and (f) Spectral distribution during the nonlinear propagation of the self-accelerating modes in (a) and (d), respectively.

We demonstrate theoretically and experimentally that a finite Airy beam changes its trajectory while maintaining its acceleration in nonlinear photorefractive media. During this process, the spatial spectrum reshapes dramatically, leading to negative (or positive) spectral defects on the initial spectral distribution under a self-focusing (or defocusing) nonlinearity. Such nonlinear control may be applicable to

nonparaxial accelerating beams, and may prove useful for exploiting these beams for various important applications.

分子或晶格结构具有手性对称性的物质将表现出旋光效应，其包括圆双折射 (Circular birefringence) 与圆二相色性 (Circular dichroism)。前者可使得入射波偏振极角发生转动，起源于物质对于左、右旋偏振波的折射率差别；而后者产生于左、右旋电磁波的吸收率不同，进而引起电磁波椭圆偏度的改变。作为 21 世纪新的人工材料，超颖材料的出现使得人们可以按照不同的需要设计旋光材料，且效应强度远远大于天然物质。超颖材料存在的等离子体激元可以将电磁能量束缚于表面亚波长的尺度内，产生极强的电磁能量密度，增强该尺度内包括非线性效应在内的多种光学效应发生的幅度。本文将超颖材料所具有的强旋光效应同其强非线性性质相结合，研究激光对其旋光效应的非线性控制能力。在 50nm 金膜表面利用聚焦离子束 (FIB) 加工出非对称裂环超颖材料，该结构对于斜入射于其上的激光将具有外手性 (Extrinsic chirality) 旋光作用。由于超颖材料在光波段具有不可避免的损耗，出射光的偏振极角与椭圆偏度均发生变化。提高入射飞秒激光功率，激发超颖材料中的双光子吸收过程，其旋光效应的幅度将发生改变，即发生非线性旋光效应。文中在共振波长，实现了 $3 \times 10^{-40} \text{cm/W}$ 的非线性旋光率，比天然旋光晶体 LiIO_3 强 3000 万倍，使得传统上认为极弱的非线性旋光效应在较弱的光强水平 (2GW/cm^2) 上仍然可以得到观察。巨非线性偏振效应的实现为非线性等离子体超颖材料在纳米尺度内实现光强和偏振调制器的应用提供了可能，并可应用于量子通信等领域中。

The phenomenon of natural optical activity is inextricably linked to chirality. In many optically active media, chirality resides in the left-right asymmetry of the constituent components of the medium. For instance, a liquid consisting of only one form of chiral molecules, that is, molecules that are not congruent with their mirror image, is likely to

exhibit optical activity.

The metamaterial consists of a periodic array of asymmetric split ring slits, which were cut by focussed ion-beam milling through a 50 nm thick gold film, as shown by SEM image of the inset of Fig 1 (a). Figure 1 (b, c) illustrate the metamaterial's linear (low-power) optical properties for wavelengths between 930 and 954 nm, where the metamaterial has a plasmonic resonance and optical activity is largest. The specific constant of nonlinear optical activity (NOA) is $3 \times 10^{-4} \text{ cm/W}$, which is more than 7 orders of magnitude stronger than NOA in natural materials such as LiIO_3 (10^{-11} cm/W), thus transforming this fundamental phenomenon of polarization nonlinear optics from an esoteric phenomenon into a major effect of nonlinear plasmonics with potential for practical applications.

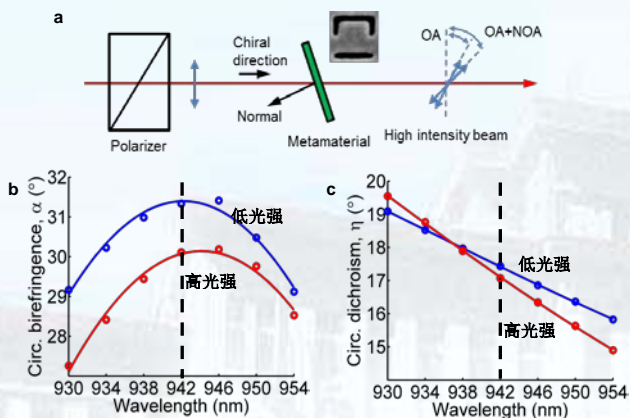


图 18 (a) 用于测量超颖材料中巨非线性旋光效应的光学系统示意图 (b, c) 超颖材料旋光效应在不同功率激光激发下的色散特性, 其等离子共振波长位置由虚线指示

Fig 18 (a) The setup for measurement of giant nonlinear optical activity from metamaterials. (b, c) Optical activity in terms of (b) circular birefringence (polarization rotation) and (c) circular dichroism (ellipticity angle) at linear (blue) and nonlinear (red) average power levels. Vertical dashed lines indicate the wavelength of 942 nm for which the plasmonic resonance locates.

结合宽场荧光寿命成像技术和远程重聚焦系统, 我们构建了一套时间分辨三维荧光光谱系统。这套系统可以在不扰动样品的情况下, 实现空间三维、时间分辨的光谱成

像。这套系统的时间分辨率可以达到 30 皮秒, 空间分辨率 1 微米, 光谱范围从 300nm 至 900nm。该系统有望在物理、化学、生物等方面的瞬态研究中得到应用。

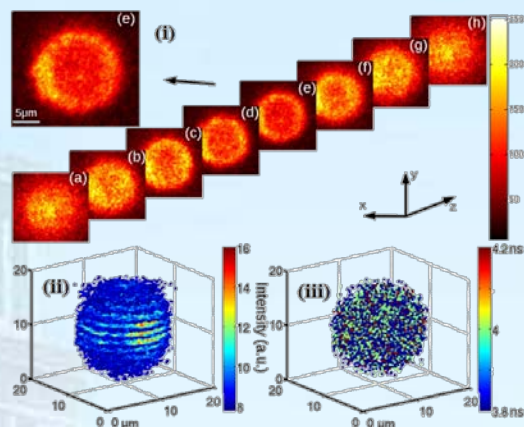


图 19 (i) 荧光微球的三维荧光强度成像的剖面图。 (ii) 从剖面图重构的三维荧光强度图。 (iii) 从二维荧光寿命图重构的三维荧光寿命图

Fig 19. (i) 3D fluorescence intensity image sections of a fluorescent microsphere as test sample with the mirror M on different positions along the optical axis. The gating time of the ICCD is 200 ps. (ii) 3D image of the sample reconstructed from these sections; (iii) 3D lifetime image of the sample reconstructed from 2D lifetime image sections with the mirror M on different positions.

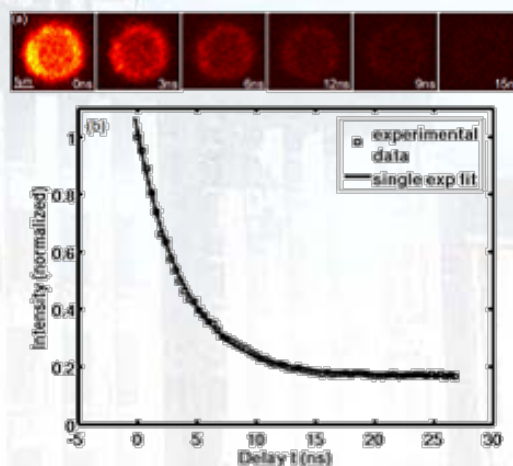


图 20 (a) 二维荧光寿命图。(b) 荧光强度的时间衰减曲线, 其中方块是实验数据, 实线是拟合数据。寿命拟合为 4.1 纳秒
Fig 20. (a) 2D fluorescence lifetime images of section (e) in Fig. 2 (i). (b) Decay curve of the fluorescence intensity; squares are experimental data points, solid curve is a single exponential fit to the data. The decay time is 4.1 ns.

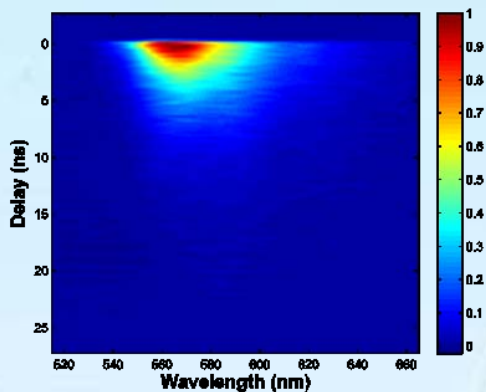


图 21 样品的时间分辨荧光图。横轴标志光谱波长，纵轴是衰减时间，伪彩标识荧光强度

Fig 21. Time-resolved fluorescence spectra of the sample. The fluorescence intensity is displayed in a pseudo-color mode as a function of both wavelength (horizontally) and time after excitation (vertically)

Three-dimensional fluorescence lifetime microscopy is achieved by combining wide-field fluorescence lifetime imaging with a remote optical refocusing method. It can achieve three dimensional time-resolved fluorescence imaging without disturbing the specimen. The system with a temporal resolution of 30 picosecond, a special resolution of 1 micrometer, and a wavelength response from 300 nm to 900 nm, has some applications in dynamic research for physics, chemistry, or biology.

研究了衬底对石墨烯表面等离子元色散以及传播的影响，提出了一种可能的利用石墨烯表面等离子元实现物质非线性探测的手段。具体的研究中我们发现衬底的克尔非线性能改变石墨烯的局域程度，但是对归一化的传播距离影响较小。基于此，我们提出了可能的利用衬底非线性特性实现光场局域控制的方案。

The properties of surface plasmons localized at the interface between graphene and Kerr-type nonlinear substrates are investigated analytically. Although the relative propagation distance remains the same, the dispersion of graphene plasmons may be affected much by the inevitable nonlinear

effect of substrates. Specifically, the wavelength of graphene plasmons can be tuned by adjusting the nonlinear permittivity of substrates.

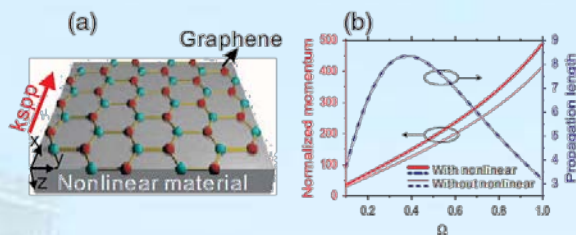


图 22 石墨烯与非线性介质的表面等离子元色散以及传播长度图。(a) 结构配置。(b) 存在与不存在介质非线性效应的色散关系与传播长度比较

Fig 22 (a) Sketch of an infinitely large graphene sheet lying on a substrate; k_{spp} represents the propagation direction of surface plasmons; (b) the dispersion relation (solid lines) and propagation distance (dashed lines) of GPs with (thick lines) and without (thin lines) nonlinear contributions from the substrate)

提出了利用石墨烯环作为高度可调的太赫兹波段光天线的应用方案。我们的研究表明太赫兹光能在石墨烯环中激发表面等离子元，表面等离子元的激发可以通过石墨烯带中的边界和波导模式来理解。在此过程中，远场辐射被转换为近场，实现了高度的光场局域。石墨烯环特别的性质是可以通过改变石墨烯的载流子浓度来改变其费米能级，从而实现等离子元共振波长的调控。

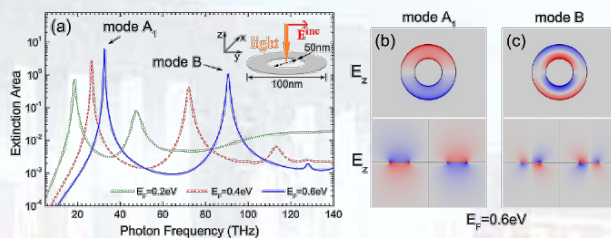


图 23 石墨烯圆环的表面等离子元共振 (a) 不同费米能量 (0.2eV, 0.4eV, 0.6eV) 石墨烯圆环的消光谱。(b) 对称模式和反对称模式表面等离子元的近场分布图

Fig 23 Surface plasmons excited by normally incident light in perfect graphene rings. (a) Extinction areas of self-standing graphene ring with three different Fermi energies of graphene. The dotted, dashed, and solid lines are corresponding to $E_F=0.2$ eV, 0.4 eV, and 0.6 eV, respectively. The inner and outer radii of the graphene ring are 25 nm and 50 nm, respectively. The extinction area is normalized to the area of the graphene ring. (b) and (c) show the z-component of electric near-field of plasmon mode A1 and B, respectively. The upper figures are under top view, while the lower figures are under section view.

Highly tunable optical antennas in terahertz range based on graphene ring structures are proposed, which employ graphene plasmons instead of traditional metallic plasmons. The plasmon resonances of the perfect graphene ring can be understood with the edge plasmons in graphene ribbons. While in the nonconcentric graphene ring, the multipolar plasmon modes appear and anti-symmetric mode splits due to symmetry breaking. Furthermore, the symmetric dipolar plasmon mode in a perfect graphene ring can concentrate electromagnetic field with an enhancement factor as large as 10^3 in terahertz waveband, which is almost 20 times larger than a gold ring with the same size.

我们采用快电子束激发的方式,在嵌套的银纳米圆环结构中,通过控制电子束激发的位置和采用边界元的理论方法,发现电子能量损失谱具有一系列的分立的损失峰,而该峰对应的等离激元模式与无限长耦合纳米线中的反对称模式符合的很好。研究表明电子束有效的激发了反对称耦合的回音壁模式,并且激发效率随着圆环结构的尺寸的改变而改变。我们的研究为产生反对称耦合表面等离激元提供了一种新的有效方案。

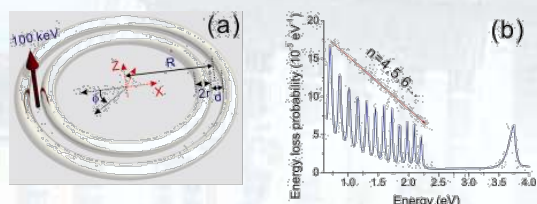


图 24. (a)快电子在嵌套纳米圆环中激发表面等离激元示意图。(b)电子能量损失谱。不同的峰值对应耦合反对称表面等离激元动量 n/R 。

Fig 24 Generation of whispering-gallery anti-symmetrically coupled plasmons in a curved coupled waveguide geometry ($R=1000$ nm, $r=30$ nm, $d=10$ nm). (a) Schematic of a nested ringlike waveguide with an electron beam (100 keV) traveling through the center of the gap. (b) Energy loss probability generation by electrons as indicated in (a).

Propagating anti-symmetrically coupled plasmons that usually cannot be excited with incident light and radiate to far field can be

efficiently generated by electron beams. An electron beam is proposed as a practical propagating anti-symmetrically coupled plasmon source due to that it couples differently to the surface plasmons than free radiation. Specifically, whispering-gallery anti-symmetrically coupled plasmons with the character of symmetrical coupled dipoles are excited by an electron beam in a nested ringlike waveguide, which is consistent with the dispersion of electron excited plasmons in an infinite-long nanowire pair.

自然界的太阳光可粗略的分为紫外(7%)、可见(50%)、红外(43%)三个部分,其中紫外所占比例虽然最小,但对人生命健康作用却不可小看:一方面其具有杀菌、促进维生素D合成、治疗慢性皮肤病等有益作用,另一方面可导致皮肤老化、白内障、免疫损伤等有害作用。研究发现超氧自由基是紫外对生物系统作用的一种主要效应产物,对各种生理病理现象有重要的调节作用。紫外光可直达肌肤的真皮层,照射到毛细血管内血液。血液的主要组成是红细胞,因此红细胞内大量的血红蛋白成为紫外光有效靶点。机体要维持正常生命活动的氧供应正是由血红蛋白完成。本文利用提纯的牛血红蛋白,体外研究紫外光辐照对其荧光性质的影响。结果表明,不同剂量的紫外光辐照可以显著提高其荧光强度(图1)。当血红蛋白溶液由过氧化氢(H_2O_2 ,一种超氧自由基)孵育处理后,紫外导致的荧光增强可以得到进一步提高。然而,不管血红蛋白溶液是否经过过氧化氢孵育处理,绿光辐照对其荧光强度并没有改善上作用。以上结果表明,过氧化氢在紫外导致的血红蛋白荧光增强过程中起催化作用,而且该荧光增强依赖于紫外辐照。本研究结果可为临床研究紫外光辐照提高血液保存时间的现象提供新的思考视角和实验依据。

Main source of visible and ultraviolet (UV) light is the nuclear fusion reactor in the middle of our solar system. Although certain skin diseases can be healed by a proper dose of UV radiation, UV light is in general

noxious: For instance, it may cause sunburn, photoaging, skin cancers, or immune suppression. Several factors play an crucial role in UVI-induced different cellular physiological and pathological responses. One of them is the production of reactive oxygen species (ROS) through a photosensitized mechanism involving energy transfer by chromophores to oxygen molecules. In this study we scrutinize the effects of ultraviolet irradiation (UVI) as well as visible irradiation on the fluorescence characteristics of bovine hemoglobin (BHb) *in vitro*. Data show that UVI results in fluorescence enhancement of BHb in a dose-dependant manner (Figure 1). Furthermore, UVI-induced fluorescence enhancement is significantly increased when BHb is pretreated with hydrogen peroxide (H_2O_2), a type of ROS. In contrast, green light irradiation does not lead to fluorescence enhancement of BHb no matter whether H_2O_2 is acting on the BHb solution or not. Taken together, these results indicate that catalysis of ROS and UVI-dependent irradiation play two key roles in the process of UVI-induced fluorescence enhancement of BHb.

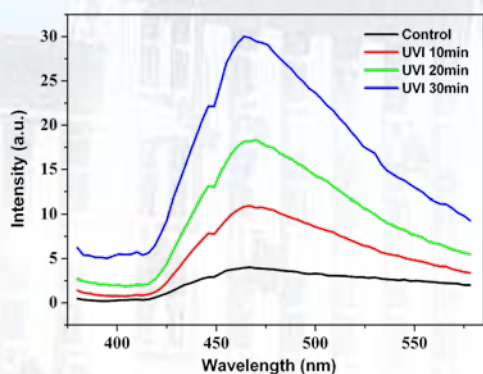


图 25 不同剂量的紫外光辐射引起血红蛋白荧光强度的变化。

Fig 25 UVI induces fluorescence enhancement of BHb in a dose-dependent manner. Spectra detection of BHb solution (at 365 nm excitation wavelength) after irradiation for 10 min, 20 min, and 30 min with 7 mW/cm^2 UV light. Black line is the fluorescence spectrum without prior UVI.

我们通过实验研究了硅酸锆微晶悬浊液中的相干背散射行为, 并在该正单轴微晶

悬浊液中成功利用泵浦光调控了光子的弱局域化行为。该现象是由于线偏振泵浦光作用下正单轴微晶的旋转取向行为引起的。我们在理论上分析了其旋转取向机制, 且理论分析结果与实现现象吻合。由于硅酸锆颗粒是正单轴微晶, 所以它们的再取向行为不同于负单轴微晶。该工作不仅极大地拓展了光控相干背散射中可用材料的范围, 而且验证了我们之前提出的单轴微晶悬浊液中微晶旋转取向行为的理论分析。

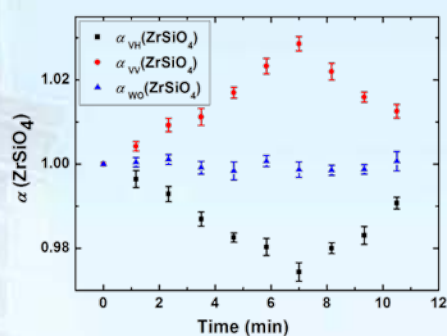


图 26 在三种不同偏振配置的情形下, 硅酸锆微晶悬浊液中相干背散射的半高宽 α 随时间的变化情况。

Fig 26 Temporal evaluation of the angular width of CBS cones from a water suspension of $ZrSiO_4$ particles.

Coherent backscattering of light from a water suspension of zirconium silicate microcrystals is experimentally studied. Optically controlled weak localization of photons is realized, which is due to the reorientation behaviors of positive uniaxial microcrystals induced by a linearly polarized pump beam. Because zirconium silicate particles are positive uniaxial microcrystals, their reorientation behaviors are contrary to negative ones. Our work widely extends the materials used in the light-controllable weak localization of photons.

提出了一种在硅基环形腔中基于四级受激拉曼散射效应实现 3427 nm 中红外激光输出的方案。我们用数值分析的方法讨论了该拉曼激光器的输入输出特性, 研究了自由载流子寿命、谐振腔长度、输入输出耦合比等参量对结果的影响。在此过程中, 我们发现了此激光器中的饱和输入现象。最后我们通过对此现象的分析, 提出了一种级联双环

拉曼器结构, 成功克服了该饱和现象的影响, 最终实现了功率更高、更稳定的中红外激光输出。

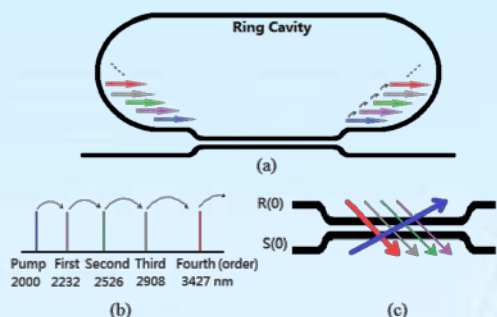


图 27 级联硅基拉曼激光器的方案: (a) 直线波导与环形谐振腔的结构 (b) 波长转换过程 (c) 定向耦合器。

Fig 27. Scheme of the fourth order silicon Raman laser: (a) the ring cavity and linear waveguide; (b) the wavelength transfer process; (c) the directional coupler.

We have numerically investigated the generation of a fourth order stimulated Raman scattering (SRS) signal in a silicon ring cavity. Output power saturation of the silicon Raman laser has been observed. The influences of effective free carrier life, length of ring cavity and coupling ratio on the signal generation are discussed based on our simulation work. Finally, we put forward a double ring cavity scheme to improve the output characteristics of the silicon Raman laser.

组织工程学的最终目标是利用细胞体外培养出具有生物学功能的大块组织或整个器官, 以期解决临床治疗过程中组织器官缺乏的问题。但由于生物组织器官的复杂性, 严重限制了组织工程技术发展和应用。动植物器官组织中的细胞在生长发育过程中往往呈现左右不对称性, 形态上往往呈现出特定的图案, 但体外培养的细胞却丧失该特性。前期我们基于光刻技术控制细胞生长的基底环境, 发现牛血管间质干细胞生长分化过程中极化方向发生左右对称性破缺, 极化方向偏好右转, 细胞最终自组织聚集成像的条纹呈现出一定的方向相似性。基于该结果, 本文依靠光刻图案化技术, 利用血管间质干细胞, 设计不同的图案化基底环境, 最终实现对细胞聚集图案的有效控制---体外模拟了肝脏最小单元肝小叶的血管二维辐射状

图案和骨最小结构骨单位同心圆图案(图 1)。该项研究为体外构建组织器官提供了一种新的设计原则, 可能有助于未来利用病人自己的干细胞体外构建组织器官, 有效解决以解决临床治疗过程中免疫排斥的问题。

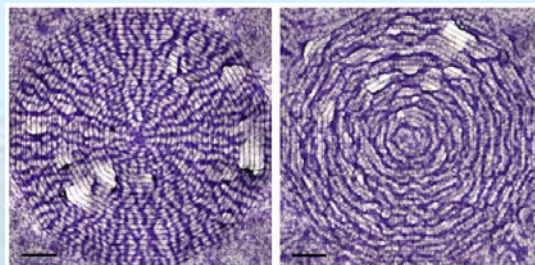


图 28 基于光刻技术的细胞图案化控制: 辐射状图案 (左) 和同心圆图案 (右)。

Fig 28 VMC patterns formed as radial (left) structures or concentric rings (Right).

Rebuilding injured tissue for regenerative medicine requires technologies to reproduce tissue/biomaterials mimicking the natural morphology. To reconstitute the tissue pattern, current approaches include using scaffolds with specific structure to plate cells, guiding cell spreading, or directly moving cells to desired locations. However, the structural complexity is limited. Left-right (LR) asymmetry often occurs in embryonic and tissue morphogenesis. However, observation of LR asymmetry is rarely reported in cultured cells. Previous study showed that vascular mesenchymal cells (VMCs) migrated along the same angle into neighboring aggregates, resulting in a macroscale structure with LR asymmetry as parallel, diagonal stripes evenly spaced throughout the culture. Here, by working in concert with cellular self-organization rather than against it, we experimentally demonstrate a method which directs self-organizing VMCs to assemble into desired multicellular patterns (Figure 2). Incorporating the inherent chirality of VMCs revealed by interfacing with microengineered substrates and VMCs' spontaneous aggregation, differences in distribution of initial cell plating can be amplified into the

formation of striking radial structures or concentric rings, mimicking the cross-sectional structure of liver lobules or osteons, respectively. As opposed to allocating cells to desired locations, the use of morphogenetic activity, e.g. cell migration and aggregation observed in embryogenesis and wound healing, permits the recapitulation of normal tissue architecture in a more natural way.

光谱表征及传感技术/Spectral Characterization and Sensing Techniques

负责人：宋峰

本方向涉及不同尺寸、形状的纳米颗粒的制备及其对稀土发光的影响以及应用光谱学和光谱仪器等方面。取得的代表性成果如下：

In this field, we mainly focused on the preparation of nanoparticles of different sizes and shapes and their influence on rare earth luminescence, applied spectroscopy and spectral instrument. This year, we obtained some important results, they are mainly shown as following:

通过宽光谱荧光上转换系统及皮秒分辨单分子计数两种测试手段测得了香豆素153在多种离子液体中的完整溶剂化响应过程，其测量时域为100fs到20ns。对于其中8种样品，检点介电连续场模型利用介电弛豫谱的文献报道值，对于该溶剂化响应过程做了预测。结果显示，溶剂化响应函数的预测值快于相应的测量值3到5倍，但随时间的演化趋势相似。同时，对溶质/离子液体系统的模拟计算结果也证实了这一差异，并且表明偏振响应过程的空间色散导致了介电连续场模型对溶剂化响应的预测偏差。

The complete solvation response of coumarin 153 (C153) has been determined over the range 10^{-13} – 10^{-8} s in a variety of ionic liquids by combining femtosecond broad-band fluorescence upconversion and picosecond time-correlated single photon counting measurements. These data are used together with recently reported dielectric data in eight ionic liquids to test the accuracy of a simple continuum model for predicting solvation dynamics. In most cases the features of the solvation response functions predicted by the dielectric continuum model are similar to the measured dynamics of C153. The predicted dynamics are, however, systematically faster than those observed, on average by a factor of 3–5. Computer simulations of a model

solute/ionic liquid system also exhibit the same relationship between dielectric predictions and observed dynamics. The simulations point to spatial dispersion of the polarization response as an important contributor to the over-prediction of solvation rates in ionic liquids.

利用溶胶凝胶法制备了 $\text{Er}^{3+}/\text{Yb}^{3+}$ 共掺 $\text{Y}_2\text{Ti}_2\text{O}_7$ 荧光粉，将其在 600°C 、 700°C 、 800°C 和 900°C 下分别进行退火处理。使用 X 射线衍射分析了样品的物相，根据 800°C 和 900°C 时出现的强烈衍射峰，说明样品得到很好地晶化。经 XRD 和 TEM 测试发现，随着退火温度的升高， $\text{Y}_2\text{Ti}_2\text{O}_7$ 发生了从非晶态到晶态的相变，相变温度约在 750°C 。

The $\text{Er}^{3+}/\text{Yb}^{3+}$ co-doped $\text{Y}_2\text{Ti}_2\text{O}_7$ phosphors were synthesized by the sol-gel method. Then the dry gel was annealed at 600°C , 700°C , 800°C and 900°C respectively. The phases of the samples were analyzed by X-ray diffraction. The samples annealed at 800°C and 900°C are well crystallized according to the strong diffraction. The XRD patterns and TEM micrographs illustrated that this kind of material would transform from the amorphous to nanocrystalline with increasing annealing temperatures and the transition temperature is about 750°C .

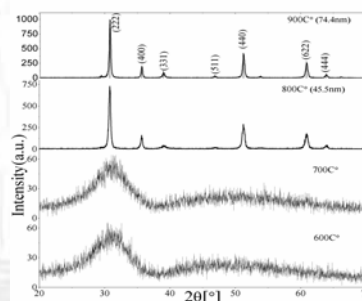


图1 分别在 720°C 、 740°C 、 750°C 、 760°C 、 780°C 退火一个小时的样品粉末 XRD。

Fig.1 XRD patterns of $\text{Er}^{3+}/\text{Yb}^{3+}$ co-doped $\text{Y}_2\text{Ti}_2\text{O}_7$ phosphors annealed at 600°C , 700°C , 800°C and 900°C for 1 h, respectively.

The complete solvation response of coumarin 153 (C153) has been determined over the range 10^{-13} – 10^{-8} s in a variety of ionic liquids by combining femtosecond broad-band fluorescence upconversion and picosecond time-correlated single photon counting measurements. These data are used together with recently reported dielectric data in eight ionic liquids to test the accuracy of a simple continuum model for predicting solvation dynamics. In most cases the features of the solvation response functions predicted by the dielectric continuum model are similar to the measured dynamics of C153. The predicted dynamics are, however, systematically faster than those observed, on average by a factor of 3–5. Computer simulations of a model solute/ionic liquid system also exhibit the same relationship between dielectric predictions and observed dynamics. The simulations point to spatial dispersion of the polarization response as an important contributor to the over-prediction of solvation rates in ionic liquids.

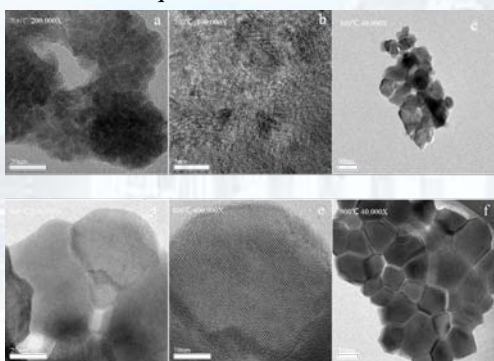


图2 $\text{Er}^{3+}/\text{Yb}^{3+}$ 共掺 $\text{Y}_2\text{Ti}_2\text{O}_7$ 在 700°C 退火的非晶态样品(a,b), 800°C 退火 (c,d,e) 和 900°C 退火的纳米晶 (f) 不同放大倍数的 TEM 图像。

Fig.2 TEM micrographs in various magnifications of $\text{Er}^{3+}/\text{Yb}^{3+}$ co-doped amorphous $\text{Y}_2\text{Ti}_2\text{O}_7$ annealed at 700°C (a and b) and nanocrystalline annealed at 800°C (c, d, and e) and 900°C (f), respectively.

分析了 $\text{Er}^{3+}/\text{Yb}^{3+}$ 共掺 $\text{Y}_2\text{Ti}_2\text{O}_7$ 的发光机理, 以及退火温度, 结构对其发光光谱的影响。分析了近红外和上转换光致发光的机理以及发光强度随退火温度的变化。上转换

发射强度随着温度持续增加, 但是近红外发射强度在 800°C 出现下降, 并分析了造成这种现象的原因。

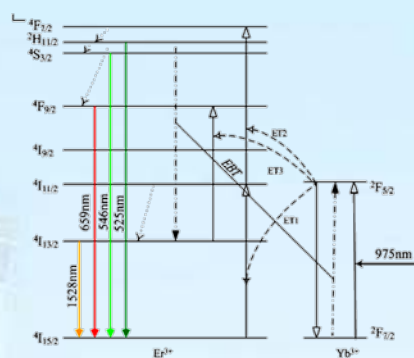


图3. $\text{Er}^{3+}/\text{Yb}^{3+}$ 的能级图以及在 975nm LD 激发下的发光过程, 包括: 无辐射多声子弛豫 (虚线), 能量转移 (ET) 和能量反向传递 (EBT)。

Fig. 3 Energy level diagrams of Er^{3+} and Yb^{3+} , as well as the proposed PL processes under 975 nm LD excitation including non-radiative multiphonon relaxation, ET and EBT (dotted lines: non-radiative multiphonon relaxation).

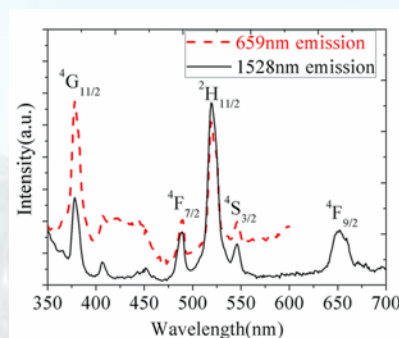


图4. 800°C 退火的 $\text{Er}^{3+}/\text{Yb}^{3+}$ 共掺 $\text{Y}_2\text{Ti}_2\text{O}_7$ 纳米晶样品的激发谱, 发射波长分别为 659nm 和 1528nm 。

Fig.4 Excitation spectra of $\text{Er}^{3+}/\text{Yb}^{3+}$ co-doped $\text{Y}_2\text{Ti}_2\text{O}_7$ nanocrystalline sample annealed at 800°C when the emissions wavelengths are fixed on 659 nm and 1528 nm .

The luminescence mechanism and influences of the annealing temperature, and the lattice structure on luminescence spectra of $\text{Er}^{3+}/\text{Yb}^{3+}$ co-doped $\text{Y}_2\text{Ti}_2\text{O}_7$ were discussed. The mechanism of NIR and UC PL, and the changes of the PL intensity with annealing temperatures were also discussed in detail. The intensity of UC emissions continuously increases with increasing annealing temperatures, but the intensity of NIR emission increases initially and then falls

down after 800°C. The EBT process extraordinarily contributes to the population of $^4I_{13/2}(Er^{3+})$ state and the red UC emission, and further causes the saturation of $^4I_{13/2}(Er^{3+})$.

通过高温熔融法制备了 $Yb^{3+}/Er^{3+}/Tm^{3+}$ 共掺的磷酸盐玻璃, 退火后, 形成玻璃陶瓷。通过 XRD 测量发现在玻璃陶瓷中形成 $LiYbP_4O_{12}$ 和 $Li_6P_6O_{18}$ 纳米晶, 玻璃陶瓷的上转换发射强度明显高于玻璃。

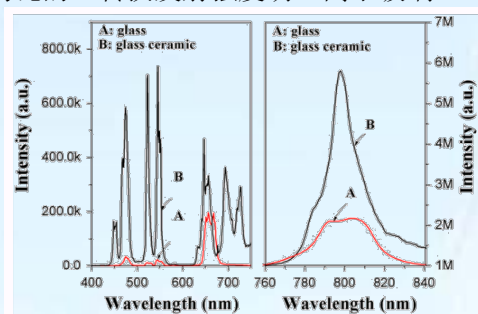


图 5. 玻璃和玻璃陶瓷的上转换发射光谱。

Fig. 5. UC emission spectra of the precursor glass and GC.

By high-temperature melting method, $Yb^{3+}/Er^{3+}/Tm^{3+}$ co-doped phosphate glass was synthesized. After annealing the precursor glass, the phosphate glass ceramic (GC) was obtained. By measuring the X-ray diffraction (XRD) spectrum, it is proved that the $LiYbP_4O_{12}$ and $Li_6P_6O_{18}$ nanocrystals have existed in the phosphate GC. The up-conversion (UC) emission intensity of the GC is obvious stronger compared to that of the glass.

通过研究上转换发射对于泵浦功率的依赖关系, 发现 Er^{3+} 的 523nm 和 546nm 绿色发光是双光子过程。但是在玻璃陶瓷中, 绿色发光是两个/三个光子过程, 这表明三光子过程参与到了其中。

By studying the dependence of UC emissions on the pump power, the 523 and 546 nm green emissions of Er^{3+} ions in the glass are two-photon processes. But in the glass ceramic, they are two/three-photon

processes. The phenomenon implies that a three-photon process has participated in the population of the two green emissions.

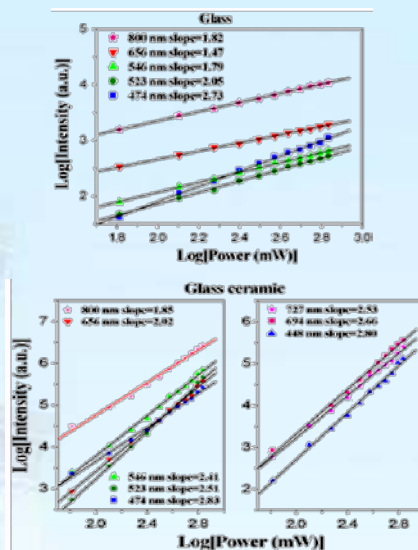


图 6. 上转换发射强度与泵浦功率的关系。

Fig. 6. Log-log plots for the dependence of the up-conversion emissions intensities on pump power.

我们讨论了 Er^{3+} 和 Tm^{3+} 的能量传递, 结果显示在玻璃陶瓷中 Tm^{3+} 到 Er^{3+} 的能量传递很强, 改变了 Er^{3+} 的上转换发射过程。

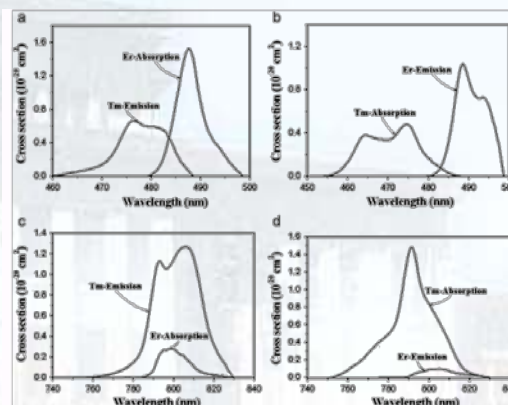


图 7. Er^{3+} 和 Tm^{3+} 的吸收截面和发射截面。

Fig. 7. (a) Spectral cross-section superposition between the fundamental $^4I_{15/2} \rightarrow ^4F_{7/2}$ absorption of Er^{3+} and $^1G_4 \rightarrow ^3H_6$ emission of Tm^{3+} in the glass, (b) Spectral cross-section superposition between the fundamental $^3H_6 \rightarrow ^1G_4$ absorption of Tm^{3+} and $^4F_{7/2} \rightarrow ^4I_{15/2}$ emission of Er^{3+} in the glass, (c) Spectral cross-section superposition between the fundamental $^4I_{15/2} \rightarrow ^4I_{9/2}$ absorption of Er^{3+} and $^3H_4 \rightarrow ^3H_6$ emission of Tm^{3+} in the glass, (d) Spectral cross-section superposition between the fundamental $^3H_6 \rightarrow ^3H_4$ absorption of Tm^{3+} and $^4I_{9/2} \rightarrow ^4I_{15/2}$ emission of Er^{3+} in the glass.

We discuss the energy transitions of Er^{3+} and Tm^{3+} . The results indicate the energy transition of Tm^{3+} to Er^{3+} is very strong in the GC, which changes the population mechanism of UC emissions of Er^{3+} .

课题小组继续就拉曼表面增强光谱展开研究。我们对倒金字塔坑金基底等离激元性能进行了研究。近场扫描光学显微镜图像显示表面等离激元主要位于凹坑的空腔之中，这也被若丹明 6G 的拉曼散射强度映射图像实验侧面的证明了。通过使用有限元法的计算结果表明，电场主要位于倒金字塔坑，并且场的分布不受其周围倒金字塔坑影响。与单一的倒金字塔坑相比，由于表面等离激元的耦合效应，局域化的电场强度在周期阵列结构中得到增强。

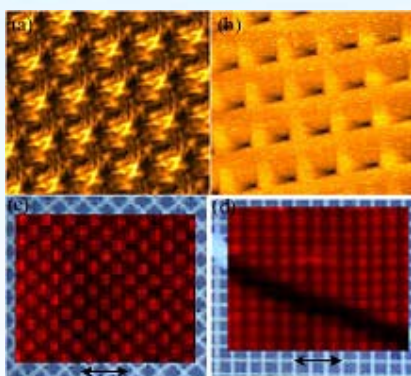


图 8. 实验结果(a,b 近场光学显微镜结果, c,d 拉曼 Mapping 成像结果)。

Fig.8 Experimental results (a, b NSOM result image, c, d Raman Mapping result image) .

The research team continued to carry out the research on SERS. The surface plasmons properties on gold film composed of inverted square pyramidal pits were investigated. The near-field scanning optical microscopy image showed that the surface plasmons were mainly located in the cavity of the pits; this is consistent with the mapping image obtained using the Raman scattering intensity of Rhodamine 6G. The calculation results obtained by using the finite element method showed that the electric field mainly located in the pyramidal pits and the field distribution was not affected by the adjacent pits around it.

Compared with the single pyramidal pit, the localized electric field intensity increased in the condition of the structure array because of the surface plasmons coupling effect.

我们自主开发了紫外可见光纤光谱仪，使用 CCD 阵列探测器为传感器，使用凹面光栅分光，光学部件全固定，具有光谱测量速度快，精度高特点。光谱仪配备狭缝或光纤输入，高速 USB2.0 通讯，广泛应用于实验室使用和 OEM 光谱测量装置中。

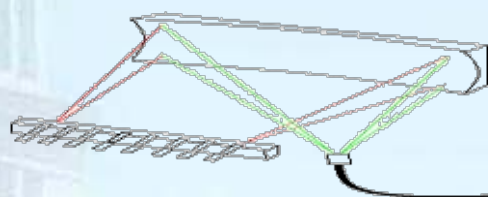


图 9. 光谱仪光路示意图。

Fig. 9 The light path diagram in the spectrometer.



图 10. 光谱仪外观图。

Fig.10 The photo of the spectrometer .

Our group manufactured our first spectrometer. The UV-VIS Fiber Optic Spectrometer is mainly composed of a sensor (linear CCD array) and a spectral module (concave grating). All the optical components are fixed on the optical bench. The spectrometer can work stably equipped with an entrance slit (option) or a fiber. It has the characteristics of high measurement speed, high measurement precision and high communication speed (USB 2.0). It is widely used in the laboratory. And also it is used in the OEM spectral measurement devices.

课题小组继续就近红外光谱仪开展研究。徐晓轩副教授参加了科技部第446

次香山科学会议--我国近红外光谱分析关键技术问题、应用与发展战略和2012年第四届近红外光谱学术会，并做了题目为“近红外拉曼光谱的应用新进展”的大会报告。

The research team continued to carry out the research on near infrared spectrometer development. Associate Professor Xiao-Xuan Xu participate in Xiangshan Science Conference Section 446 - "Key technique,

application and development strategy on Near Infrared Spectroscopy in China" held by the Ministry of Science and Technology and the Fourth Near Infrared Spectroscopy Academic Council (2012). And he reported at the meeting with the topic for "The new progress of near-infrared Raman spectroscopy application".

光场调控及其应用/Manipulation of Optical Fields and Its Application

负责人: 王慧田

本方向主要开展连续光和飞秒脉冲矢量光场和光学涡旋等新型光场的调控生成、焦场工程、非线性光学效应、微加工和微操纵等方向的研究。取得的代表性成果如下:

In this field, we mainly focused on the generation of the new optical fields such as vector fields and optical vortex by continuous wave and femtosecond pulse; the focusing engineering, the nonlinear effect, the micro manipulation and fabrication by the new optical fields. This year, we obtained some respective results as following.

强飞秒激光在 Kerr 介质中传输时能够激发非线性成丝效应, 光丝在强场物理、材料加工等领域具有重要应用, 但成丝机理复杂尤其是对随机噪声敏感, 目前仍难以控制。我们研究了杂化矢量光场的塌缩行为, 提出一种新的控制机制: 通过设计光场空间偏振结构对非线性响应过程进行调控, 实现了对飞秒激光非线性成丝的主动控制, 并通过交叉耦合模型从理论上给予严格证明。

Scientific Reports 2, 1007 (2012).

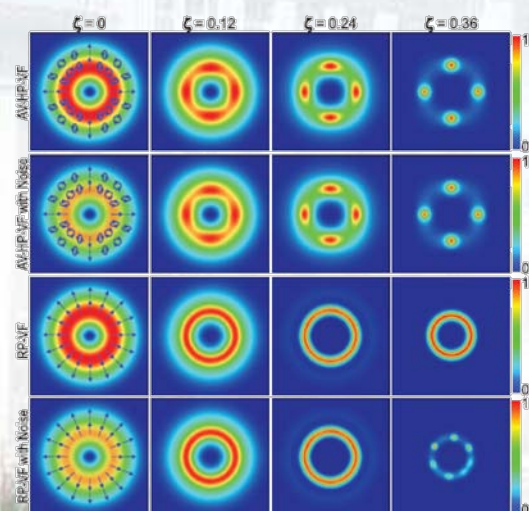


图1 数值模拟几种典型光场的塌缩行为。

Fig 1 Numerical simulated collapsing behavior of several classic light fields.

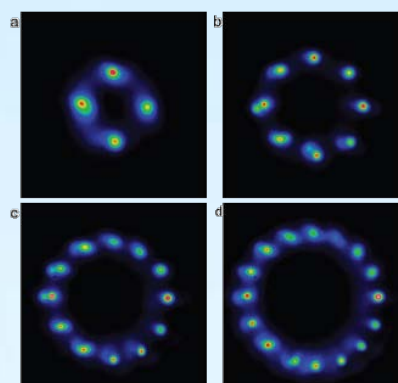


图2 实验测得的杂化矢量光场的光丝分布图。

Fig 2 Experimental measured collapsing patterns of hybridly polarized light field.

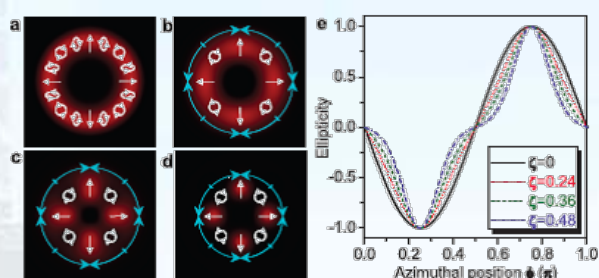


图3 交叉耦合模型计算结果。

Fig 3 Theoretical prediction by Cross-coupling model.

Intensive femtosecond laser would inspire nonlinear filamentation when propagate in Kerr medium, which has important application in many branches of physics such as strong field physics, materials processing. However, suffering from the complex underlying mechanism especially its sensitivity to random noise, the filamentation process is still hardly controllable. We study the collapse behavior of a hybridly polarized light field, and propose a novel controlling mechanism: regularizing the medium nonlinear response by engineering the spatial polarization structure of light field. Following

this idea, the nonlinear filamentation process can be well controlled. A cross-coupling model is also proposed as a theory interpretation.



发表论文/Publications in Journal

1. Mengxin Ren, Eric Plum, Jingjun Xu, and Nikolay I. Zheludev, "Giant nonlinear optical activity in a plasmonic metamaterial", *Nat. Commun.* 3, 833 (2012).*
2. Fu-Cai Liu, T. Makino, T. Yamazaki, K. Ueno, A. Tsukazaki, T. Fukumura, Yong-Fa Kong and M. Kawasaki, "Ultrafast time-resolved Faraday rotation in EuO thin films", *Phys. Rev. Lett.* 108(25), 257401 (2012). (IF=7.370)
3. Penghong Liu, Wei Cai, Lei Wang, Xinzheng Zhang, and Jingjun Xu, "Tunable terahertz optical antennas based on graphene ring structures", *Appl. Phys. Lett.* 100, 153111 (2012).
4. Sheng. Liu, Yi. Hu, Peng. Zhang, Xuetao. Gan, Cibo. Lou, Daohong. Song, Jianlin. Zhao, Jingjun. Xu, and Zhigang. Chen, "Symmetry-breaking diffraction and dynamic self-trapping in optically induced hexagonal photonic lattices", *App. Phys. Lett.*, 100, 061907 (2012).
5. Xiaoyang Duan, Shuqi Chen, Haifang Yang, Hua Cheng, Junjie Li, Wenwei Liu, Changzhi Gu and Jianguo Tian, "Polarization-insensitive and wide-angle plasmonically induced transparency by planar metamaterials," *Appl. Phys. Lett.* 101, 143105 (2012).
6. Zhou Xiang-Feng, Dong Xiao, Zhao Zhisheng, Oganov, Artem R., Tian Yongjun, Wang Hui-Tian, "High-pressure phases of NaAlH₄ from first principles", *Appl. Phys. Lett.* 100, 061905 (2012)
7. Ling-Jun Kong, Xi-Lin Wang, Si-Min Li, Yongnan Li, Jing Chen¹, Bing Gu, and Hui-Tian Wang, "Spin Hall effect of reflected light from an air-glass interface around the Brewster's angle", *Appl. Phys. Lett.* 100, 071109 (2012)
8. Lei Wang, Wei Cai, Xinzheng Zhang, and Jingjun Xu, "Surface plasmons at the interface between graphene and Kerr-type nonlinear media", *Opt. Lett.* 37(13), 2730-2732 (2012).
9. Wending Zhang, Ligang Huang, Feng Gao, Fang Bo, Li Xuan, Guoquan Zhang and Jingjun Xu, "Tunable add/drop channel coupler based on an acousto-optic tunable filter and a tapered fiber", *Opt. Lett.* 37(7), 1241-1243 (2012).
10. Sheng Liu, Yi Hu, Peng Zhang, Xuetao Gan, Cibo Lou, Daohong Song, Jianlin Zhao, Jingjun Xu, and Zhigang Chen, "Tunable self-shifting Bloch modes in anisotropic hexagonal photonic lattices," *Opt. Lett.* 37, 2184-2186 (2012)
11. Yi Hu, Zhe Sun, Domenico Bongiovanni, Daohong Song, Cibo Lou, Jingjun Xu, Zhigang Chen, and Roberto Morandotti, "Reshaping the trajectory and spectrum of nonlinear Airy beams," *Opt. Lett.* 37, 3201-3203 (2012)
12. X. He, Z.-b. Liu, and D. N. Wang, "Wavelength-tunable, passively mode-locked fiber laser based on graphene and chirped fiber Bragg grating," *Optics Letters* 37, 2394-2396 (2012).
13. Tian Tian, Yong-Fa Kong, Shi-Guo Liu, Wei Li, Li Wu, Shao-Lin Chen and Jingjun Xu, "The photorefractive of molybdenum-doped lithium niobate crystals", *Opt. Lett.* 37(13), 2679-2681 (2012). (IF=3.399)
14. Yin-Feng Dong, Shi-Guo Liu, Yong-Fa Kong, Shao-Lin Chen, Romano Rupp and Jing-Jun Xu, "Fast photorefractive response of vanadium-doped lithium niobate in the visible", *Opt. Lett.* 37(11), 1841-1843 (2012). (IF=3.399)
15. Yongnan Li, Xi-Lin Wang, Hu Zhao, Ling-Jun Kong, Kai Lou, Bing Gu, Chenghou Tu, and Hui-Tian Wang, "Young's two-slit interference of vector light fields", *Opt. Letters* 37 1790-1792 (2012)
16. Peilong Hong, Jianbin Liu, and Guoquan Zhang, "Two-photon superbunching of thermal light via multiple two-photon-path interference", *Phys. Rev. A* 86, 013807 (2012).

* 选录论文/Selected papers

17. Ming Kang, Jing Chen, Bing Gu, Yongnan Li, Luat T. Vuong, and Hui-Tian Wang, "Spatial splitting of spin states in subwavelength metallic microstructures via partial conversion of spin-to-orbital angular momentum", *Phys. Rev. A* 85, 035801 (2012)
18. Kong, Ling-Jun, Qian, Sheng-Xia, Ren Zhi-Cheng, Wang, Xi-Lin, Hui-Tian Wang, "Effects of orbital angular momentum on the geometric spin Hall effect of light", *Phys. Rev. A* 85, 035804 (2012)
19. W. H. Hu, L. Jin, Y. Li, and Z. Song, "Probability-preserving evolution in a non-Hermitian two-band model", *Phys. Rev. A* 86, 042110 (2012).
20. Feifei Xin, Zhaohui Zhai, Xiaojie Wang, Yongfa Kong, Jingjun Xu, and Guoquan Zhang, "Threshold behavior of the Einstein oscillator, electron-phonon interaction, band-edge absorption and small hole polarons in LiNbO₃:Mg crystals", *Phys. Rev. B* 86, 165132 (2012).
21. T. Makino, Fu-Cai Liu, T. Yamasaki, Y. Kozuka, K. Ueno, A. Tsukazaki, T. Fukumura, Yong-Fa Kong and M. Kawasaki, "Ultrafast optical control of magnetization in EuO thin films", *Phys. Rev. B* 86(6), 064403 (2012). (IF=3.691)
22. L. Jin, Z. Song, "Phase diagram and scaling behavior of a PT symmetric non-Hermitian Bose-Hubbard system", *Ann. Phys.* 11, 017 (2012).
23. L. Jin, Z. Song "Hermitian scattering behavior for the non-Hermitian scattering center", *Phys. Rev. A*. 85, 012111 (2012).
24. X. Z. Zhang, L. Jin, Z. Song, "Perfect State Transfer in PT-symmetric Non-Hermitian Networks", *Phys. Rev. A*. 85, 012106 (2012).
25. M.X. Huo, Ying Li, Z. Song, C.P. Sun, "Photon-like flying qubit in the coupled cavity array", *Int.J. Quant. Inf.* 10, 1250002 (2012).
26. Qiang Wu, Shangyu Guo, Yinxing Ma, Feng Gao, Chengliang Yang, Ming Yang, Xuanyi Yu, Xinzhen Zhang, Romano A. Rupp, and Jingjun Xu, "Optical refocusing three-dimensional wide-field fluorescence lifetime imaging microscopy", *Opt. Express* 20(2) 960-965 (2012) (*selected by Virtual Journal for Biomedical Optics*).
27. Jun Qian, Zongqiang Chen, Jing Chen, Yudong Li, Jingjun Xu and Qian Sun, "Two-dimensional angularly selective optical properties of gold nanoshell with holes", *Opt. Express*, 20, 14614-4620 (2012)
28. Zheng Cao, Xinyuan Qi, Xuanqi Feng, Zhaoyu Ren, Guoquan Zhang, and Jintao Bai, "Light controlling in transverse separation modulated photonic lattices", *Opt. Express* 20(17), 19119-19124 (2012).
29. Yang Yang, Weiping Zang, Zhiyu Zhao, Jianguo Tian, "Optical forces on Mie Particles in an Airy evanescent field", *Opt. Express* 20, 25681-25692 (2012).
30. Xiang-Tian Kong, Wei-Guo Yan, Zu-Bin Li, and Jian-Guo Tian, "Optical properties of metal-multi-insulator-metal plasmonic waveguides," *Opt. Express* 20(11): 12133-12146 (2012).
31. Shou-Jun Zheng, Yong-Fa Kong, Hong-De Liu, Shao-Lin Chen, Ling Zhang, Shi-Guo Liu and Jing-Jun Xu, Pyroelectric effect in green light-assisted domain reversal of Mg-doped LiNbO₃ crystals, *Opt. Express*, 20(27) 29131-29136 (2012). (IF=3.587)
32. Kai Lou, Sheng-Xia Qian, Xi-Lin Wang, Yongnan Li, Bing Gu, Chenghou Tu, and Hui-Tian Wang, "Two-dimensional microstructures induced by femtosecond vector light fields on silicon", *Opt. Express* 20, 1120-1127(2012)

33. Bing Gu, Fan Ye, Kai Lou, Yongnan Li, Jing Chen, and Hui-Tian Wang, "Vectorial self-diffraction effect in optically Kerr medium", *Opt. Express* 20, 149-157 (2012)
34. Ming Kang, Tianhua Feng, Hui-Tian Wang, and Jensen Li, Wave front engineering from an array of thin aperture antennas", *Opt. Express* 20, 15882-15890 (2012)
35. HX Cui, X L Wang, B Gu, YN Li, J Chen and HT Wang, "Angular diffraction of an optical vortex induced by the Gouy phase", *J. Opt.* 14 055707 (2012)
36. QH Guo, H X Cui, J Lei, M Kang, XL Wang, YN Li, J Chen and HT Wang, "Enhanced optical angular momentum in cylinder waveguides with negative-index metamaterials", *J. Opt.* 14 045703(2012)
37. Kai Lou, Sheng-Xia Qian, Zhi-Cheng Ren, Xi-Lin Wang, Yongnan Li, Chenghou Tu, and Hui-Tian Wang, "Self-formed two-dimensional near-wavelength microstructures on copper induced by multipulse femtosecond vector optical fields", *JOSA B*, Vol. 29, Issue 9, 2282-2287 (2012)
38. Guo, Qing-Hua, Kang, Ming, Li, Teng-Fei, Cui, Hai-Xu, Gu, Bing, Chen Jing, Wang Hui-Tian, "Spin-sensitive distribution of electromagnetic field via spin-orbit interaction in structured metamaterials", *J. Appl. Phys.* 112, 013102 (2012)
39. Fei Tian, Xiao Dong, Zhisheng Zhao, Julong He and Hui-Tian Wang "Superhard F-carbon predicted by ab initio particle-swarm optimization methodology", *J. Phys.: Condens. Matter* 24 165504(2012)
40. Ming Kang, Jing Chen, Xi-Lin Wang, and Hui-Tian Wang "Twisted vector field from an inhomogeneous and anisotropic metamaterial", *JOSAB*.29.000572(2012)
41. Si-Min Li , Yongnan Li, Xi-Lin Wang, Ling-Jun Kong, Kai Lou, Chenghou Tu, Yongjun Tian, Hui-Tian Wang, "Taming the Collapse of Optical Fields", *Scientific Reports* 2, 1007(2012)
42. An-Chang Shi, Bao-Hui Li, "Self-assembly of diblock copolymers under confinement", *Soft Matter*. DOI: 10.1039/c2sm27031e (First published on the web 19 Nov 2012). (IF=4.390)
43. Leiting Pan, Xiaoxu Wang, Shuying Yang, Xian Wu, Imshik Lee, Xinzheng Zhang, Romano A. Rupp, and Jingjun Xu , "Ultraviolet irradiation-dependent fluorescence enhancement of hemoglobin catalyzed by reactive oxygen species", *PLoS ONE* 7(8) e44142-6 (2012).
44. En-Jun Wang, Peng Zhang, Yong-Mei Chen, Zhan-Wei Liu, Tao He and Ya-An Cao, "Improved visible-light photocatalytic activity of titania activated by nitrogen and indium modification", *J. Mater. Chem.* 22, 14443-14449 (2012). (IF=5.968)
45. Li Wu, Yi Zhang, Ming-Yuan Gui, Pei-Zhi Lu, Li-Xia Zhao, Shu Tian, Yong-Fa Kong and Jing-Jun Xu, "Luminescence and energy transfer of a color tunable phosphor: Dy^{3+} , Tm^{3+} , and Eu^{3+} -coactivated $KSr_4(BO_3)_3$ for warm white UV LEDs", *J. Mater. Chem.* 22, 6463-6470 (2012). (IF=5.968)
46. Ji-Xiang Yuan, Qiang Wu, Peng Zhang, Jiang-Hong Yao, Tao He and Ya-An Cao, "Synthesis of indium borate and its application in photodegradation of 4-Chlorophenol", *Environ. Sci. Technol.* 46, 2330-2336 (2012). (IF=5.228)
47. Y.-L. Liu, H.-L. Liu, Z.-B. Liu, W.-P. Zang, and J.-G. Tian, "Effects of solvent on nonlinear absorption properties of tetraphenylporphyrin compounds in the nanosecond regime," *Optik* 123, 1015-1018 (2012).
48. Zongqiang Chen, Jing Chen, Yudong Li, Deng Pan, Wenqiang Lu, Zhiqiang Hao, Jingjun Xu, and Qian Sun, "Simulation of nanoscale multifunctional interferometric logic gates based on coupled metal gap waveguides", *Photonics Technology Letters, IEEE* 24 (16), 1366-1368 (2012)

49. Xuezhi Zhang, Ming Feng, Xinzheng Zhang and Jingjun Xu, "Mid-infrared light generation by high order SRS effect in silicon ring cavity", *J. Opt.* 14, 015201-6 (2012).
50. Wei Cai, Lei Wang, Yinxiao Xiang, Xinzheng Zhang, and Jingjun Xu, "Propagating anti-symmetrically coupled plasmons generation by electron beams," *Opt. Commun.* 285(21), 4608-4611 (2012).
51. Zhaohui Zhai, Yanfei Tu, Yiling Dou, Jingjun Xu and Guoquan Zhang, "Bragg-matching characterization of atomic coherence gratings in electromagnetically induced transparency solid with a confocal scheme", *Opt. Commun.* 285, 277-280 (2012).
52. Yu Yin, Song Feng, Ming Chengguo, "Survey and research on up-conversion emission character and energy transition of $\text{Yb}^{3+}/\text{Er}^{3+}/\text{Tm}^{3+}$ co-doped phosphate glass and glass ceramic", *Opt. Commun.* 285(24), 4739-4744 (2012)
53. Zhang Gong, Song Feng, Ming Chengguo, "Photoluminescence properties and pump-saturation effect of $\text{Er}^{3+}/\text{Yb}^{3+}$ co-doped $\text{Y}_2\text{Ti}_2\text{O}_7$ nanocrystals", *Journal of Luminescence* 132(3), 774-779 (2012).
54. Daohong. Song, Cibo. Lou, Zhuoyi. Ye, Jingjun. Xu, and Zhigang. Chen , "Experiments on Linear and Nonlinear Localization of Optical Vortices in Optically Induced Photonic Lattices", *Int. Journal of Opt.* 2012, 273857 (2012).
55. Yan Li, Yudong Li, Weike Shi, Shuqi Chen, Guangzi Zhang, Zhibo Liu, Qian Sun, Jianguo Tian, Yanfei Xu and Yongsheng Chen: "Periodic microstructures fabricated by multiplex interfering femtosecond laser beams on grapheme sheet", *Int. J. Nanomanufacturing* Vol. 8(3), 221-230, 2012.
56. Jianxiong Li, Shuqi Chen, Ping Yu, Hua Cheng, Lunjie Chen and Jianguo Tian, "Indirectly Manipulating Nanoscale Localized Fields of Bowtie Nanoantennas with Asymmetric Nanoapertures," *Plasmonics*, Online First.
57. Hua Cheng, Shuqi Chen, Haifang Yang, Junjie Li, Xin An, Changzhi Gu and Jianguo Tian, "In A polarization insensitive and wide-angle dual-band nearly perfect absorber in the infrared regime," *J. Opt.* 14 085102 (2012).
58. Ying, Cui-Feng, Zhou, Wen-Yuan, Ye, Qing, Li Zu-bin, Tian, Jian-Guo, "Mini-band states in graded periodic 1D photonic superstructure", *Applied Physics B: Lasers and Optics*, 107 (2), 369-374. (2012).
59. Jun Qian, Wudeng Wang, Yudong Li, Jingjun Xu, and Qian Sun, "Optical Extinction Properties of Perforated Gold-Silica-Gold Multilayer Nanoshells" *J. Phys. Chem. C*, 116, 10349-10355(2012)
60. F. Xing, Z.-B. Liu, Z.-C. Deng, X.-T. Kong, X.-Q. Yan, X.-D. Chen, Q. Ye, C.-P. Zhang, Y.-S. Chen, and J.-G. Tian, "Sensitive Real-Time Monitoring of Refractive Indexes Using a Novel Graphene-Based Optical Sensor," *Sci. Rep.* 2, 908 (2012).
61. Ting-Hsuan Chen, Xiao-Lu Zhu, Lei-Ting Pan, Xing-Juan Zeng, Alan Garfinkel, Yin Tintut, Linda L. Demer, Xin Zhao and Chih-Ming Ho, "Directing Tissue morphogenesis via Self-Assembly of Vascular Mesenchymal Cells", *Biomaterials* 33, 9019-9026 (2012).
62. H. Pei, W. Li, Y. Liu, D. Wang, J. Wang, J. Shi, and S. Cao, "Ring-opening metathesis polymerization of norbornene derivatives for multifunctionalized all-optical photorefractive polymers with a non-conjugated main chain", *Polymer* 53, 138-144 (2012).
63. Jin Wang, Qing Ye, Zhichao Deng, Wenyuan Zhou, Tengqian Sun, Chunping Zhang, Jianguo Tian. "Effect of tissue fluid on accurate determination of the complex refractive index of animal tissue", *Journal of Biomedical Optics*, 17(7), 075011(2012).

64. Jin Wang, Qing Ye, Zhichao Deng, TengqianSun, Wenyuan Zhou, Chunping Zhang, Jianguo Tian. "Estimation of the complex refractive index of epoxy resin phantom using EDTRM", *Journal of Modern Optics*, 59(13),1158-1162(2012)
65. X.-Q. Yan, Z.-B. Liu, Y.-S. Chen, and J.-G. Tian, "Polarization characteristics of nonlinear refraction and nonlinear scattering in several solvents," *Journal of the Optical Society of America B-Optical Physics* 29, 2721-2728 (2012).
66. Jian-Ming SUN, M. Helm, W. Skorupa, B. Schmidt and A. Mücklich, "Highly efficient silicon light emitting diodes produced by doping engineering", *Frontiers of Optoelectronics* 5(1), 7-12 (2012). (**Review**)
67. Yong-Fa Kong, Shi-Guo Liu and Jing-Jun Xu, "Recent advances in the photorefraction of doped lithium niobate crystals", *Materials*, 5(10), 1954-1971 (2012). (**Review**) (IF=1.677)
68. Yong-Qiang Cao, Yan-L-long Yu, Peng Zhang, Lan-Lan Zhang, Tao He and Ya-An Cao, "Enhanced visible-light photocatalytic activity of TiO₂ by nitrogen and nickel-chlorine modification." *Sep. Purif. Technol.* (Accepted, 23 Nov 2012). (IF=2.921)
69. Hua Yu, Hui Guo, Ming Zhang, Yan Liu, Min Liu and Li-Juan Zhao, "Distribution of Nd³⁺ ions in oxyfluoride glass ceramics", *Nanoscale Res. Lett.* 7, 275 (2012). (IF=2.726)
70. Tong-Qing Sun, Xiao-Dong Zhou, Yu Zhang, Shao-Lin Chen, Shi-Guo Liu, Yong-Fa Kong and Jingjun Xu, "Growth and thermal properties of tetragonal double tungstate KLa(WO₄)₂ crystal", *Mater. Res. Bull.* 47(11), 3233-3237 (2012). (IF=2.105)
71. Chao Zhang, Jin Yang, Feng Chen, Yong-Fa Kong, "Optical damage of Zr:LiNbO₃ waveguides produced by proton implantation", *Nucl. Instr. Meth. B* 286, 209-212 (2012). (IF=1.211)
72. Peng Zhang, Xu-Cen Lu, C.L. Zhang and Jiang-Hong Yao, "Energy band and absorption coefficient of quantum dots in a well structures", *Acta Phys. Pol. A* 122(1), 1111-1115 (2012). (IF=0.444)
73. Yi Zhang, Li Wu, Min-Yuan Ji, Biao Wang, Yong-Fa Kong and Jing-Jun Xu, "Structure and photoluminescence properties of KSr₄(BO₃)₃: Eu³⁺ red-emitting phosphor", *Opt. Mater. Express* 2, 92-102 (2012).
74. Mark Maroncelli, Xin-Xing Zhang, Min Liang, Durba Roy and Nikolaus P. Ernsting, "Measurements of the complete solvation response of coumarin 153 in ionic liquids and the accuracy of simple dielectric continuum predictions", *Disc. Faraday Soc.* 154, 409 (2012).
75. Jin Wang, Qing Ye, Zhichao Deng, TengqianSun, Wenyuan Zhou, Chunping Zhang, Jianguo Tian."Accurate determination of the complex refractive index of solid tissue-equivalent phantom", *SPIE Proceedings*, 8427,842729(2012)
76. Z.-B. Liu, Z. Guo, X.-L. Zhang, J.-Y. Zheng, and J.-G. Tian, "Increased optical nonlinearities of multi-walled carbon nanotubes covalently functionalized with porphyrin," *Carbon* 51, 419-426 (2013).
77. Junmei Li, Xiaoxuan Xu, Yufang Wang, Meng Wang, Zhifu Dong, Wanhui Tian, Jiaming Sun, Cunzhou Zhang, Bin Wang, "The observation of the localized surface plasmons and its coupling", *Journal of Raman Spectroscopy*, 43 (7), 817-963 (2012)
78. Fan Shi, Wei Li, Pidong Wang, Jun Li, Qiang Wu, Zhenhua Wang, Xinzheng Zhang, "Optically Controlled Coherent Backscattering from a Water Suspension of Positive Uniaxial Microcrystals ", *Chin. Phys. Lett.* 29(1) 014206-3 (2012).
79. HAO Zhi-Qiang LI Yu-Dong, CHEN Jing, CHEN Zong-Qiang, XU Jing-Jun, SUN Qian, "Beam Manipulation by Metallic Nanoslit Arrays with Perpendicular Cuts inside Slits", *Chin. Phys. Lett.* 29, 114212-114214 (2012).

80. Shi Shu-Dong, Li Wei, Du Peng, Song Feng, "Removing paint from a metal substrate using a flattened top laser", Chinese Physics B 21(10), 104209 (2012)
81. H. Zhao, Z. Liu, X. Zhang, J. Tian, C. Chen, Y. Zhu, and J. Zheng, "Synthesis, Photophysical and Electrochemical Properties of Amide-Linked Phthalocyanine-Fullerene Dyad," Chinese Journal of Chemistry 30, 1766-1770 (2012).
82. Z. Liu, X. Zhang, X. Yan, Y. Chen, and J. Tian, "Nonlinear optical properties of graphene-based materials," Chinese Science Bulletin 57, 2971-2982 (2012).
83. Yudong Li, Xiangyang Gao, Meiling Jiang, Qian Sun, Jianguo Tian: "Fabrication of magneto-optical microstructure by femtosecond laser pulses", Chin. Opt. Lett. Vol. 10(10), 102201(2012).
84. 孔勇发, 刘士国, 刘宏德, 陈绍林, 张玲, 许京军, "掺铈铈酸锂系列晶体", 人工晶体学报, 41(增刊), 111-116 (2012) (综述)
85. 刘敏, 余华, 张盼, 张铭, 刘艳, 赵丽娟, "Al₂O₃ 对氟氧化物玻璃微结构和析晶的影响", 物理学报, 61(11), 118102 (2012) (IF=1.027)
86. 梁毅, 张心正, 王振华, 吴强, 许京军, "非相干非线性光学理论方法及其进展", 物理, 41(5), 316-322 (2012)。
87. 程辉, 董江舟, 巢晖, 姚江宏, 曹亚安, "TiO₂ 表面氧空位对 RuP₂/TiO₂/ITO 薄膜电极光致电荷转移的影响", 物理化学学报, 28(4), 850-856 (2012) (IF=0.78)
88. 程辉, 姚江宏, 曹亚安, "表面 In 掺杂 TiO₂ 的 N719/TiO₂-Inx%/FTO 薄膜电极的光电转换效率", 物理化学学报, 28(11), 2632-2640 (2012) (IF=0.78)
89. 郭丽梅, 匡元江, 杨晓丹, 于彦龙, 姚江宏, 曹亚安, "偏硼酸铈催化剂光催化还原 CO₂ 合成 CH₄", 物理化学学报 (接收, 2012.11.21) (IF=0.78)
90. 郝志强, 陈靖, 陈宗强, 陆文强, 许京军, 孙骞, "内嵌凹槽的金属亚波长狭缝的共振投射特性的分析", 光电子激光, 23, 1211-1215, (2012)。
91. 寇松姿, 孟桂先, 潘雷霆, 王晓旭, 鞠治强, 李任植, "Computational Simulation and Application for a Novel Microfluidic Multishear Device", 南开大学学报 45(2), 31~36 (2012)。

出版专著:

1. Z. Chen, and R. Morandotti eds, "Nonlinear Photonics and Novel Phenomena", Springer 978-1-4614-3537-2 (2012).
2. Y. Hu, G. A. Siviloglo, P. Zhang, N.K. Efremidis, D. N. Christodoulides, and Z. Chen, "Generation and control of accelerating Airy beams", Invited Book Chapter in "Nonlinear Photonics and Novel Phenomena", Springer 978-1-4614-3537-2 (2012).
3. P. Zhang, Cibo Lou, Yi Hu, Sheng Liu, Jianlin Zhao, Jingjun Xu, and Z. Chen, "Spatial beam dynamics mediated by hybrid nonlinearity", Invited Book Chapter in "Nonlinear Photonics and Novel Phenomena", Springer 978-1-4614-3537-2 (2012).
4. An-Chang Shi, Baohui Li, "Block Copolymers under Confinement", in Polymer Science: A Comprehensive Reference, Elsevier BV, Amsterdam (2012).
5. 宋峰, "Metal enhanced fluorescence of rare earth materials", Invited Book Chapter in "Nanotechnology in Optics", Nanosociety (2012).

专利/Patents

申请专利/ Patents Applied

- [1] 201210123998.5; 一种高效率镍/氧化镍/硼酸镍复合光催化剂; 发明; 曹亚安, 郭丽梅。
(2012.1.1)
- [2] 201210042474.3; 钢管管端内外径双臂四探头测量装置及其测量方法; 发明; 叶青、梅剑春、田建国。(2012.2.24)
- [3] 201210042473.9; 钢管管端内外径测量中轴心误差消除方法; 发明; 梅剑春、叶青、田建国。(2012.2.24)
- [4] 201210045148.8; 一种掺钕磷酸钷激光晶体及其制备方法和应用; 发明; 孙同庆, 孔勇发, 许京军。(2012.2.27)
- [5] 201210062141.7; 基于全内反射的混合物折射率测量方法; 发明; 叶青、邓志超、王槿、孙腾骞、张春平、田建国。(2012.3.12)
- [6] 201210062142.1; 聚焦全内反射法测量物质折射率分布; 发明; 叶青、孙腾骞、王槿、邓志超、张春平、田建国。(2012.3.12)
- [7] 201210203315.7; 一种近化学计量比钽酸锂晶体的制备方法; 发明; 孙军、许京军、李威、杨金凤、张玲、孔勇发、张华。(2012.6.19)
- [8] 201210203084.X; 一种近化学计量比铌酸锂晶体的制备方法; 发明; 孙军、许京军、李威、张华、张玲、孔勇发、杨金凤。(2012.6.19)
- [9] 20120196836.4; 一种基于石墨烯偏振效应的折射率实时测定方法和装置; 发明; 刘智波、邢飞、叶青、邓志超、田建国。(2012.7.12)
- [10] 201210322007.6; 一种基于物理吸附的石墨烯薄膜转移方法; 发明; 刘智波、陈旭东、田建国。(2012.9.20)

授权专利/ Patents Approved

- [1] ZL200910068819.0; 掺锡铌酸锂晶体; 发明; 刘士国, 孔勇发, 王利忠, 陈绍林, 黄自恒, 张玲, 许京军。(2012.1.25)
- [2] ZL201110064153.9; 基于掺铟铌酸锂多孔材料的上转换绿光随机激光器; 发明; 张心正、石凡、禹宣伊、许京军、李威、唐柏权、吴强、孔勇发。(2012.5.23)
- [3] ZL201110131763.6; 一种新型太阳能电池荧光增效薄膜材料的指标; 发明; 余华、赵丽娟、胡男。(2012.11.21)
- [4] ZL201120143055.X; 电子延时安全插座; 实用新型; 梅剑春、周文远、叶青、田建国。
(2012.4.11)

国际合作与交流/International Cooperation and Exchange

来访人员名单/Visitors List

序号	姓名	国家或地区	单位	技术职称	报告题目	来访时间	来访目的
1.	Peter Hertel	德国	Univ. of Osnabrueck	教授	[1] Lectures on Computational Physics [2] Lectures on Fundamental Optics	2012.3.25-5.6 2012.10.25-12.9	讲学
2.	An-Chang Shi	加拿大	McMaster University	教授		2012.4.19-21	学术交流
3.	Jeff Z. Y. Chen	加拿大	University of Waterloo	教授	Monte Carlo simulation of membrane structure/polymer interaction	2012.5.29	学术交流
4.	Irena Drevenšek Olenik	斯洛文尼亚	斯特藩研究所	副教授	Tunable photonic structures from polymer-liquid crystal composites	2012.8.19-2013.2.13	合作研究
5.	Romano Rupp	奥地利	维也纳大学	教授		2012.8.19-2013. 2.13	合作研究
6.	Kaiming Zhou	英国	Aston University	博士	Tilted fibre Bragg grating and micromachining with femtosecond laser	2012年8月3日-9日	学术交流
7.	Yasuo Tomita	日本	日本电气通信大学	教授	“Photopolymerizable nanoparticle-polymer nanocomposite materials for holographic digital data storage” and “Third- and high-order nonlinear optical responses of semiconductor quantum dot-polymer”	2012年8月21日-28日	学术交流

8.	Michael Meingassner	奥地利	维也纳大学	硕士生		2012.8.28-2012.12.31	合作研究
9.	Robert A. Wickham	加拿大	University of Guelph	Associate Professor	Dynamics of Microstructural Transitions in Block Copolymer Melts	2012.11.14-21	工作访问 讲学
10.	刘照伟	美国	University of California, San Diego	Assistant Professor	Plasmonics, Metamaterials and Their Applications in Active and Passive Light Manipulations	2012.11.13-14	工作访问 学术交流
11.	李向平	澳大利亚	Swinburne University of Technology	博士	“Plasmonic keys” under three-dimensional orientation-unlimited polarization nanoscopy	2012.11.23-25	工作访问 学术交流
12.	Giusy Scalia	韩国	国立首尔大学	助理教授	Alignment of Carbon Nanotubes in Liquid Crystals	2012.11.28-2012. 12.1	学术交流
13.	廖骏伟	台湾	长庚大学	教授	Metal Enhanced Fluorescence	2012.11.30	工作访问 学术交流
14.	L. Jay Guo	美国	密歇根大学	教授		2012.11.3-2012.11.4	学术交流
15.	Eric Plum	英国	南安普顿大学	讲师	Reconfiguring Photonic Metamaterials	2012.12.9-12.11	工作访问 学术交流
16.	Kevin F. MacDonald	英国	南安普顿大学	项目主管	Programme Manager for Photonic Metamaterials, Senior Research Fellow	2012.12.9-12.11	工作访问 学术交流
17.	Diana C. U. Pinzon	西班牙	光子科学研究所	讲师	Unraveling molecular behavior through multidimensional ultrafast optical spectroscopies	2012.12.19-2013.1.8	工作访问 学术交流
18.	Alejandro F. Botero	西班牙	光子科学研究所	讲师	Harnessing light through nano- and micro-structuring of materials for sensing and light-harvesting	2012.12.19-2013.1.8	工作访问 学术交流

19.	Blaz Tasic	斯洛文尼亚	斯特藩研究所	硕士生		2012.12.3-2013.2.5	合作研究
20.	Svyatoslav A. Shlenov	俄罗斯	莫斯科大学国际激光中心	教授	Femtosecond laser filaments in air	2012.8.3-2012.8.8	学术交流
21.	Alexander P. Alodjants	俄罗斯	弗拉基米尔大学	教授	BEC phenomena and coherent effects with atomic polaritons trapped in microstructures	2012.8.3-2012.8.8	学术交流
22.	Alexey O. Kucherik	俄罗斯	弗拉基米尔大学	教授	Laser forming of thin films with controlled morphology	2012.8.3-2012.8.8	学术交流
23.	Alexey Taychenachev	俄罗斯	俄罗斯科学院激光物理所	教授	Coherent population trapping resonances in alkali-atom vapors: principles, theory and applications to atomic clocks and magnetometers	2012.8.3-2012.8.8	学术交流
24.	Alina Manshina	俄罗斯	圣彼得堡大学	教授	Laser-induced chemical transformations	2012.8.3-2012.8.8	学术交流
25.	Vladimir Pastukhov	俄罗斯	莫斯科大学国际激光中心	研究生	Influence of metal spherical nanoantenna on the resonance fluorescence spectrum of two-level atoms	2012.8.3-2012.8.8	学术交流
26.	Andrey Pavlov	俄罗斯	莫斯科大学国际激光中心	研究生	New approach to calculation of far fields planar metamaterials	2012.8.3-2012.8.8	学术交流
27.	Anton Nadezhdin	俄罗斯	莫斯科大学国际激光中心	研究生	Efficiency of organic solar cells as a function of their size	2012.8.3-2012.8.8	学术交流
28.	Sergey Svyakhovskiy	俄罗斯	莫斯科大学物理系	博士生	Dynamical diffraction of femtosecond laser pulses in 1D photonic crystals	2012.8.3-2012.8.8	学术交流
29.	Vyacheslav Leschenko	俄罗斯	俄罗斯科学院激光物理所	研究生	Coherent addition of parametrically amplified femtosecond pulses	2012.8.3-2012.8.8	学术交流

30.	Sergey Kuznetsov	俄罗斯	俄罗斯科学院激光物理所	研究生	Development of the cooling laser with doubling cavity for an ytterbium standard	2012.8.3-2012.8.8	学术交流
31.	Anastasiia Povolotckai	俄罗斯	圣彼得堡大学	博士生	Photoinduced phenomena of Au-Ag reduction from solution	2012.8.3-2012.8.8	学术交流
32.	Evgeniia Khairullina	俄罗斯	圣彼得堡大学	研究生	The study of surfactants influencing laser induced copper deposition process	2012.8.3-2012.8.8	学术交流

出访人员名单/Personnel exchange Researchers List

序号	姓名	国家或地区	单位	职称或职位	出访时间	出访目的
1.	高峰	澳大利亚	悉尼大学	副教授	2012.4-	合作研究
2.	张心正	斯洛文尼亚	斯特藩研究所	教授	2012.7.9-2012.7.31	合作研究
3.	张心正	德国	明斯特大学	教授	2012.8.1-2012.8.9	合作交流
4.	王振华	美国	堪萨斯州立大学	讲师	2012.1.1-2012.1.2.3	访问学习
5.	宋峰	俄罗斯	莫斯科大学	教授	2012.10.26-10.31	学术会议
6.	宋峰	德国	巴德绍尔高中学	教授	2012.7.20-7.29	IYPT 竞赛
7.	宋峰	爱沙尼亚	塔林大学	教授	2012.7.15-7.20	物理奥赛
8.	宋峰	印度	新德里大学	教授	2012.4.30-5.8	物理亚赛

研究生交流情况/Personnel exchange Students List

序号	姓名	国家或地区	单位	博士生/硕士生	出访时间	出访目的
1.	任梦昕	英国	南安普顿大学	博士生	2011.4-2012.2	合作研究
2.	张学智	美国	Rice University	博士生	2011.4-2012.6	合作研究
3.	张荣纯	德国	Martin-Luther University, Halle-Wittenberg	博士生	2012.4.1-7.29	合作研究
4.	张新星	德国	洪堡大学	博士生	2012.1	联合培养
5.	刘悦	美国	Rutgers, The State University of New Jersey	博士生	2012.9	联合培养
6.	董校	美国	纽约州立大学石溪分校	博士生	2012.10	联合培养
7.	韦晨	美国	亚利桑那大学	博士生	2011.7-2013.7	联合培养

引进人才名单/New Staff

序号	姓名	性别	出生年月	职称	研究方向
1	任梦昕	男	1985.6	讲师	非线性光子学

国内、国际会议报告/Talks at Conferences

- 1 Huitian Wang et al. "Vector Fields and their Novel Properties", Frontiers in Optics 2012, Rochester.USA , 2012.10.14-18, (invited talk)
- 2 Jiaming Sun, "Manipulation of the light emission from Er-doped Si nanoclusters in SiO₂". The 4th Sino-German Symposium, Berlin, Germany, Sep 18-23 (2012). (Invited talk)
- 3 Guoquan Zhang, Fang Bo, Rong Dong, Jingjun Xu, "Phase coupling and control of light speed in photorefractive media", International Conference on Coherent and Nonlinear Optics, St. Petersburg, Russia, May 11-15(2005). (invited talk)
- 4 Fang Bo, Lei Xu, Jie Wang, Guoquan Zhang, and Jingjun Xu, "Active chromatic control and resonant improvement on the transverse-phase-modulation-induced group delay of light", 2012 Photonics Asia, Beijing, China, Nov 5-7(2012) (invited talk).
- 5 Yongfa Kong, Shiguo Liu, Jingjun Xu, "Optical damage resistance and light-induced domain reverse in doped lithium niobate crystals", The 2nd Russian-Chinese Laser Physics Symposium, Moscow, Russia, Oct. 26-31 (2012). (invited talk)
- 6 Feng Song, "Erbium heavy doped glasses and fibers for lasers", The 2nd Russian-Chinese Laser Physics Symposium, Moscow, Russia, Oct. 26-31 (2012). (invited talk)
- 7 Qiang Wu, Ming Yang, Zhandong Chen, Jingjun Xu, "Femtosecond laser microstructured silicon: principles and applications", 2nd Russian-Chinese Laser Physics Symposium, Moscow, Russia, October 26-31 (2012). (invited talk)
- 8 Fan Shi, Xuanyi Yu, Xinzheng Zhang, Pidong Wang, Yongfa Kong, and Jingjun Xu, "Visible tri-wavelength upconversion luminescence macroporous LN:Er with submicrometer transport mean free path", The First Taishan Academic Forum in Advanced Materials-University of Jinan, Jinan, China, March 03-05 (2012) (invited talk)
- 9 Yongfa Kong, Jingjun Xu, "New progress in optical damage controlling of lithium niobate crystals", The 2nd Chinese-Russian Workshop / Youth Summer School on Laser Physics, Fundamental and Applied Photonics, Tianjin, China, Aug. 3-8 (2012), p17-18. (invited talk)
- 10 Feng Song, "Erbium-Ytterbium co-doped fiber lasers with high concentration and high gain", The 2nd Chinese-Russian Workshop / Youth Summer School on Laser Physics, Fundamental and Applied Photonics, Tianjin, China, Aug. 3-8 (2012), p17-18. (invited talk)
- 11 Baohui Li, "Conformation transitions and scaling behavior of a strongly charged polyelectrolyte chain: A replica-exchange Monte-Carlo study", East Asia Joint Seminars on Statistical Physics, Suzhou, China, March 17-20 (2012). (Invited talk)
- 12 Baohui Li, "Scaling behavior of a strongly charged polyelectrolyte chain: A replica-exchange Monte-Carlo study", Workshop and Summer School on Coulomb Many-body System, Shanghai, China, June 12-14 (2012). (Invited talk)
- 13 Zhigang. Chen, "Spatial nonlinear dynamics in photonic lattices", International Workshop "Nonlinear dynamics, theory and experiment", PUEBLA, MEXICO, Feb 2012.
- 14 Zhigang. Chen, "Optical control with Airy beams and the like", International workshop on "Novel trends in nonlinear photonics", Montreal, Canada, Feb, 2012
- 15 Qiang Wu, Yinxing Ma, Shangyu Guo, Jingjun Xu, "Optical refocusing three-dimensional wide-field fluorescence lifetime imaging microscopy", 2nd Chinese-Russian Workshop /

- Youth Summer School on Laser Physics, Fundamental and Applied Photonics, Tianjin, China, August 3-8 (2012). (oral presentation)
- 16 Lei Xu, Yi Yin, Fang Bo, Jingjun Xu, and Guoquan Zhang, "Linear and nonlinear localized modes in the width-disordered one-dimensional waveguide arrays" 2012 Photonics Asia, Beijing, China, Nov 5-7(2012) (oral talk).
 - 17 Zhaohui Zhai, Jingjun Xu, and Guoquan Zhang, "Transfer of Topological Charges in an Electromagnetically Induced Transparency Solid," in Conference on Lasers and Electro-Optics (CLEO 2012), San Jose, California, USA, May 5-11, 2012 (oral talk).
 - 18 Peilong Hong, Jianbin Liu, and Guoquan Zhang, "Two-photon super bunching of thermal light" Frontiers in Optics (FiO) 2012, Rochester, NY, USA, October 14-18(2012) (oral talk)
 - 19 Lei Wang, Wei Cai, Xinzheng Zhang, Jingjun Xu, "Surface Plasmons at the Interface between Graphene and Kerr-Type Nonlinear Medium", The Sixth International Conference on Nanophotonics (ICNP2012) Beijing, May 27-30 (2012). (oral)
 - 20 Xu, Lei and Yin, Yi and Bo, Fang and Xu, Jingjun and Zhang, Guoquan, "Nonlinear evolution of transverse Anderson modes of light in the disordered one-dimensional waveguide arrays", Frontiers in Optics (FiO) 2012, Rochester, NY, USA, October 14-18(2012) (poster)
 - 21 Penghong Liu, Wei Cai, Lei Wang, Xinzheng Zhang, Jingjun Xu, "Light Excited Surface Plasmons in Graphene Ring Structures", FiO/LS (Frontiers in Optics/Laser Science)2012, Rochester, USA, Oct. 14-18 (2012). (Poster)
 - 22 Ming Yang, Zhandong Chen, Bin Zhang, Qiang Wu, and Jingjun Xu, "The appearance and absence of femtosecond laser induced periodic surface structures on silicon by one laser pulse", The 2nd International Symposium on Laser Interaction with Matter, Xi' an, Shaanxi, P. R. China, Sept. 9-12 (2012). (oral presentation)
 - 23 Zhandong Chen, Qiang Wu, Ming Yang, Jingjun Xu, "Plasma generation and evolution during femtosecond laser ablation of silicon", 2nd International Symposium on Laser Interaction with Matter (LIMIS 2012), Xi'an, P. R. China, September 9-12 (2012). (oral presentation)
 - 24 Penghong Liu, Wei Cai, Lei Wang, Xinzheng Zhang, Jingjun Xu, "Tunable terahertz optical antennas based on graphene ring structures", International Symposium on NanoPhotonics, Beijing (2012.2.12-14)
 - 25 Ying Cui-Feng, Zhou Wen-Yuan, Li Yi, Ye Qing, Zhang Cun-Ping, Tian Jian-Guo, "Band-edge lasing and miniband lasing in 1-D dual-periodic photonic crystal", Proceedings of SPIE - The International Society for Optical Engineering, 8425, (2012)
 - 26 Zidong Pei, Qian Hu, Yongfa Kong, Romano Rupp, Jingjun Xu, "Fabrication of lithium niobate p-n junctions", 2012 Symposium on Photonics and Optoelectronics (SOPO), Shanghai, China, May 21-23 (2012). Page(s): 1 - 4, Digital Object Identifier: [10.1109/SOPO.2012.6270514](https://doi.org/10.1109/SOPO.2012.6270514).
 - 27 Jiaming Sun, Qiongqiong Hou, "Silicon based MOS light emitting devices fully processed by atomic layer deposition technology", The 1st International Conference on ALD Applications & 2nd China ALD conference, Shanghai, China, Oct 14-16 (2012).
 - 28 Qiongqiong Hou, Fanjie Meng, Jiaming Sun, "Electrical and optical properties of ZnO:Al and ZnAl₂O₄ films grown by atomic layer deposition", The 1st International Conference on

- ALD Applications & 2nd China ALD conference, Shanghai, China, Oct 14-16 (2012).
- 29 Jun Sun, Jingjun Xu, Yongfa Kong, Ling Zhang, "Progress in research on practical stoichiometric lithium niobate crystals", The 3rd International Symposium on Rare Earth Resource Utilization (ISRERU-3), The 3rd Special Symposium on Advances in Functional Materials (AFM-3), Changchun, China, Dec 9-12 (2012)
 - 30 孔勇发, 刘士国, 刘宏德, 陈绍林, 张玲, 许京军, "掺铈铌酸锂晶体", 第十六届全国凝聚态光学性质学术会议, 郑州, (2012.7.24-28)。(大会报告)
 - 31 徐晓轩, "近红外拉曼光谱的应用新进展", 2012 年第四届近红外光谱学术会, 桂林 (2012.9) (大会报告)
 - 32 李宝会, "聚电解质单链构象转变和标度行为的模拟研究", "大分子体系功能结构的理论模拟" 研讨会, 南京 (2012.5.11-13)。(邀请报告)
 - 33 孙甲明, 侯琼琼, 孟凡杰, "原子层沉积技术在掺杂纳米层状结构发光材料研究的应用进展情况", 第四届全国掺杂纳米材料发光性质学术会议 (NMLP2012), 呼和浩特 (2012.8.10-15) (邀请报告)
 - 34 孔勇发, 刘士国, 刘宏德, 陈绍林, 张玲, 许京军, "高价掺杂铌酸锂晶体", 第 16 届全国晶体生长与材料学术会议, 合肥 (2012.10.21-24) (邀请报告)
 - 35 刘宏德, 张荣, 刘士国, 张玲, 孔勇发, 许京军, "掺铈铌酸锂晶体的紫外-可见抗光损伤性能研究", 中国材料大会 2012, 太原 (2012.7.14-16)
 - 36 张华, 杨金凤, 徐海霞, 黄绍龙, 张玲, 孙军, 孔勇发, 黄存新, 许京军, "同成分铌酸锂晶体中反位铌的扩散研究", 中国材料大会 2012, 太原 (2012.7.14-16)
 - 37 杨金凤, 黄存新, 孙军, 张华, 徐海霞, 黄绍龙, 张玲, 孔勇发, 许京军, "铌酸锂晶体锂含量的精确测量研究", 中国材料大会 2012, 太原 (2012.7.14-16)
 - 38 孙同庆, 张宇, 吴学谦, 高玲玲, 陈绍林, 孔勇发, 许京军, " Nd^{3+} 离子掺杂 $\text{KGdP}_4\text{O}_{12}$ 晶体的生长与光谱性质", 第 16 届全国晶体生长与材料学术会议, 合肥 (2012.10.21-24)
 - 39 葛新宇, 孔勇发, 辛菲菲, 张国权, 李威, 许京军, "四价掺杂铌酸锂晶体紫外光折变性能研究", 第 16 届全国晶体生长与材料学术会议, 合肥 (2012.10.21-24)
 - 40 张芳馨, 武莉, 张毅, 王标, 孔勇发, 许京军, "色度可调的 $\text{KSr}_4(\text{BO}_3)_3: \text{Dy}^{3+}, \text{Tm}^{3+}, \text{Eu}^{3+}$ 荧光粉的荧光性质和能量传递机理", 第 16 届全国晶体生长与材料学术会议, 合肥 (2012.10.21-24)
 - 41 Qionqiong Hou, Fanjie Meng, Jiaming Sun, "Preparation of ZnAl_2O_4 films by atomic layer deposition technology", 第四届全国掺杂纳米材料发光性质学术会议 (NMLP2012), 呼和浩特 (2012.8.10-15) (优秀墙报奖)
 - 42 郑守君, 孔勇发, 刘宏德, 陈绍林, 许京军, "铌酸锂晶体光诱导畴反转过程的机理分析", 第 16 届全国晶体生长与材料学术会议, 合肥 (2012.10.21-24) (优秀墙报奖)
 - 43 田甜, 孔勇发, 刘士国, 李威, 陈绍林, 张玲, 许京军, "掺钼铌酸锂晶体的全色存储", 第 16 届全国晶体生长与材料学术会议, 合肥 (2012.10.21-24) (张贴报告)
 - 44 黄明, 孔勇发, 陈绍林, 刘士国, 张玲, 许京军, "掺镁铌酸锂晶体回音壁模式谐振腔",

- 第 16 届全国晶体生长与材料学术会议，合肥（2012.10.21-24）（张贴报告）
- 45 张荣，刘宏德，刘士国，张玲，陈绍林，孙军，孔勇发，许京军，“铈酸锂晶体的光辅助畴反转的动态研究”，第 16 届全国晶体生长与材料学术会议，合肥（2012.10.21-24）（张贴报告）
 - 46 李芳，武莉，张毅，王标，孔勇发，许京军，“ Eu^{3+} 掺杂的 $\text{KSr}_4(\text{BO}_3)_3$ 红色荧光粉的结构及发光性能”，第 16 届全国晶体生长与材料学术会议，合肥（2012.10.21-24）（张贴报告）
 - 47 张国权，“双光子光栅、光脉冲的存储”，第十六届激光科学研讨会，湖北宜昌，（2012.10.30-2012.11.3）
 - 48 蔡卫，“等离激元、快电子与石墨烯相关研究”，第二届原子分子光物理青年科学家论坛，武汉（2012.11.17-18）
 - 49 唐莉勤，徐燕，张心正，易三铭，许京军“无序光子晶格中平衡扩展态的研究”，泰山学术论坛——光电材料与器件专题，邀请报告，中国青岛（2012.10.26-28）
 - 50 洪佩龙，张国权，经典光的高可见度双光子干涉，第十届全国量子光学会议，广州，2012 年 7 月 14-17 日。
 - 51 张文定，黄礼刚，高峰，张国权，许京军，“基于声光可调谐滤波器和锥形光纤的可调谐上下通道耦合器”，第十六届全国凝聚态光学性质学术会议，郑州，2012 年 7 月 24 日-28 日。
 - 52 薄方，高峰，张国权，许京军，“动态折射率调制体系内的慢光”，首届全国原子分子光物理青年科学家论坛，北京，2012 年 2 月 8 日-10 日。
 - 53 薄方，翟召辉，刘泽，许京军，张国权，“非线性法珀腔内光群速的减慢和加快”，第二届全国原子分子光物理青年科学家论坛，武汉，2012 年 11 月 16 日-18 日。
 - 54 张文定，黄礼刚，高峰，薄方，许京军，张国权，“具有均匀插入损耗的宽带全光纤声光可调谐耦合器”，第十五届全国基础光学与光物理学术讨论会，广西南宁，2012 年 12 月 14 日-19 日
 - 55 陈宗强，王午登，陈靖，李玉栋，孙骞，“介电纳米光波导的 T 型分光特性的研究”，首届全国物理学科博士生论坛，北京（2012.9）（邀请报告）
 - 56 云志强，李威，罗维维，吴强，张心正，魏汝省，徐现刚，“ 6H-SiC 的飞秒激光超衍射加工”，第十六届全国凝聚态光学性质学术研讨会(OPCM2012)，口头报告，中国郑州（2012.7.24-28）
 - 57 吴玉娥，李文华，易三铭，李威，吴强，张心正，“利用交叉相位调制分析超衍射连续谱的色散”，第十六届全国凝聚态光学性质学术研讨会(OPCM2012)，口头报告，中国郑州（2012.7.24-28）
 - 58 梁毅，叶卓艺，宋道红，张心正，许京军，“Three-Airy beam 的非线性研究”，第十六届全国凝聚态光学性质学术研讨会(OPCM2012)，口头报告，中国郑州（2012.7.24-28）
 - 59 易三铭，徐燕，王萌，李威，吴强，张心正，“激光直写超衍射加工光致热氧化机理研究”，第十六届全国凝聚态光学性质学术研讨会(OPCM2012)，口头报告，中国郑州（2012.7.24-28）
 - 60 徐晓轩，第 446 次香山科学会议—我国近红外光谱分析关键技术问题、应用与发展战略，中国北京，（2012.11）

学术组织与期刊任职/Academic Service

国内学术组织任职/Service to the Domestic Professional Societies

序号	姓名	任职机构	职位	任期
1	许京军	中国高校知识产权研究会	副理事长	2008-
2	许京军	中国光学学会	理事	2006-
3	许京军	天津市光学学会	副理事长	2010-
4	许京军	天津市激光技术学会	副理事长	2010-
5	许京军	应用光学国家重点实验室	主任	2009-
6	孔勇发	中国材料研究学会青年工作委员会	理事	2011—2014
7	宋峰	天津市物理学会	常务理事兼秘书长	2008.7-
8	宋峰	天津市激光技术学会	副理事长	2009-2014
9	田建国	天津市光学学会	常务理事	
10	孙骞	天津市光电子学会	常委	2006-
11	张天浩	天津市照明学会	常务理事	2008-2012
12	宋峰	中国仪器仪表学会光电技术与系统成分会	常务理事	2007.6-
13	孔勇发	中国硅酸盐学会晶体生长与材料分会	理事	2012-2015
14	孙甲明	中国物理学会发光分会	委员	2010—2014
15	孙甲明	全国掺杂纳米发光学会	委员	2010—2014
16	孙骞	中国光学学会光电技术委员会	委员	2006-
17	徐晓轩	中国仪器仪表学会分析仪器分会近红外光谱专业委员会	学术委员	2009-2013
18	孙军	国家标准化管理委员会人工晶体标准化技术委员会	委员	2012.9—
19	宋峰	科学出版社	第二届教材建设委员会物理学科委员	2010.10-2015.12
20	宋峰	信息科学部	第五届专家咨询委员会学术秘书	2011.4-2014.4
21	宋峰	德州学院物理系	兼职教授	2007-2011
22	宋峰	南通大学	兼职教授	2008-2012

国内外期刊任职/Service to the Journals

序号	姓名	任职机构	职位	任期
1	许京军	journal of Optics	topic editor	
2	许京军	Frontiers of Physics in China	编委	2008-2011

3	宋 峰	Applied Optics	编委	2009-2012
4	许京军	《光学学报》	副主编	2008-
5	宋 峰	《大学物理》	副主编	2009.5-
6	许京军	《红外与毫米波学报》	编委	
7	许京军	《物理》	编委	2007-2011
8	许京军	《物理学进展》	编委	2009-2012
9	许京军	Chinese Physics Letters	编委	2009-
10	许京军	《中国光学与应用光学》	编委	2008-
11	孔勇发	《激光技术》	编委	2010-2013
12	孔勇发	《人工晶体学报》	编委	2012-2016
13	张国权	《激光技术》	编委	2011-2014
14	张国权	《激光与光电子学进展》	编委	2010-2013
15	宋 峰	《清洗世界》	编委	2011-

获奖情况/Awards & Honors

典型软物质系统自组装行为的研究

2011 年度天津自然科学奖二等奖

获得者：李宝会、孙平川、陈铁红、尹玉华、金庆华、丁大同

获奖教师/Award for excellent teachers

天津市 2011 年度“131”创新型人才培养工程第一层次

入选者：宋峰

获奖学生/Award for excellent students

教育部“博士研究生学术新人奖”：王 瑾

研究生国家奖学金：

博士生：王 垒 王 瑾

硕士生：马寅星 邓志超

南开大学优秀学生干部：梁 毅

南开大学优秀毕业生：辛非非 任梦昕 朱美玲

南开大学三好学生：高 原

南开大学奖学金：

一等奖学金：李建雄 潘 岳 孔令军 娄 凯

二等奖学金：张文定 王 垒 刘鹏翊 李思弢 钱升霞 任志成

三等奖学金：翟召辉 洪佩龙

学位论文/Dissertations

1. 博士学位论文 Dissertation for Doctoral Degree

- [1] 辛非非, 掺杂铌酸锂晶体紫外带边光折变性质与缺陷结构的研究; 导师: 张国权
- [2] 叶卓艺, 光诱导光子学微结构中的光传输与光调控研究; 导师: 陈志刚
- [3] 任梦昕, 超颖材料非线性光学效应及其应用; 导师: 许京军
- [4] 石凡, 无序介质中光子局域化行为的研究及调控; 导师: 许京军
- [5] 张学智, 中红外硅基环形谐振腔中若干非线性效应及其应用研究; 导师: 许京军
- [6] 刘欣, 光束在周期性微结构材料中的传播和应用研究; 导师: 臧维平
- [7] 刘富才, 几种金属氧化物材料的非线性光学性能的研究; 导师: 孔勇发
- [8] 迟鹏, 嵌段共聚物自组装行为与聚电解质单链构象的蒙特卡罗模拟; 导师: 李宝会
- [9] 杨荣巧, 受限环境下两嵌段共聚物及其与均聚物共混体系自组装行为模拟研究; 导师: 史安昌、李宝会
- [10] 董江舟, 低维功能材料的制备和光电性质的研究; 导师: 曹亚安
- [11] 程辉, 染料敏化太阳能电池光阳极的制备、性质和光电转换机理研究; 导师: 姚江宏
- [12] 曹雪, ITO、AZO 靶材用纳米粉体的制备与 III-V 族半导体合金薄膜的生长研究; 导师: 舒永春
- [13] 李燕丽, 二氧化硅基质复合材料及荧光共轭聚合物制备与表征; 导师: 徐章程
- [14] 康明, 基于亚波长金属微结构的光场调控; 导师: 王慧田
- [15] 施曙东, 脉冲激光除漆的理论模型、数值计算与应用研究; 导师: 宋峰

2. 硕士学位论文 Dissertation for Master Degree

- [1] 李斌, 纵向调制的波导阵列中光传输特性的研究; 导师: 张国权
- [2] 赵飞, 铌酸锂晶体中光诱导铁电畴反转的研究; 导师: 张国权
- [3] 潘登, 基于表面等离激元的若干微纳光学器件; 导师: 孙骞
- [4] 孔凡磊, 微纳光学器件与应用的研究; 导师: 孙骞
- [5] 孟涛, 光诱导表面金属微纳结构及表面等离子激元的激发; 导师: 张心正
- [6] 王莲莲, 基于 PDMS 的光流体环形谐振腔激光器的研究; 导师: 禹宣伊
- [7] 周开, 心率波动随机模型研究及应用; 导师: 张天浩
- [8] 赵明铎, 褪黑激素分泌受抑的光谱灵敏性及光谱对抗性研究; 导师: 张天浩
- [9] 闫峥, 光折变空间孤子形成规律研究; 导师: 张天浩
- [10] 丁芳媛, 近红外组织血氧监测仪在乳房重建中的应用; 导师: 张天浩
- [11] 尹鹏飞, 基于时间分辨技术的组织光学参数测量的研究; 导师: 周文远
- [12] 辛建康, 基于蒙特卡洛方法的粗糙表面光散射特性的研究; 导师: 周文远
- [13] 李莉, 石墨烯微结构制备研究; 导师: 刘智波
- [14] 马强, 碳纳米材料光学非线性增强研究; 导师: 刘智波
- [15] 石伟科, 聚合物中功能微结构制备的研究; 导师: 李玉栋

- [16] 张光子, 磁介质表面飞秒微加工的研究; 导师: 李玉栋
- [17] 杨涛, 基于偏振传感和物联网的实验室信息网络架设; 导师, 周文远
- [18] 郭燕磊, 光子晶体的表面自发辐射增强效应; 导师, 周文远
- [19] 张建峰, 铌酸锂晶体热释电性能调控研究; 导师: 孔勇发
- [20] 刘文波, 铌酸锂晶体的光生伏打效应研究; 导师: 孔勇发
- [21] 朱美玲, 铌酸锂晶体中光辅助畴反转的研究; 导师: 孔勇发、刘宏德
- [22] 郑先明, 金纳米粒子的表面修饰及其光电性质研究; 导师: 曹亚安
- [23] 张铭, 掺钕氟氧化物玻璃陶瓷的制备和微晶结构研究; 导师: 赵丽娟
- [24] 张盼, 稀土掺杂氟化物纳米晶溶液的制备及光学特性研究; 导师: 赵丽娟
- [25] 王亚洲, 氟氧化物玻璃陶瓷中可调控白光发光材料的研制; 导师: 赵丽娟
- [26] 孟凡杰, 利用原子层沉积方法制备硅基 MOS 器件研究; 导师: 孙甲明
- [27] 闫艳花, 超声雾化法制备 Er^{3+} 掺杂 SnO_2 薄膜结构与性质研究; 导师: 孙甲明
- [28] 王云峰, ZnO 纳米结构的制备及光学性质研究; 导师: 姚江宏
- [29] 栾星, 锗半导体纳秒激光烧蚀的理论研究; 导师: 姚江宏
- [30] 胡永能, 水热法小批量 SnO_2 纳米粉体的制备研究; 导师: 舒永春
- [31] 王俊, 近化学计量比铌酸锂晶体制备及其畴极化反转电场的研究; 导师: 张玲
- [32] 樊文博, InP 量子点肖特基势垒探测器的制备与表征; 导师: 徐章程
- [33] 孟楠, MEH-PPV /硫化铅量子点光探测器的制备与表征; 导师: 徐章程
- [34] 赵建彬, 掺钙及掺铝近化学计量比铌酸锂晶体的生长及抗光损伤性能的研究; 导师: 刘士国
- [35] 李广平, 纳米 ZnO 粉体的制备与性能研究; 导师: 邢晓东
- [36] 张宇, 稀土离子掺杂钨酸镧钾和磷酸钪钾晶体的生长和光谱性质研究; 导师: 孙同庆
- [37] 董职福, 硅微纳加工及其拉曼光谱表征; 导师: 徐晓轩
- [38] 杜鹏, 脉冲激光除漆实验研究与激光除漆试验机的制作; 导师: 宋峰
- [39] 王芳, 基于三角法的激光测距技术; 导师: 宋峰
- [40] 张超, 金属纳米结构光学性质的 DDA 及 FDTD 模拟; 导师: 宋峰
- [41] 张功, 铒镱共掺 $\text{Y}_2\text{Ti}_2\text{O}_7$ 纳米晶与薄膜的发光性质及泵浦饱和效应; 导师: 宋峰

Giant nonlinear optical activity in a plasmonic metamaterial

Mengxin Ren,^{1,2} Eric Plum,^{2,*} Jingjun Xu,¹ and Nikolay I. Zheludev^{2,†}

¹Key Laboratory of Weak Light Nonlinear Photonics, Nankai University, Tianjin 300457, P.R. China

²Optoelectronics Research Centre and Centre for Photonic Metamaterials, University of Southampton, SO17 1BJ, UK

(Dated: March 15, 2012)

In 1950, a quarter of a century after his first ever nonlinear optical experiment when intensity dependent absorption was observed in uranium-doped glass, Sergey Vavilov predicted that birefringence, dichroism and polarization rotatory power should be dependent on light intensity. It required the invention of the laser to observe the barely detectable effect of light intensity on the polarization rotary power of the optically active lithium iodate crystal, the phenomenon now known as the nonlinear optical activity, a high-intensity counterpart of the fundamental optical effect of polarization rotation in chiral media. Here we report that a plasmonic metamaterial exhibits nonlinear optical activity 30 million times stronger than lithium iodate crystals thus transforming this fundamental phenomenon of polarization nonlinear optics from an esoteric phenomenon into a major effect of nonlinear plasmonics with potential for practical applications.

Since its discovery by François J. D. Arago in 1811 [1], optical activity, that is the ability to rotate the polarization state of light, has acquired great importance in spectroscopy, analytical chemistry, crystallography and molecular biology and it is associated with the biochemistry of life [2]. It is now well understood that the effect is linked to chirality. In dissipative media optical activity manifests itself as circular birefringence, leading to polarization rotation, and circular dichroism, i.e. differential transmission of circularly polarized waves, that yields a change of the degree of ellipticity of the propagating wave. In contrast to the Faraday effect, which causes polarization rotation in the presence of static magnetic fields, polarization rotation due to natural optical activity is reciprocal, i.e. it does not distinguish between opposite directions of wave propagation.

The dependence of optical activity on the intensity of light was discussed by Vavilov in 1950 [3], a quarter of a century after the first effect of light self-action, the intensity-dependent absorption, was observed in uranium-doped glass [4]. The symmetry, wave propagation and quantum mechanical description of the phenomenon that later acquired the name of nonlinear optical activity (NOA) was then rigorously derived [5–11].

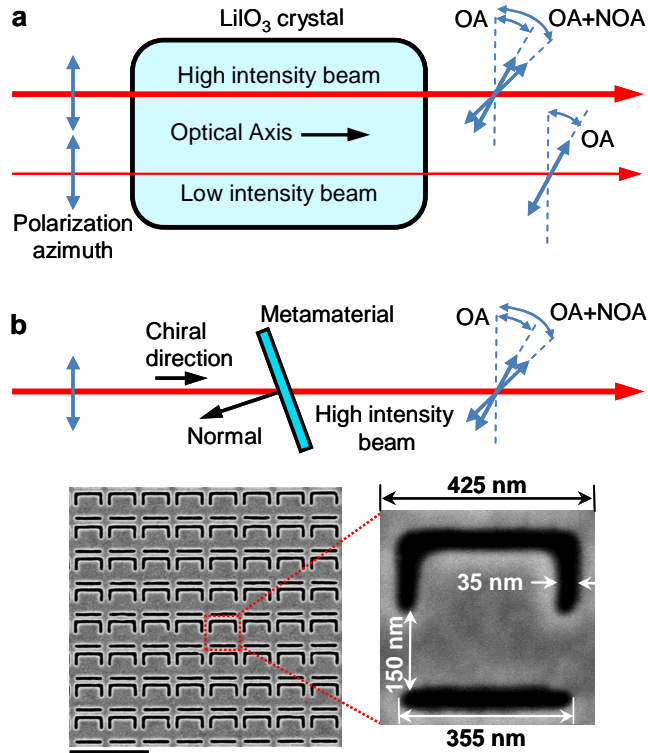


FIG. 1: **Nonlinear optical activity (NOA):** (a) To observe NOA in 1979 in a LiIO_3 crystal, intensity dependent change of the polarization azimuth of about 0.02° was recovered on a background of 8000° of natural rotation by comparing the polarization state in high and low intensity channels using a pulsed laser [12]. (b) Observation of NOA in a gold plasmonic metamaterial along a chiral direction, where nonlinearity is resonantly enhanced by nanoscale confinement of light. The scanning electron micrograph shows a fragment of the gold nanostructure ($1 \mu\text{m}$ scale bar) and detailed dimensions of a single meta-molecule.

Observation of NOA due to the fast electronic mechanism of nonlinearity became possible in 1979 using a high intensity single-mode nanosecond pulsed laser and the natural crystal of lithium iodate that is simultaneously a highly nonlinear and strongly optically active medium [12] (see Figure 1a). Shortly after that, transient pump-probe measurements of nonlinear optical activity were performed in the chiral cholesteric phase of a liquid crystal exploiting the thermal mechanism of nonlinearity [13]. Thermal NOA was also seen in optically active crystals [14–16]. Since then nonlinear optical activity has been observed in a number of chiral liquids [17–20]. Neverthe-

*Electronic address: erp@orc.soton.ac.uk

†Electronic address: niz@orc.soton.ac.uk; URL: www.nanophotonics.org.uk

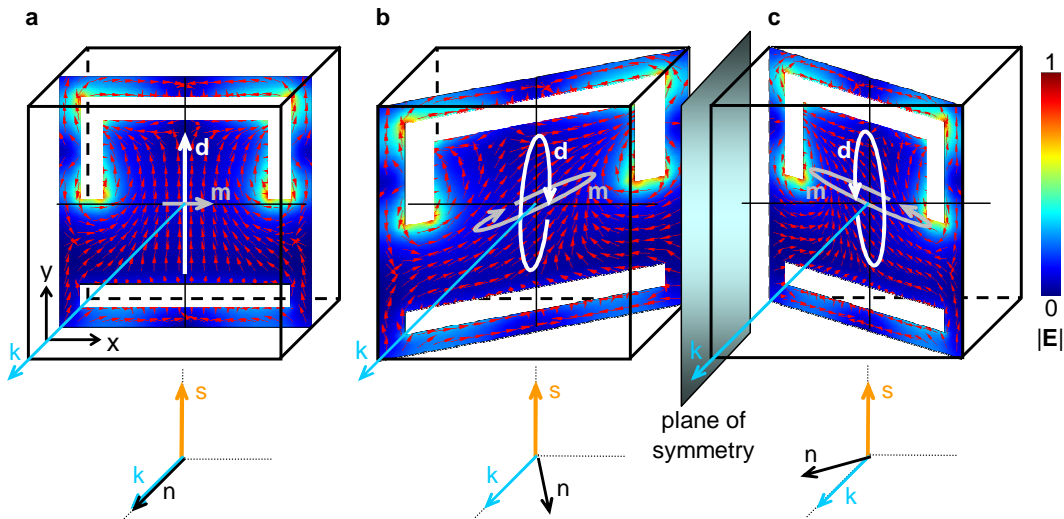


FIG. 2: **Chiral scattering in plasmonic metamaterial:** Electric field magnitude $|E|$ (color map) and instantaneous directions of the electric field (small red arrows) inside the metamaterial gold film, for excitation with y-polarized light at (a) normal incidence, (b) $+20^\circ$ oblique incidence (experimental case) and (c) -20° oblique incidence. At normal incidence the unit cell's total electric \mathbf{d} and magnetic \mathbf{m} dipoles trace perpendicular directions. No polarization change is observed in this case (a). At oblique incidence vectors \mathbf{d} and \mathbf{m} trace ellipses with main axes that are not perpendicular to one another. The scattered wave's polarization is now different from that of the incident wave. The polarization change reverses with reversing sense of chirality of the mutual arrangement of the incident light wave (vector \mathbf{k}) and the metamaterial's normal \mathbf{n} and symmetry axis \mathbf{s} : scenarios (b) and (c) are mirror-symmetric and will show optical activity equal in amplitude but opposite in sign.

less, the effect remained challenging to detect, making it unsuitable for routine practical applications even in spectroscopy.

Although nonlinear optical activity in natural media was weak, hopes have been growing that a stronger effect could be found in artificial media. Indeed, an observation of optical activity in artificial media (twisted jute) in the millimeter wave part of the spectrum was reported by J. Bose as far back as 1898 [21]. Recently, with the development of metamaterials (periodic media structured on the sub-wavelength scale), it has become possible to design optimized photonic structures with specific optical activity orders of magnitude larger than in natural media [22–25]. It was found, for instance, that artificial circular birefringence could be so strong, that while it is normally a correction to the refractive index, in some metamaterials it makes the refractive index negative for one circular polarization [26, 27]. Moreover, recent experiments in waveguides revealed that a chiral inclusion containing a varactor nonlinear element forces a strong intensity dependent rotation of the polarization state of microwave radiation [28]. At the same time, resonant local field enhancement in plasmonic metamaterials can dramatically amplify the nonlinear response of hybridized materials, such as silicon [29, 30] and carbon nanotubes [31], and even the metal forming the metamaterial itself [32, 33].

The phenomenon of natural optical activity is inextricably linked to chirality. In many optically active media chirality resides in the left-right asymmetry of the constituent components of the medium. For instance a liquid consisting of only one form of chiral molecules,

i.e. molecules that are not congruent with their mirror image, is likely to exhibit optical activity. Here the best known natural example is sugar solution where optical activity is routinely used to measure the concentration of the syrup. Optical activity may also result from chiral arrangements of non-chiral molecules, as it may be found in crystals of quartz or lithium iodate. Chirality can also emerge from the mutual arrangement of the beam of light and the medium, creating what is known in crystallography as a “screw direction”. For instance a regular array of oriented molecules that are not chiral in their own right, could make an arrangement with a beam of light that lacks mirror symmetry and shows optical activity [34, 35]. In general, only crystals whose point group contains no inversion center could have screw directions. Polarization rotation in certain crystal classes of symmetry along certain directions is underpinned by this mechanism of optical activity [36], which is also routinely observed in liquid crystals [37] and metamaterials [38]. True circular birefringence and dichroism can also be found in these cases.

Here we report that a plasmonic metamaterial exhibits a huge nonlinear optical activity in the optical part of the spectrum. It is 30 million times stronger than in the lithium iodate crystal [12]. This magnitude of the nonlinear polarization effect was achieved by combining strong metamaterial optical activity due to extrinsic chirality with strong metamaterial optical nonlinearity: in this artificial medium the figure of merit that represents specific nonlinear polarization rotation ($^\circ/\text{cm}$) per unit of intensity (W/cm^2) is $3 \times 10^{-4} \text{ }^\circ\text{cm}/\text{W}$ (compare with

10^{-11} °cm/W for lithium iodate). As a result nonlinear rotation on the order of degrees can be seen at an average laser power level of only a few mW.

I. RESULTS

A. Optical activity due to extrinsic chirality

The metamaterial consists of a periodic array of asymmetric split ring slits, which were cut by focussed ion-beam milling through a 50 nm thick gold film supported by a $500 \mu\text{m}$ thick fused quartz substrate. The overall size of the metamaterial array is $100 \times 100 \mu\text{m}^2$ with a period of 425 nm and the individual meta-molecules lack two-fold rotational symmetry, see Figure 1b. Figure 2 illustrates the origin of chirality and optical activity in this material for oblique incident angles. It is caused by circular differential forward scattering of incident photons that may be traced down to the scattering contributions of the unit cell's effective electric \mathbf{d} and magnetic \mathbf{m} dipole moments induced by the incident wave. It is well known from the molecular theory that optical activity requires the molecule to exhibit magnetic and electric responses simultaneously in such a way that there is a non-zero projection of the induced magnetic dipole on the induced electric dipole [2, 39]. In this case the forward scattered wave will exhibit polarization rotation as electric and magnetic dipoles will emit orthogonal polarization components with a phase lag. The mechanism for extrinsic chirality in metamaterials is illustrated by the finite element method simulations in Figure 2 for a single meta-molecule excited by an incident y-polarized wave. At normal incidence the field distribution in the unit cell of the metamaterial is mirror-symmetric with respect to the y-direction. The total electric and magnetic moments of the unit cell oscillate along strictly perpendicular directions: no optical activity is observed in this case, see Figure 2a. At oblique incidence the total induced magnetic and electric moments are tracing ellipses whose main axes are not perpendicular anymore and conditions are right for the meta-molecule to scatter with a polarization change. This polarization effect is optical activity and it will change sign with changing chirality of the arrangement, as illustrated by Figures 2b and 2c.

B. Measurements of linear optical activity and anisotropy

We studied linear and intensity dependent optical activity using a femtosecond mode-locked tunable laser with 115 fs pulse duration and 80 MHz repetition rate. Figure 3 illustrates the metamaterial's linear (low power) optical properties for wavelengths between 930 nm and 954 nm, where the metamaterial has a plasmonic resonance and optical activity is largest. In general, in media of low symmetry optical activity coexists with anisotropy

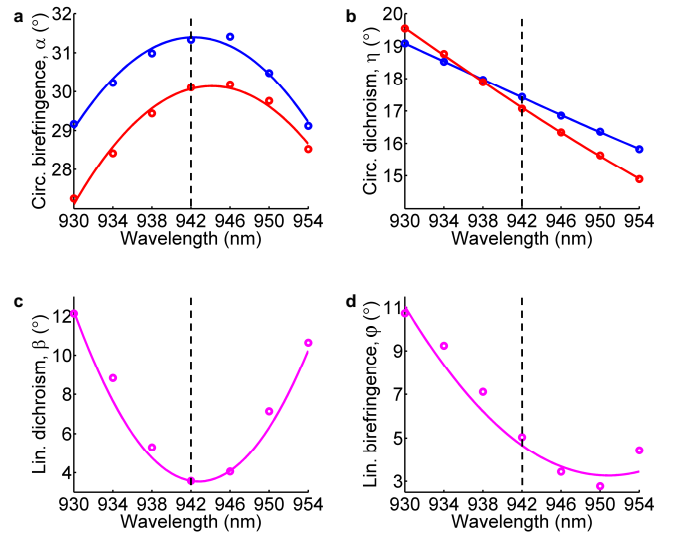


FIG. 3: **Giant linear polarization effects in a plasmonic nanostructure:** Optical activity in terms of (a) circular birefringence (polarization rotation) and (b) circular dichroism (ellipticity angle) at linear and nonlinear average power levels of $50 \mu\text{W}$ (blue) and 5mW (red), respectively; optical anisotropy in terms of (c) linear dichroism and (d) linear birefringence at $50 \mu\text{W}$ average power. Vertical dashed lines indicate the wavelength of 942 nm for which the power dependence of NOA has been studied.

that manifests itself as differential refraction (birefringence) and transmission (dichroism) for orthogonal linear polarizations.

Upon propagation through an optically active and anisotropic medium, a wave with initially linear polarization becomes elliptically polarized and its polarization azimuth rotates. For moderate polarization changes it may be shown that rotation of the polarization azimuth contains contributions resulting from circular birefringence α and linear dichroism β , while the ellipticity of the transmitted wave will contain contributions from circular dichroism η and linear birefringence φ . These four contributions can be separated by measuring polarization rotation and ellipticity angle as functions of the input polarization azimuth of an initially linearly polarized wave, providing $\alpha, \beta, \eta, \varphi \ll \pi$ (see Methods).

Figure 3 presents measurements of circular birefringence and dichroism (optical activity) and linear birefringence and dichroism (anisotropy) in the metamaterial sample observed as functions of wavelength at the incident angle of 20° to the normal (measurements taken at -20° show rotation and ellipticity angles of the same magnitude but opposite signs). We note that optical activity is overwhelmingly the dominant contribution to the polarization azimuth and ellipticity changes at the resonance wavelength of 942 nm: here anisotropy contributes only up to 12% to the total polarization azimuth rotation and 30% to ellipticity. Detailed measurements of the intensity dependent polarization changes reported below were performed at this wavelength.

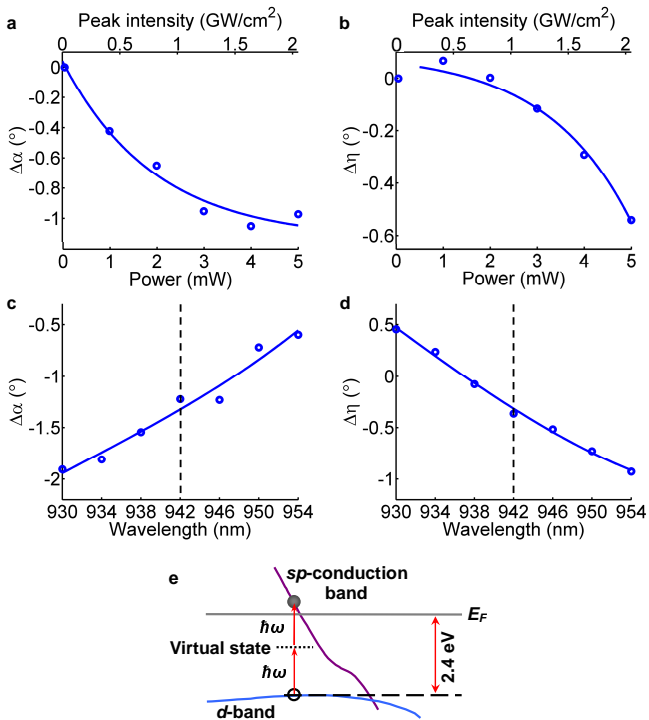


FIG. 4: **Nonlinear optical activity of a plasmonic metamaterial:** Power dependent changes of the metamaterial’s (a) circular birefringence $\Delta\alpha$ and (b) circular dichroism $\Delta\eta$ for a fixed wavelength of 942 nm. Spectral dependence of nonlinear (c) circular birefringence and (d) circular dichroism for a fixed average power of 5 mW (relative to 50 μ W in all cases; guides to the eye are shown alongside experimental data points). The wavelength of 942 nm, for which the power dependence of NOA has been studied, is marked by dashed lines. (e) Sketch of the Au band structure and the two-photon absorption process, where a d -band electron is excited to the sp -conduction band above the Fermi level E_F via absorption of two photons $\hbar\omega$.

C. Measurements of nonlinear optical activity

The intensity dependence of optical activity was studied using the same laser source as for the linear characterization. While we performed the linear measurements at an average power of 50 μ W, the laser power was ramped up to 5 mW for nonlinear measurements, which corresponds to a peak intensity of $I = 2$ GW/cm² as the beam is focused to a spot size of 8 μ m in diameter. This is sufficient to see a profound change of the light polarization state with intensity, as illustrated by Figure 4a,b. Here results are represented in terms of changes relative to the low-intensity values of circular birefringence $\Delta\alpha$ and circular dichroism $\Delta\eta$. The most obvious effect of increasing intensity is a suppression of optical activity: at 942 nm polarization rotation is reduced by 1.0°, while the ellipticity angle drops 0.5°.

To determine the strength of nonlinear optical activity we shall be concerned with the gradient of the polarization azimuth rotation change with increas-

ing incident intensity that is measured to be about $\Delta\alpha/I = -0.8$ °cm²/GW, before nonlinearity starts to saturate above 1 GW/cm². Here nonlinearity resides in the gold film of thickness 53 nm along the direction of propagation. Thus the specific constant of nonlinear optical activity is $\Omega = 3 \times 10^{-4}$ °cm/W (this accounts for the 50% reflection of the metamaterial sample). This is more than 7 orders of magnitude stronger than NOA in natural materials such as LiIO₃ (10^{-11} °cm/W [12]), sucrose (2×10^{-11} °cm/W [17, 20]), α -pinene ($\leq 10^{-11}$ °cm/W [20]) and ruthenium salt solution [18, 19].

The spectral dependence of nonlinear optical activity is shown by Figure 4c,d. Nonlinear circular birefringence becomes more pronounced towards shorter wavelengths, while nonlinear circular dichroism changes sign at about 937 nm. As illustrated by Figure 3a, the increase of light intensity reduces the overall polarization rotation throughout the studied spectral range.

II. DISCUSSION

The nonlinearity of the metamaterial resides in the nonlinearity of its metal framework. It is mainly caused by the nonlinear process of direct two-photon absorption between the d and sp states in the gold band structure, see Figure 4e. Here direct two-photon absorption occurs through a virtual state when the energy $\hbar\omega$ of two incident photons is combined to bridge the gap $\Delta E = 2.4$ eV, between the d states and states above the Fermi level: $\Delta E/2 < \hbar\omega < \Delta E$. As the energy gap cannot be bridged by individual photons directly, “Fermi-smearing”, which dominates the nonlinearity of gold in the visible, is less important in our case. This inherited nonlinearity of gold is resonantly enhanced more than 300 times by the nanostructure through the virtue of strong field concentration at the edges of the grooves, which support a plasmonic mode (see bright hot-spots of field maps in Figure 2) [32]. Pump-probe experiments [32] also confirmed that this is a very fast nonlinearity because its main mechanism requires both the pump and the probe photons to be present simultaneously. This degenerate cubic optical nonlinearity gives rise to a nonlinear absorption coefficient on the order of 10^{-5} m/W. Importantly, the spectral maxima of the absorption nonlinearity and optical activity in this metamaterial overlap as they are underpinned by the same plasmonic resonance, which arises from the asymmetry of the metamaterial pattern [25, 32]. The asymmetry of the plasmonic structure results in excitation of a strong anti-phased current mode through weak free-space coupling, which ensures low radiation losses and therefore a narrow Fano-type optical resonance [40]. Here two-photon absorption reduces not only the intensity of light transmitted through the nanostructure, but it also hampers the chiral dipole scattering efficiency by dampening the underlying plasmon oscillations. Manifestation of this is a suppression of circular birefringence at high intensities (Figure 3a).

It may be expected that similarly large nonlinear polarization effects can be observed at resonances in a wide range of plasmonic metamaterials. In particular, large nonlinear optical activity may also occur in intrinsically 3D-chiral metamaterials and chiral plasmonic interfaces [41] may show nonlinear versions of other polarization effects such as asymmetric transmission [42].

In summary, we report that engineering of chiral and nonlinear optical properties in plasmonic metamaterial allows the observation of nonlinear optical activity that is millions of times stronger than in natural crystals. Observation of this giant polarization effect provides a powerful illustration that nanoscale nonlinear plasmonics of metamaterials offers extremely strong effects unfolding in nanoscale volumes of nonlinear medium that could lead to applications in modulation of light intensity and polarization in nanophotonic devices.

III. METHODS

A. Definition of polarization parameters

The polarization state of polarized light is characterized by the polarization azimuth Φ and the ellipticity angle ζ which are defined by the polarization ellipse, that is the trace of the end of the electric field vector as seen by an observer looking into the beam, see Figure 5a.

B. Separation of optical activity and optical anisotropy

Upon propagation through an optically active and anisotropic medium, a wave with initially linear polarization becomes elliptically polarized and its polarization azimuth rotates. For moderate polarization changes it may be shown that the polarization azimuth change $\Delta\Phi$ contains contributions resulting from circular birefringence α and linear dichroism β . On the other hand, the ellipticity angle ζ of the initially linearly polarized wave after interacting with the sample will contain contributions from circular dichroism η and linear birefringence φ .

Indeed, in the slow envelope approximation, evolution of the polarization state of light in linear media is governed by the following set of equations for the components of the four-dimensional Stokes vector \mathbf{S} , which in a Cartesian coordinate frame can be written as follows (formula 3.24, ref. 10):

$$\frac{d}{dz}(S_\mu e^{2\text{Im}\{k\}z}) = \frac{i\omega}{4c}(\Omega_\alpha E_j^* \sigma_{ji}^\mu \sigma_{ik}^\alpha E_k - \Omega_\alpha^* E_k^* \sigma_{kj}^\alpha \sigma_{ji}^\mu E_i) \quad (1)$$

Here z is the propagation direction, k and ω are the wave number and frequency, c is the speed of light, \mathbf{E} is the electric field vector, σ^α are Pauli spin matrices, δ_{ij} is the

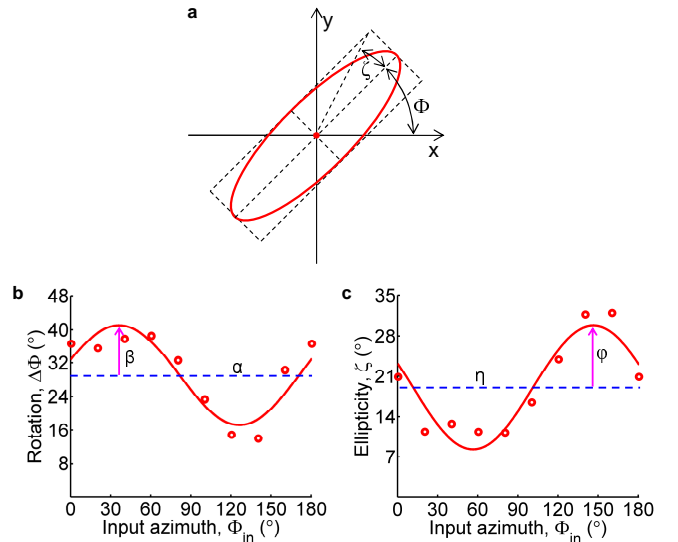


FIG. 5: **Measuring optical activity and optical anisotropy:** (a) Polarization azimuth Φ and ellipticity angle ζ of the polarization ellipse (red) define the polarization state of a polarized electromagnetic wave. (b) Polarization azimuth rotation $\Delta\Phi$ and (c) ellipticity angle ζ as a function of the azimuth Φ_{in} of the linearly polarized incident wave. The individual contributions of circular birefringence α and circular dichroism η correspond to the average levels of rotation and ellipticity of the transmitted wave, while the corresponding modulations arise from linear dichroism β and linear birefringence φ , respectively. The data shown was taken at 20° oblique incidence for a wavelength of 930 nm and low intensity (0.02 GW/cm^2).

Kronecker delta, and (formulae 3.19 and 3.21, ref. 10)

$$\Omega_\alpha = \sigma_{ji}^\alpha (\varepsilon_{ij} + ik\Gamma_{ijz} - n^2\delta_{ij})/n, \quad (2)$$

where ε_{ij} are cartesian components of the dielectric coefficient describing anisotropy and Γ_{ijz} are cartesian components of the nonlocality tensor describing optical activity. They are defined by the constitutive equation for the nonlocal anisotropic response (formula 2.14, ref. 10):

$$P_i = \frac{1}{4\pi} [(\varepsilon_{ij} - \delta_{ij})E_j + \Gamma_{ijn}\nabla_n E_j] \quad (3)$$

Therefore, it follows from the linear nature of equation (1) that small changes of the Stokes vector components and thus small polarization changes that are induced by the anisotropic and nonlocal effects are additive.

Now, by measuring the sample's polarization rotation $\Delta\Phi$ and ellipticity angle ζ as functions of the input polarization azimuth Φ_{in} of an initially linearly polarized wave, one can separate these four contributions, providing $\alpha, \beta, \eta, \varphi \ll \pi$.

Precise formulae for these contributions are given by formulae 3.41, 3.48 and 3.49 in ref. 10. For our consideration here it is important that for initially linearly polarized waves polarization rotation and induced ellipticity are proportional to $\text{Re}(\Gamma_{xyz})$ and $\text{Im}(\Gamma_{xyz})$ describing

circular birefringence and circular dichroism correspondingly. Polarization rotation and induced ellipticity also have components that oscillate with the incident polarization azimuth Φ_{in} as $\sin(2\Phi_{\text{in}})$. They are proportional to linear dichroism described by $\text{Im}(\varepsilon_{11} - \varepsilon_{22})$ and linear birefringence described by $\text{Re}(\varepsilon_{11} - \varepsilon_{22})$.

Within this approximation we retrieve circular birefringence α by measuring the Φ_{in} -independent (average) component of the polarization azimuth rotation;

we retrieve circular dichroism η by measuring the Φ_{in} -independent (average) component of the ellipticity angle; we retrieve data on linear birefringence φ by measuring the amplitude of oscillation of the ellipticity angle with the incident polarization azimuth; we retrieve data on linear dichroism β by measuring the amplitude of oscillation of the polarization azimuth rotation with the incident polarization azimuth, see Figure 5b,c.

-
- [1] Arago, F. J. D. Mémoire sur une modification remarquable qu'éprouvent les rayons lumineux dans leur passage à travers certains corps diaphanes et sur quelques autres nouveaux phénomènes d'optique. Mémoires de la classe des sciences math. et phys. de l'Institut Impérial de France **1**, 93 (1811).
- [2] Barron, L. D. Molecular light scattering and optical activity. Cambridge University Press, (2004).
- [3] Vavilov, S. I. Mikrostruktura Sveta (Microstructure of Light). USSR Academy of Sciences Publishing, Moscow, (1950).
- [4] Wawilow, S. I. and Lewschin, W. L. Die beziehungen zwischen fluoreszenz und phosphoreszenz in festen und flüssigen medien. Z. Phys. **35**, 920–936 (1926).
- [5] Zheludev, I. S. Axial tensors of the third rank and the physical effects they describe. Sov. Phys. Crystallogr. **9**, 418–420 (1965).
- [6] Akhmanov, S. A. and Zharikov, V. I. Nonlinear optics of gyrotropic media. JETP Lett. **6**(5), 137–140 (1967).
- [7] Kielich, S. Natural and magneto-optical rotation in the presence of an intense light beam. Phys. Lett. **25A**, 517–518 (1967).
- [8] Atkins, P. W. and Barron, L. D. Quantum field theory of optical birefringence phenomena. i. linear and nonlinear optical rotation. P. Roy. Soc. Lond. A Mat. **304**(1478), 303–317 (1968).
- [9] Petrenko, A. and Zheludev, N. Physical mechanisms of nonlinear optical activity in crystals. Optica Acta: International Journal of Optics **31**(10), 1177–1184 (1984).
- [10] Svirko, Y. P. and Zheludev, N. I. Polarization of light in nonlinear optics. Wiley, New York, (1998).
- [11] Zheludev, N., Petrenko, A., Svirko, I., and Filippova, G. Nonlinear optical activity in weakly and strongly nonlinear media: Direct and cascade processes-bistability and stochasticity. Akademiia Nauk SSSR Izvestiia Seriiia Fizicheskaiia **48**, 603–610 (1984).
- [12] Akhmanov, S. A., Zhdanov, B. V., Zheludev, N. I., Kovrigin, A. I., and Kuznetsov, V. I. Nonlinear optical activity in crystals. JETP Lett. **29**(5), 264–268 (1979).
- [13] Garibyan, O. V., Zhdanov, B. V., Zheludev, N. I., Kovrigin, A. I., and Kuznetsov, V. I. Thermal nonlinear optical rotation in cholesteric liquid crystals. Kristallografiya (Soviet Physics Crystallography) **26**, 787–791 (1981).
- [14] Vlasov, D. and Zaitsev, V. Experimental observation of nonlinear optical activity. JETP Lett. **14**, 112–115 (1971).
- [15] Borshch, V. V., Lisitsa, M. P., Mozol', P. E., and Fekeshgazi, I. V. Self-induced rotation of the direction of polarization of light in crystals of 422 symmetry. Sov. J. Quantum Electron. **8**, 393–395 (1978).
- [16] Zheludev, N., Ruddock, I., and Illingworth, R. Intensity dependence of thermal nonlinear optical activity in crystals. Appl. Phys. B **49**(1), 65–67 (1989).
- [17] Cameron, R. and Tabisz, G. Observation of two-photon optical rotation by molecules. Mol. Phys. **90**(2), 159–164 (1997).
- [18] Mesnil, H. and Hache, F. Experimental evidence of third-order nonlinear dichroism in a liquid of chiral molecules. Phys. Rev. Lett. **85**(20), 4257–4260 (2000).
- [19] Mesnil, H., Schanne-Klein, M., Hache, F., Alexandre, M., Lemerrier, G., and Andraud, C. Experimental observation of nonlinear circular dichroism in a pump-probe experiment. Chem. Phys. Lett. **338**(4-6), 269–276 (2001).
- [20] Markowicz, P., Samoc, M., Cerne, J., Prasad, P., Pucci, A., and Ruggeri, G. Modified z-scan techniques for investigations of nonlinear chiroptical effects. Opt. Express **12**(21), 5209–5214, Oct (2004).
- [21] Bose, J. On the rotation of plane of polarisation of electric waves by a twisted structure. P. R. Soc. London **63**(389-400), 146–152 (1898).
- [22] Plum, E., Fedotov, V. A., Schwanecke, A. S., Zheludev, N. I., and Chen, Y. Giant optical gyrotropy due to electromagnetic coupling. Appl. Phys. Lett. **90**, 223113 (2007).
- [23] Kuwata-Gonokami, M., Saito, N., Ino, Y., Kauranen, M., Jefimovs, K., Vallius, T., Turunen, J., and Svirko, Y. Giant optical activity in quasi-two-dimensional planar nanostructures. Phys. Rev. Lett. **95**, 227401 (2005).
- [24] Decker, M., Ruther, M., Kriegl, C. E., Z. J., Soukoulis, C., Linden, S., and Wegener, M. Strong optical activity from twisted-cross photonic metamaterials. Opt. Lett. **34**, 2501–2503 (2009).
- [25] Plum, E., Liu, X.-X., Fedotov, V. A., Chen, Y., Tsai, D. P., and Zheludev, N. I. Metamaterials: Optical activity without chirality. Phys. Rev. Lett. **102**(11), 113902 (2009).
- [26] Plum, E., Zhou, J., Dong, J., Fedotov, V. A., Koschny, T., Soukoulis, C. M., and Zheludev, N. I. Metamaterial with negative index due to chirality. Phys. Rev. B **79**, 035407 (2009).
- [27] Zhang, S., Park, Y.-S., Li, J., Lu, X., Zhang, W., and Zhang, X. Negative refractive index in chiral metamaterials. Phys. Rev. Lett. **102**, 023901 (2009).
- [28] Shadrivov, I. V., Fedotov, V. A., Powell, D. A., Kivshar, Y. S., and Zheludev, N. I. Electromagnetic wave analogue of an electronic diode. New J. Phys. **13**(3), 033025 (2011).
- [29] Cho, D., Wu, W., Ponizovskaya, E., Chaturvedi, P., Bratkovsky, A., Wang, S., Zhang, X., Wang, F., and

- Shen, Y. Ultrafast modulation of optical metamaterials. *Opt. Express* **17**(20), 17652–17657 (2009).
- [30] Dani, K., Ku, Z., Upadhyaya, P., Prasankumar, R., Brueck, S., and Taylor, A. Subpicosecond optical switching with a negative index metamaterial. *Nano Lett.* **9**(10), 3565–3569 (2009).
- [31] Nikolaenko, A. E., Angelis, F. D., Boden, S. A., Papasimakis, N., Ashburn, P., Fabrizio, E. D., and Zheludev, N. I. Carbon nanotubes in a photonic metamaterial. *Phys. Rev. Lett.* **104**, 153902 (2010).
- [32] Ren, M., Jia, B., Ou, J.-Y., Zhang, E. P. J., MacDonald, K. F., Nikolaenko, A. E., Xu, J., Gu, M., and Zheludev, N. I. Nanostructured plasmonic medium for terahertz bandwidth all-optical switching. *Adv. Mater.* **23**(46), 5540–5544 (2011).
- [33] Wurtz, G., Pollard, R., Hendren, W., Wiederrecht, G., Gosztola, D., Podolskiy, V., and Zayats, A. Designed ultrafast optical nonlinearity in a plasmonic nanorod metamaterial enhanced by nonlocality. *Nat. Nanotechnol.* **6**, 107–111 (2011).
- [34] Hameka, H. Resonance fluorescence in gases and molecular crystals. *J. Chem. Phys.* **38**(9), 2090–2111 (1963).
- [35] Buckingham, A. and Dunn, M. Optical activity of oriented molecules. *J. Chem. Soc. A* **38**(9), 1988–1991 (1971).
- [36] Sirotnin, Y. and Shaskolskaya, M. *Fundamentals of Crystal Physics*. Imported Pubn., (1983).
- [37] Williams, R. Optical rotatory effect in the nematic liquid phase of *p*-azoxyanisole. *Phys. Rev. Lett.* **21**, 342–344 (1968).
- [38] Plum, E., Fedotov, V. A., and Zheludev, N. I. Optical activity in extrinsically chiral metamaterial. *Appl. Phys. Lett.* **93**, 191911 (2008).
- [39] Condon, E. Theories of optical rotatory power. *Rev. Mod. Phys.* **9**(4), 432–457 (1937).
- [40] Khardikov, V. V., Iarko, E. O., and Prosvirnin, S. L. Trapping of light by metal arrays. *J. Opt.* **12**, 045102 (2010).
- [41] Hecht, L. and Barron, L. D. Rayleigh and raman optical activity from chiral surfaces. *Chem. Phys. Lett.* **225**, 525–530 (1994).
- [42] Fedotov, V. A., Mladyonov, P. L., Prosvirnin, S. L., Rogacheva, A. V., Chen, Y., and Zheludev, N. I. Asymmetric propagation of electromagnetic waves through a planar chiral structure. *Phys. Rev. Lett.* **97**, 167401 (2006).

IV. ACKNOWLEDGEMENTS

The authors are grateful to Edward Rogers, Kevin F. MacDonald, Jun-Yu Ou and Andrey Nikolayenko for assistance with experiment and preparation of samples. This work was supported by The Leverhulme Trust, The Royal Society (London), the UK Engineering and Physical Sciences Research Council (programme grant EP/G060363/1) and the P. R. China (‘111 Project’ grant B07013 and ‘973 Program’ grant 2007CB307002).

V. AUTHOR CONTRIBUTIONS

The idea of the experiment was conceived by N.I.Z. and E.P.; M.R. assembled the polarimeter and carried out the measurements; N.I.Z. wrote the paper with assistance from E.P.; all authors discussed the results and analyzed the data; J.J.X. and N.I.Z. supervised the work.

VI. ADDITIONAL INFORMATION

Competing financial interests: The authors declare no competing financial interests.

Tunable terahertz optical antennas based on graphene ring structures

Penghong Liu, Wei Cai, Lei Wang, Xinzheng Zhang, and Jingjun Xu

Citation: *Appl. Phys. Lett.* **100**, 153111 (2012); doi: 10.1063/1.3702819

View online: <http://dx.doi.org/10.1063/1.3702819>

View Table of Contents: <http://apl.aip.org/resource/1/APPLAB/v100/i15>

Published by the [American Institute of Physics](#).

Related Articles

Spectroscopic ellipsometry of split ring resonators at infrared frequencies

Appl. Phys. Lett. **100**, 161105 (2012)

Compact, low power radio frequency cavity for femtosecond electron microscopy

Rev. Sci. Instrum. **83**, 043705 (2012)

Atmospheric pressure dielectric barrier microplasmas inside hollow-core optical fibers

J. Appl. Phys. **111**, 073304 (2012)

Optical trapping force reduction and manipulation of nanoporous beads

Appl. Phys. Lett. **100**, 153702 (2012)

A graphene electron lens

Appl. Phys. Lett. **100**, 153106 (2012)

Additional information on *Appl. Phys. Lett.*

Journal Homepage: <http://apl.aip.org/>

Journal Information: http://apl.aip.org/about/about_the_journal

Top downloads: http://apl.aip.org/features/most_downloaded

Information for Authors: <http://apl.aip.org/authors>

ADVERTISEMENT

<p>INSTRUMENTS FOR ADVANCED SCIENCE</p> 	<p>Gas Analysis</p> <p>dynamic measurement of reaction gas streams catalysis and thermal analysis molecular beam studies dissolved species probes fermentation, environmental and ecological studies</p>	<p>Surface Science</p> <p>UHV TPD SIMS end point detection in ion beam etch elemental imaging - surface mapping</p>	<p>Plasma Diagnostics</p> <p>plasma source characterisation etch and deposition process reaction kinetic studies analysis of neutral and radical species</p>	<p>Vacuum Analysis</p> <p>partial pressure measurement and control of process gases reactive sputter process control vacuum diagnostics vacuum coating process monitoring</p>
	<p>contact Hiden Analytical for further details: info@hiden.co.uk www.HidenAnalytical.com</p> <p>CLICK TO VIEW OUR PRODUCT CATALOGUE</p>			

Tunable terahertz optical antennas based on graphene ring structures

Penghong Liu, Wei Cai,^{a)} Lei Wang, Xinzheng Zhang, and Jingjun Xu^{b)}

The Key Laboratory of Weak-Light Nonlinear Photonics, Ministry of Education, School of Physics and TEDA Applied Physics School, Nankai University, Tianjin 300457, China

(Received 13 January 2012; accepted 25 March 2012; published online 11 April 2012)

Highly tunable optical antennas in terahertz range based on graphene ring structures are proposed, which employ graphene plasmons instead of traditional metallic plasmons. The plasmon resonances of the perfect graphene ring (PGR) can be understood with the edge plasmons in graphene ribbons. While in the nonconcentric graphene ring, the multipolar plasmon modes appear and anti-symmetric mode splits due to symmetry breaking. Furthermore, the symmetric plasmon mode in a graphene ring can concentrate electromagnetic field with an enhancement factor as large as 10^3 in terahertz waveband, which is almost 20 times larger than a gold ring with the same size. © 2012 American Institute of Physics. [<http://dx.doi.org/10.1063/1.3702819>]

Optical antennas, which can convert far-field radiation into localized energy and vice versa, have attracted many research interests due to their enormous applications in sensing, photodetection, photovoltaic technique, light emission, and spectroscopy.¹ Various metallic antennas have been extensively demonstrated in a variety of systems including solid tips,^{2,3} particles,⁴ bowtie,⁵ Yagi-Uda array,⁶ and so on. And all of these researches are based on the common starting point-metallic plasmons. Meanwhile, graphene,⁷ a single layer of carbon atoms packed in hexagonal structures, can also bind surface plasmons.⁸ Recently, beyond the theoretical investigations on excitation of graphene plasmons with a dipole source^{9,10} and propagating plasmons in graphene ribbon waveguides,^{11,12} the existence of graphene plasmons are verified experimentally in graphene microribbons¹³ and extend graphene sheets.¹⁴ Graphene plasmons possess more electromagnetic confinement, lower dissipation loss than metallic plasmons.⁹ More importantly, graphene plasmons are more easily tunable by changing the doping level of graphene *via* chemical or electrostatic gating¹⁵ than metallic plasmons. Therefore, in principle, optical antennas using graphene have several important advantages compared to metallic antennas. First, the resonance frequencies of graphene antennas mostly lie in the infrared and terahertz ranges, which have tremendous importance, since many biological materials have molecular vibration frequencies in these regions. Second, the properties of graphene can be easily controlled by changing the parameters of graphene (e.g., Fermi energy, environmental temperature, and relaxation time), thus it opens up an opportunity to actively control the properties of graphene antennas. Third, graphene antennas hold more robust ability of electromagnetic field concentration than metallic plasmons, hence graphene antennas support a stronger electromagnetic field platform for light-matter interactions. On the other hand, ring structures, due to their high degree of symmetry, continue to be research hot-spots in a wide range discipline. The resonances of perfect metallic ring were obtained using analytical model by Aizpurua *et al.*¹⁶ Then, symmetric-broken ring structures,

including nonconcentric ring-disks¹⁷ and split rings,¹⁸ were also demonstrated. So, it is natural for us to consider the performance of graphene ring structures for the applications as terahertz antennas, which can open an avenue for next generation applicable optical antennas.

We start by analyzing the plasmon resonances of self-standing perfect graphene rings (PGRs). A plane wave is normally incident on a graphene ring whose inner radius is 25 nm and outer radius is 50 nm, as indicated in the inset of Fig. 1(a). The extinct areas of graphene rings with three different Fermi energies E_F are calculated. And the extinction area is normalized to the physical area of the ring structures in the whole paper. Here, the conductivity of graphene is computed within the local-random phase approximation (RPA)¹⁹ with an intrinsic relaxation time $\tau = \mu E_F / e v_F^2$, where $v_F \approx c/300$ is the Fermi velocity and $\mu = 10\,000 \text{ cm}^2/\text{Vs}$ is the measured DC mobility.²⁰ Maxwell's equations were solved by using the finite-element commercial software COMSOL. In Fig. 1(a), the extinction spectra show that two obvious distinct resonance peaks (labeled as A₁ and B for convenience) lay in the range of 10-100 THz for each graphene ring. Surprisingly, the extinction area of mode A₁ can almost exceed over an order of magnitude the physics size of the ring, which is almost as large as gold rings with the same size. However, the gold ring is much thicker than graphene one.¹⁸ This physical effect has been employed for total light absorption by engineering of graphene disks.²¹ In order to further understand the nature of these plasmon modes, the *z*-component electric near-field of modes A₁ and B are calculated and demonstrated in Figs. 1(b) and 1(c), respectively. The upper figures are under top view, while the lower are under section view (along positive-*x*). The near-fields and dispersions of plasmon modes A₁ and B are fully consistent with the first and second edge modes in infinite-long graphene ribbons,^{11,12} respectively. Thus, the origin of the plasmon modes in PGRs can be interpreted from coupling of dipolar modes at the inner surface and outer surface of the graphene rings similar to the case of a thin slab. And plasmon mode A₁ is symmetric bonding mode with large radiation and B is anti-symmetric bonding mode with low radiation. Due to the symmetry of the PGRs and the electrostatic of the modes, the higher-order coupled modes are not excited by light.

^{a)}Electronic mail: weicai@nankai.edu.cn.

^{b)}Electronic mail: jjxu@nankai.edu.cn.

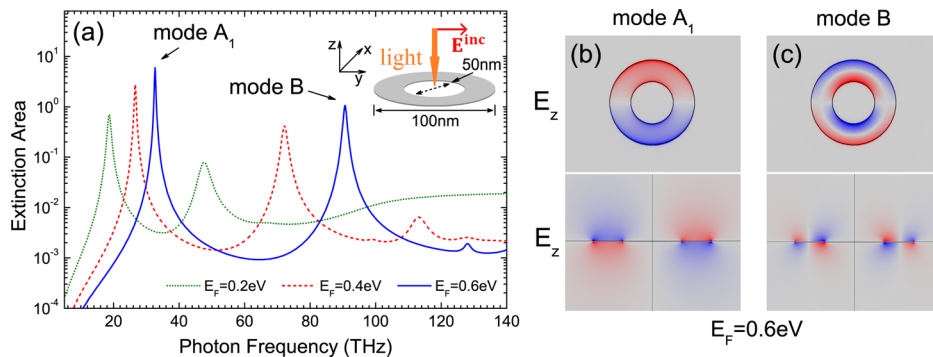


FIG. 1. Surface plasmons excited by normally incident light in perfect graphene rings. (a) Extinction areas of self-standing graphene ring with three different Fermi energies of graphene. The dotted, dashed, and solid lines are corresponding to $E_F = 0.2$ eV, 0.4 eV, and 0.6 eV, respectively. The inner and outer radii of the graphene ring are 25 nm and 50 nm, respectively. The extinction area is normalized to the area of the graphene ring. (b) and (c) show the z -component of electric near-field of plasmon mode A_1 and B, respectively. The upper figures are under top view, while the lower figures are under section view.

Furthermore, the plasmon resonance wavelenghtes of PGRs can be tuned not only by varying the size of the rings akin to metallic rings¹⁶ but also by changing the Fermi energies of the graphene. As the increasing of the Fermi energies of graphene, the resonance wavelenghtes of both symmetric plasmon mode A_1 and anti-symmetric plasmon mode B blue-shift accompanying with the increasing of the extinction areas [Fig. 2(a)]. This behavior can be interpreted by applying the resonance condition that the wave vector k_{spp} propagating along the ring is related to the ring circumference by $k_{spp} = n/R$, where n is the order of the mode, which enters through the decomposition of the fields into different components with $\exp(in\phi)$ on azimuthal angle ϕ , and R is the major radius of the ring. In the considered frequency range, the surface plasmon in graphene approximately satisfies^{8,9} $k_{spp} \approx \hbar\omega^2 / (2\alpha_0 E_F c)$, where $\alpha_0 = e^2/\hbar c$ is the fine-structure constant. Thus, we have the plasmon frequency $\omega_{spp} \approx \sqrt{2n\alpha_0 E_F c / \hbar R} \propto \sqrt{n E_F / R}$. This rough estimate shows that the resonance frequencies can be tuned by changing the Fermi energy E_F of the size parameter R , which makes graphene antennas more repeat useful than metallic optical antennas. In addition, the plasmon resonances of nanostructures can be strongly influenced by different kinds of substrates.²² Thus, graphene rings with $E_F = 0.6$ eV supported on substrates with different dielectric permittivities ϵ are considered [Fig. 2(b)], and the diameter and height of the substrate are chosen as 300 nm and 100 nm, respectively. The plasmon resonance frequencies and extinction areas of the symmetric plasmon mode A_1 and anti-symmetric mode B are calculated under this geometry. One can see that the extinction areas of both modes are qualitatively the same order only with a small decreasing as the

increasing of the dielectric permittivity of the substrate. On the other hand, the plasmon resonance peaks of modes A_1 and B red-shift as the dielectric constant of substrate increases, which is consistent with the property of edge modes in graphene ribbons. This effect can be understood by that the dispersion lines of edge plasmons with higher dielectric constant substrate lie more far to light line in vacuum,^{9,11} which means that the lower resonance frequencies for the plasmon modes A_1 and B with the same momentum $k_{spp} = 1/R$ in graphene rings.

We now examine the plasmon resonances in self-standing nonconcentric graphene rings (NCGRs) which are closer to experiments, and the physics of supported NCGRs is similar. As the inset in Fig. 3(a) indicated, there is an eccentricity δ between inner surface ring and outer surface ring compared with PGRs and the polarization direction of incident light is along y axis. Similar to the case of PGRs, the extinction area is calculated for $\delta = 20$ nm and shown in Fig. 3(a). There are more plasmon resonance peaks (labeled as A_1, A_2, A_3, B' and A_5 , respectively) compared with PGRs. The z -component and amplitude of electric near-fields for each mode are sketched in Figs. 3(b)–3(f). A close inspection of the near-fields shows that these plasmon modes can be divided into two categories: the first kind labeled as A_1, A_2, A_3 , and A_5 are multipolar plasmon modes with $n = 1, 2, 3$, and 5. They have $2n$ electric field maximums along the circumference, which is similar to the bonding symmetric mode A_1 of PGRs. And the other kind labeled as B' comes from the anti-symmetric mode B in PGRs. Specifically, the vanishing of the plasmon mode $n = 4$ with eight field maximums along the ring can be explained by that this mode is hybrid with the anti-symmetric mode B' , as verified

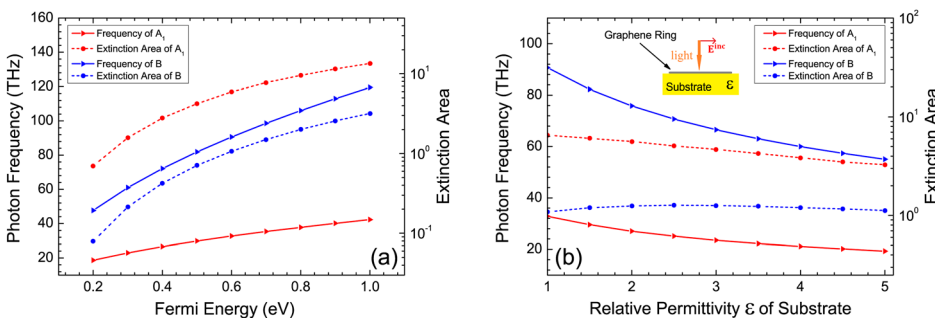


FIG. 2. Plasmon resonance frequencies and extinction areas of the symmetric mode A_1 and anti-symmetric mode B in perfect graphene rings as a function of (a) the Fermi energy of graphene and (b) the relative dielectric permittivity of the substrate ϵ .

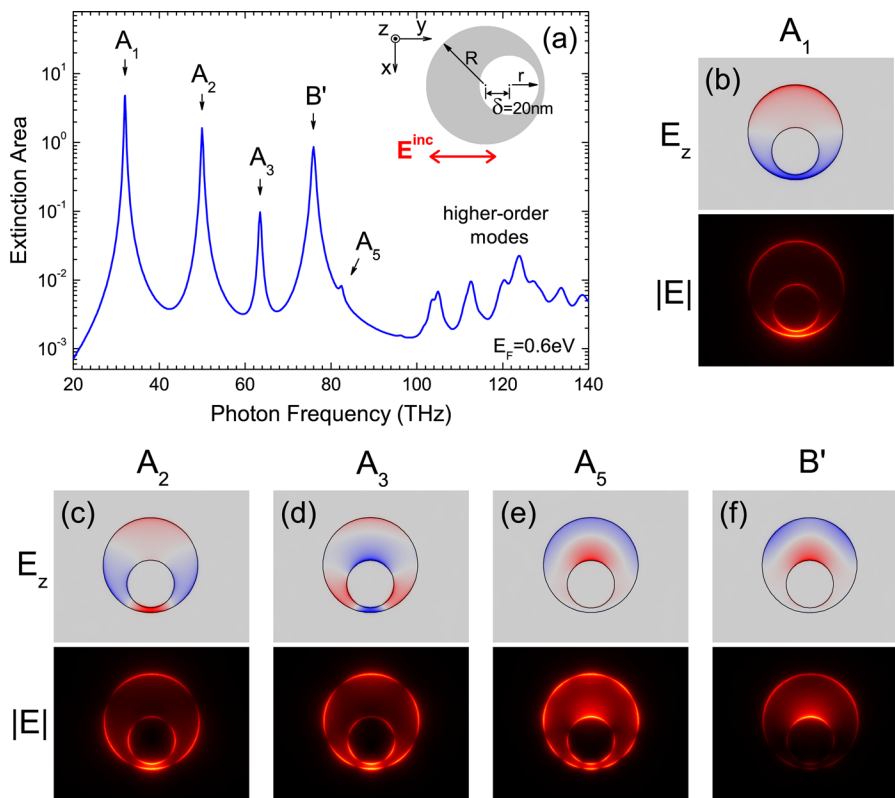


FIG. 3. Plasmon resonances in nonconcentric graphene ring structures. (a) Extinction area of the nonconcentric graphene ring with eccentricity $\delta = 20$ nm. A y -polarization plane wave incidents on the nonconcentric graphene ring (the insert figure). Except for the symmetric plasmon modes A_1 and anti-symmetric plasmon mode B' , multipolar plasmon modes labeled as A_2 , A_3 , and A_5 appear under this configuration. (b)-(f) show the electric near-fields of plasmon modes A_1 , A_2 , A_3 , A_5 , and B' , respectively. Upper pictures are top view of z -component electric field, while the lower figures show the electric amplitude of electric near-field.

in Fig. 3(f). This effect may result in Fano lineshape in the extinction cross-section.²³

To further explore the properties of plasmon mode B' , the light frequencies dependence of extinction areas for two eccentricities $\delta = 1$ nm and $\delta = 2$ nm are shown in Fig. 4(a) compared with the plasmon mode B in PGRs. The antibonding plasmon mode B splits into two plasmon modes (labeled as B' and B'') as the increasing of the eccentricity, which can be understood as that there are two ribbons with different widths in NCGRs. The plasmon frequencies of graphene ribbons scale like¹² $1/\sqrt{W}$, where W is the width of the graphene ribbon. The higher energy mode B'' mainly comes from the right part of the NCGRs, while the lower energy mode B' is the result of the left part. To confirm this point, the lower frequency plasmon mode B' is compared with the

infinitely long ribbon with the same width of the wider part of the NCGRs in Fig. 4(b). The resonance frequencies are almost the same, but with subtle difference which may due to the inhomogeneous width in the NCGRs. By the way, only the low frequency mode B' exists in Fig. 3(a) is due to that the high energy mode B'' is larger than 140 THz and out of the frequency range. The inset of Fig. 4(b) shows that the extinction area of the plasmon mode B' , which maintains around one and does not change a lot with eccentricity.

Fig. 5 shows the effect of symmetry breaking by changing the eccentricity δ . The major effects are red-shift of the symmetric plasmon mode A_1 and multipolar plasmons A_2 , A_3 as the increasing of ring eccentricity [Fig. 5(a)]. Now, the interaction between the inner face and outer face of the ring is no longer symmetric, which causes the appearance of

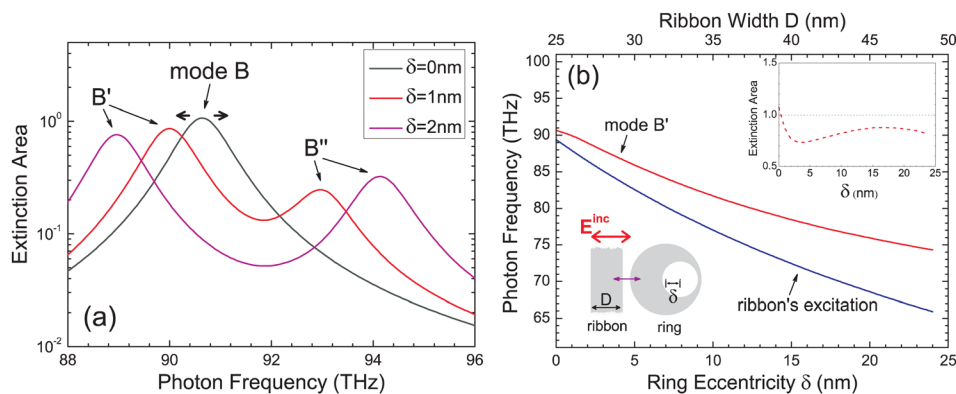


FIG. 4. Spitting of the anti-symmetric plasmon modes B in nonconcentric graphene rings. (a) Extinction areas versus incident light frequency for three different eccentricities 0 nm, 1 nm, and 2 nm, respectively. There are two split plasmon modes exist due to symmetry breaking. The lower and higher energy modes B' and B'' are corresponding to the left wide and right narrow ribbon plasmons, respectively. (b) Comparison of the plasmon mode of a graphene ribbon with the same width as the wide side of the nonconcentric graphene ring and the lower frequency plasmon mode B' of nonconcentric graphene rings. Inset shows the extinction area of plasmon mode B' for the ring.

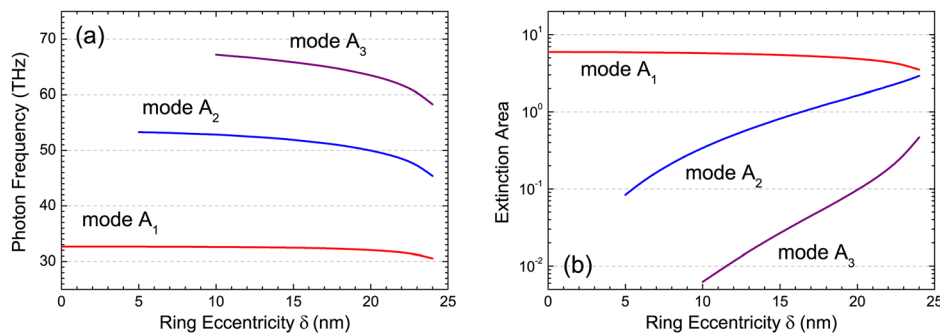


FIG. 5. Dependence of multipolar plasmons in nonconcentric graphene rings on the eccentricity δ . (a) Frequencies of the plasmon modes A_1 , A_2 , and A_3 versus the eccentricity of the ring. (b) Extinction areas of the modes A_1 , A_2 , and A_3 versus ring's eccentricity.

multipolar plasmons. The extinction areas are also shown in Fig. 5(b). The intensities of the multipolar modes A_2 and A_3 are increasing a lot as the increasing of δ , whereas the intensity of the symmetric plasmon mode A_1 changes a little and larger than other multipolar modes. Therefore, symmetric plasmon mode A_1 is the best choice in real applications because it is insensitive to the imperfection of the structure and with high intensity.

For the applications using optical antennas, the ability of enhancement of electromagnetic field is a very important factor.¹ Thus, in Fig. 6, the maximum electric field enhancement factors of plasmon mode A_1 with different eccentricities of NCGRs are calculated. The solid line shows that the enhancement factor is almost one thousand for self-standing PGRs, which is about 20 times larger than gold nanoring with similar size.¹⁶ Further, the enhancement of electric field can almost reach 3000 with crescent shape NCGRs. Moreover, the cases of PGRs with substrates (the dashed and dotted lines in Fig. 6 are corresponding to the dielectric constant of substrates $\epsilon = 2$ and $\epsilon = 3$, respectively) are also demonstrated. Although the electric field enhancement factors decrease in supported graphene rings, the value is also larger than 700 for $\epsilon = 2$ (which is close to common substrate for graphene-SiO₂), which is almost 14 times larger than gold nanoring. These enhancement effects indicate potential applications in terahertz surface-enhanced Raman scattering

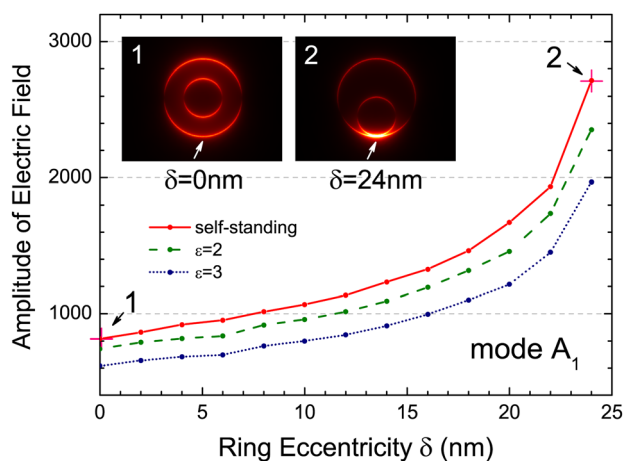


FIG. 6. Maximum electric field enhancement factor of plasmon mode A_1 versus the eccentricity of graphene ring δ . The solid line is corresponding to self-standing graphene rings, and the dashed and dotted lines are graphene rings supported on substrates with dielectric constant $\epsilon = 2$ and $\epsilon = 3$, respectively. Insets show the amplitudes of the electric near-field with eccentricities $\delta = 0$ nm and $\delta = 24$ nm for self-standing graphene rings, respectively. And the two inset pictures are under the same color scale.

(SERS) as well as nonlinear optical effects. The insets of Fig. 6 show the electric field amplitudes with two different eccentricities $\delta = 0$ nm and $\delta = 24$ nm, respectively. There are two electric field maximums in PGRs. Differently, the electric fields are mostly concentrated on the narrow gap region in NCGRs.

In this paper, we have proposed a kind of highly tunable optical antennas in terahertz range based on graphene nanostructures. Specifically, PGRs and NCGRs are separately investigated. The plasmon resonances of PGRs in the terahertz range are understood in the context of edge modes in graphene ribbons and can be easily tuned by changing the doping level of graphene instead of the size or the dielectric permittivity of substrate, whereas the plasmon modes of NCGRs can be classified into azimuthal-dependent multipolar modes and split anti-symmetric modes. The symmetric bonding plasmon mode of PGRs is very stable and with much stronger electric field enhancement factor than metallic structures, which has great potential in sensing or spectroscopic applications.

This work is supported by the Fundamental Research Funds for the Central Universities, the National Natural Science Foundation of China (11004112 and 10874093), the National Basic Research Program of China (2010CB934101), the 111 Project (B07013), International S&T cooperation program of China (2011DFA52870), and Oversea Famous Teacher Project (MS2010NKDX0230).

¹L. Novotny and N. van Hulst, *Nat. Photonics* **5**, 83 (2011).

²J. Wessel, *J. Opt. Soc. Am. B* **2**, 1538 (1985).

³E. J. Sánchez, L. Novotny, and X. S. Xie, *Phys. Rev. Lett.* **82**, 4014 (1999).

⁴U. C. Fischer and D. W. Pohl, *Phys. Rev. Lett.* **62**, 458 (1989).

⁵R. D. Grober, R. J. Schoelkopf, and D. E. Prober, *Appl. Phys. Lett.* **70**, 1354 (1997).

⁶T. Kosako, Y. Kadoya, and H. F. Hofmann, *Nat. Photonics* **4**, 312 (2010).

⁷A. K. Geim and K. S. Novoselov, *Nature Mater.* **6**, 183 (2007).

⁸M. Jablan, H. Buljan, and M. Soljacić, *Phys. Rev. B* **80**, 245435 (2009).

⁹F. H. L. Koppens, D. E. Chang, and F. J. García de Abajo, *Nano Lett.* **11**, 3370 (2011).

¹⁰A. Y. Nikitin, F. Guinea, F. J. García-Vidal, and L. Martín-Moreno, *Phys. Rev. B* **84**, 195446 (2011).

¹¹A. Y. Nikitin, F. Guinea, F. J. García-Vidal, and L. Martín-Moreno, *Phys. Rev. B* **84**, 161407(R) (2011).

¹²J. Christensen, A. Manjavacas, S. Thongrattanasiri, F. H. L. Koppens, and F. J. García de Abajo, *ACS Nano* **6**, 431 (2012).

¹³L. Ju, B. Geng, J. Horng, C. Girit, M. Martin, Z. Hao, H. A. Bechtel, X. Liang, A. Zettl, Y. R. Shen, and F. Wang, *Nat. Nanotechnol.* **6**, 630 (2011).

¹⁴Z. Fei, G. O. Andreev, W. Bao, L. M. Zhang, A. S. McLeod, C. Wang, M. K. Stewart, Z. Zhao, G. Dominguez, M. Thiemens, M. M. Fogler, M. J.

- Tauber, A. H. Castro-Neto, C. N. Lau, F. Keilmann, and D. N. Basov, *Nano Lett.* **11**, 4701 (2011).
- ¹⁵K. F. Mak, M. Y. Sfeir, Y. Wu, C. H. Lui, J. A. Misewich, and T. F. Heinz, *Phys. Rev. Lett.* **101**, 196405 (2008).
- ¹⁶J. Aizpurua, P. Hanarp, D. S. Sutherland, M. Käll, G. W. Bryant, and F. J. García de Abajo, *Phys. Rev. Lett.* **90**, 057401 (2003).
- ¹⁷F. Hao, Y. Sonnefraud, P. Van Dorpe, S. A. Maier, N. J. Halas, and P. Nordlander, *Nano Lett.* **8**, 3983 (2008).
- ¹⁸S. D. Liu, Z. S. Zhang, and Q. Q. Wang, *Opt. Express* **17**, 2906 (2009).
- ¹⁹B. Wunsch, T. Stauber, F. Sols, and F. Guinea, *New J. Phys.* **8**, 318 (2006).
- ²⁰K. S. Novoselov, A. K. Geim, S. V. Morozov, D. Jiang, Y. Zhang, S. V. Dubonos, I. V. Grigorieva, and A. A. Firsov, *Science* **306**, 666 (2004).
- ²¹S. Thongrattanasiri, F. H. L. Koppens, and F. J. García de Abajo, *Phys. Rev. Lett.* **108**, 047401 (2012).
- ²²Z. Li, K. Bao, Y. Fang, Z. Guan, N. J. Halas, P. Nordlander, and H. Xu, *Phys. Rev. B* **82**, 241402 (2010).
- ²³B. Luk'yanchuk, N. I. Zheludev, S. A. Maier, N. J. Halas, P. Nordlander, H. Giessen, and C. T. Chong, *Nature Mater.* **9**, 707 (2010).

Polarization-insensitive and wide-angle plasmonically induced transparency by planar metamaterials

Xiaoyang Duan, Shuqi Chen, Haifang Yang, Hua Cheng, Junjie Li et al.

Citation: *Appl. Phys. Lett.* **101**, 143105 (2012); doi: 10.1063/1.4756944

View online: <http://dx.doi.org/10.1063/1.4756944>

View Table of Contents: <http://apl.aip.org/resource/1/APPLAB/v101/i14>

Published by the [American Institute of Physics](http://www.aip.org).

Related Articles

Optimizing the band gap of effective mass negativity in acoustic metamaterials

Appl. Phys. Lett. **101**, 241902 (2012)

Competing nonlinearities with metamaterials

Appl. Phys. Lett. **101**, 231904 (2012)

Theoretical and experimental study of the backward-wave radiation using resonant-type metamaterial transmission lines

J. Appl. Phys. **112**, 104513 (2012)

Experimental verification of field rotating with invisibility by full tensor transmission-line metamaterials

Appl. Phys. Lett. **101**, 224105 (2012)

Line-source excitation of realistic conformal metasurface cloaks

J. Appl. Phys. **112**, 104902 (2012)

Additional information on *Appl. Phys. Lett.*

Journal Homepage: <http://apl.aip.org/>

Journal Information: http://apl.aip.org/about/about_the_journal

Top downloads: http://apl.aip.org/features/most_downloaded

Information for Authors: <http://apl.aip.org/authors>

ADVERTISEMENT

AIP | Applied Physics
Letters

SURFACES AND INTERFACES
Focusing on physical, chemical, biological, structural, optical, magnetic and electrical properties of surfaces and interfaces, and more...

ENERGY CONVERSION AND STORAGE
Focusing on all aspects of static and dynamic energy conversion, energy storage, photovoltaics, solar fuels, batteries, capacitors, thermoelectrics, and more...

EXPLORE WHAT'S NEW IN APL

SUBMIT YOUR PAPER NOW!

Labels in the 3D schematic: 1 μ m-thick LPCVD Silicon Dioxide, Source, Gate, Drain, Metal Vias, Ground Ring.

Labels in the energy conversion diagram: NO_2 , CO_2 , CH_4 , QDs.

Polarization-insensitive and wide-angle plasmonically induced transparency by planar metamaterials

Xiaoyang Duan,¹ Shuqi Chen,^{1,a)} Haifang Yang,² Hua Cheng,¹ Junjie Li,² Wenwei Liu,¹ Changzhi Gu,² and Jianguo Tian^{1,b)}

¹The Key Laboratory of Weak Light Nonlinear Photonics, Ministry of Education, School of Physics and Teda Applied Physics School, Nankai University, Tianjin 300071, China

²Beijing National Laboratory for Condensed Matter Physics, Institute of Physics, Chinese Academy of Sciences, P. O. Box 603, Beijing 100190, China

(Received 30 July 2012; accepted 18 September 2012; published online 3 October 2012)

We present the design, characterization, and experimental demonstration of a polarization-insensitive wide-angle plasmonically induced transparency (PIT) planar metamaterial (MM) in the near-infrared regime. A four-level plasmonic system is proposed to explain and analyze the forming mechanisms of the PIT planar MM, whose results agree closely with the simulated and experimental results. This shows that the local asymmetrical nanostructure leading to the plasmon-assisted interaction is the key to producing PIT, but it does not mean that PIT cannot be achieved by the whole symmetrical nanostructure. This work offers a further step in developing optical modulation. © 2012 American Institute of Physics. [<http://dx.doi.org/10.1063/1.4756944>]

Plasmonically induced transparency (PIT) in metamaterials (MMs) is a fascinating phenomenon that mimics quantum interference of electromagnetically induced transparency (EIT) in laser-driven atomic systems.^{1–6} This phenomenon opens a narrow transparency window within a transmission stop band through a highly efficient plasmon coupling between two artificially resonant elements, where bright mode energy is transformed into dark mode. It has been found that PIT underlies many particular useful applications, such as slow light,⁷ sensing,^{8,9} and optical switching.¹⁰ Being different from other methods showing the classical analogue of EIT such as mechanical oscillators,¹¹ split-ring resonators,¹² optical resonators,^{13,14} and metallic nanoparticle arrays,¹⁵ PIT is an excellent example of merging between plasmonics and MMs. This lays the foundation for manipulating light by using metal nanostructures to achieve effective EIT-like optical properties for media. Because of the inherent limitations in applying EIT, PIT has received much attention due to the prominent advantages of room temperature manipulability, artificially controlling spectral response, and the ability to integrate with nanoplasmonic circuits.

In spite of many obvious advantages, the previously designed PIT devices principally have an inherent drawback. They strongly depend on the polarization and angle of incident waves on the asymmetry of the structures. Most studies show that introducing a broken symmetry to the spatial arrangement of the bright and dark resonators is a prerequisite for PIT,^{1–5} since the asymmetry permits excitation of the otherwise forbidden dark mode. The degree of asymmetry determines the coupling strength of the bright and dark modes. Therefore, the previous devices also strongly depend on the incident angle.

In this letter, we present the design, characterization, and experimental demonstration of a PIT planar MM in the

near-infrared regime. We demonstrate that PIT can be achieved by symmetrical planar MMs. Meanwhile, a four-level plasmonic system is proposed to explain and analyze the forming mechanisms of the PIT planar MM, whose results agree with the simulated and experimental results. The PIT planar MM is polarization-insensitive, and the transparency window remains high with large incident angles for both transverse electric (TE) and transverse magnetic (TM) configurations.

Motivated by the drawbacks mentioned above, here we propose a PIT planar MM fabricated on a quartz substrate, in which the top metallic layer consists of four rotationally aligned “=” pairs (see Fig. 1(a)). Based on the concept of EIT in atomic physics, we use a general description of an EIT-like plasmonic system (see Fig. 1(b)) to demonstrate and quantitatively describe the near-field coupling among meta-atoms.^{1–3} Corresponding to the geometric position of the gold bars, the system consists of three artificial states, a radiative plasmonic state $|1\rangle = \tilde{A}_1(\omega)e^{i\omega t}$ (bright mode), a dark plasmonic state $|2\rangle = \tilde{A}_2(\omega)e^{i\omega t}$ (dark mode), and an additional plasmonic state $|3\rangle = \tilde{A}_3(\omega)e^{i\omega t}$ (additional mode), which have resonant frequencies ω_{01} , ω_{02} , ω_{03} , and damping factors γ_1 , γ_2 , γ_3 , respectively. The damping factors combine radiative and non-radiative damping due to the intrinsic loss. A four-level plasmonic system is formed by three states of coupled meta-atoms and a continuum state (ground state $|0\rangle$). We assume that the dark mode does not couple with the external field, while geometrical parameters g_1 and g_3 indicate how strongly the bright mode and additional mode couple with the external field $E_0 = \tilde{E}_0 e^{i\omega t}$. We also define κ_{12} as the coupling parameter between $|1\rangle$ and $|2\rangle$, and κ_{23} as the coupling parameter between $|2\rangle$ and $|3\rangle$. The coupling between $|1\rangle$ and $|3\rangle$ is ignored due to their geometrical and functional similarity. Then, the field amplitude of all states can be described as a system of linearly coupled Lorentzian oscillators

^{a)}Email: schen@nankai.edu.cn.

^{b)}Email: jjtian@nankai.edu.cn.

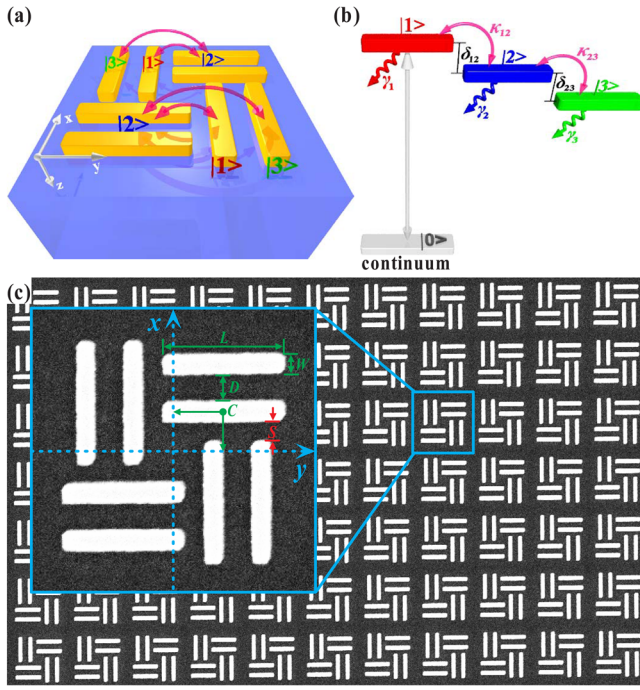


FIG. 1. (a) Unit cell of the PIT planar MM. The pink arrows indicate the near-field coupling between meta-atoms. (b) Coupled four-level plasmonic system for the PIT planar MM. (c) SEM of the sample with $S = 140$ nm. Inset: Amplified figure of the unit cell, showing the definitions of the geometrical parameters: $L = 900$ nm, $W = 150$ nm, $D = 200$ nm.

$$\begin{bmatrix} \omega - \omega_{01} + i\gamma_1 & \kappa_{12} & 0 \\ \kappa_{12} & \omega - \omega_{02} + i\gamma_2 & \kappa_{23} \\ 0 & \kappa_{23} & \omega - \omega_{03} + i\gamma_3 \end{bmatrix} \begin{bmatrix} \tilde{A}_1 \\ \tilde{A}_2 \\ \tilde{A}_3 \end{bmatrix} = - \begin{bmatrix} g_1 \tilde{E}_0 \\ 0 \\ g_3 \tilde{E}_0 \end{bmatrix}. \quad (1)$$

In Eq. (1), the complex amplitude of the bright mode \tilde{A}_1 is directly proportional to the polarizability of the PIT system. Therefore, the normalized energy extinction $P(\omega)$, namely the sum of reflection and absorption, is obtained as

$$P(\omega) = \frac{|\tilde{A}_1|}{|\tilde{E}_0|} = \left| \frac{\frac{-g_3 \kappa_{12} \kappa_{23}}{(\omega - \omega_{02} + i\gamma_2)(\omega - \omega_{03} + i\gamma_3) - \kappa_{23}^2} - g_1}{\kappa_{12}^2 (\omega - \omega_{03} + i\gamma_3)} \right|. \quad (2)$$

The optimized structure was achieved by using the finite-element-method (FEM)-based commercial software COMSOL Multiphysics.¹⁶ The parameters were chosen to match closely those of technologically feasible physical systems. The three-dimensional simulations were performed with a plane-wave source incident in the z direction. The refractive index of quartz substrate is 1.5. The optical constants of bulk gold in the infrared spectral regime are described by the Drude model with the plasma frequency $\omega_p = 2\pi \times 2.175 \times 10^{15} \text{ s}^{-1}$ and the damping constant $\omega_c = 2\pi \times 6.5 \times 10^{12} \text{ s}^{-1}$.¹⁷ Owing to the surface scattering and grain boundary effects in the thin gold film, the damping constant in our simulations is three times larger than in bulk gold.^{2,9} Periodic boundary conditions

were used for the x - y plane, and waveguide port boundary conditions were used on the other boundaries.

A series of samples were fabricated by standard E-beam deposition and E-beam lithography. First, a layer of ITO material (100 nm) was deposited on a 0.5-mm-thick quartz substrate by a RF magnetic sputtering system. The top patterned layer was defined with electron beam lithography. Then Cr (5 nm) and Au (100 nm) were deposited by an electron beam evaporator, and the pattern transfer was completed by lift-off in acetone. Both samples had a total area of $300 \mu\text{m} \times 300 \mu\text{m}$. Figure 1(c) shows the scanning electron microscopy (SEM) image of the fabricated PIT planar MM. It has a period of $2.1 \mu\text{m}$ in both the x and y directions. The top gold layer consists of eight identical gold bars. L and W are the length and width of the each bar, respectively. D is the fixed distance between two bars in each “=” pair. C is the coordinate of the inner bar. The interspace between two close “=” pairs is defined as S , which is 300 nm, 220 nm, 140 nm, and 60 nm for four samples, corresponding to the coordinate of C (375, 450) nm, (335, 410) nm, (295, 370) nm, and (255, 330) nm, respectively.

To study the PIT tuning feature of the designed PIT planar MM, we give the simulated and experimental transmission spectra as a function of the interspace S in Fig. 2. The PIT feature is apparent in the transmission spectra. The simulated transmission spectra obtained by FEM and four-level plasmonic system are shown in Fig. 2(a). The FEM simulation considers an x -polarized TEM beam normally incident to the PIT planar MM. There is a broad transmission dip in the case of maximum interspace $S = 300$ nm. Then, a tiny transmission peak emerges within the broad transmission dip with decreasing S . Finally, the transmission peak reaches $T(\omega) = 51.2\%$ at $2.85 \mu\text{m}$ in the case of minimum interspace $S = 60$ nm. The evolution of the PIT feature in the transmission spectra shows that the coupling strength between bright and dark modes strongly depends on S . We also fit the simulated transmission spectra according to $T(\omega) = 1 - P(\omega)$ from analytical derivation. This analytical derivation agrees closely with the FEM analysis for the different interspaces in Fig. 2(a), which confirms the validity of our design.

The transmission spectra were obtained at room temperature with a Fourier-transform infrared spectrometer (Bruker VERTEX 70, tungsten lamp) combined with an infrared microscope ($36\times$ magnification objective, liquid N_2 -cooled MCT 77 K detector). The transmission of the sample was recorded by averaging data from 64 measurements to improve the signal-to-noise ratio. Before measuring the PIT sample, the transmission was calibrated with a blank structure without gold bars. The corresponding experimental transmission spectra in Fig. 2(b) agree qualitatively with the simulation. To show the variety of the PIT tuning feature, every graph shows the transmission spectrum of maximum interspace $S = 300$ nm along with different interspaces. We can see that the experimental results for $S = 300$ nm, 220 nm, and 140 nm agree closely with the simulation, while the experimental result for minimum interspace $S = 60$ nm is appreciably different from that of the simulation. These discrepancies between experiment and simulation are likely due to the fabrication tolerances such as the inhomogeneity of the interspace S especially for the sample with $S = 60$ nm. Considering that the optical properties of metamaterials with

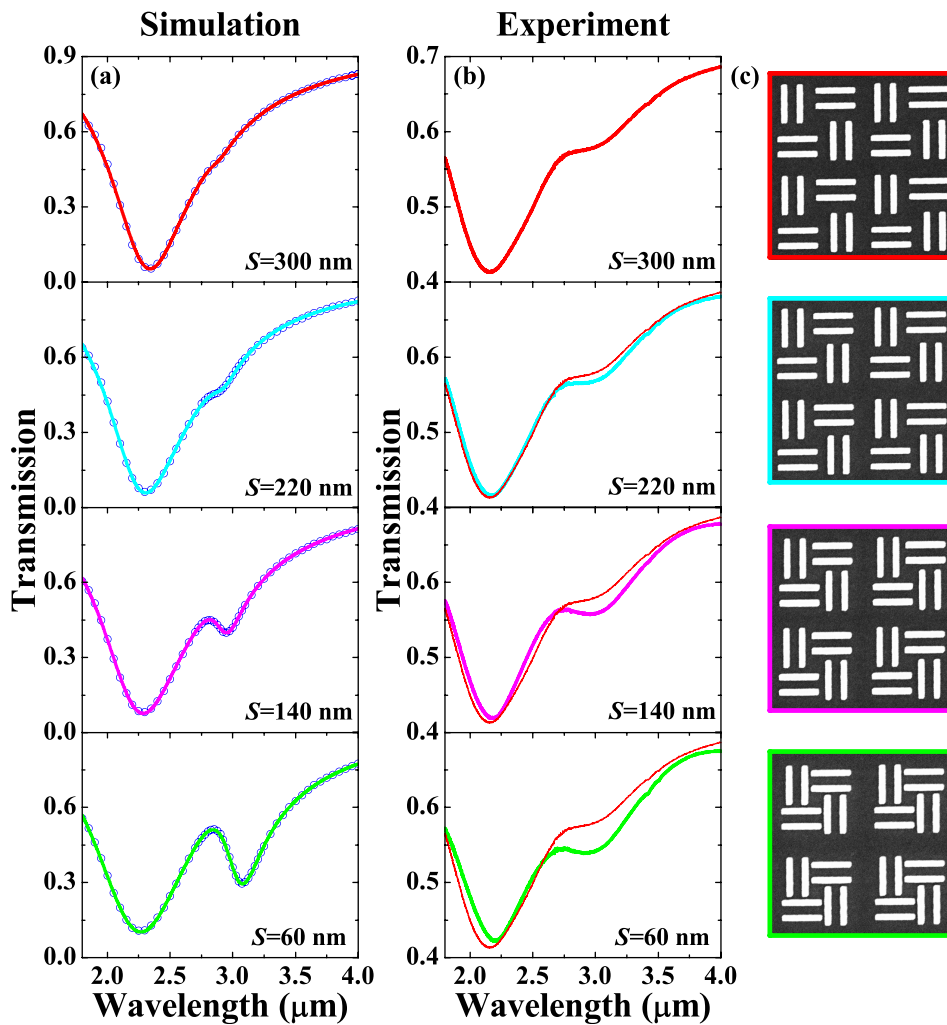


FIG. 2. (a) Simulated transmission spectra achieved by FEM (blue-circled curves) and four-level plasmonic system (color-solid lines) for different interspaces S . (b) Corresponding experimental transmission spectra. The transmission spectrum of $S=300$ nm is shown in every graph by a fine red-solid line to guide the eyes. (c) Top-view SEM of the corresponding samples.

periodic structure are quite sensitive to the homogeneity, previous experimental attempts have not been successful owing to the difficulties with nanofabrication.^{2,5} Even so, the experimental PIT tuning feature clearly agrees with the simulation for the $S=300$ nm transmission spectrum in every graph. Therefore, our experimental results verify our analyses of the PIT phenomenon to a great extent.

To get insight into the nature of the designed PIT planar MM, we calculated the surface current density distribution and the magnetic field amplitude distribution of the top metallic layer for the x -polarized TEM wave with a $2.85\text{-}\mu\text{m}$

wavelength (see Fig. 3). The “=” pairs parallel to the y -axis, which may function as a magnetic quadrupole antenna,¹⁸ can serve as the dark mode. The “=” pairs parallel to the x -axis, which may function as two similar optical dipole antennas,¹⁹ can serve as the bright mode and additional mode. With the maximum interspace $S=300$ nm (nearly without coupling to the dark mode), the bright mode and additional mode are strongly excited by the incident beam with a strong magnetic field and high surface current densities (as shown in Fig. 3(a)). By decreasing the interspace to 60 nm (with strong coupling to the dark mode), the magnetic field and surface

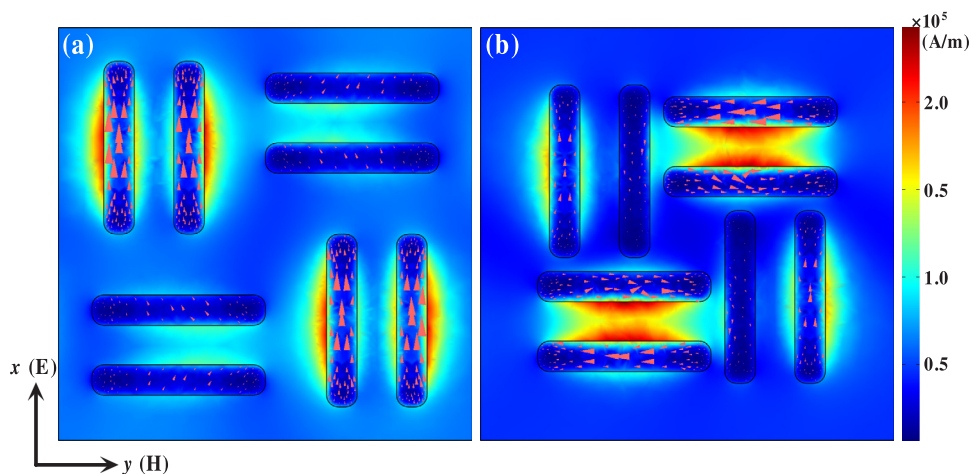


FIG. 3. Colormaps and pink arrows, respectively, represent the distributions of the amplitude of the magnetic fields and induced surface current densities of the top metallic elements at a $2.85\text{-}\mu\text{m}$ wavelength for (a) $S=300$ nm and (b) $S=60$ nm.

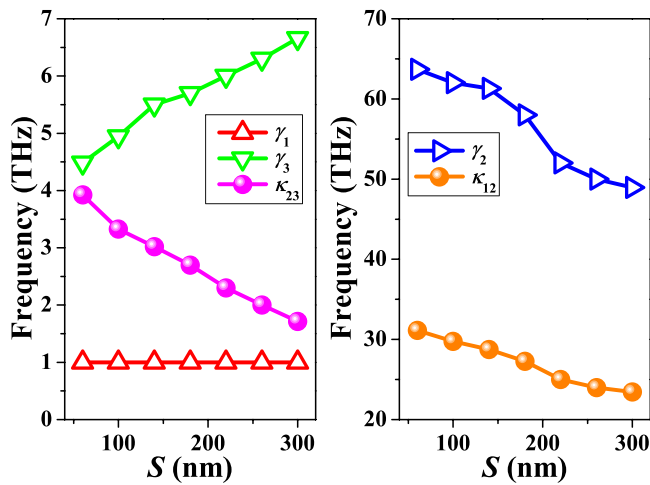


FIG. 4. Extracted simulated coupling and damping parameters as a function of interspace S . Values of γ_1 , γ_2 , γ_3 , κ_{12} , and κ_{23} are extracted by fitting the simulated transmission spectra.

current are coupled back to the dark mode, leading to destructive interference and a suppressed state in the bright mode. Therefore, the magnetic field and surface current densities of the bright mode and additional mode decrease greatly (as shown in Fig. 3(b)), which corresponds to PIT. Because the additional mode is farther from the dark mode than the bright mode, the coupling strength between the additional mode and dark mode is weaker than that between the bright mode and dark mode. For all separations, the coupling among the bright, dark and additional modes leads to a narrow transmission peak in the broad dip.

To examine the coupling and damping parameters of our plasmonic system (see Fig. 1(b)), Fig. 4 shows the fitting values of γ_1 , γ_2 , γ_3 , κ_{12} , and κ_{23} as a function of interspace S in frequency units. The resonant frequencies of the three modes are approximately $\omega_{01} = 125$ THz, $\omega_{02} = 119$ THz and $\omega_{03} = 100$ THz, respectively. We define $\delta_{12} = \omega_{01} - \omega_{02}$ and $\delta_{23} = \omega_{02} - \omega_{03}$ as the small detuning. Due to the positions of meta-atoms, the coupling between $|1\rangle$ and $|2\rangle$ is much stronger than between $|2\rangle$ and $|3\rangle$, which corresponds to $\kappa_{12} > \kappa_{23}$. Significantly, κ_{12} and κ_{23} are nearly inversely proportional to S , which determines the modulation strength of our PIT planar MM. The damping factors γ_1 , γ_2 , and γ_3 correspond to the decay rate in atomic physics, which is inversely proportional to spectral linewidth. As S decreases, the radiative damping component of γ_2 increases significantly, which means that the magnetic field and surface current are coupled back to the dark mode, leading to the emerging of the transmission peak. On the other hand, γ_1 and γ_3 are roughly constant, which agrees with the result that all linewidths of the spectrum are the same. Such quantitative results confirm our expectation about the relationship between the interspace and coupling strength of meta-atoms.

Polarization-insensitive performance and wide-angle incident beams are important in practical applications. In some cases, the most possible light needs to be used, which may contain arbitrarily polarized components. Moreover, the excited beam is not always normally incident to the sample in many cases. To show the polarization-insensitive behavior of the designed PIT planar MM, we plotted the transmission spectra as a function of polarization angle ϕ for $S = 300$ nm and $S = 60$ nm in Figs. 5(a) and 5(b), respectively. As the

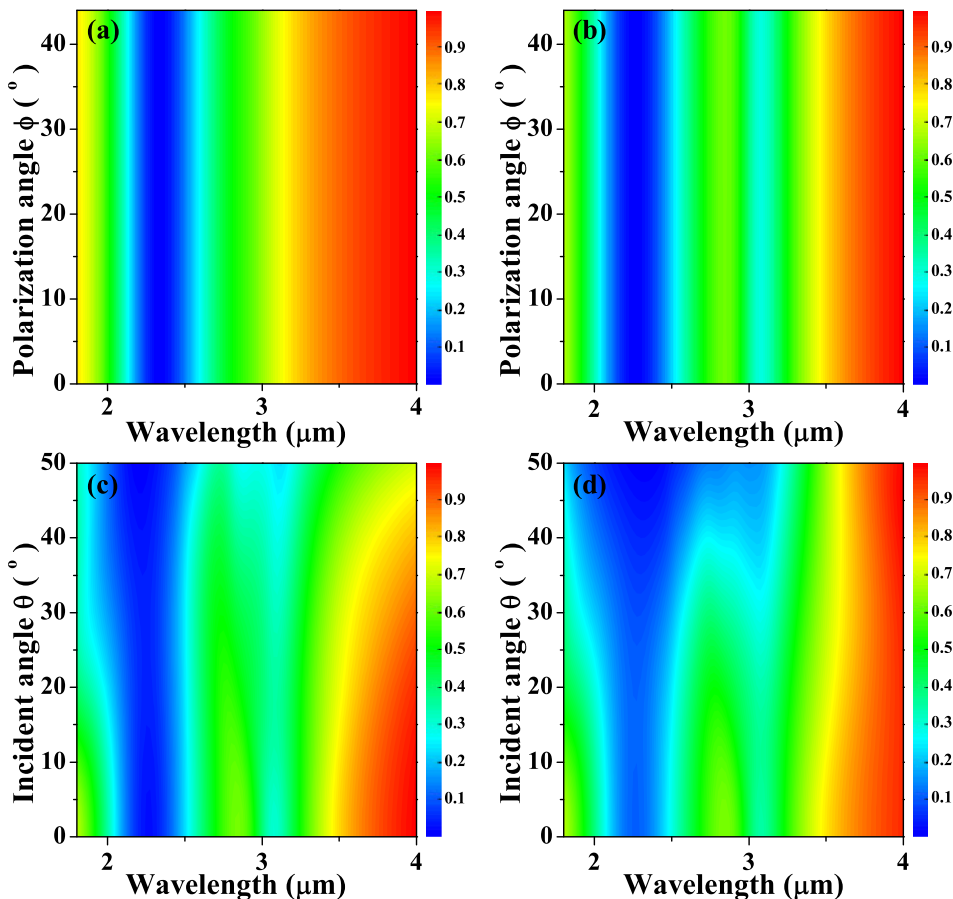


FIG. 5. Simulated transmission spectra as a function of wavelength and the polarization angle for (a) $S = 300$ nm and (b) $S = 60$ nm. Simulated angular dispersion of the transmission spectra for both (c) TE polarization and (d) TM polarization in the case of $S = 60$ nm.

PIT planar MM has a fourfold rotational symmetry, we only need to take into account the polarizations from 0° to 45° in the simulation. Results show that the transmission spectra of the designed PIT planar MM are polarization-insensitive. The PIT feature of the designed structure can also work over a wide range of incident angles θ . Figures 5(c) and 5(d) gives the simulated angular dispersion of the transmission spectra for TE and TM polarization for $S = 60$ nm, respectively. For the TE case, the PIT feature is nearly independent of incident angle, since the electric field can effectively provide the strong electric resonance at all incident angles. For the TM case, the PIT feature can be maintained with increasing the incident angle. However, when the incident angle is beyond 30° , there is a monotonic decrease in the transmission. With increasing incident angle, the horizontal projection of the incident electric field decreases and can no longer efficiently drive a strong electric resonance. The maximal incident angle is about 10° in the previously designed PIT device;²⁰ however, our designed PIT planar MM maintains quite well for both TE and TM radiations over a wide range of incident angles.

In conclusion, we have numerically and experimentally demonstrated a PIT planar MM based on coupled meta-atoms. This shows that the local asymmetrical nanostructure leading to the plasmon-assisted interaction is the key to producing PIT, but it does not mean that PIT must depend on the polarization and the angle of incident waves. The analyses done have been kept general and so can be easily extended to other antenna geometries. This kind of PIT planar MM will help to overcome some of the limitations of customary designs developed so far. Our work offers a further step forward in developing optical modulation.

This work was supported by the Chinese National Key Basic Research Special Fund (Grant No. 2011CB922003), the Natural Science Foundation of China (Grants Nos. 61008002, 91023041, 50825206, and 11174362), the Spec-

alized Research Fund for the Doctoral Program of Higher Education (Grant No. 20100031120005), the National Basic Research Program of China (Grant No. 2009CB930502), the Knowledge Innovation Project of CAS (Grant No. KJCX2-EW-W02), the Fundamental Research Funds for the Central Universities, and the 111 project (Grant No. B07013).

- ¹S. Zhang, D. A. Genov, Y. Wang, M. Liu, and X. Zhang, *Phys. Rev. Lett.* **101**, 047401 (2008).
- ²N. Liu, L. Langguth, T. Weiss, J. Kästel, M. Fleischhauer, T. Pfau, and H. Giessen, *Nature Mater.* **8**, 758 (2009).
- ³A. Artar, A. A. Yanik, and H. Altug, *Nano Lett.* **11**, 1685 (2011).
- ⁴A. E. Çetin, A. Artar, M. Turkmen, A. A. Yanik, and H. Altug, *Opt. Express* **19**, 22607 (2011).
- ⁵R. Taubert, M. Hentschel, J. K'Stel, and H. Giessen, *Nano Lett.* **12**, 1367 (2012).
- ⁶M. Fleischhauer, A. Imamoglu, and J. P. Marangos, *Rev. Mod. Phys.* **77**, 633 (2005).
- ⁷B. Tang, L. Dai, and C. Jiang, *Opt. Express* **19**, 628 (2011).
- ⁸Z.-G. Dong, H. Liu, J.-X. Cao, T. Li, S.-M. Wang, S.-N. Zhu, and X. Zhang, *Appl. Phys. Lett.* **97**, 114101 (2010).
- ⁹N. Liu, T. Weiss, M. Mesch, L. Langguth, U. Eigenthaler, M. Hirscher, C. Sönnichsen, and H. Giessen, *Nano Lett.* **10**, 1103 (2010).
- ¹⁰J. Chen, P. Wang, C. Chen, Y. Lu, H. Ming, and Q. Zhan, *Opt. Express* **19**, 5970 (2011).
- ¹¹P. Tassin, L. Zhang, T. Koschny, E. N. Economou, and C. M. Soukoulis, *Phys. Rev. Lett.* **102**, 053901 (2009).
- ¹²L. Zhang, P. Tassin, T. Koschny, C. Kurter, S. M. Anlage, and C. M. Soukoulis, *Appl. Phys. Lett.* **97**, 241904 (2010).
- ¹³Q. Xu, S. Sandhu, M. L. Povinelli, J. Shakya, S. Fan, and M. Lipson, *Phys. Rev. Lett.* **96**, 123901 (2006).
- ¹⁴J. B. Lassiter, H. Sobhani, M. W. Knight, W. S. Mielczarek, P. Nordlander, and N. J. Halas, *Nano Lett.* **12**, 1058 (2012).
- ¹⁵V. Yannopapas, E. Paspalakis, and N. V. Vitanov, *Phys. Rev. B* **80**, 035104 (2009).
- ¹⁶*COMSOL Multiphysics User's Guide*, Version 3.5 (Comsol AB, Burlington, MA, 2008).
- ¹⁷M. A. Ordal, L. L. Long, R. J. Bell, S. E. Bell, R. R. Bell, R. W. Alexander, Jr., and C. A. Ward, *Appl. Opt.* **22**, 1099 (1983).
- ¹⁸V. M. Shalaev, W. Cai, U. K. Chettiar, H.-K. Yuan, A. K. Sarychev, V. P. Drachev, and A. V. Kildishev, *Opt. Lett.* **30**, 3356 (2005).
- ¹⁹L. Novotny, *Phys. Rev. Lett.* **98**, 266802 (2007).
- ²⁰Y. Lu, X. Jin, S. Lee, J. Y. Rhee, W. H. Jang, and Y. P. Lee, *Adv. Nat. Sci.: Nanosci. Nanotechnol.* **1**, 045004 (2010).

Spin Hall effect of reflected light from an air-glass interface around the Brewster's angle

Ling-Jun Kong, Xi-Lin Wang, Si-Min Li, Yongnan Li, Jing Chen et al.

Citation: *Appl. Phys. Lett.* **100**, 071109 (2012); doi: 10.1063/1.3687186

View online: <http://dx.doi.org/10.1063/1.3687186>

View Table of Contents: <http://apl.aip.org/resource/1/APPLAB/v100/i7>

Published by the [American Institute of Physics](http://www.aip.org).

Related Articles

A graphene solution to conductivity mismatch: Spin injection from ferromagnetic metal/graphene tunnel contacts into silicon

J. Appl. Phys. **113**, 17C502 (2013)

A simple formulation for magnetoresistance in metal-insulator granular films with increased current

J. Appl. Phys. **113**, 073911 (2013)

Enhanced inverse spin-Hall effect in ultrathin ferromagnetic/normal metal bilayers

Appl. Phys. Lett. **102**, 072401 (2013)

Devices with electrically tunable topological insulating phases

Appl. Phys. Lett. **102**, 063503 (2013)

Very large magnetoresistance and spin state transition in Ba-doped cobaltites

J. Appl. Phys. **113**, 053909 (2013)

Additional information on *Appl. Phys. Lett.*

Journal Homepage: <http://apl.aip.org/>

Journal Information: http://apl.aip.org/about/about_the_journal

Top downloads: http://apl.aip.org/features/most_downloaded

Information for Authors: <http://apl.aip.org/authors>

ADVERTISEMENT

AIP | Applied Physics
Letters

SURFACES AND INTERFACES
Focusing on physical, chemical, biological, structural, optical, magnetic and electrical properties of surfaces and interfaces, and more...

ENERGY CONVERSION AND STORAGE
Focusing on all aspects of static and dynamic energy conversion, energy storage, photovoltaics, solar fuels, batteries, capacitors, thermoelectrics, and more...

EXPLORE WHAT'S NEW IN APL

SUBMIT YOUR PAPER NOW!

Spin Hall effect of reflected light from an air-glass interface around the Brewster's angle

Ling-Jun Kong (孔令军),¹ Xi-Lin Wang (汪喜林),¹ Si-Min Li,¹ Yongnan Li (李勇男),¹ Jing Chen,¹ Bing Gu (顾兵),¹ and Hui-Tian Wang (王慧田)^{1,2,a)}

¹*School of Physics and Key Laboratory of Weak Light Nonlinear Photonics, Nankai University, Tianjin 300071, China*

²*National Laboratory of Solid State Microstructures, Nanjing University, Nanjing 210093, China*

(Received 29 November 2011; accepted 1 February 2012; published online 16 February 2012)

We have developed a modified theory of the spin Hall effect of reflected light from a planar interface composed of two dielectric media and obtain the analytical expression valid for any incident angle including the Brewster's angle. We improved the experimental method and measured the spin-dependent transverse displacement of reflected light from a planar air-glass interface around the Brewster's angle. The experimental results are in agreement with the theoretical prediction. © 2012 American Institute of Physics. [doi:10.1063/1.3687186]

Although the phenomenon of light reflection at the interface as a well-known phenomenon has been extensively studied for a long time, there have still some intriguing issues,^{1,2} such as for the situation of the reflection of a Gaussian beam at the planar dielectric interface near the Brewster's angle.³⁻⁵ The spin Hall effect of light, which is an effect of spin-dependent transverse displacement of the wave packet perpendicular to the gradient of the refractive index, has attracted the growing interest. Since the spin Hall effect of light was first pioneered in 2004,⁶ Bliokh *et al.* proposed a systematic analysis based on the conservation of angular momentum and calculated the transverse displacement of a polarized Gaussian beam reflected or refracted at an interface separating two homogeneous media.⁷⁻⁹ In addition, Bliokh *et al.* presented a unified theory and a direct observation for the spin Hall effect of light in an effectively inhomogeneous and anisotropic medium.¹⁰

Hosten and Kwiat measured the transverse displacement caused by spin-dependent splitting of the refracted light by using the weak measurement technique.¹¹ Subsequently, the spin Hall effect of light has been theoretically and experimentally studied under different conditions, such as left-handed materials,¹² uniaxial crystal,¹³ and photon tunneling,¹⁴ in particular, and has been used to detect the spin moments of particles.¹⁵ Due to the difficulty in the theoretical analysis and experimental measurement, the spin Hall effect of reflected light near the Brewster's angle was not explored in Ref. 16. It is of great importance to explore the spin Hall effect of reflected light from a planar interface around the Brewster's angle, in particular, at the Brewster's angle. In Ref. 17, Luo *et al.* explored theoretically and experimentally the spin Hall effect of light reflected near the Brewster's angle, in which they did not obtain the analytical expression. In this letter, we give an analytical expression valid in a wide angle range (in particular, at the Brewster's angle) and improve the experimental method to observe the transverse displacement more directly, for spin Hall effect of reflected light from a planar air-glass interface around the Brewster's angle.

Considering a monochromatic Gaussian beam is reflected from the planar interface separated by air and a homogeneous glass, as shown in Fig. 1. A coordinate system (x, y, z) is attached at the air-glass interface, where the z axis is normal to the interface. The Gaussian beam is incident on the interface at an incident angle θ_{i0} of central wavevector \mathbf{k}_{i0} related by Snell's law in the xz plane. Its reflected beam has the central wavevector \mathbf{k}_{r0} . Two coordinate systems, (x_i, y_i, z_i) and (x_r, y_r, z_r) , are associated with the incoming and reflected beams, with the y_i and y_r axes parallel to the y axis and with the z_i and z_r being along the \mathbf{k}_{i0} and \mathbf{k}_{r0} . The incoming Gaussian beam has a wavelength of λ and a corresponding wavevector of $k_0 = 2\pi/\lambda$ in vacuum. Based on the Fourier analysis, the incoming Gaussian beam can be expressed as the superposition of a continuous spectrum of uniform plane wave component (with the \mathbf{k}_i) propagating in a wide range of directions.

Under the paraxial approximation, the electric field of the incoming p -polarized Gaussian beam (its electric vector is in the xz plane) can be written as

$$E_i(y_i, z_i) \propto \exp\left[-j\frac{k_0}{2q(z_i)}y_i^2\right], \quad (1)$$

where $q(z_i)$ donates the complex radius of curvature of the incoming Gaussian beam

$$\frac{1}{q(z_i)} = \frac{1}{R(z_i)} - j\frac{2}{k_0w^2(z_i)}. \quad (2)$$

Here, $R(z_i) = z_i[1 + (k_0w_0^2/2z_i)^2]$ is the radius of curvature, $w^2(z_i) = w_0^2[1 + (2z_i/k_0w_0^2)^2]$ is the spot radius, and w_0 is the radius of the beam waist for the incoming Gaussian beam.

The Gaussian beam can be treated as a linear superposition of all the component plane waves. By the Fourier transform, Eq. (1) can be rewritten as

$$E_i(y_i, z_i) \propto \int_{-\infty}^{+\infty} A_i(k_{iy})\exp[-j(k_{iy}y_i + k_{iz}z_i)]dk_{iy}, \quad (3)$$

where $A_i(k_{iy})$ represents the amplitude distribution of uniform plane waves propagating in a wide range of directions

^{a)}Electronic addresses: htwang@nankai.edu.cn and htwang@nju.edu.cn.

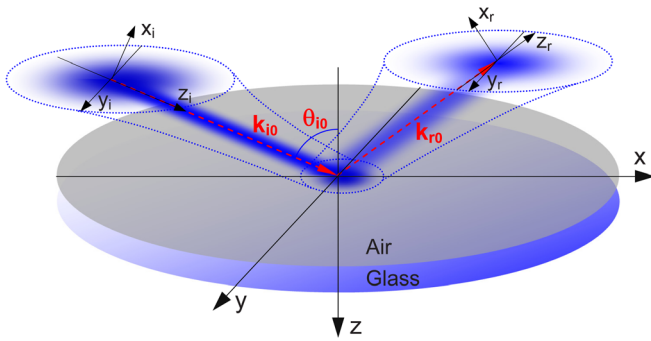


FIG. 1. (Color online) The scheme of the spin Hall effect of reflected light from an air-glass interface.

$$A_i(k_{iy}) = \exp(jk_{iz}z_i) \exp\left[-q(z_i) \frac{k_{iy}^2}{j2k_0}\right]. \quad (4)$$

The reflected beam can be written as follows:^{11,16}

$$E_r(y_r, z_r) \propto \int_{-\infty}^{+\infty} \left[r_p |h\rangle^r - \cot\theta_{i0} \frac{k_{ry}}{k_0} (r_s + r_p) |v\rangle^r \right] \times A_r(k_{ry}) \exp[-j(k_{ry}y_r + k_{rz}z_r)] dk_{ry}, \quad (5)$$

where $|h\rangle^r$ and $|v\rangle^r$ are the basis vectors of the horizontal and vertical polarizations of the reflected beam, $\mathbf{k}_r = \mathbf{k}_i - 2\hat{\mathbf{z}}(\hat{\mathbf{z}} \cdot \mathbf{k}_i)$, and $\mathbf{r}_r = \mathbf{r}_i - 2\hat{\mathbf{z}}(\hat{\mathbf{z}} \cdot \mathbf{r}_i)$ (see Refs. 18 and 19). r_p and r_s denote the Fresnel reflection coefficients of the p - and s -polarized components, respectively. By using the following relations:

$$\begin{aligned} |h\rangle^r &= (|+\rangle + |-\rangle)/\sqrt{2}, \\ |v\rangle^r &= (|+\rangle - |-\rangle)/j\sqrt{2}, \end{aligned} \quad (6)$$

where $|+\rangle$ and $|-\rangle$ are the basis vectors of the right- and left-handed circular polarizations, respectively, after integration, we obtain the reflected field as follows:

$$\begin{aligned} E_r(y_r, z_r) &\propto \{ |+\rangle [r_p + jq^{-1}(z_r)(r_s + r_p)y_r \cot\theta_{i0}] \\ &+ |-\rangle [r_p - jq^{-1}(z_r)(r_s + r_p)y_r \cot\theta_{i0}] \} \\ &\times \exp\left[-j \frac{k_0}{2} \frac{y_r^2}{q(z_r)}\right]. \end{aligned} \quad (7)$$

By using the definition of the intensity barycenter of the beam

$$\delta_{|\pm\rangle} = \frac{\int_{-\infty}^{+\infty} I_{|\pm\rangle} y_r dy_r}{\int_{-\infty}^{+\infty} I_{|\pm\rangle} dy_r}, \quad (8)$$

apart from terms including powers of $1/k_0$ higher than the second, we have

$$\delta_{|\pm\rangle} = \pm w_0 \frac{r_p(r_s + r_p)C}{(r_s + r_p)^2 + r_p^2 C^2}, \quad (9)$$

where the factor $C = k_0 w_0 \tan\theta_{i0}$. Equation (9) is the analytical expression of the displacement of spin-dependent splitting. Here, it should be pointed out that we have confirmed

our analytical expression to be in agreement with the numerical simulation results in Ref. 17.

One should be emphasized that in Refs. 11 and 16, the second power of $1/k_0$ was also neglected, correspondingly, the term of $(r_s + r_p)^2$ in Eq. (9) disappears. Evidently, when the second power of $1/k_0$ is also neglected, Eq. (9) degenerates into Eq. (1) in Ref. 16. More importantly, Eq. (1) in Ref. 16 is invalid around the Brewster's angle (in particular, at the Brewster's angle), which results in the divergence of the spin Hall effect of light (that violates physical reality), due to $r_p \rightarrow 0$. Equation (9) is valid for any incident angle including the Brewster's angle.

Figure 2 shows the experimental scheme similar to that in Refs. 11, 16, and 17. A Gaussian beam from a He-Cd laser with a beam waist of $w'_0 = 0.56$ mm at the exit of the laser passes in sequence through a half-wavelength plate (HWP), a lens L1 (with a focal length of $f_1 = 50$ mm), and a polarizer P1 to produce a focused p -polarized beam on the air-glass interface of prism. The focused p -polarized Gaussian beam near the Brewster's angle is reflected from the air-glass interface of prism, where the spin Hall effect of light takes place, and then the reflected beam is split into the two parts in the transverse (y) direction.

To measure the transverse displacement, the weak measurement as an universal and effective technique is extensively used as in Refs. 11, 16, and 17, in which there is a common keypoint that the deviation angle Δ from orthogonal configuration of the second polarizer P2 in Fig. 2 is chosen to be small, because the greater magnification of the transverse displacement can be achieved. In particular, in the small deviation angle situation, the magnification caused by Δ is independent of the incident angle θ_{i0} . In contrast, due to the introduction of the correction term in our modified theory, the magnification depends on the incident angle θ_{i0} even if in the small deviation angle situation. However, we find that when choosing $\Delta = \pm 45^\circ$ as shown in Fig. 2(b), the magnification becomes independent of the incident angle θ_{i0} . It is regret that there has no magnification in the situation of $\Delta = \pm 45^\circ$ (magnification is always unity), even so we can still use a lens L2 (with a focal length of $f_2 = 100 \pm 4$ mm) to achieve the magnification. Although its magnification is not so large, this is already enough for our measurement. The reflection spot on the interface of prism is in the front plane

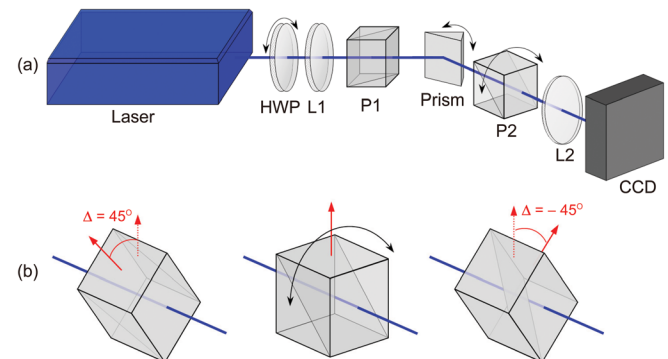


FIG. 2. (Color online) (a) Experimental scheme. The laser is a linearly polarized He-Cd laser at 441.6 nm and with a power of 144 mW, HWP is a half-wave plate, P1 and P2 are two Glan polarizers, and L1 and L2 are lenses. (b) The orientation geometry of the polarizer P2 in our experiment.

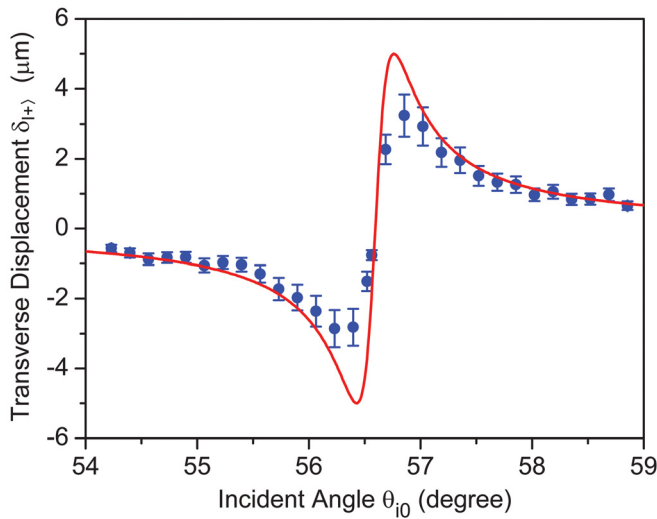


FIG. 3. (Color online) Shift of the $|+\rangle$ spin component, $\delta_{|+\rangle}$, as a function of angle of incidence near the Brewster's angle. Solid line and circles are the theoretical and experimental results.

of L2. A CCD is used to acquire the intensity images of the reflected beam and then to measure the magnified relative displacements $\delta_{\pm 45^\circ}$ of the intensity barycenter of the beam under the situations of $\Delta = \pm 45^\circ$. Thus, we can deduce the original shifts $\delta_{|\pm\rangle}$ caused by the spin Hall effect of light as follows:

$$\delta_{\pm 45^\circ} = -F\delta_{|\pm\rangle}, \quad (10)$$

where $F = \lambda f_2 / (\pi w_0^2)$ is the magnification factor caused by the lens L2 only.

We measure the Brewster's angle to be $\theta_B = 56.595^\circ \pm 0.005^\circ$ and then deduce the refractive index of the glass to be 1.5163 ± 0.0003 at $\lambda = 441.6$ nm. Figure 3 depicts the transverse displacement $\delta_{|+\rangle}$ of the $|+\rangle$ spin component, as a function of the incident angle θ_{i0} around the Brewster's angle. The displacement increases and reaches the theoretical (experimental) first maximum of -5.10 (-2.86 ± 0.05) μm at the theoretical (experimental) value of 56.43° ($\sim 56.30^\circ \pm 0.01^\circ$) and then decreases. At the Brewster's angle, the displacement becomes zero. After passing through the Brewster angle, the displacement increases and reaches the theoretical (experimental) second maximum of 5.10 (2.93 ± 0.05) μm at the theoretical (experimental) value of 56.76° ($\sim 56.85^\circ \pm 0.01^\circ$) and then decreases. In addition, it should be pointed out that the magnification of $F = 135 \pm 6$ in our experiment. Evidently, the experiment should be in agreement with the theory, although there is some deviation. One of the dominant reasons for such a devi-

ation originates from the fact that it is difficult to accurately determine the position of the light spots by CCD, due to the too weak intensity. We can know from Eq. (9) that at the incident angles of $56.43^\circ < \theta_B$ and $56.76^\circ > \theta_B$, where $r_s = (-1 \mp C)r_p$, the spin-dependent displacement reaches the maxima. At the Brewster's angle, the displacement is zero, as shown in Eq. (9).

As is well known, the reflected Gaussian beam is strongly distorted at the Brewster's angle. However, the distortion is mainly the longitudinal direction and the reflected beam is still symmetric about the xz plane (implies the barycenter of the field intensity is at $y = 0$).²⁰ Therefore, we can ignore the influence of the distortion on the transverse displacement.

In summary, we have given a modified theory of the spin Hall effect of reflected light from a planar interface separated by two dielectric media around the Brewster's angle and obtained the analytical expression. We measured experimentally the spin-dependent displacement of the reflected light at an air-glass interface around the Brewster's angle. The experimental results are in agreement with the theoretical prediction.

This work is supported by the National Basic Research Program (973 Program) of China under Grant No. 2012CB921900 and the National Natural Science Foundation of China under Grants 10934003.

¹F. Goos and H. Hänchen, *Ann. Phys.* **436**, 333 (1947).

²K. Artmann, *Ann. Phys.* **437**, 87 (1948).

³M. V. R. K. Murty and R. P. Shukla, *Appl. Opt.* **22**, 1094 (1983).

⁴Y. Fainman and J. Shamir, *Appl. Opt.* **23**, 3188 (1984).

⁵Q. Li and R. J. Vernon, *IEEE Trans. Antennas Propag.* **54**, 3449 (2006).

⁶M. Onoda, S. Murakami, and N. Nagaosa, *Phys. Rev. Lett.* **93**, 083901 (2004).

⁷K. Y. Bliokh and Y. P. Bliokh, *Phys. Rev. Lett.* **96**, 073903 (2006).

⁸K. Y. Bliokh, *Phys. Rev. Lett.* **97**, 043901 (2006).

⁹K. Y. Bliokh and Y. P. Bliokh, *Phys. Rev. E* **75**, 066609 (2007).

¹⁰K. Y. Bliokh, A. Niv, V. Kleiner, and E. Hasman, *Nat. Photonics* **2**, 748 (2008).

¹¹O. Hosten and P. Kwiat, *Science* **319**, 787 (2008).

¹²H. L. Luo, S. C. Wen, W. X. Shu, Z. X. Tang, Y. H. Zou, and D. Y. Fan, *Phys. Rev. A* **80**, 043810 (2009).

¹³Y. Qin, Y. Li, X. B. Feng, Z. P. Liu, H. Y. He, Y. F. Xiao, and Q. H. Gong, *Opt. Express* **18**, 16832 (2010).

¹⁴H. L. Luo, S. C. Wen, W. X. Shu, and D. Y. Fan, *Phys. Rev. A* **82**, 043825 (2010).

¹⁵C. M. Krowne, *Phys. Lett. A* **373**, 466 (2009).

¹⁶Y. Qin, Y. Li, H. Y. He, and Q. H. Gong, *Opt. Lett.* **34**, 2551 (2009).

¹⁷H. L. Luo, X. X. Zhou, W. X. Shu, S. C. Wen, and D. Y. Fan, *Phys. Rev. A* **84**, 043806 (2011).

¹⁸R. F. Gragg, *Am. J. Phys.* **56**, 1092 (1988).

¹⁹M. Merano, N. Hermosa, and J. P. Woerdman, *Phys. Rev. A* **82**, 023817 (2010).

²⁰A. Aiello, M. Merano, and J. P. Woerdman, *Opt. Lett.* **34**, 1207 (2009).

Surface plasmons at the interface between graphene and Kerr-type nonlinear media

Lei Wang, Wei Cai,* Xinzheng Zhang, and Jingjun Xu

The Key Laboratory of Weak-Light Nonlinear Photonics, Ministry of Education, School of Physics and TEDA Applied Physics School, Nankai University, Tianjin 300457, China

*Corresponding author: weicai@nankai.edu.cn

Received April 9, 2012; accepted April 30, 2012;

posted May 7, 2012 (Doc. ID 166360); published June 27, 2012

The properties of surface plasmons localized at the interface between graphene and Kerr-type nonlinear substrates are investigated analytically. Although the relative propagation distance remains the same, the dispersion of graphene plasmons may be affected much by the inevitable nonlinear effect of substrates. Specifically, the wavelength of graphene plasmons can be tuned by adjusting the nonlinear permittivity of substrates. © 2012 Optical Society of America

OCIS codes: 240.6680, 250.5403, 190.3270.

Graphene is well suited for a number of photonic applications [1–3] due to its interesting optical and electronic properties [4,5]. In particular, the collective electron excitations in graphene [6,7] have attracted much attention. Recently, graphene plasmons (GPs) have been studied theoretically in doped graphene sheets [8–10], graphene ribbons [11–13], and graphene disk arrays [14] and were detected and investigated experimentally [15,16]. GPs are believed to be a conveniently tunable means for strong light–matter interactions in the IR and terahertz range [8,9]. However, the nonlinear contribution from substrates to the properties of GPs was ignored in previous work. This is unjustified because the strong electromagnetic field of GPs (the enhancement factor can be as large as 10^5 [10]) makes the nonlinear contribution from substrates an inevitable and important factor. Moreover, the investigation of such GPs provides a method to determine the nonlinear properties of substrates that will facilitate precise probing of nonlinear material in the IR and terahertz range.

An extended doped graphene sheet can bind surface plasmons with TM polarization provided that $\text{Im}\sigma > 0$ [7], where σ is the conductivity of graphene. The dispersion relation of GPs without the nonlinear contribution from substrates is given by [8]

$$-i\frac{4\pi\sigma}{c} = \frac{\epsilon_s}{\sqrt{\eta^2 - \epsilon_s}} + \frac{1}{\sqrt{\eta^2 - 1}}, \quad (1)$$

where c is the speed of light in vacuum, ϵ_s is the dielectric permittivity of the substrate, and η denotes the plasmon wave vector normalized to the free light wavenumber ω/c . In the following, the electrostatic limit of this expression is used since η is usually much larger than unity and the dielectric permittivity of substrates. Therefore, the dispersion of GPs is described by

$$\eta \approx \frac{ic(\epsilon_s + 1)}{4\pi\sigma}. \quad (2)$$

We will not discuss here a possible Pockels-type nonlinearity of the substrate but the always present Kerr-type effect [17]. Equation (2) cannot be corrected by

simply replacing ϵ_s with the electric field intensity dependent permittivity

$$\epsilon_n = \epsilon_l + \alpha|\mathbf{E}|^2. \quad (3)$$

α is the Kerr coefficient of the substrate, \mathbf{E} is the electric field in the substrate, and ϵ_l and ϵ_n are the linear and total dielectric permittivities of the substrate, respectively.

In this Letter, we investigate theoretically the dispersion and propagation distance of GPs when an infinitely large graphene sheet is lying on a nonlinear substrate [Fig. 1(a)]. For simplicity, the nonlinear response of the substrate is assumed to be isotropic. Then the electric field has the form $\mathbf{E}(\mathbf{r}, t) = \mathbf{E}(z) \exp(i\beta x - i\omega t)$ with respect to the coordinate system indicated in Fig. 1(a). β is the momentum of GPs. Inserting this field into Maxwell's equations, we obtain

$$iH_y = E'_x - i\eta E_z, \quad H'_y = i\epsilon_n E_x, \quad -\eta H_y = \epsilon_n E_z. \quad (4)$$

Here $\xi = kz$ and $\eta = \beta/k$ are the normalized length and momentum (normalized to the vacuum wave vector $k = \omega/c$). The prime denotes differentiation with respect to ξ . By eliminating the electric field terms in Eq. (5), we find

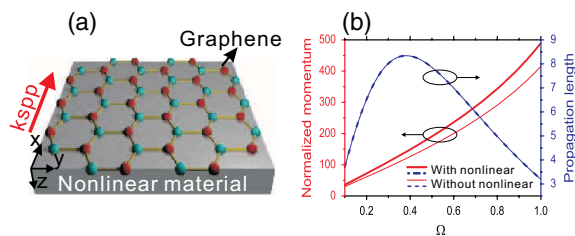


Fig. 1. (Color online) (a) Sketch of an infinitely large graphene sheet lying on a substrate; k_{spp} represents the propagation direction of surface plasmons; (b) the dispersion relation (solid lines) and propagation distance (dashed lines) of GPs with (thick lines) and without (thin lines) nonlinear contributions from the substrate. The photon energy is $\Omega = \hbar\omega/E_F$ with $E_F = 0.4$ eV. Momentum in units of ω/c and propagation length in units of the surface plasmon wavelength.

$$\left(\frac{H'_y}{\epsilon_n}\right)' = \left(\frac{\eta^2}{\epsilon_n} - 1\right)H_y. \quad (5)$$

Substituting the electric field terms from Eq. (4) into Eq. (3) gives

$$\left(\frac{H'_y}{\epsilon_n}\right)^2 = \frac{\epsilon_n - \epsilon_l}{\alpha} - \left(\frac{\eta H_y}{\epsilon_n}\right)^2. \quad (6)$$

We differentiate Eq. (6), substitute into Eq. (5), and arrive at

$$\left(H_y^2 \frac{2\eta^2 - \epsilon_n}{\epsilon_n}\right)' = \epsilon_n \left(\frac{\epsilon_n - \epsilon_l}{\alpha}\right)'. \quad (7)$$

The solution is

$$H_y^2 = \frac{\epsilon_n}{2\eta^2 - \epsilon_n} \frac{\epsilon_n^2 - \epsilon_l^2}{2\alpha}. \quad (8)$$

The derivatives coincide with Eq. (7), and the values of both sides vanish deep below the substrate surface where there is neither a magnetic nor an electric field. Equation (8) expresses the magnetic field in terms of the dielectric permittivities and normalized momentum η . Note that η , α , and ϵ_l are constants.

Assuming that the graphene sheet lies at $z = 0$, the nonlinear substrate occupies the region $z > 0$ with the dielectric permittivity ϵ_n , and the dielectric function is ϵ in the region $z < 0$ (see Fig. 1). The electromagnetic field in the nonlinear substrate region is

$$H_y = A, \quad E_x = \frac{H'_y}{i\epsilon_n} = \frac{A'}{i\epsilon_n}, \quad E_z = -\frac{\eta H_y}{\epsilon_n} = -\frac{\eta A}{\epsilon_n}, \quad (9)$$

where $A(z)$ is the amplitude of the magnetic field. The electromagnetic fields in the region $z < 0$ can be written as

$$H_y = B e^{\kappa \xi}, \quad E_x = \frac{H'_y}{i\epsilon} = \frac{\kappa B}{i\epsilon} e^{\kappa \xi}, \quad E_z = -\frac{\eta H_y}{\epsilon} = -\frac{\eta B}{\epsilon} e^{\kappa \xi}, \quad (10)$$

where $\kappa = \sqrt{\eta^2 - \epsilon}$ describes the confinement of the field. B is the amplitude of the magnetic field.

From the continuity requirements of E_x and H_y [$(H_y|_{z<0} - H_y|_{z>0}) = 4\pi\sigma E_x \delta(z)/c$] at $\xi = 0$, we obtain the relations

$$\frac{A'(0)}{\epsilon_n} = \frac{\kappa B}{\epsilon}, \quad A(0) = \left(1 - \frac{4\pi\sigma\kappa}{i\epsilon\epsilon}\right)B. \quad (11)$$

Inserting them into Eq. (6) at $\xi = 0$ gives

$$\frac{\epsilon_n(0) - \epsilon_l}{\alpha} = \left(\frac{\kappa A(0)}{\epsilon + i4\pi\sigma\kappa/c}\right)^2 + \left(\frac{\eta A(0)}{\epsilon_n}\right)^2. \quad (12)$$

We combine this with Eqs. (8) and (11) and obtain the dispersion relation of GPs, namely

$$-i\frac{4\pi\sigma(\omega)}{c} = \epsilon_n \sqrt{\frac{\epsilon_n + \epsilon_l}{\eta^2(3\epsilon_n - \epsilon_l) - 2\epsilon_n^2}} + \frac{\epsilon}{\kappa}, \quad (13)$$

where $\epsilon_n = \epsilon_n(0)$. With $\alpha = 0$, $\epsilon_n(0) = \epsilon_l$, and $\epsilon = 1$, our result reduces to Eq. (1), as expected.

If the normalized momentum η is much larger than unity and the dielectric permittivity of the substrate, the normalized momentum of GPs can be simplified to

$$\eta \approx \kappa \approx \frac{ic}{4\pi\sigma(\omega)} \left(\epsilon_n \sqrt{\frac{\epsilon_n + \epsilon_l}{3\epsilon_n - \epsilon_l}} + \epsilon\right). \quad (14)$$

Again, $\epsilon_n = \epsilon_n(0) = \epsilon_l + \alpha|\mathbf{E}(0)|^2$. $\sigma(\omega)$ is the in-plane complex conductivity of graphene. The dispersion of GPs is given by $\text{Re}(\eta)$, their propagation distance by $L = 1/\text{Im}(\eta)$.

To demonstrate the effect of substrate nonlinearity, we focus on a material with $\epsilon_l = 7.84$ and $\alpha = 9.99 \times 10^{-19} \text{ m}^2 \text{ V}^{-1}$ [18]. The conductivity of graphene is computed within the local random phase approximation [19] with an intrinsic relaxation time $\tau = \mu E_F / e v_F^2$, where $v_F \approx c/300$ is the Fermi velocity, $\mu = 1.00 \text{ m}^2 \text{ V}^{-1} \text{ s}^{-1}$ the measured DC mobility [20], and $E_F = 0.4 \text{ eV}$ the Fermi energy. Because of the large field enhancement factor [10], we simply assume an electric field intensity of $E(0)^2 = 3 \times 10^{18} \text{ V}^2 \text{ m}^{-2}$ at the interface between graphene and the substrate. Indeed, the electric field at the surface of graphene and substrates depends on specific experimental conditions. The dispersion relation and propagation distance of GPs with and without nonlinear contributions from the substrate are calculated by resorting to Eqs. (14) and (2), respectively; see Fig. 1(b).

Without the nonlinear contribution from the substrate, the momentum of GPs is several hundred times larger than the free light momentum (the thin solid line) within a photon energy range from 0.04 to 0.4 eV. The relative propagation length reaches its maximum 8.5 at an energy of about 0.15 eV (thin dashed line). If, however, the nonlinear contribution is taken into account, the momentum of GPs increases by 13% at the energy 0.15 eV (thick solid line), but the relative propagation distance remains the same (thick dashed line), which means that the nonlinear effect effectively changes the wavelength of GPs.

The nonlinear part in the dielectric permittivity of a substrate not only depends on the nonlinear coefficient but also on the light intensity; see Eq. (3). So it is natural to consider how the nonlinear dielectric permittivity $\alpha E(0)^2$ affects the properties of GPs. Figures 2(a) and 2(b) visualize dispersion and propagation distance of GPs, respectively. We find that the positive nonlinear dielectric permittivity leads to a momentum enhancement of GPs while barely affecting the propagation length. This behavior indicates that it is possible to enhance localization of GPs by increasing the incident electric field or changing to another kind of substrate with a larger positive nonlinear coefficient. In addition, the nonlinear contribution with a negative nonlinear coefficient always diminishes the confinement of GPs except for a small photon energy window. Surprisingly,

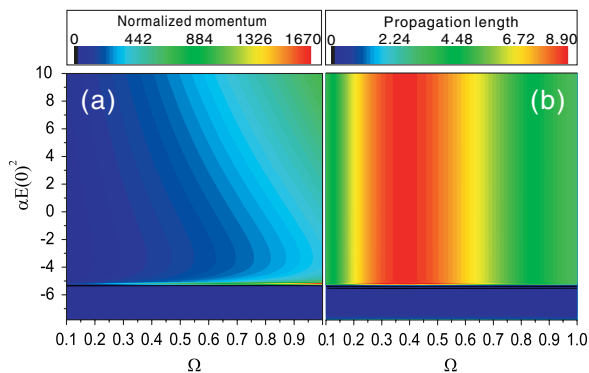


Fig. 2. (Color online) Dependence of the (a) dispersion relation and (b) relative propagation length of GPs on the nonlinear dielectric permittivity $\alpha E(0)^2$ in the system [Fig. 1(a)]. Ω is the ratio of photon energy $\hbar\omega$ by Fermi energy $E_F = 0.4$ eV.

Table 1. Momenta and Propagation Distances of GPs with Different Substrates at Light Wavelength $9.7 \mu\text{m}$

Materials	SiO ₂	SiC	GaAs
η (linear)	30.5065	135.2358	150.3004
η (nonlinear)	30.5032	132.6673	131.8185
L (linear)	8.1585	11.8847	8.1596
L (nonlinear)	8.1585	11.9918	8.1596

the momentum of GPs increases strongly in this region $[-5.4 < \alpha E(0)^2 < -4]$, which may find application in the wavelength range larger than $6 \mu\text{m}$. By the way, this behavior verifies our initial remark that it is incorrect to generalize the dispersion of GPs by simply inserting the nonlinear dielectric permittivity from Eq. (3) into Eq. (2).

Finally, in Table 1, we compare the nonlinear contributions to GPs of several materials [17]. Although negligible for materials with a small nonlinear coefficient (like SiO₂), they are notable in strongly nonlinear materials (such as SiC or GaAs). The momenta of GPs are 2% and 14% larger, respectively, for our reference light intensity.

In summary, in this Letter we investigate analytically the effect of a nonlinear substrate on the properties of GPs. The confinement of these plasmons can be enhanced without impairing the propagation distance. The effect is important when analyzing GPs or designing applications with them.

This work was supported by the National Natural Science Foundation of China (11004112), the National Basic Research Program of China (2010CB934101), the International S&T Cooperation Program of China (2011DFA52870), the 111 Project (B07013), the Fundamental Research Funds for the Central Universities, and by the Oversea Famous Teacher Project (MS2010NKDX0230). We thank P. Hertel for critically reading the manuscript and advice.

References

1. F. Bonaccorso, Z. Sun, T. Hasan, and A. C. Ferrari, *Nat. Photon.* **4**, 611 (2010).
2. M. Liu, X. Yin, E. Ulin-Avila, B. Geng, T. Zentgraf, L. Ju, F. Wang, and X. Zhang, *Nature* **474**, 64 (2011).
3. A. Vakil and N. Engheta, *Science* **332**, 1291 (2011).
4. A. K. Geim and K. S. Novoselov, *Nat. Mater.* **6**, 183 (2007).
5. A. K. Geim, *Science* **324**, 1530 (2009).
6. E. H. Hwang and S. Das Sarma, *Phys. Rev. B* **75**, 205418 (2007).
7. S. A. Mikhailov and K. Ziegler, *Phys. Rev. Lett.* **99**, 016803 (2007).
8. M. Jablan, H. Buljan, and M. Soljačić, *Phys. Rev. B* **80**, 245435 (2009).
9. F. H. L. Koppens, D. E. Chang, and F. J. García de Abajo, *Nano Lett.* **11**, 3370 (2011).
10. A. Yu. Nikitin, F. Guinea, F. J. García-Vidal, and L. Martín-Moreno, *Phys. Rev. B* **84**, 195446 (2011).
11. J. Christensen, A. Manjavacas, S. Thongrattanasiri, F. H. L. Koppens, and F. J. García de Abajo, *ACS Nano* **6**, 431 (2012).
12. A. Yu. Nikitin, F. Guinea, F. J. García-Vidal, and L. Martín-Moreno, *Phys. Rev. B* **84**, 161407(R) (2011).
13. A. Yu. Nikitin, F. Guinea, F. J. García-Vidal, and L. Martín-Moreno, *Phys. Rev. B* **85**, 081405(R) (2012).
14. S. Thongrattanasiri, F. H. L. Koppens, and F. J. García de Abajo, *Phys. Rev. Lett.* **108**, 047401 (2012).
15. L. Ju, B. Geng, J. Horng, C. Girit, M. Martin, Z. Hao, H. A. Bechtel, X. Liang, A. Zettl, Y. R. Shen, and F. Wang, *Nat. Nanotechnol.* **6**, 630 (2011).
16. Z. Fei, G. O. Andreev, W. Bao, L. M. Zhang, A. S. McLeod, C. Wang, M. K. Stewart, Z. Zhao, G. Dominguez, M. Thiemens, M. M. Fogler, M. J. Tauber, A. H. Castro-Neto, C. N. Lau, F. Keilmann, and D. N. Basov, *Nano Lett.* **11**, 4701 (2011).
17. R. W. Boyd, *Nonlinear Optics*, 3rd ed. (Academic, 2010).
18. V. Ta'eed, N. J. Baker, L. Fu, K. Finsterbusch, M. R. E. Lamont, D. J. Moss, H. C. Nguyen, B. J. Eggleton, D.-Y. Choi, S. Madden, and B. Luther-Davies, *Opt. Express* **15**, 9205 (2007).
19. B. Wunsch, T. Stauber, F. Sols, and F. Guinea, *New J. Phys.* **8**, 318 (2006).
20. K. S. Novoselov, A. K. Geim, S. V. Morozov, D. Jiang, Y. Zhang, S. V. Dubonos, I. V. Grigorieva, and A. A. Firsov, *Science* **306**, 666 (2004).

Tunable add/drop channel coupler based on an acousto-optic tunable filter and a tapered fiber

Wending Zhang,¹ Ligang Huang,¹ Feng Gao,^{1,*} Fang Bo,¹ Li Xuan,² Guoquan Zhang,^{1,3} and Jingjun Xu^{1,2}

¹MOE Key Laboratory of Weak-Light Nonlinear Photonics, TEDA Applied Physics School and School of Physics, Nankai University, Tianjin 300457, China

²State Key Laboratory of Applied Optics, Changchun Institute of Optics, Fine Mechanics and Physics, Chinese Academy of Sciences, Changchun 130033, China

³e-mail: zhanggq@nankai.edu.cn

*Corresponding author: fenggao@nankai.edu.cn

Received November 24, 2011; revised January 2, 2012; accepted February 15, 2012;
posted February 23, 2012 (Doc. ID 158509); published March 28, 2012

We report a tunable add/drop channel coupler based on an acousto-optic tunable filter and a tapered fiber. The coupling efficiency and central wavelength of the add/drop channel coupler are tunable by simply tuning the power and frequency of the driving radio frequency signal. Further possible improvements on the configuration are also discussed. © 2012 Optical Society of America

OCIS codes: 060.2310, 060.2430, 060.2330, 060.2280.

In recent years, the add/drop channel coupler has attracted much attention [1] because of its potential applications in wavelength-division-multiplexing (WDM) systems [2], which is one of the most important components for enhancing the efficiency and flexibility of the fiber communication network. Early studies on the add/drop channel coupler focused mainly on the incorporation of fiber Bragg gratings (FBGs) to achieve wavelength selectivity [3–4]. Because the FBG device has to be operated in the reflection mode [5], it may introduce unwanted optical feedback and extra loss in retrieving the reflected signal. Subsequently, a component composed of two parallel identical long-period fiber grating (LPFG) was introduced into the add/drop channel coupler [6–7], and it was operated in the transmission mode and did not have problems in the reflection mode [8]. Besides, there were also other configurations for the add/drop channel coupler, for example, the combination of the LPFG with either the FBG [9] or the tapered fiber [10]. However, it was difficult for the above configurations to control effectively the spectral characteristics such as the coupling efficiency and, more importantly, the central wavelength of the add/drop channel coupler. The most recent work with controllable spectral parameters was based on two parallel identical LPFGs with voltage-controllable coil heaters [11]. In this Letter, we report a tunable add/drop channel coupler based on an acousto-optic tunable filter (AOTF) and a tapered fiber. The output of the AOTF shows the band-rejection characteristic, and the output of the tapered fiber shows the bandpass characteristic. The coupling efficiency and the central wavelength of the add/drop channels could be adjusted by tuning the power and frequency of the driving radio frequency (RF) signal applied to the AOTF. At the same time, possible improvements on the configuration were also discussed.

It is known that the AOTF is composed of an acoustic wave generation system and an unjacketed single-mode fiber (SMF) [12]. When the acoustic wave propagates along the unjacketed SMF, a periodic modulation of the refractive index is produced with a period of hundreds of micrometers in the core of the unjacketed

SMF, and such a core refractive index modulation would induce a mode-coupling between the core fundamental mode (LP_{01}^{co}) and the copropagation cladding modes (LP_{1u}^{cl}) when the phase matching condition is satisfied [13]:

$$\lambda = \left(n_{01}^{co} - n_{1u}^{cl} \right) \Lambda, \quad (1)$$

where λ is the central wavelength; n_{01}^{co} and n_{1u}^{cl} are the effective index of the core and cladding modes, respectively; and Λ is the acoustic wavelength in the unjacketed SMF. As a result, the nonresonant mode propagates in the core and the resonant mode propagates in the cladding of the AOTF. Thus, the mode coupling between them generates a notch in the transmission spectrum of the AOTF. If a tapered fiber with its uniform waist part is close enough to the AOTF right after the acousto-optic (AO) interaction region of the AOTF (see Fig. 1), the cladding mode in the AOTF can be coupled to the cladding mode of the tapered fiber via an evanescent wave. The cladding mode in the uniform waist part of the tapered fiber will be coupled to its core mode through a transition zone with its diameter increasing exponentially up to that of the tail fiber and then propagating along the tapered fiber [14]. Therefore, the nonresonant and resonant modes can be separated and directed to the outputs of the AOTF and the tapered fiber, respectively. The output of the AOTF (Port 2) would show the band-rejection characteristic, and that of the tapered fiber (Port 3)

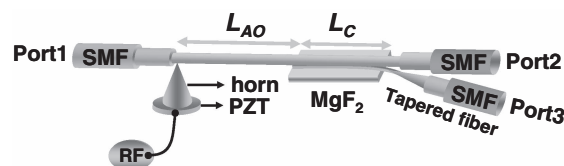


Fig. 1. Experimental configuration of the tunable add/drop channel coupler: L_{AO} , length of AO interaction region; L_C , length of the evanescent wave coupling region supported by a low-index MgF_2 substrate and dipped into a refractive-index-matched liquid.

would show the bandpass characteristic; i.e., the structure works as an add/drop channel coupler. In addition, the coupling efficiency and the central wavelength of the output signals can be adjusted by tuning the power and frequency of the driving RF signal applied to the AOTF.

Figure 1 is the experimental configuration of the tunable add/drop channel coupler. The structure of the AOTF was the same as that in a previous work we reported [15]. An axial mode piezoelectric transducer (PZT) was attached to a cone acoustic transducer, and the other side of it was attached to a steel plate as a mount. The unjacketed SMF had a step index of $\Delta = 0.32\%$, with a core radius of $\rho_{co} = 4.5 \mu\text{m}$ and a cladding radius of $\rho_{cl} = 62.5 \mu\text{m}$. The outer diameter of the SMF was etched down to $30 \mu\text{m}$ by the hydrofluoric acid, and the length of the etched region was 38 mm. The uniform waist part of the tapered fiber was fabricated with a diameter of $18 \mu\text{m}$ and a length of 14 mm, and the transition zone of the tapered fiber was 5 mm. The uniform waist part of the tapered fiber was attached along the etched SMF of the AOTF with a coupling length of $L_C = 10 \text{ mm}$. To increase the coupling efficiency, the coupling region was dipped into a refractive-index-matched liquid ($n = 1.450$), where the acoustic wave was absorbed and therefore the AO interaction length L_{AO} was limited to 28 mm. The whole coupling region was supported by a piece of MgF_2 substrate with a lower refractive index of ~ 1.37 .

RF power of 0.4 dBm was applied to the PZT at a frequency of 0.850 MHz. With an unpolarized light from a broadband light source coupled into Port 1 of the SMF, the transmission spectra of Ports 2 and 3 were measured. The experimental results are presented in Fig. 2. The black solid curve denotes the transmission spectrum of Port 2, and it shows a band-rejection characteristic with a peak efficiency of -17.1 dB at the central wavelength 1562.7 nm due to the mode coupling between the LP_{01}^{co} and LP_{11}^{cl} modes. The red dashed curve denotes the transmission spectrum of Port 3, showing a bandpass characteristic with peak efficiency of -5.1 dB . The two measured spectra are complementary with each other. Furthermore, by coupling the light into Port 3, i.e., adding

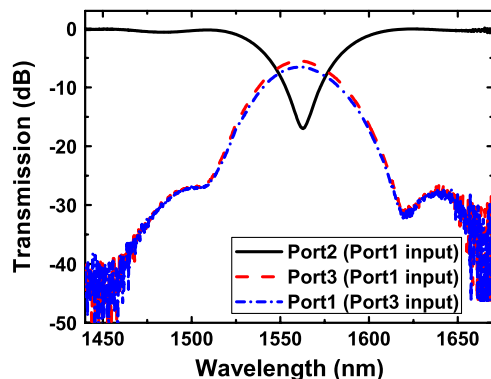


Fig. 2. (Color online) The black solid and red dashed curves denote the output spectra of Ports 2 and 3, respectively, when coupling the light into Port 1. The blue dashed-dotted curve denotes the output spectrum at Port 1 of the AOTF by coupling the light into the tapered fiber.

the signal to the SMF via the tapered fiber, the output spectrum of Port 1 was measured and depicted as the blue dashed-dotted curve in Fig. 2. One sees that the blue dashed-dotted curve coincides with the red dashed curve, which means that the signal adding and dropping are almost of the same loss of -5.1 dB . Note that the bandwidth of the add/drop channels could be narrowed by increasing the AO interaction length L_{AO} [16].

With the light coupling into Port 1, the spectral tunability of Port 3 is presented in Fig. 3. By increasing the RF driving power from -9.6 dBm to 0.4 dBm at 0.850 MHz , the peak bandpass coupling efficiency of Port 3 can be adjusted from -13 to -5.1 dB at the same central wavelength of 1562.7 nm , as shown in Fig. 3(a). Furthermore, the spectral central wavelength of the Port 3 is blue-shifted linearly with a tuning slope of -0.88 nm/kHz when one increases the driving RF frequency. For example, the central wavelength of Port 3 can be tuned from 1594.7 to 1539.8 nm , covering both the C and L bands, when the RF frequency is tuned from 0.820 to 0.880 MHz , as shown in Fig. 3(b). Meanwhile, the spectral central wavelength of Port 3 is always in coincidence with that of Port 2.

With this configuration, the coupling efficiency and the central wavelength of the add/drop channels can be adjusted quickly and easily [7,10]. Furthermore, it is easy to incorporate into optical communication systems because of its all-SMF structure [13].

The above experimental results have demonstrated the feasibility of the configuration. Moreover, the bandpass coupling efficiency can be increased further on to reduce the loss of the signal, which is very important for practical applications of optical communication [7,10,11]. A theoretical calculation based on the experiment [17] shows that the bandpass coupling efficiency depends on the coupling length L_C in a significant way. The bandpass coupling efficiency reaches a maxima at a coupling length of $L_C = 15 \text{ mm}$, as shown by the solid curve in Fig. 4. The coupling length L_C can be finely adjusted in the experiments with a translation stage under the monitoring of a stereomicroscope. The relationship between the bandpass coupling efficiency and L_C was measured experimentally, and the results are shown by the solid squares in Fig. 4. One sees that the experimental

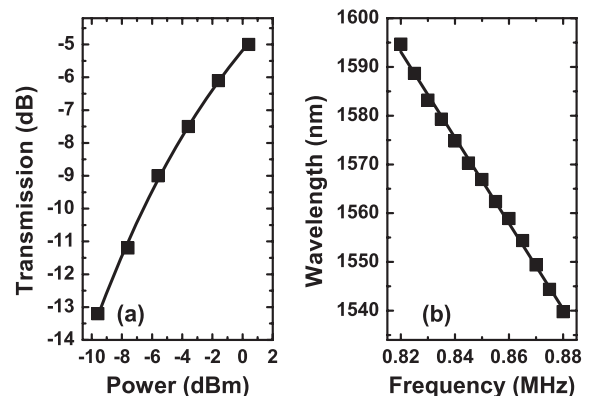


Fig. 3. (a) Bandpass coupling efficiency tunability and (b) central wavelength tunability of Port 3 from the tapered fiber.

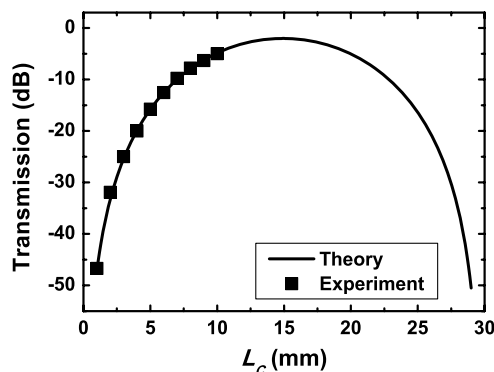


Fig. 4. The solid curve and solid squares denote the simulation and experimental results of the bandpass coupling efficiency as a function of L_C , respectively.

results agree with the theoretical prediction very well. Note that the maximally available coupling length L_C is 10 mm in our experiment, so there is still a large space to improve the bandpass coupling efficiency by increasing L_C . Besides, the bandpass coupling efficiency could also be improved, for example, by setting the uniform waist part of the tapered fiber to an appropriate diameter so that the cladding modes of the two fibers have similar effective index. Furthermore, the transition zone of the tapered fiber should be long enough and the diameter of the tapered fiber should vary slowly enough to decrease the coupling loss in the transition zone [10].

In conclusion, we have experimentally realized a tunable add/drop channel coupler based on an AOTF and a tapered fiber. The coupling efficiency and the central wavelength of the add/drop channels can be controlled by tuning the power and frequency of the driving RF signal applied to the AOTF. At the same time, possible improvements on the configuration are discussed. Combined with our recent fiber-winding AOTF structure in which multi-AOTFs are driven synchronously by one cuneal acoustic transducer [15], the tunable multichannel add/drop coupler can be fabricated. Such add/drop couplers are very useful for coarse WDM applications.

This work is supported by the 973 Program (2010CB934101), the Chinese National Key Basic Research Special Fund (2011CB922003), the International S&T Cooperation Program of China (2011DFA52870), the National Natural Science Foundation of China (90922030, 11174153, 10804054, and 10904077), the 111 Project (B07013), the Natural Science Foundation of Tianjin, the Cultivation Fund of the Key Scientific and Technical Innovation Project, Ministry of Education of China (708022), and the Fundamental Research Funds for the Central Universities.

References

1. H. A. Haus and Y. Lai, *J. Lightwave Technol.* **10**, 57 (1992).
2. B. Moslehi, P. Harvey, J. Ng, and T. Jansson, *Opt. Lett.* **14**, 1088 (1989).
3. J. L. Archambault, P. St. J. Russell, S. Barcelos, P. Hua, and L. Reekie, *Opt. Lett.* **19**, 180 (1994).
4. I. Baumann, J. Seifert, W. Nowak, and M. Sauer, *IEEE Photon. Technol. Lett.* **8**, 1331 (1996).
5. G. Meltz, W. W. Morey, and W. H. Glenn, *Opt. Lett.* **14**, 823 (1989).
6. K. S. Chiang, Y. Q. Liu, M. N. Ng, and S. P. Li, *Electron. Lett.* **36**, 1408 (2000).
7. Y. Q. Liu, K. S. Chiang, Y. J. Rao, Z. L. Ran, and T. Zhu, *Opt. Express* **15**, 17645 (2007).
8. A. M. Vengsarkar, P. J. Lemaire, J. B. Judkins, V. Bhatia, T. Erdogan, and J. E. Sipe, *J. Lightwave Technol.* **14**, 58 (1996).
9. Y. Q. Liu, Q. Liu, and K. S. Chiang, *Opt. Lett.* **34**, 1726 (2009).
10. A. P. Luo, K. Gao, F. Liu, R. H. Qu, and Z. J. Fang, *Opt. Commun.* **240**, 69 (2004).
11. Y. G. Han, S. B. Lee, C. S. Kim, and M. Y. Jeong, *Opt. Lett.* **31**, 703 (2006).
12. B. Y. Kim, J. N. Blake, H. E. Engan, and H. J. Shaw, *Opt. Lett.* **11**, 389 (1986).
13. H. S. Park, K. Y. Song, S. H. Yun, and B. Y. Kim, *J. Lightwave Technol.* **20**, 1864 (2002).
14. T. A. Birks and Y. W. Li, *J. Lightwave Technol.* **10**, 432 (1992).
15. W. D. Zhang, F. Gao, F. Bo, Q. Wu, G. Q. Zhang, and J. J. Xu, *Opt. Lett.* **36**, 271 (2011).
16. H. Li, T. Liu, C. Y. Wen, Y. C. Soh, and Y. Zhang, *Opt. Eng.* **42**, 3409 (2003).
17. K. S. Chiang, F. Y. M. Chan, and M. N. Ng, *J. Lightwave Technol.* **22**, 1358 (2004).

Photorefraction of molybdenum-doped lithium niobate crystals

Tian Tian,¹ Yongfa Kong,^{2,3} Shiguo Liu,¹ Wei Li,² Li Wu,¹ Shaolin Chen,² and Jingjun Xu^{1,2,4}

¹School of Physics, Nankai University, Tianjin 300071, China

²MOE Key Laboratory of Weak-Light Nonlinear Photonics and TEDA Applied Physics School, Nankai University, Tianjin 300457, China

³e-mail: kongyf@nankai.edu.cn

⁴e-mail: jjxu@nankai.edu.cn

Received April 9, 2012; revised May 3, 2012; accepted May 4, 2012;

posted May 7, 2012 (Doc. ID 166324); published June 26, 2012

Molybdenum-doped lithium niobate crystals were grown under different polarization conditions and their holographic properties were investigated. In contrast to current dopants, hexavalent molybdenum prefers niobium sites. Thereby, holographic storage becomes possible from the ultraviolet to the visible with considerably lower response time. The response time of 0.5 mol. % Mo-doped LiNbO₃ can be especially shortened to as small as 0.35 s with a still high saturation diffraction efficiency of about 60% at 351 nm. Molybdenum-doped lithium niobate thus is a promising candidate for all-color holographic storage applications. © 2012 Optical Society of America

OCIS codes: 160.3730, 210.2860, 190.5330.

Lithium niobate (LiNbO₃, or LN) is one of the most used synthetic crystals at present. This is because the compound presents a very interesting combination of properties and characteristics that make it possible to tailor its behavior for useful devices [1]. Holographic data storage promises to be the next generation storage technology [2–4]. Despite many efforts, it is not yet mature enough for commercial application because the ideal material is lacking [5]. Although the mainstream research material, iron-doped LiNbO₃ (LN:Fe), performs well in some respects, it still is too slow and volatile, to mention just two deficiencies. Even if LiNbO₃ is doped with iron and manganese (LN:Fe, Mn), which solves the volatility problem [6], the material still responds very slowly.

Substituting ions of the pure crystal by dopants is the essence of the silicon technology that has been so successful [7], and the same is true for its LiNbO₃ counterpart. For example, waveguides (regions of increased refractive index) can be fabricated by titanium in-diffusion or by proton exchange [8]. Photorefractive properties (change of refractive index upon illumination) can be improved by doping with Fe^{3+/2+}, Mn^{3+/2+}, Cu^{2+/+}, or Ce^{3+/2+} [9,10]. The resistance to optical damage (unwanted refractive index changes upon illumination) may be enhanced by doping with Mg²⁺, Zn²⁺, In³⁺, Hf⁴⁺, or Zr⁴⁺ [11–15]. The problems of LiNbO₃ for real applications may be tracked down to insufficient control of defects. A systematic analysis of the effects of currently used dopants reveals that their valences are all below 5+, the valence of Nb. Therefore, they preferably occupy Li sites. This gives rise to the thought that, if LiNbO₃ is doped with ions of valence 6+ or more, these ions may occupy Nb sites and thereby induce new effects. Here, we report on the photorefractive properties of LiNbO₃ doped with the hexavalent molybdenum ion Mo⁶⁺ (LN:Mo).

A series of LN:Mo crystals, which were grown along the *c*-axis by the conventional Czochralski technique, were used in this investigation. The [Li]/[Nb] composition was chosen as 48.38/51.62. The doping concentration of MoO₃ is 0.1, 0.3, 0.5, 1.0, and 2.0 mol. %, labeled as LN:Mo0.1, LN:Mo0.3, LN:Mo0.5, LN:Mo1.0, and LN:Mo2.0, respectively. The as-grown crystals were annealed at

1150 °C for 10 h in room atmosphere and artificially poled under an electric current of 70 mA for 15 min at 1170 °C. The polarization conditions proved to influence the crystal's color, so we selected various electric currents for LN:Mo0.5. Finally, 3.0 mm and 1.0 mm thick *y*-oriented plates were cut and polished to optical grade.

The holographic properties of LN:Mo crystals in UV-visible range were investigated by two-wave mixing in transmission geometry. Four wavelengths were chosen for the measurement, namely, 351, 488, 532, and 671 nm from an Ar⁺ laser and cw frequency-doubled solid-state lasers, respectively. The extraordinarily polarized laser was split into two beams of equal intensity (intensity per beam 320, 400, 400, and 3000 mW/cm², respectively). Two mutually coherent beams irradiated these 3.0 mm thick plates with a crossing angle of 30 deg. The grating vector was aligned along the *c*-axis to exploit the largest electro-optic coefficient *r*₃₃. The measured diffraction efficiency is defined as $\eta = I_d / (I_d + I_t)$, where *I*_{*d*} and *I*_{*t*} are the diffracted and transmitted intensity of the readout beam, respectively. The photorefractive response time constant τ_r and the saturation diffraction efficiency η_s are described by the function of $\eta(t) = \eta_s [1 - \exp(-t/\tau_r)]^2$.

The optical absorption spectra of LN:Mo crystals were measured at room temperature by a Beckman DU-8B spectrophotometer with light transmitting through 1.0 mm thick *y*-plates. We obtained the absorption change by subtracting the measured light absorption of CLN from that of LN:Mo, within the wavelength range from 300 to 800 nm. The X-ray single crystal diffraction analysis was performed with a Bruker SMART APEX CCD area-detector diffractometer at room temperature. X-ray photoelectron spectroscopy (XPS) was recorded using a Kratos Axis Ultra DLD spectrometer.

The photorefractive properties of LN:Mo samples are shown in Fig. 1. For comparison, nominally pure congruent LiNbO₃ (CLN) and 0.03 wt. % Fe₂O₃-doped LN (LN:Fe0.03) were also measured. Due to strong absorption, the holographic storage of LN:Fe0.03 at 351 nm was not measured. We can see that holographic gratings were established for all LN:Mo crystals from UV to the visible.

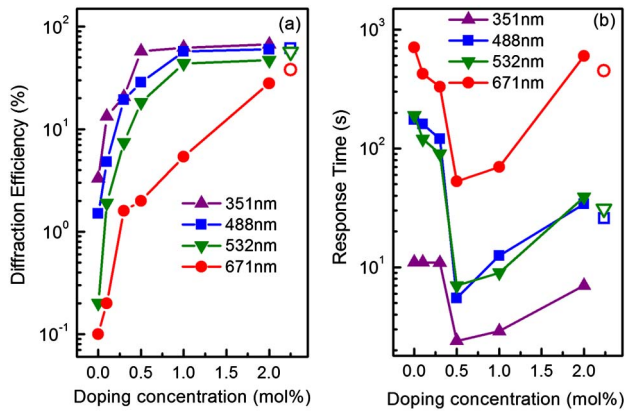


Fig. 1. (Color online) Photorefractive characteristics of LN:Mo crystals from UV to the visible. The light intensity is 320, 400, 400, and 3000 mW/cm² for 351, 488, 532, and 671 nm lasers, respectively. The hollow symbols are for LN:Fe0.03.

The diffraction efficiency increases, while the response time shortens, when the light wavelength varies from 671 to 351 nm. When the doping concentration of Mo increases, the diffraction efficiency increases, while the response time decreases at first, reaches the minimum value at 0.5 mol.%, and then increases. These results indicate that 0.5 mol.% Mo is the optimized doping concentration.

We found that the color of LN:Mo crystals varies with the polarization conditions, so different electric current was selected for LN:Mo0.5. The relationships between the photorefractive properties of LN:Mo0.5 and polarization currents are shown in Fig. 2. We can see that the influence of polarization current on the diffractive efficiency is not large; it increases slightly at 351 nm, gradually increases at 488 and 532 nm; and decreases at first, reaches minimum value at 125 mA, and then increases at 145 mA for a 671 nm laser. But the response time decreases with increasing polarization current and reached minimum value at 145 mA; it is 0.35, 5.5, 3.0, and 2.0 s at 351, 488, 532, and 671 nm, respectively. This is about one to three orders of magnitude shorter as compared with

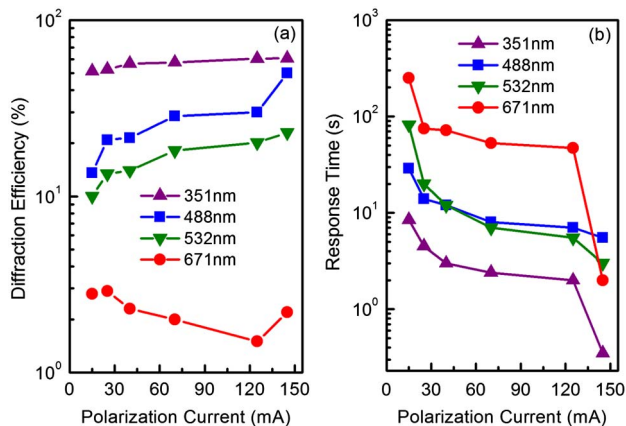


Fig. 2. (Color online) UV-visible photorefractive characteristics of LN:Mo0.5 crystals polarized under various polarization currents for 15 min. The light intensity per beam is 320, 400, 400, and 3000 mW/cm² for 351, 488, 532, and 671 nm lasers, respectively.

as-grown CLN or LN:Fe 0.03. In particular, at 351 nm, the response time of 0.35 s is very small without impairing the diffraction efficiency of 60.7%. As we know, UV holographic storage in LN:Fe is nearly impossible due to strong absorption.

Then the origin of the fast response of LN:Mo crystals in the UV to visible range was investigated. As we know from other LN dopants, a defect ion has a unique energy level within the bandgap. It can serve as a photorefractive center if the ion may change its valance upon illumination, such as Fe^{3+/2+}, Mn^{3+/2+}, Cu^{2+/+}, or Ce^{3+/2+} [9,10]. However, the light's wavelength must fit the energy difference to the conduction or valance band. Although the energy level of a localized defect ion is not sharp, a one-center model cannot explain the large range of photorefractive sensitivity from UV to the visible.

Thus, the nature of the photorefractive center has to be clarified. We investigated the light erasing behavior of photorefractive gratings in the LN:Mo crystals. As expected, fitting the data by a single exponential function $\eta = \eta_0 \exp(-t/\tau_0)$ resulted in a large deviation, while a sum of two exponentials $\eta = \eta_1 \exp(-t/\tau_1) + \eta_2 \exp(-t/\tau_2)$, where $\eta_{0,1,2}$ is the amplitude and $\tau_{0,1,2}$ is time constant, respectively, reproduced the measured values quite well. This implies that at least two kinds of photorefractive centers are involved.

The valence of Mo ions in LN:Mo was determined by XPS. Six peaks can be distinguished when analyzing the intensity versus energy curve, as shown in Fig. 3. According to previous research [16,17] these peaks allow us to identify the valence of the Mo ions as 4+, 5+, and 6+, respectively. The crystal structure of LN:Mo was checked by X-ray single crystal diffraction analysis. The results show that the normal structure of LN remained intact. Mo⁶⁺ ions push regular Nb⁵⁺ to Li sites, forming new defects of Mo_{Nb}⁺ and a larger amount of anti-site Nb⁵⁺.

Figures 4(a) and 4(b) show the absorption difference between LN:Mo and CLN. A pronounced absorption peak in the UV region and a wide absorption region from 400 to 800 nm was observed for LN:Mo. The wide range of the continuous absorption spectrum means that charge carriers can be excited from different energy levels at various wavelengths. This is essential for all-color holographic storage. Figure 4(b) indicates that increasing

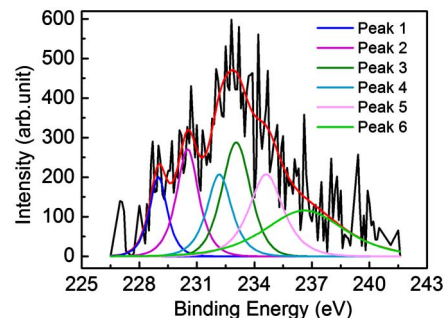


Fig. 3. (Color online) XPS spectra of LN:Mo. The experimental curve can be fitted to six peaks by the XPS Peaks software. These peaks could be divided into three groups: peaks 1 and 4, peaks 2 and 5, and peaks 3 and 6, corresponding to Mo ions as 4+, 5+, and 6+, respectively.

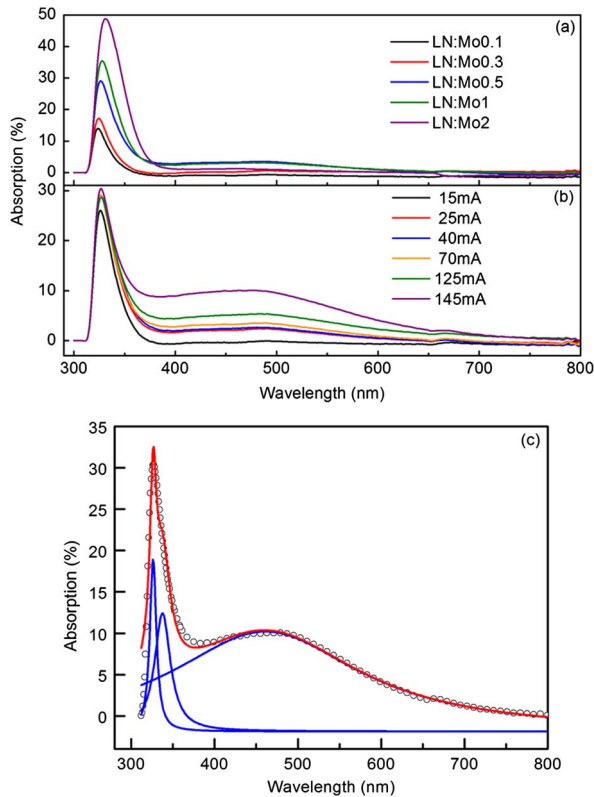


Fig. 4. (Color online) Absorption difference of LN:Mo relative to CLN: (a) LN:Mo with various doping concentration; (b) sample LN:Mo0.5 polarized under various current for 15 min; and (c) The fitting curve of LN:Mo0.5 polarized under 145 mA for 15 min, where the circles represent experimental data and the solid lines are fitting curves, the fitting peaks centered at about 326, 337, and 461 nm, respectively.

polarization current also has the effect of reduction. A fit of the absorption spectrum to a sum of Lorentz functions revealed three peaks centered at about 326, 337, and 461 nm, as shown in Fig. 4(c). The oscillation around 660 nm may come from the change of detector in the spectrometer.

According to the broadly accepted Li-vacancy model, the main intrinsic defects of CLN are Li vacancies (V_{Li}^-) and anti-site Nb^{5+} (Nb_{Li}^{4+}). The UV photorefraction of CLN is related to $O^{2-/-}$ near V_{Li}^- ($O^{2-/-} - V_{Li}^-$), and $O^{2-/-} - V_{Li}^-$, $O^{2-/-} - Mg_{Nb}^{3-}$, and $O^{2-/-} - Zr_{Nb}^-$ are the UV photorefractive centers in LN:Mg and LN:Zr [18,19]. Thus, it is reasonable to assume that $O^{2-/-}$ ions close to V_{Li}^- and Mo_{Nb}^+ ($O^{2-/-} - Mo_{Nb}^+$) are the UV photorefractive centers in LN:Mo as well. The UV absorption edge of CLN has been attributed to the presence of Li vacancies; actually of $O^{2-/-} - V_{Li}^-$ ions, in the vicinity of V_{Li}^- [20]. Because the UV peak at 326 nm is close by the ultraviolet absorption edge of CLN, it should be correlated with the $O^{2-/-} - V_{Li}^-$ defect, while the 337 nm peak corresponds to $O^{2-/-} - Mo_{Nb}^+$. It is well known that small polarons (an electron trapped at Nb_{Li}^{4+}) together with bipolarons (a pair of electrons trapped at adjacent Nb_{Li}^{4+} and Nb_{Nb}^{5+}) play the role of photorefractive centers in CLN [21,22].

The energy levels of the bipolaron and the small polaron are approximately 2.5 eV and 1.6 eV, corresponding to the absorption bands at 490 and 780 nm, respectively. Since the latter can be observed only at temperatures below 80 K [23], the absorption band at 470 nm could be attributed to bipolarons.

In summary, hexavalent molybdenum-doped lithium niobate crystals were grown under different polarization conditions and characterized. LN:Mo allows for holographic storage from UV to the visible with excellent properties. The response time can be shortened to as small as 0.35 s with a still-high saturation diffraction efficiency of about 60% at 351 nm. These features can be attributed to Mo^{6+} ions occupying regular Nb sites. This novel defect cannot be created by other dopants currently in use. Our results make LN:Mo an excellent candidate for all-color holographic data storage.

This work was financially supported by the Chinese National Key Basic Research Special Fund (No. 2011 CB922003), the International S&T Cooperation Program of China (2011DFA52870), and the Fundamental Research Funds for the Central Universities (65030091 and 65010961). The authors thank Prof. Peter Hertel (Osnabrück University) for useful discussions.

References

1. L. Arizmendi, *Phys. Status Solidi A* **201**, 253 (2004).
2. D. Psaltis and F. Mok, *Sci. Am.* **273**, 70 (1995).
3. M. Haw, *Nature* **422**, 556 (2003).
4. L. Dhar, *Nat. Photon.* **2**, 403 (2008).
5. A. Hellemaans, *Science* **286**, 1502 (1999).
6. K. Buse, A. Adibi, and D. Psaltis, *Nature* **393**, 665 (1998).
7. H. J. Queisser and E. E. Haller, *Science* **281**, 945 (1998).
8. D. Kip, *Appl. Phys. B* **67**, 131 (1998).
9. W. Phillips, J. J. Amodei, and D. L. Staebler, *RCA Rev.* **33**, 94 (1972).
10. D. K. McMillen, T. D. Hudson, J. Wagner, and J. Singleton, *Opt. Express* **2**, 491 (1998).
11. G. Zhong, J. Jian, and Z. Wu, *J. Opt. Soc. Am.* **70**, 631 (1980).
12. T. R. Volk, V. J. Pryalkin, and M. M. Rubiniina, *Opt. Lett.* **15**, 996 (1990).
13. Y. Kong, J. Wen, and H. Wang, *Appl. Phys. Lett.* **66**, 280 (1995).
14. E. P. Kokanyan, L. Razzari, I. Cristiani, V. Degiorgio, and J. B. Gruber, *Appl. Phys. Lett.* **84**, 1880 (2004).
15. Y. Kong, S. Liu, Y. Zhao, H. Liu, S. Chen, X. Zhang, R. Rupp, and J. Xu, *Appl. Phys. Lett.* **91**, 081908 (2007).
16. J. E. Devries, H. C. Yao, R. J. Baird, and H. S. Gandhi, *J. Catal.* **84**, 8 (1983).
17. S. O. Grim and L. J. Matienzo, *Inorg. Chem.* **14**, 1014 (1975).
18. F. Liu, Y. Kong, W. Li, H. Liu, S. Liu, Y. Zhao, H. Liu, S. Chen, and J. Xu, *Opt. Lett.* **35**, 10 (2010).
19. P. Herth, T. Granzow, D. Schaniel, T. Woike, M. Imlau, and E. Krätzig, *Phys. Rev. Lett.* **95**, 067404 (2005).
20. X. Li, Y. Kong, H. Liu, L. Sun, J. Xu, S. Chen, L. Zhang, Z. Huang, S. Liu, and G. Zhang, *Solid State Commun.* **141**, 113 (2007).
21. F. Schirmer, M. Imlau, C. Merschjann, and B. Schoke, *J. Phys. Condens. Matter* **21**, 123201 (2009).
22. L. Hesselink, S. S. Orlov, A. Liu, A. Akella, D. Lande, and R. R. Neurgaonkar, *Science* **282**, 1089 (1998).
23. J. L. Ketchum, K. L. Sweeney, L. E. Halliburton, and A. F. Armington, *Phys. Lett. A* **94**, 450 (1983).

Young's two-slit interference of vector light fields

Yongnan Li,¹ Xi-Lin Wang,¹ Hu Zhao,¹ Ling-Jun Kong,¹ Kai Lou,¹ Bing Gu,¹ Chenghou Tu,¹ and Hui-Tian Wang^{1,2,*}

¹*School of Physics and MOE Key Laboratory of Weak Light Nonlinear Photonics, Nankai University, Tianjin 300071, China*

²*National Laboratory of Solid State Microstructures, Nanjing University, Nanjing 210093, China*

*Corresponding author: htwang@nju.edu.cn

Received January 25, 2012; accepted March 3, 2012;

posted March 8, 2012 (Doc. ID 162134); published May 16, 2012

We explore the peculiar interference behaviors of the vector fields in the Young's two-slit configuration. The interference patterns have a chessboard structure in the middle region and depend on the topological charge and the initial phase of the input vector field. The results have potential applications such as characterizing the topological properties of the arbitrary vector fields. © 2012 Optical Society of America

OCIS codes: 260.0260, 260.3160, 260.5430, 260.6042.

One of the salient features of light is coherence, which describes all properties of the correlation among physical quantities of light. Recently, the interference of the light fields with spatial phase distribution has given rise to a number of effects. For instance, the optical vortices result in the effects of diffraction in the single slit [1] and interference in the double slit [2] due to the presence of orbital angular momentum (OAM). A multi-pinhole interferometer was proposed to probe the OAM of optical vortices [3,4]. In particular, the OAM can be used to unveil the lattice properties hidden in diffraction patterns using a simple triangular aperture [5].

Recently, manipulating the states of polarization (SoPs) has become a subject of rapidly growing interest [6]. The polarization as an additional freedom can be used to control light field, such as creation of the vector fields [7,8], which have spatially inhomogeneous SoPs. The radially polarized field can be tightly focused into a spot beyond the diffraction limit and with the strong longitudinal field [9]. The azimuthally polarized fields can be highly focused into a dark hollow doughnut [10]. The vector fields have resulted in many unexpected effects and applications, such as nonlinear optics [11,12], quantum information [13,14], near-field optics [15], optical trapping [16,17], and imaging [18].

Here we explore theoretically and experimentally the two-slit interference of the vector light fields. The fringe structure carries the information of the polarization distribution and then unveils the vector characteristics of the light fields. As a result, the two-slit interference can serve as an alternative way of measuring the topological charge of the polarization distribution of the vector fields.

The azimuthal-variant local linearly polarized vector field can be expressed in the xy plane as [8]

$$\mathbf{E}(x, y) = E_{\hat{x}}(x, y)\hat{x} + E_{\hat{y}}(x, y)\hat{y}, \quad (1)$$

with $E_{\hat{x}}(x, y) = \cos(\ell\varphi + \varphi_0)$ and $E_{\hat{y}}(x, y) = \sin(\ell\varphi + \varphi_0)$, where $\varphi = \arctan(y/x)$. \hat{x} and \hat{y} are the unit vectors in the $+x$ and $+y$ directions, respectively. The integer ℓ is the topological charge in the azimuthal direction φ and the initial phase φ_0 (with a value range of $\varphi_0 \in [-\pi, \pi]$) determines the direction of polarization in the $+x$ direction. The local linearly polarized vector field described by

Eq. (1) has a singularity caused by the polarization uncertainty located at the origin of the (x, y, z) system.

Different from the scalar fields with the homogeneous distribution of SoPs, the Young's two-slit interference of vector field should exhibit some novel effects, due to the inhomogeneous distribution of SoPs. A monochromatic vector field described by Eq. (1) falls on the two slits A and B, which are placed in the xy plane, equidistant from the origin and parallel to the y direction. The vector fields transmitted through two slits act as two secondary *line* sources and then the light fields from them are superposed on the observation screen parallel to the xy plane. Let b be the separation of the slits, a the slit width, and d the distance of the observation screen from the xy plane. Suppose the slit width a is narrow enough, the slit length is infinite, and the separation b is small enough compared to d . Thus, inside the two slits the light polarization can be considered to be homogeneous in the x direction while it is still space-varying in the y direction.

The local linearly polarized vector field can be decomposed into two orthogonal x - and y -polarized components, which can be independently treated. The x and y components transmitted through the two slits A and B depend only on y independent of x

$$E_{\hat{x}}^{A(B)}(y) = \cos[\ell\varphi_{A(B)} + \varphi_0], \quad (2)$$

$$E_{\hat{y}}^{A(B)}(y) = \sin[\ell\varphi_{A(B)} + \varphi_0], \quad (3)$$

where $\varphi_A = \arctan(-2y/b)$, $\varphi_B = \arctan(2y/b)$, and $\varphi_A = -\varphi_B$. For the x and y components, the interference intensity distributions are written as

$$I_{\hat{x}}(x, y) \propto 1 + \cos(2\ell\varphi_B) \cos(2\varphi_0) + [\cos(2\ell\varphi_B) + \cos(2\varphi_0)] \cos \phi, \quad (4a)$$

$$I_{\hat{y}}(x, y) \propto 1 - \cos(2\ell\varphi_B) \cos(2\varphi_0) + [\cos(2\ell\varphi_B) - \cos(2\varphi_0)] \cos \phi, \quad (4b)$$

where $\phi = 2\pi bx/\lambda d$ and the terms including $\cos \phi$ indicate the interference effect. Hence the distribution of the total intensity is

$$I(x, y) = I_x(x, y) + I_y(x, y) \propto 1 + \cos(2\ell\varphi_B) \cos \phi. \quad (5)$$

A factor $\cos(2\ell\varphi_B)$ in Eqs. (4) and (5) and a factor $\cos(2\varphi_0)$ in Eq. (4) are from the contribution of the vector field; that is to say, they embody the intrinsic feature of the two-slit interference of the vector field.

We now explore experimentally the Young's two-slit interference of the vector field. A He-Ne laser at $\lambda = 632.8$ nm as a light source is used to create the vector fields described by Eq. (1), by the method in [8]. The created vector field falls normally on the two slits with $a \sim 0.2$ mm and $b \sim 0.8$ mm. A CCD with a distance $d \sim 500$ mm from the slits is used to acquire the interference patterns. A polarizer can be inserted between the slits and CCD and then to acquire the interference patterns of the x and y components.

Figure 1 shows the measured interference patterns of four $\ell = 1$ vector fields with $\varphi_0 = 0, \pi/4, \pi/2$ and $3\pi/4$. Figures 2 and 3 show the situations of two vector fields with ($\ell = 2, \varphi_0 = 0$) and ($\ell = 3, \varphi_0 = 0$), respectively.

As shown in Figs. 1–3, differently from the well-known Young's two-slit interference of the scalar light field, the interference patterns of the vector light fields exhibit the spatial structure in the y (slits) direction besides in the x direction. The interference pattern of the total field depends only on ℓ independent of φ_0 . In contrast, the interference patterns of the x and y components depend on both ℓ and φ_0 , in particular, the shift between the interference fringes of the x and y components, depending on φ_0 . The behavior of the Young's two-slit interference of the vector light fields can be understood as follows.

We find from Eqs. (4) and (5) that the interference fringes described by $I_x(x, y)$, $I_y(x, y)$, and $I(x, y)$ have

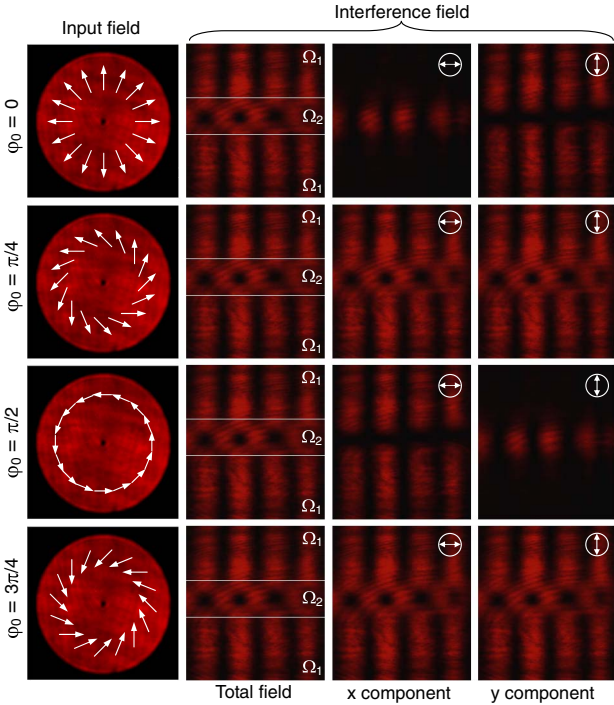


Fig. 1. (Color online) Patterns of the Young's two-slit interference of the $\ell = 1$ vector fields with $\varphi_0 = 0, \pi/4, \pi/2$ and $3\pi/4$. The left column gives the SoP distributions of the corresponding input vector fields.

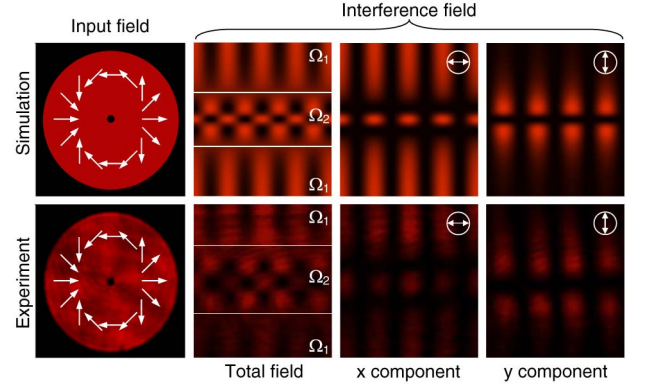


Fig. 2. (Color online) Patterns of the Young's two-slit interference of the vector field with ($\ell = 2, \varphi_0 = 0$). The left column shows the SoP distributions of the input vector fields.

the same period of $\Lambda = \lambda d/b$ in the x direction perpendicular to the slits. The interference fringe of $I(x, y)$ is independent of the initial phase φ_0 . Comparing Eq. (4a) with Eq. (4b), we can find $I_x(x, y)|_{\varphi_0=\pm\pi/2} = I_y(x, y)|_{\varphi_0=0, \pm\pi}$ and $I_y(x, y)|_{\varphi_0=\pm\pi/2} = I_x(x, y)|_{\varphi_0=0, \pm\pi}$, implying that the interference fringes of the x and y components have a shift of a half of fringe period ($\Lambda/2$) when $\varphi_0 = 0, \pm\pi/2$ and $\pm\pi$. When $\varphi_0 = \pm\pi/4$ or $\pm 3\pi/4$, however, we have $I_x(x, y)|_{\varphi_0=\pm\pi/4, \pm 3\pi/4} = I_y(x, y)|_{\varphi_0=\pm\pi/4, \pm 3\pi/4}$, suggesting that the interference fringes described by $I_x(x, y)$ and $I_y(x, y)$ are completely identical, so that the interference fringe of $I(x, y)$ has the same pattern as that of the x or y component. Except for $\varphi_0 = 0$ (or $\pm\pi$), $\pm\pi/4$ (or $\pm 3\pi/4$) and $\pm\pi/2$, the shift between the interference fringes of the x and y components is between 0 and $\Lambda/2$.

The interference pattern can be separated into two kinds of regions in the y direction, by the boundaries of $y = \pm b/2 \tan(\pi/4\ell)$, where the total intensity is independent of x and is a half of the maximum intensity. The first region is within a range of $|y| > b/2 \tan(\pi/4\ell)$, referred to as the region Ω_1 , as shown in Figs. 1–3, away from the centerline $y = 0$. The second one belongs to the region of $-b/2 \tan(\pi/4\ell) < y < b/2 \tan(\pi/4\ell)$, referred to as the region Ω_2 , in the immediate vicinity of the centerline $y = 0$.

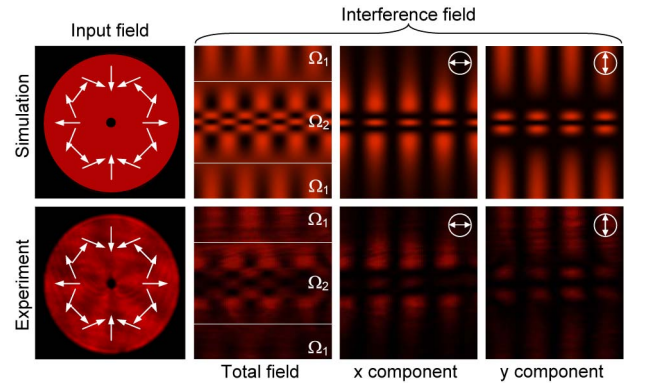


Fig. 3. (Color online) Patterns of the Young's two-slit interference of the vector field with ($\ell = 3, \varphi_0 = 0$). The left column shows the SoP distributions of the input vector fields.

In region Ω_1 , we can consider $y \rightarrow \pm\infty$ ($\varphi_B \rightarrow \pm\pi/2$). So Eqs. (4) and (5) can be simplified as $I_x^{\Omega_1}(x) \propto 1 + \cos(\ell\pi) \cos(2\varphi_0) + [\cos(\ell\pi) + \cos(2\varphi_0)] \cos\phi$, $I_y^{\Omega_1}(x) \propto 1 - \cos(\ell\pi) \cos(2\varphi_0) + [\cos(\ell\pi) - \cos(2\varphi_0)] \cos\phi$, and $I^{\Omega_1}(x) = 1 + \cos(\ell\pi) \cos\phi$, respectively. When $2\varphi_0$ and $\ell\pi$ have the opposite phase, $I_x^{\Omega_1}(x) \equiv 0$. In contrast, the interference fringe of the y -polarized component is similar to that of the well-known two-slit interference, and the interference fringe for an odd ℓ has a shift of a half of fringe period with respect to that for an even ℓ . If $2\varphi_0$ and $\ell\pi$ are in phase, the interference behaviors are opposite to the above situation. If $\varphi_0 = \pm\pi/4$ and $\pm 3\pi/4$, the interference fringes of the x - and y -polarized components have no difference for any integer ℓ . The interference fringe of the total field is independent of φ_0 , but the interference fringes between the odd ℓ and the even ℓ have a relative shift of $\Lambda/2$.

More interestingly, interference behavior is in the region Ω_2 . The intensity is modulated by both x and y , unlike in the region Ω_1 . For the x or y component, the field intensity (bright or dark) at the origin of $(x, y) = (0, 0)$ is determined by φ_0 only independent of ℓ . For instance, when $\varphi_0 = \pm\pi/2$ ($\varphi_0 = 0$ or π), the x - and y -polarized intensities at the origin are the minimum and the maximum (the maximum and the minimum), respectively. In contrast, when $\varphi_0 = \pm\pi/4$ or $\pm 3\pi/4$, the x - and y -polarized intensities at the origin are both the maximum. Based on this, we can determine the initial phase φ_0 of the input vector fields. The total intensity is always the maximum at the origin, that is to say, the origin is always bright for any ℓ and φ_0 . When $\cos\phi = 1$ (i.e., $2\pi bx/\lambda d = 2m\pi$, where m is an integer), the total intensity exhibits the maximum for $2\ell\varphi_B = 2m\pi$ while the minimum for $2\ell\varphi_B = (2m + 1)\pi$. If $\cos\phi = -1$ (i.e., $2\pi bx/\lambda d = 2m\pi \pm \pi$), the total intensity is the minimum for $2\ell\varphi_B = 2m\pi$ while the maximum for $2\ell\varphi_B = (2m + 1)\pi$. In the region Ω_2 , therefore, the interference pattern exhibits a chessboard structure; in particular, the total number of the bright and dark regions is equal to $2\ell - 1$ in the $x = m\Lambda$ or $x = (m \pm 1/2)\Lambda$ lines. Based on this, we can determine the topological charge ℓ of the input vector field.

In summary, we investigate the peculiar behaviors of the two-slit interference of the vector fields. The results reveal that the interference pattern of the total intensity is allowed to determine the topological charge of the input vector field, while the interference patterns of the x

and y components can be used to determine the initial phase of the input vector field. This method should also be effective for characterizing the topological properties of the complex vector fields, for example, the vector fields with hybrid SoPs [19] and the vector vortex fields with the higher-order SoPs [20].

This work is supported by the National Basic Research Program (973 Program) of China under Grant No. 2012CB921900, and the National Natural Science Foundation of China (NSFC) under grant 10934003.

References

1. D. P. Ghai, P. Senthilkumaran, and R. S. Sirohi, *Opt. Lasers Eng.* **47**, 123 (2009).
2. H. I. Sztul and R. R. Alfano, *Opt. Lett.* **31**, 999 (2006).
3. C. S. Guo, S. J. Yue, and G. X. Wei, *Appl. Phys. Lett.* **94**, 231104 (2009).
4. G. C. G. Berkhout and M. W. Beijersbergen, *Phys. Rev. Lett.* **101**, 100801 (2008).
5. J. M. Hickmann, E. J. S. Fonseca, W. C. Soares, and S. Chávez-Cerda, *Phys. Rev. Lett.* **105**, 053904 (2010).
6. Q. Zhan, *Adv. Opt. Photon.* **1**, 1 (2009).
7. C. Maurer, A. Jesacher, S. Furhapter, S. Bernet, and M. Ritsch-Marte, *New J. Phys.* **9**, 78 (2007).
8. X. L. Wang, J. P. Ding, W. J. Ni, C. S. Guo, and H. T. Wang, *Opt. Lett.* **32**, 3549 (2007).
9. R. Dorn, S. Quabis, and G. Leuchs, *Phys. Rev. Lett.* **91**, 233901 (2003).
10. S. Sato and Y. Kozawa, *J. Opt. Soc. Am. A* **26**, 142 (2009).
11. S. Sato and Y. Kozawa, *Opt. Lett.* **34**, 3166 (2009).
12. A. A. Ishaaya, L. T. Vuong, T. D. Grow, and A. L. Gaeta, *Opt. Lett.* **33**, 13 (2008).
13. C. Gabriel, A. Aiello, W. Zhong, T. G. Euser, N. Y. Joly, P. Banzer, M. Förtsch, D. Elser, U. L. Andersen, Ch. Marquardt, P. St. J. Russell, and G. Leuchs, *Phys. Rev. Lett.* **106**, 060502 (2011).
14. J. T. Barreiro, T. C. Wei, and P. G. Kwiat, *Phys. Rev. Lett.* **105**, 030407 (2010).
15. W. Chen and Q. Zhan, *Opt. Lett.* **34**, 722 (2009).
16. Y. Q. Zhao, J. S. Edgar, G. D. M. Jeffries, D. McGloin, and D. T. Chiu, *Phys. Rev. Lett.* **99**, 073901 (2007).
17. X. L. Wang, J. Chen, Y. N. Li, J. P. Ding, C. S. Guo, and H. T. Wang, *Phys. Rev. Lett.* **105**, 253602 (2010).
18. F. Lu, W. Zheng, and Z. Huang, *Opt. Lett.* **34**, 1870 (2009).
19. X. L. Wang, Y. N. Li, J. Chen, C. S. Guo, J. P. Ding, and H. T. Wang, *Opt. Express* **18**, 10786 (2010).
20. G. Milione, H. I. Sztul, D. A. Nolan, and R. R. Alfano, *Phys. Rev. Lett.* **107**, 053601 (2011).



Taming the Collapse of Optical Fields

Si-Min Li¹, Yongnan Li¹, Xi-Lin Wang¹, Ling-Jun Kong¹, Kai Lou¹, Chenghou Tu¹, Yongjun Tian³
& Hui-Tian Wang^{1,2}

SUBJECT AREAS:

NONLINEAR OPTICS
OPTICAL MANIPULATION AND
TWEEZERS
APPLIED PHYSICS
ULTRAFAST LASERS

Received
27 September 2012

Accepted
20 November 2012

Published
20 December 2012

Correspondence and
requests for materials
should be addressed to
H.T.W. (htwang@nju.
edu.cn; htwang@
nankai.edu.cn)

¹MOE Key Laboratory of Weak Light Nonlinear Photonics and School of Physics, Nankai University, Tianjin 300071, China, ²National Laboratory of Solid State Microstructures, Nanjing University, Nanjing 210093, China, ³State Key Laboratory of Metastable Materials Science and Technology, Yanshan University, Qinhuangdao 066004, China.

Field collapse, which occurs in various nonlinear systems, has attracted much attention, owing to its universality, complexity, and applicability. A great challenge and expectation is to achieve the controllable and designable collapsing pattern. Here we predict theoretically and demonstrate experimentally the novel collapsing behaviors of the vector optical fields in a self-focusing Kerr medium. Surprisingly, the results reveal that the collapse of the vector optical field is controllable and designable by engineering the distribution of hybrid states of polarization, and has the robust feature insensitive to the random noise. Our idea has its significance which it opens a new window for manipulating the optical field and the different kinds of field, and then facilitates to push the related researches.

Optical field will undergo collapse at the input power above a certain critical power when an intense laser field propagates in a transparent self-focusing medium^{1–5}. The high intensity as the collapse exacerbates will induce other nonlinear effects, such as multiphoton and saturable absorptions, to counterbalance self-focusing, resulting ultimately in filamentation^{3–12}. Filamentation is an interesting and important topic due to its underlying physics and practical implication in many branches of physics^{13–18}. A great challenge and expectation is to tame the randomness and then to realize the controllable and even designable filamentation. For this purpose, several methods have been proposed such as, controlling the input power and divergence angle¹⁹, shaping the field profile^{20,21}, using amplitude/phase mask^{22–25}, and introducing spatial regularization²⁶.

Polarization, as an intrinsic and fundamental vectorial nature of light, plays an indispensable role in the interaction of light with matter. Trisorio and Hauri²⁷ demonstrated the spatial control on two filaments using circularly polarized femtosecond laser pulses. Fibich and Ilan^{3,28} presented a theoretical prediction that under the *nonparaxial* condition solely, the vectorial (polarization) effect of the homogeneously linearly-polarized field can lead to two filaments. However, polarization and its diversity of spatial distribution are not yet utilized fully. For the field collapse and the multiple filamentation, besides the self-focusing effect which is a requirement for the propagation medium, a prerequisite is that the optical field should be axial-symmetry breaking in and of itself. Therefore, to achieve the active control for the field collapse and the multiple filamentation, the key points are that the axial-symmetry breaking must be controllable and even designable, and the randomness must be effectively suppressed simultaneously. A question is raised that whether the state of polarization (SoP) of light, as a degree of freedom, can be used to break the axial symmetry of optical field and to then availably control the field collapse and multiple filamentation. Vector optical fields with spatially inhomogeneous SoP distribution^{29,30} provide indeed such an opportunity and possibility, due to the designability and diversity of SoP distribution.

Results

In this paper, we present an idea that the axial-symmetry breaking of optical field by engineering the azimuthally-variant SoP distribution controls the collapsing filamentation. We perform, to the best of our knowledge, the first study of the collapse of the vector optical fields in a self-focusing Kerr medium. The experimental results are in excellent agreement with our theoretical prediction. Some novel features are found, including the controllable, designable and robust features. The present study can contribute further to the study of collapsing filamentation in other nonlinear systems and other kinds of fields.

An important route breaking the axial symmetry of optical field is based on the *azimuthally-variant hybrid-polarized* vector field (AV-HP-VF), which is a family of vector optical field with a “top-hat-like” intensity profile excluding a central singularity caused by the polarization uncertainty³⁰. Under the weak focusing condition, the focused AV-HP-VF exhibits a uniform-intensity focal ring instead of a focal spot³⁰. Its radially variant amplitude $A(r)$ can be described by the generalized hypergeometric function; nevertheless, as a well approximation, $A(r)$ can take the form of $A(r) = a_0 r \exp(-r^2/2r_0^2)$, where r_0 is the radius of the focal ring. Inasmuch as the weak focusing



does not change the SoP distribution, the focused AV-HP-VF in a polar coordinate system (r, ϕ) can be written as

$$\mathbf{E}(r, \phi) = A(r) [\cos \delta |H\rangle + e^{-j\pi/2} \sin \delta |V\rangle], \quad (1)$$

where $\delta = m\phi + \phi_0$ (m is the topological charge and ϕ_0 is the initial phase), and $|H\rangle$ and $|V\rangle$ are two unit vectors indicating the horizontally and vertically polarized components, respectively. For the AV-HP-VF with m and ϕ_0 , the local linear polarizations are located at a series of azimuthal positions $\phi^{lin}(n) = n\pi/2m - \phi_0/m$, whereas local circular polarizations are at a series of $\phi^{cir}(n) = (2n+1)\pi/4m - \phi_0/m$ (where $n = 0, 1, \dots, 4m-1$). Differently from the optical vortex³¹, the AV-HP-VFs carry no orbital angular momentum though they also have a strictly zero field at the central singularity³². By contrast, an azimuthally-variant linearly-polarized vector field (AV-LP-VF) can be written as follows

$$\mathbf{E}(r, \phi) = A(r) [\cos \delta |H\rangle + \sin \delta |V\rangle]. \quad (2)$$

Compared Eq. (2) with Eq. (1), it can be found the unique difference that the horizontally and vertically polarized components have a phase difference of $-\pi/2$ for AV-HP-VF, while are in phase for AV-LP-VF.

To theoretically explore the nonlinear propagation behavior of a vector optical field in a Kerr medium, the $(2+1)$ -dimensional *vector-version* nonlinear Schrödinger (NLS) equation should be used. Under the slowly varying amplitude approximation, the vector-version NLS equation can be divided into a pair of coupled NLS equations for two orthogonal horizontal and vertical components

$$\frac{\partial \psi_H}{\partial \zeta} = \frac{j}{4} \nabla_{\perp}^2 \psi_H + \frac{j\alpha P}{3P_C} (3|\psi_H|^2 \psi_H + 2|\psi_V|^2 \psi_H + \psi_V^2 \psi_H^*), \quad (3a)$$

$$\frac{\partial \psi_V}{\partial \zeta} = \frac{j}{4} \nabla_{\perp}^2 \psi_V + \frac{j\alpha P}{3P_C} (3|\psi_V|^2 \psi_V + 2|\psi_H|^2 \psi_V + \psi_H^2 \psi_V^*), \quad (3b)$$

where ψ_q ($q = H, V$) is the nondimensional q -component normalized by the total field, $\psi_q(\rho, \phi; \zeta) = E_q(\rho, \phi; \zeta) / \sqrt{\iint [|E_H(\rho, \phi; \zeta)|^2 + |E_V(\rho, \phi; \zeta)|^2] \rho d\rho d\phi}$. $\rho = r/r_0$, $\zeta = z/L_d$ ($L_d = \pi r_0^2/\lambda$) are the nondimensional cylindrical coordinates. $P = 2n_0\epsilon_0 c \iint [|E_H(r, \phi; z)|^2 + |E_V(r, \phi; z)|^2] r dr d\phi$ is the power, $P_C = \alpha \lambda^2 / 4\pi n_0 n_2$ is the critical power for self-focusing, n_0 and n_2 are the linear and nonlinear refractive indices of the Kerr medium, α is a constant dependent on the initial field shape³³, c is the speed of light in vacuum, and λ is the wavelength, respectively. On the right-hand side of Eq. (3), the first term represents the contribution from the diffraction described by the transverse Laplacian $\nabla_{\perp}^2 = \partial^2/\partial \rho^2 + \frac{1}{\rho} \partial/\partial \rho + \frac{1}{\rho^2} \partial^2/\partial \phi^2$, and the second term is from the Kerr nonlinearity.

We performed a large number of simulations using Eq. (3) under $P = 10P_C$ in a self-focusing Kerr medium. When the spatial random noise is added in simulation, the random noise with a level of $\pm 10\%$ amplitude is used. The first and second rows in Fig. 1 illustrate the simulation results for the collapsing behavior of the focused AV-HP-VF (with $m = 1$ and $\phi_0 = 0$) described by Eq. (1), without and with random noise, respectively. By comparison, the third and fourth rows in Fig. 1 show the simulation results for the AV-LP-VF (with $m = 1$ and $\phi_0 = 0$) described by Eq. (2), which is the well-known radially-polarized vector field (RP-VF)²⁹, without and with random noise. Although both AV-HP-VF and RP-VF display the same focusing ring, their nonlinear propagation behaviors are quite different. Figure 2 shows the simulated collapsing patterns of the AV-HP-VFs with $m = 1$ ($\phi_0 = 0$ and $\pi/4$) and $m = 2$ ($\phi_0 = 0$ and $\pi/8$) when the spatial random noise is added. Summarizing all the simulation results performed, we can draw following conclusions. For the AV-HP-VF with the given m and ϕ_0 , (i) the azimuthally-variant hybrid

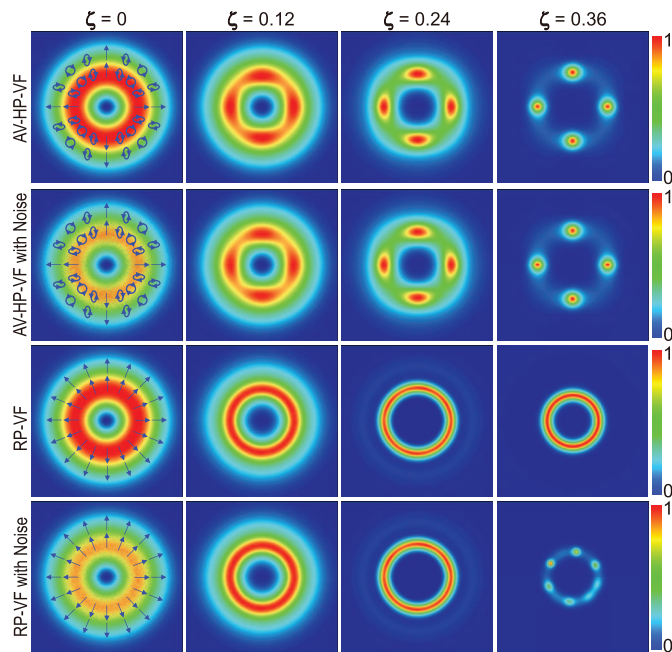


Figure 1 | Simulated nonlinear propagation behaviors of AV-HP-VF with $m = 1$ and $\phi_0 = 0$ in equation (2). The first and second rows correspond to the cases without and with random noise, respectively. For comparison, the RP-VFs without and with random noise are also shown in the third and fourth rows. The four columns (from left to right) correspond to four propagation distances ($\zeta = 0, 0.12, 0.24, 0.36$). The SoP distributions are also shown in the first column.

SoP distribution leads to the axial-symmetry breaking; (ii) the field undergoes the collapse to converge into the deterministic filaments; (iii) the number of filaments is $4m$ depending solely on m ; (iv) the filaments are always located at the azimuthal positions $\phi^{lin}(n)$, where their local SoPs are linearly polarized; (v) the collapsing pattern exhibits a $4m$ -fold rotation (C_{4m}) symmetry; and (vi) the collapsing patterns persist among simulations, with and without different random noise, implying that collapsing patterns are insensitive to noise. Meanwhile, for the AV-LP-VFs, (i) the purely ideal AV-LP-VF always remains in the axially symmetric ring, indicating that the purely ideal AV-LP-VF cannot converge to the deterministic multiple filaments; and (ii) the collapsing filaments produced by AV-LP-VF with the random noise has the uncertainty, similar with the collapses of optical vortices³¹ and polarization vortices³⁴.

To experimentally confirm our theoretical prediction and numerical simulations, all the required vector fields with different m and ϕ_0 were created by using the experimental scheme³⁰. The created AV-HP-VFs and AV-LP-VFs were weakly focused into a uniform-intensity focal ring and then incident into the CS₂ cell with a length of 10 mm, by an achromatic lens with a focal length of $f = 300$ mm. The intensity patterns of the field transmitted from the CS₂ cell are imaged on a detector (Beamview, Coherent Inc.) using an achromatic lens with a focal length of $f = 60$ mm. The experimental results of the AV-LP-VFs (not shown here) reveal that the number

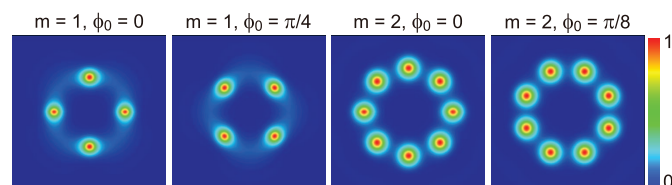


Figure 2 | Simulated collapsing patterns of AV-HP-VFs with different m and ϕ_0 at a propagation distance of $\zeta = 0.36$ with random noise.



and positions of the induced collapsing filaments have the uncertainty among the experiments, depending on the spatial random fluctuation of the input field. Any one of the measured collapsing patterns of the $m = 1$ charge AV-HP-VFs, with four different ϕ_0 ($= 0, \pi/8, \pi/4, 3\pi/8$), consists of four deterministic filaments and exhibits a fourfold rotation (C_4) symmetry (Fig. 3). The four patterns have no difference in nature, whereas their unique difference is that the patterns from Fig. 3a–d are rotated counterclockwise in sequence by an angle of $\pi/8$. Figure 4 shows the measured collapsing patterns of AV-HP-VFs (with $\phi_0 = 0$) for $m = 1, 2, 3, 4$. The m -charge AV-HP-VF produces $4m$ deterministic filaments, where $m = 1, 2, 3, 4$, with the number of filaments being 4, 8, 12, 16, respectively. The collapsing pattern exhibits a $4m$ -fold rotation (C_{4m}) symmetry. In particular, the positions of filaments for any AV-HP-VF always coincide with those of the local linear polarizations in the azimuthal dimension. The collapsing patterns of the AV-HP-VF with a given m and ϕ_0 persist among experiments, implying that the collapsing patterns are indeed insensitive to the random noise. Moreover, the collapsing pattern of the AV-HP-VF is controllable and designable by engineering the spatial hybrid SoP structure.

Discussion

To understand the physics behind the collapse of AV-HP-VF, a cross-coupling model is presented (Fig. 5). Multiple filamentation requires the simultaneous spatial confinements in both the radial and azimuthal dimensions. The self-confinement in the radial dimension is due to the focal ring. However, it is of great interest and of crucial importance to reveal the mechanism behind the axial symmetry breaking that leads to the multiple filamentation. Therefore, we ignore the radial terms $\partial^2/\partial\rho^2$ and $\partial/\partial\rho$ in the transverse Laplacian ∇_{\perp}^2 , while concentrate only on the azimuthal term $\partial^2/\partial\phi^2$ in Eq. (3). The Kerr medium is divided into N equal-length thin segments (each thin segment has a normalized length of $\Delta\zeta = L/N$), so that the nondepletion approximation is valid within any thin segment. After the focused AV-LP-VF described in Eq. (2) passing through the 1st segment, based on Eq. (3), ψ_H and ψ_V can be expressed as follows

$$\psi_H|_{\zeta=\Delta\zeta} = [A + j(B + C)] \cos \delta, \quad (4a)$$

$$\psi_V|_{\zeta=\Delta\zeta} = [A + j(B + C)] \sin \delta, \quad (4b)$$

thereby obtaining

$$(|\psi_H|^2 + |\psi_V|^2)|_{\zeta=\Delta\zeta} = A^2 + (B + C)^2, \quad (5)$$

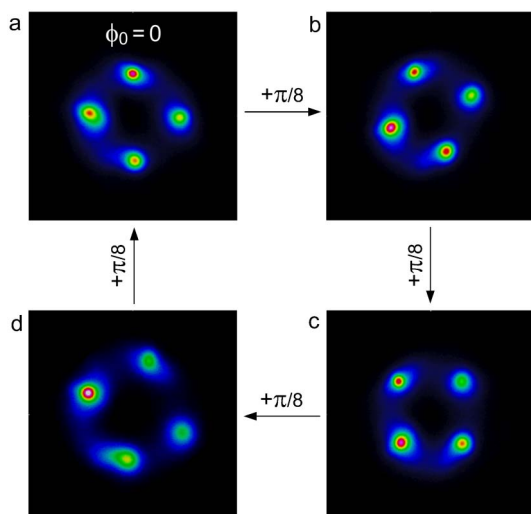


Figure 3 | Measured collapsing patterns of AV-HP-VFs with $m = 1$ for different ϕ_0 . (a) $\phi_0 = 0$. (b) $\phi_0 = \pi/8$. (c) $\phi_0 = \pi/4$. (d) $\phi_0 = 3\pi/8$.

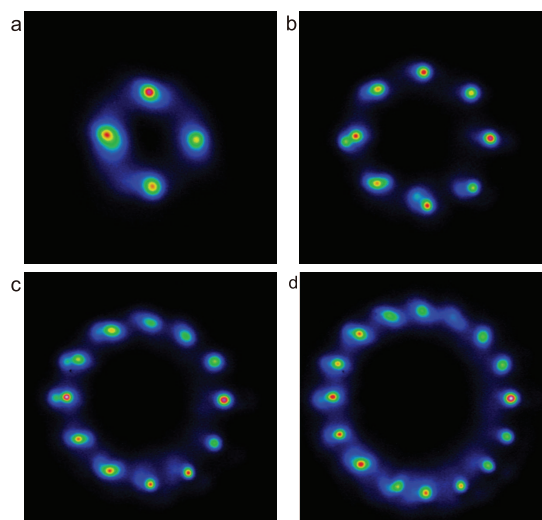


Figure 4 | Measured collapsing patterns of AV-HP-VFs with $\phi_0 = 0$ for different m . (a) $m = 1$. (b) $m = 2$. (c) $m = 3$. (d) $m = 4$.

where $B = -Am^2\Delta\zeta/4$ and $C = \alpha PA^3\Delta\zeta/P_C$. Based on Eqs. (4) and (5), we can find: (i) the horizontal and vertical components are always held in phase, implying that spatial SoP distribution has no change; and (ii) the intensity distribution still exhibits axial symmetry. Therefore, a purely ideal AV-LP-VF can never produce the deterministic multiple filamentation, which is in excellent agreement with the simulation (the third row of Fig. 1). As such, any azimuthal position is equivalent or indistinguishable. In the presence of azimuthal perturbations, axial symmetry breaking will lead to the filamentation^{1–5} (also see the fourth row of Fig. 1).

After the AV-HP-VF described in Eq. (1) passing through the 1st segment, based on Eq. (3), ψ_H and ψ_V can be expressed as follows

$$\psi_H|_{\zeta=\Delta\zeta} = \{A + j[B + (C/3)(1 + 2\cos^2 \delta)]\} \cos \delta, \quad (6a)$$

$$\psi_V|_{\zeta=\Delta\zeta} = j\{A + j[B + (C/3)(1 + 2\sin^2 \delta)]\} \sin \delta, \quad (6b)$$

thereby obtaining

$$(|\psi_H|^2 + |\psi_V|^2)|_{\zeta=\Delta\zeta} = A' + B' \cos(4\delta), \quad (7a)$$

where

$$A' = A^2 + (B - C)^2 - (B + 5C/6)(C/3), \quad (7b)$$

$$B' = -(B - 5C/6)(C/3). \quad (7c)$$

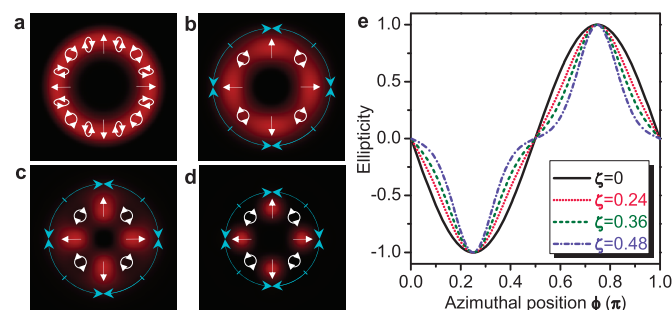


Figure 5 | Cross-coupling model for the collapse of AV-HP-VF. (a) The intensity and SoP distributions in the input plane. (b) Those behind the first segment. (c) Those behind the n th segment. (d) Those in the output plane. Arc arrows indicate the energy exchange directions. (e) The simulated evolution of S_3 of azimuthal hybrid SoPs for the AV-HP-VF with $m = 1$ and $\phi_0 = 0$ (only the azimuthal range from $\phi = 0$ to π is shown).

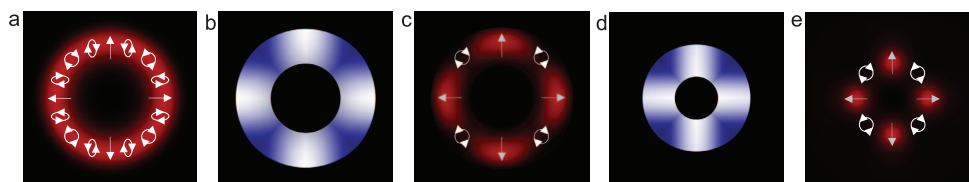


Figure 6 | Azimuthal self-focusing model for the collapse of AV-HP-VF. (a) Input focused AV-HP-VF. (b) Induced azimuthal self-focusing lenses. (c) Axial-symmetry broken AV-HP-VF. (d) Induced azimuthal self-focusing lenses with the shorter “focal length”. (e) Collapsing filaments.

Equation 7 suggests that the nonlinear cross-coupling results in the energy redistribution of AV-HP-VF in the azimuthal dimension (or the axial symmetry breaking). It should be pointed out that the intensity distribution still holds the axial symmetry in the absence of nonlinearity ($n_2 = 0 \rightarrow C = 0 \rightarrow B' = 0$). As an example, the AV-HP-VF with $m = 1$ and $\phi_0 = 0$ is considered (Figs. 5a–d). In the input plane ($\zeta = 0$), the focused AV-HP-VF has the azimuthally-invariant intensity distribution, while the azimuthally-variant hybrid SoP distribution (Fig. 5a). After the 1st segment, the cross-coupling results in the energy exchange in the azimuthal dimension toward the locations at $\phi^{lin}(n)$ from those at $\phi^{cir}(n)$ (Fig. 5b). As the propagation distance increases, more energy is transferred toward the locations at $\phi^{lin}(n)$ after the j th segment (Fig. 5c). In the output plane (Fig. 5d), the cross-coupling leads to the energy almost converging into the azimuthal locations at $\phi^{lin}(n)$. The axial symmetry of the focused AV-HP-VF is broken ultimately to form four deterministic filaments. From Eq. 6, the cross-coupling acquires an additional phase, which makes the phase difference between the horizontal and vertical components to not always preserve $\pi/2$, resulting in the SoP evolution in contrast to AV-LP-VF. However, at two series of azimuthal locations, $\phi^{lin}(n)$ and $\phi^{cir}(n)$, the SoPs have no change. The simulated evolution of the azimuthal-variant hybrid SoPs, by the Stokes parameter S_3 characterizing the ellipticity³⁰, during the nonlinear propagation of the AV-HP-VF with $m = 1$ and $\phi_0 = 0$ confirmed the above prediction (Fig. 5e). As propagation distance increases, the local ellipticity has a tendency to decrease (i.e. the local polarization ellipse will become flatter). Except for at the special azimuthal locations of $\phi^{lin}(n)$ and $\phi^{cir}(n)$, the SoPs have indeed no change, like the above discussion from the cross-coupling model.

To understand the collapsing filaments, the azimuthal self-focusing model is also very beneficial (Fig. 6). The self-focusing phenomenon originates from the spatially variant refractive index change. In an isotropic Kerr medium under the same intensity, the induced refractive index change depends on the SoP of optical field ($\Delta n^{lin} > \Delta n^{el} > \Delta n^{cir}$), where Δn^{lin} , Δn^{el} , and Δn^{cir} are the refractive index changes induced by the linearly, elliptically, and circularly polarized light, respectively³⁵. As a result, the refractive index change induced by the AV-HP-VF is azimuthally variant, leading to the axial-symmetry breaking. The local linear and circular polarizations are located at $\phi^{lin}(n)$ and $\phi^{cir}(n)$ (where $n = 0, 1, 2, 3$) for the AV-HP-VF with $m = 1$ and $\phi_0 = 0$ (Fig. 6a). Therefore, the induced four azimuthal self-focusing lenses have their centers located at $\phi^{lin}(n)$ and their edges located at $\phi^{cir}(n)$ (Fig. 6b). The input field undergoes the azimuthal multiple-nucleation self-focusing, making the energy converge toward the four locations at $\phi^{lin}(n)$ (Fig. 6c). As the propagation distance increases, the “focal lengths” of the induced azimuthal self-focusing lenses become shorter (Fig. 6d), and then the energy converges ultimately into the four deterministic filaments (Fig. 6e). In particular, Δn^{lin} is greater than 50% Δn^{cir} , which is the reason why AV-HP-VF can suppress the random noise (the robust feature) during the deterministic collapsing filamentation.

We have presented the theoretical prediction and conducted the experimental evidence on the novel collapsing behaviors of AV-HP-VF in the self-focusing Kerr medium. The azimuthally-variant hybrid SoP structure is crucial in the axial symmetry breaking. The collapsing filamentation has the controllable and robust features.

The m -charge AV-HP-VF produces $4m$ filaments with $4m$ -fold rotation (C_{4m}) symmetry. The number of multiple filaments is a function solely of m , and their locations are determined by both m and ϕ_0 . Our results suggest that engineering the hybrid SoP structure can tame the randomness and then realize the designable collapsing filamentation. This study only concentrated on the collapsing behavior; thus, the higher-order nonlinearity, which is important in the postcollapse process, has been neglected. Of course, we also simulated the multiple filamentation when the higher-order Kerr effect is considered, the results indicate a novel feature that the relative phase difference among the multiple filaments is stable and insensitive to the input fluctuations of the pulse energy, which is quite different from the reported fact that the relative phase difference is unstable and sensitivity to the small fluctuations of the pulse energy, i.e., loss of phase of collapse³⁶. Our idea may offer an alternative route to produce the controllable and robust multiple filamentation in other nonlinear systems, thereby facilitating the development of additional surprising applications. This work has the great significance that it not only opens a new window for manipulating the optical field and facilitates to push the related researches, but also has a certain reference value for manipulating the different kinds of field.

Methods

Generation of femtosecond vector fields. We follow the same method as Ref. 30 for creating the vector fields required in this study. The used light source is a Ti:sapphire regenerative amplifier femtosecond laser system (Coherent Inc.), which provides a fundamental Gaussian mode with a central wavelength of 800 nm, a pulse duration of 35 fs, and a repetition rate of 1 kHz. An achromatic 1/2 wave plate and a broadband polarized beam splitter were used to control incident laser fluence on the sample surface. Another achromatic 1/2 wave plate was used to change the polarization direction of the incident femtosecond laser into the vector field generation unit, where all the elements are achromatic to suppress pulse broadening as much as possible. The created AV-HP-VFs and AV-LP-VFs have a “top-hat-like” spatial profile, excluding a central singularity caused by the SoP uncertainty, with a radius of 1.5 mm, a pulse energy of 6.0 μ J, and a pulse duration of \sim 65 fs.

1. Robinson, P. A. Nonlinear wave collapse and strong turbulence. *Rev. Mod. Phys.* **69**, 507–573 (1997).
2. Bergé, L. Wave collapse in physics: principles and applications to light and plasma waves. *Phys. Reports* **303**, 259–370 (1998).
3. Fibich, G. & Ilan, B. Vectorial and random effects in self-focusing and in multiple filamentation. *Physica D* **157**, 112–146 (2001).
4. Couairon, A. & Mysyrowicz, A. Femtosecond filamentation in transparent media. *Phys. Reports* **441**, 47–189 (2007).
5. Bergé, L., Skupin, S., Nuter, R., Kasparian, J. & Wolf, J. P. Ultrashort filaments of light in weakly ionized, optically transparent media. *Rep. Prog. Phys.* **70**, 1633–1713 (2007).
6. Chiao, R. Y., Garmire, E. & Townes, C. H. Self-trapping of optical beams. *Phys. Rev. Lett.* **13**, 479–482 (1964).
7. Bespalov, V. I. & Talanov, V. I. Filamentary structure of light beams in nonlinear liquids. *JETP Lett.* **3**, 307–312 (1966).
8. Kelley, P. L. Self-focusing of optical beams. *Phys. Rev. Lett.* **15**, 1005–1008 (1965).
9. Varma, S., Chen, Y. H. & Milchberg, H. M. Trapping and destruction of long-range high-intensity optical filaments by molecular quantum wakes in air. *Phys. Rev. Lett.* **101**, 205001 (2008).
10. Braun, A., Korn, G., Liu, X., Du, D., Squier, J. & Mourou, G. Self-channeling of high-peak-power femtosecond laser pulses in air. *Opt. Lett.* **20**, 73–75 (1995).
11. Kasparian, J. & Wolf, J. P. Physics and applications of atmospheric nonlinear optics and filamentation. *Opt. Express* **16**, 466–493 (2008).
12. Kasparian, J., Rodriguez, M., Méjean, G., Yu, J., Salmon, E., Wille, H., Bourayou, R., Frey, S., André, Y. B., Mysyrowicz, A., Sauerbrey, R., Wolf, J. P. & Wöste, L. White-light filaments for atmospheric. *Science* **301**, 61–64 (2003).



13. Kolesik, M., Wright, E. M. & Moloney, J. V. Femtosecond filamentation in air and higher-order nonlinearities. *Opt. Lett.* **35**, 2550–2552 (2010).
14. D'Amico, C., Houard, A., Franco, M., Prade, B., Mysyrowicz, A., Couairon, A. & Tikhonchuk, V. T. Conical forward THz emission from femtosecond-laser-beam filamentation in air. *Phys. Rev. Lett.* **98**, 235002 (2007).
15. Alfano, R. R. & Shapiro, S. L. Emission in the region 4000 to 7000 Å via four-photon coupling in glass. *Phys. Rev. Lett.* **24**, 584–587 (1970).
16. Hauri, C. P., Kornelis, W., Helbing, F. W., Heinrich, A., Couairon, A., Mysyrowicz, A., Biegert, J. & Keller, U. Generation of intense, carrier-envelope phase-locked few-cycle laser pulses through filamentation. *Appl. Phys. B* **79**, 673–677 (2004).
17. Rohwetter, P., Kasparian, J., Stelmaszczyk, K., Hao, Z., Henin, S., Lascoux, N., Nakaema, W. M., Petit, Y., Queißer, M., Salamé, R., Salmon, E., Wöste, L. & Wolf, J. P. Laser-induced water condensation in air. *Nature Photon* **4**, 451–456 (2010).
18. Belgiorio, F., Cacciatori, S. L., Clerici, M., Gorini, V., Ortenzi, G., Rizzi, L., Rubino, E., Sala, V. G. & Faccio, D. Hawking radiation from ultrashort laser pulse filaments. *Phys. Rev. Lett.* **105**, 203901 (2010).
19. Jin, Z., Zhang, J., Xu, M. H., Lu, X., Li, Y. T., Wang, Z. H., Wei, Z. Y., Yuan, X. H. & Yu, W. Control of filamentation induced by femtosecond laser pulses propagating in air. *Opt. Express* **13**, 10424–10430 (2005).
20. Dubietis, A., Tamošauskas, G., Fibich, G. & Ilan, B. Multiple filamentation induced by input-beam ellipticity. *Opt. Lett.* **29**, 1126–1128 (2004).
21. Grow, T. D. & Gaeta, A. L. Dependence of multiple filamentation on beam ellipticity. *Opt. Express* **13**, 4594–4599 (2005).
22. Pfeifer, T., Gallmann, L., Abel, M. J., Neumark, D. M. & Leone, S. R. Circular phase mask for control and stabilization of single optical filaments. *Opt. Lett.* **31**, 2326–2328 (2006).
23. Kandidov, V. P., Aközbeke, N., Scalora, M., Kosareva, O. G., Nyakk, A. V., Luo, Q., Hosseini, S. A. & Chin, S. L. A method for spatial regularisation of a bunch of filaments in a femtosecond laser pulse. *Quantum Electronics* **34**, 879–880 (2004).
24. Hao, Z. Q., Stelmaszczyk, K., Rohwetter, P., Nakaema, W. M. & Woeste, L. Femtosecond laser filament-fringes in fused silica. *Opt. Express* **19**, 7799–7806 (2011).
25. Hao, Z. Q., Zhang, J., Xi, T. T., Yuan, X. H., Zheng, Z. Y., Lu, X., Yu, M. Y., Li, Y. T., Wang, Z. H., Zhao, W. & Wei, Z. Y. Optimization of multiple filamentation of femtosecond laser pulses in air using a pinhole. *Opt. Express* **15**, 16102–16109 (2007).
26. Kandidov, V. P., Aközbeke, N., Scalora, M., Kosareva, O. G., Nyakk, A. V., Luo, Q., Hosseini, S. A. & Chin, S. L. Towards a control of multiple filamentation by spatial regularization of a high-power femtosecond laser pulse. *Appl. Phys. B* **80**, 267–275 (2005).
27. Trisorio, A. & Hauri, C. P. Control and characterization of multiple circularly polarized femtosecond filaments in argon. *Opt. Lett.* **32**, 1650–1652 (2007).
28. Fibich, G. & Ilan, B. Deterministic vectorial effects lead to multiple filamentation. *Opt. Lett.* **26**, 840–842 (2001).
29. Zhan, Q. Cylindrical vector beams: from mathematical concepts to applications. *Adv. Opt. Photon.* **1**, 1–57 (2009).
30. Wang, X. L., Li, Y. N., Chen, J., Guo, C. S., Ding, J. P. & Wang, H. T. A new type of vector fields with hybrid states of polarization. *Opt. Express* **18**, 10786–10795 (2010).
31. Vuong, L. T., Grow, T. D., Ishaaya, A. A., Gaeta, A. L., 't Hooft, G. W., Eliel, E. R. & Fibich, G. Collapse of optical vortices. *Phys. Rev. Lett.* **96**, 133901 (2006).
32. Wang, X. L., Chen, J., Li, Y. N., Ding, J. P., Guo, C. S. & Wang, H. T. Optical orbital angular momentum from the curl of polarization. *Phys. Rev. Lett.* **105**, 253602 (2010).
33. Fibich, G. & Gaeta, A. L. Critical power for self-focusing in bulk media and in hollow waveguides. *Opt. Lett.* **25**, 335–337 (2000).
34. Ishaaya, A. A., Vuong, L. T., Grow, T. D. & Gaeta, A. L. Self-focusing dynamics of polarization vortices in Kerr media. *Opt. Lett.* **33**, 13–15 (2008).
35. Sutherland, R. L. *Handbook of Nonlinear Optics* (second Edition, Marcel Dekker, Inc., 2003).
36. Shim, B., Schrauth, S. E., Gaeta, A. L., Klein, M. & Fibich, G. Loss of phase of collapsing beams. *Phys. Rev. Lett.* **108**, 043902 (2012).

Acknowledgements

This work was supported by the 973 Program of China under Grant No. 2012CB921900, and the National Natural Science Foundation of China under Grants 10934003.

Author contributions

S.M. Li presented idea, performed the experiments, carried out simulations, and wrote the manuscript. Y.N. Li assisted with the experiments and the discussion of mechanism. X.L. Wang presented the method for generating the vector fields. L.J. Kong and K. Lou assisted with the experiments and the discussion. C.H. Tu provided technical support. Y.J. Tian assisted with the discussion of mechanism and wrote the manuscript. H.T. Wang planned the project, presented the idea and the mechanism, guided and supervised the simulations and experiments, and wrote the manuscript.

Additional information

Competing financial interests: The authors declare no competing financial interests.

License: This work is licensed under a Creative Commons Attribution-NonCommercial-ShareAlike 3.0 Unported License. To view a copy of this license, visit <http://creativecommons.org/licenses/by-nc-sa/3.0/>

How to cite this article: Li, S.M. *et al.* Taming the Collapse of Optical Fields. *Sci. Rep.* **2**, 1007; DOI:10.1038/srep01007 (2012).



Sensitive Real-Time Monitoring of Refractive Indexes Using a Novel Graphene-Based Optical Sensor

Fei Xing¹, Zhi-Bo Liu¹, Zhi-Chao Deng¹, Xiang-Tian Kong¹, Xiao-Qing Yan^{1,2}, Xu-Dong Chen¹, Qing Ye¹, Chun-Ping Zhang¹, Yong-Sheng Chen² & Jian-Guo Tian¹

¹The Key Laboratory of Weak Light Nonlinear Photonics, Ministry of Education, Teda Applied Physics School and School of Physics, Nankai University, Tianjin 300071, China, ²The Key Laboratory of Functional Polymer Materials and Center for Nanoscale Science & Technology, Institute of Polymer Chemistry, College of Chemistry, Nankai University, Tianjin 300071, China.

Based on the polarization-sensitive absorption of graphene under conditions of total internal reflection, a novel optical sensor combining graphene and a microfluidic structure was constructed to achieve the sensitive real-time monitoring of refractive indexes. The atomic thickness and strong broadband absorption of graphene cause it to exhibit very different reflectivity for transverse electric and transverse magnetic modes in the context of a total internal reflection structure, which is sensitive to the media in contact with the graphene. A graphene refractive index sensor can quickly and sensitively monitor changes in the local refractive index with a fast response time and broad dynamic range. These results indicate that graphene, used in a simple and efficient total internal reflection structure and combined with microfluidic techniques, is an ideal material for fabricating refractive index sensors and biosensor devices, which are in high demand.

In recent years, graphene has emerged as a novel two-dimensional (2D) material in the field of materials science due to its prominent intrinsic electronic, thermal, mechanical, structural and chemical properties¹. Highly sensitive biosensors and electrochemical sensors based on graphene field-effect transistors have been widely developed for sensing gases^{2,3}, liquids^{4,5} and biomolecules⁶⁻⁸. Because graphene has a 2D structure, with each of its atoms exposed, its electrical properties are very sensitive to changes in the charge environment induced by the reaction or adsorption of analytes on its surface. However, a transistor-based graphene sensor requires the measuring of current changes on the graphene surface; therefore, the temporal and spatial resolution is greatly restricted relative to that of optical sensors. Due to its high carrier mobility and zero-bandgap characteristics, graphene exhibits unique and desirable optical properties, such as broadband and tunable absorptions^{9,10} and strong polarization-dependent effects¹¹⁻¹⁴. Thus, new high-performance graphene-based optical sensors are expected to be capable of characterizing surface structural changes and biomolecular interactions.

For optical sensors, measurements of refractive index changes are important for a variety of applications in biosensing, drug discovery, environmental monitoring, and gas- and liquid-phase chemical sensing. Various methods for obtaining these measurements have been developed¹⁵. At present, refractive-index-sensing technologies based on surface plasmon resonance (SPR) are widely used based on their ability to provide highly sensitive label-free real-time data¹⁶. The most common modulation approaches used in high-performance SPR sensors are based on the spectroscopy of surface plasmons in wavelength or angular domains. However, when measuring a range of wavelengths or angles, optical focusing limits the sensitivity, resolution, dynamic range and other functionalities of a spectroscopy-based SPR instrument and produces notable deficiencies in the real-time performance (>ms) of the sensor in question. An SPR sensor with amplitude modulation can produce fast, real-time monitoring and imaging functions, but its performance is typically worse than that of spectroscopy-based SPR sensors. Moreover, biomolecules adsorb poorly on gold, limiting the sensitivity of conventional SPR biosensors.

In this study, we present a strategy for sensing changes in refractive indexes using graphene optical sensors; in particular, this strategy is based on the different reflection behaviors of transverse-magnetic (TM) and transverse-electric (TE) modes under total internal reflection conditions. The model used in this investigation consists of a graphene layer sandwiched between a high-index medium (medium 1, refractive index n_1) and a low-index medium (medium 2, refractive index n_2) (Fig. 1a). As has been observed for the SPR sensor, the differences in

SUBJECT AREAS:
OPTICS AND PHOTONICS
OPTICAL MATERIALS
SENSORS
OPTICAL PHYSICS

Received
24 September 2012

Accepted
26 October 2012

Published
30 November 2012

Correspondence and requests for materials should be addressed to Z.-B.L. (nkzblu@gmail.com) or J.-G.T. (jitian@nankai.edu.cn)

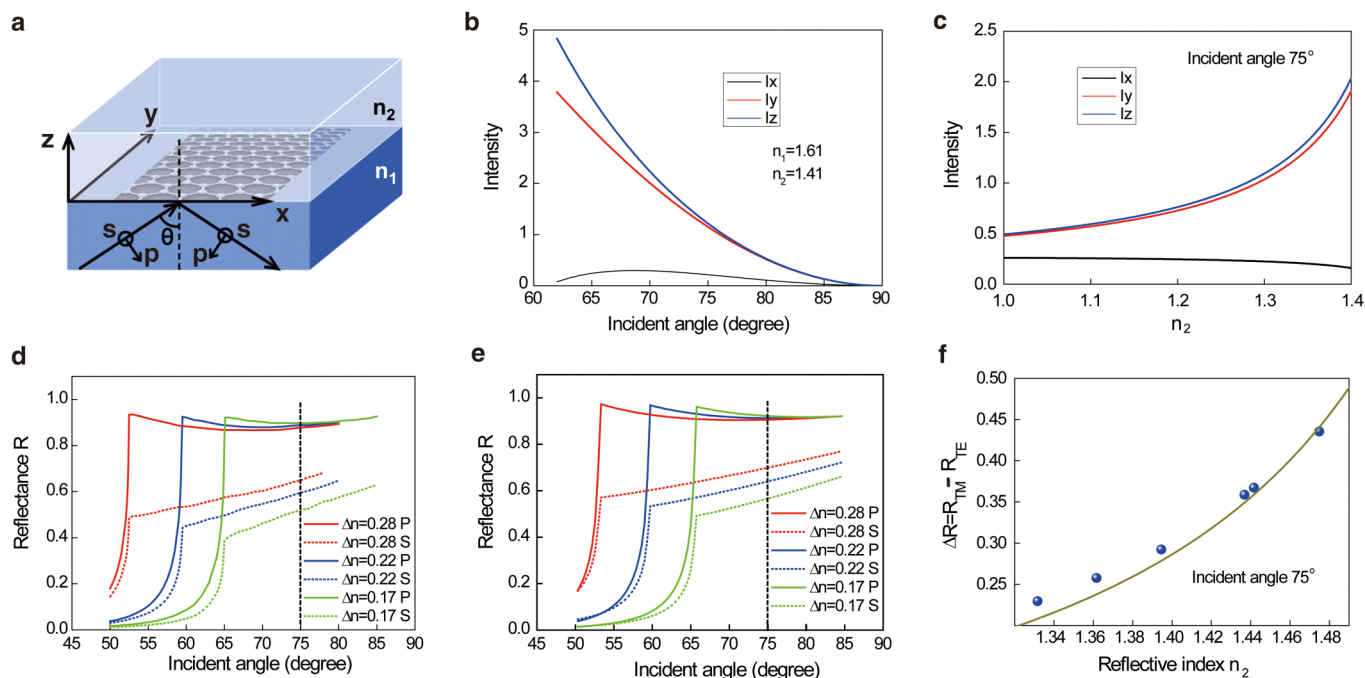


Figure 1 | The polarization-dependent features in graphene sandwiched structure. (a) A schematic illustration of graphene sandwiched between two dielectric layers. (b) A plot of the intensities of the evanescent waves for the x and z components at p -polarization and the y component at s -polarization with different incident angles. (c) A plot of the intensities of the evanescent waves for the x and z components at p -polarization and the y component at s -polarization with different refractive indexes n_2 . The incident angle is 75° . (d) The experimental results of reflectance for s - and p -polarized light with different $\Delta n = n_1 - n_2$ using a derivative total reflection method. (e) The theoretical results of reflectance for s - and p -polarized light with different Δn based on Maxwell's boundary conditions. (f) The experimental (circles) and theoretical (line) results of ΔR with different refractive indexes n_2 .

reflectance between the TE and TM modes are sensitive to variations in the refractive index n_2 under fixed n_1 conditions. Therefore, using a graphene sensing layer, a change of refractive index with broad dynamic range can be measured under total internal reflection. The polarization-dependent absorption effect of graphene allows us to use the balanced detection scheme. The balanced detection solves the problems of real-time detection, and improves the measurement sensitivity. With intensity modulation, the graphene-based refractive index sensor (GRIS) assessed in this study demonstrates a high sensitivity of 10^5 per refractive index units (RIU^{-1}), a fast real-time response of ~ 10 μs , and a large dynamic range with $\Delta n > 0.5$, where $\Delta n = n_1 - n_2$ is the difference in refractive indexes between medium 1 and medium 2. Because the detection limit depends only on the signal-to-noise ratio, the detector sensitivity and the response time of the detector, GRIS is expected to achieve high sensitivity and fast response time easily. Furthermore, the various advantages of graphene, such as its stability, low cost, rich functionality, easily controlled thickness, and strong mechanical strength, make it a promising candidate for refractive index sensing and indicate its potential for wider applications, particularly in biological and chemical sensing.

Results

Polarization-dependent reflection and absorption. Due to its unique electronic structure, in which conical-shaped conduction and valence bands meet at the Dirac point, a pristine monolayer of graphene that has been scaled to an atomic thickness demonstrates frequency-independent optical conductance and strong broadband absorption per unit mass ($\pi\alpha = 2.3\%$)¹⁷. Moreover, its unique polarization-dependent effects^{11,13} and use as fiber¹² and planar waveguide polarizers¹⁴ have been investigated. Given the unique 2D structure of graphene, its optical properties can be more fully utilized when surface waves propagate through the graphene plane. Under total internal reflection (TIR), a fraction of the incident energy

can penetrate through the interface of medium 1 and medium 2; this energy fraction propagates along this interface and is known as the evanescent field. At $z=0$, the intensity components (I_{0x} , I_{0y} and I_{0z}) of the evanescent fields induced by TE (s -polarized) and TM (p -polarized) incident light are shown in Fig. 1b¹⁸ with $n_1 = 1.61$ and $n_2 = 1.41$. The intensities of the evanescent field for the s - and p -polarized incident lights at $z=0$ are $I_{0s} = I_{0y}$ and $I_{0p} = I_{0x} + I_{0z}$. When graphene is placed between two media, the relative proportions of the intensity components that are parallel or orthogonal to the graphene plane will result in different propagation behaviors for s - and p -polarized light. Furthermore, the x , y , and z intensity components are also dependent on the change of n_2 when n_1 is fixed (Fig. 1c). Thus, it is expected that the reflectance of the structure shown in Fig. 1a will differ significantly for distinct proportions of incident s - and p -polarized light.

Using a derivative total reflection method (Fig. S3), the reflectance of the prism/graphene/substrate tri-layer structure can be obtained for s - and p -polarized incident light (Fig. 1d). The refractive indexes of the substrate can be changed by employing different solvents, such as water (1.33174), alcohol (1.36169), butyl alcohol (1.39466), N,N-dimethylformamide (1.47497), dimethylamine (1.43697), and chloroform (1.44176). Fig. 1D presents the experimental results of the reflectance for s - and p -polarized light with different values of $\Delta n = n_1 - n_2$ using a derivative total reflection method (See Method and Fig. S3). Four-layer graphene grown by chemical vapor deposition (CVD) was transferred to the bottom of a prism. There are many kinds of methods to define the number of graphene layers, such as the transmittance, Raman spectroscopy¹⁹ and SPR²⁰. In our experiment, the number of graphene layers was defined by the transmittance (Fig. S4) and Raman spectroscopy (Fig. S5). The absorbance of graphene samples with different number of layers were shown in Fig. S4. When the absorbance of graphene sample is about 9%, the number of graphene layers is determined to be four by combining with it Raman spectroscopy as shown in Fig. S5. And the optimized



number of graphene layer for this sensor application is four in our current studies. The changes in n_2 were achieved using different liquid solvents. The reflectance R of the tri-layer structure for s -polarized light is much smaller than the reflectance for p -polarized light, which indicates that graphene has a greater absorption for s -polarized light when transmission is prevented by TIR²¹.

The general theory regarding light diffraction by tri-layer structures (Fig. 1a) that consist of a loss layer (graphene) sandwiched between two semi-infinite dielectrics (medium 1 and medium 2) states that the manner in which the transition takes place is also governed by Maxwell's boundary conditions, which state that the tangential components of the electric (E) and magnetic (H) fields are continuous across boundaries²². The intermediate graphene layer has a complex optical constant with $\hat{n}=n+ik$, where n is the real refractive index of graphene and k is its extinction coefficient^{23–25}. The thickness d is relative to the number of layers of graphene (e.g., $d=0.34$ nm for a single layer of graphene). Based on the boundary conditions and Snell's law, the reflectance of tri-layer structures can be obtained for s - and p -polarized light (see Supplementary theory). As shown in Fig. S2, the graphene layer stores more energy for TE waves than for TM waves. Thus, in situations involving the total reflectance of light, the reflectance of TE waves is less than that of TM waves. The reflectances of s - and p -polarized light appear to vary with the incident angle of the light and the refractive indexes of the substrates. Thus, the reflectance differences observed in this experiment are a function of both the incident angle and the refractive indexes of the media that are used. The polarization-dependent reflection experiments of single-layer and bi-layer graphene were performed. The corresponding results were shown in Fig. S6. The theoretical simulations based on Maxwell's boundary condition are in agreement with the experimental results, which supports our theoretical model.

For a given incident angle (e.g., 75°), the difference ($\Delta R=R_{TM}-R_{TE}$) in reflectance between s - and p -polarized incident light is strongly dependent on Δn (Fig. 1f). Figures 1e and 1f (solid line) provide the theoretical results generated by Maxwell's boundary conditions (see Supplementary theory) with $\hat{n}=2.6+1.6i$ and $d=1.36$ nm (four layers). The observed value of $k=1.6$ is slightly larger than the reported value of $k=1.3$ ²⁵. One possible reason for this discrepancy is that the graphene sample used in this analysis was grown using CVD and therefore has a less even distribution than the mechanically exfoliated graphene. When medium 1 and the graphene layer are fixed, the change in the refractive index of medium 2 can be determined by measuring ΔR for a given incident angle.

Device design. We designed a simple, real-time refractive index measuring system that used GRIS in combination with a microfluidic system. The experimental setup is shown in Fig. 2a and uses a 523 nm continuous wave laser as a light source. First, circularly polarized light obtained by adjusting a Glan-Taylor polarizer and a quarter-wave plate was focused on the GRIS at the center of its microfluid channel. The inset of Fig. 2a shows the structure of the GRIS, and the full diagram of the microfluid GRIS is provided in Fig. S8. Second, a multi-layer graphene coating was transferred to a right-angle prism using CVD and the cast microfluid channel was bonded to the graphene layer to form a microfluid channel/graphene/prism sandwich structure (see Fig. S7 for the detailed process). In this step, the focused spot must be small enough to ensure that it can be fully irradiated inside the microfluid channel. Third, the incident angle of circularly polarized light was adjusted in accordance with the refractive index of the fluid to be measured, allowing TIR to occur as incident light passed through the microfluid channel. Fourth, the reflected light was separated into s - and p -polarized light using a polarization beam splitter (PBS) and then detected by a balanced

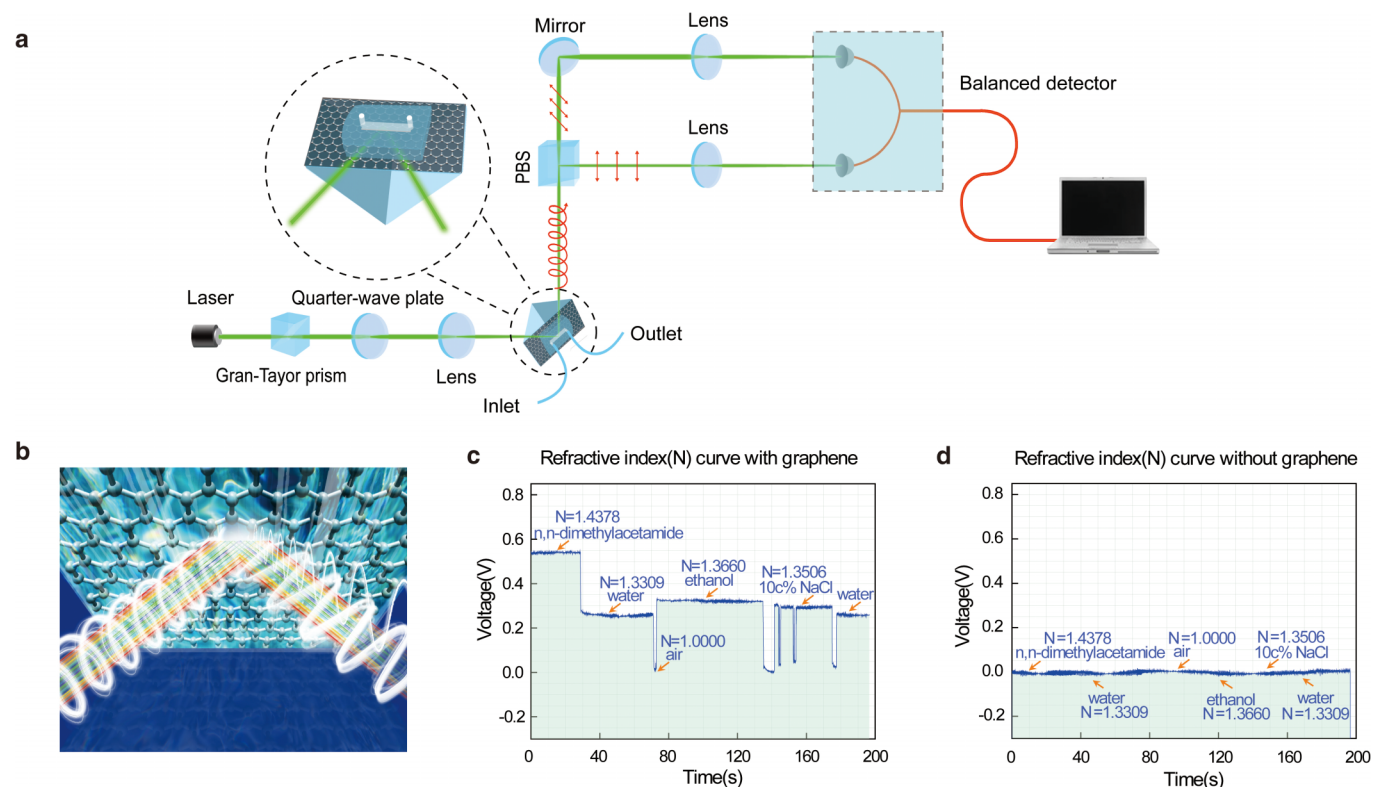


Figure 2 | A sensitive, real-time microfluid refractive index measuring system. (a) A schematic illustration of the measuring system. The enlarged diagram shows the sandwiched structure of the GRIS. PBS separated the circularly polarized light into s - and p -polarized lights. (b) A schematic illustration of the GRIS. The light source can be a laser of any wavelength or even natural light. The absorption of s -polarized light is much greater than that of p -polarized light when fluid is flowing. (c and d) The real-time voltage signal change of microfluid with and without graphene when injecting N,N -dimethyl acetamide, deionized water, air, ethanol, air, a solution of 10% NaCl, air and water successively at a flow rate of $10 \mu\text{L/s}$.



detector. A balanced detector consisted of two well-matched photodetectors was used to detect the difference between the photocurrents in the two optical input signals²⁶. Due to the polarization-sensitive absorption of graphene under total internal reflection, the intensity of the *p*-polarized light changed little before and after microfluid injections, whereas the microfluid injection greatly altered the measured intensity of the *s*-polarized light, as shown in Fig. 2b and Fig. 1d. The signal from the balanced detector is measured relative to the difference $\Delta R = R_{TM} - R_{TE}$ in reflectance between the *s*- and *p*-polarized incident lights. Thus, the signal from the balanced detector can be used to monitor the change in the refractive index of the fluid. After a calibration using standard liquids known, the GRIS can be used for refractive index measuring. Furthermore, before signal measurements, a substance (generally air or water) should be chosen to calibrate the detector, and the output voltage of the balanced detector should be adjusted to 0 V for this reference substance. During the measurement process, the refractive index of the internal microfluid channel at each moment corresponds to a particular voltage calculated by subtracting the intensity of the *s*-polarized light from that of the *p*-polarized light measured by the balanced detector. The voltage varies with the microfluid's refractive index; fluids with larger refractive indexes produce higher calculated voltages.

Discussion

One of the prominent features of the GRIS is its broad measuring range, as its signal depends on the value of Δn . To demonstrate this advantage, an experiment was conducted at room temperature with an incident angle of 83°; under these conditions, the refractive index of the prism was 1.51. When the incident power before the GRIS was 0.202 mW, the power of the *p*-polarization in front of the balanced detector was 10.33 μ W. Subsequently, using air for calibration purposes, we injected N,N-dimethyl acetamide, deionized water, air, absolute ethyl alcohol, air, a solution of 10% NaCl, air and water in turn at a flowing speed of 10 μ L/s, generating a relationship curve indicating the real-time voltage signal change of the microfluid, as shown in Fig. 2c. The real-time refractive index range was easily measured for refractive indexes ranging from 1 to 1.438. In fact, the dynamic range of the GRIS depends on the refractive index of the prism. If a prism with a refractive index of 1.71 is used, the refractive index of chlorobenzene (1.57) can be easily measured. The most commonly used method of measuring real-time refractive indexes employs an SPR sensor based on the modulation of incident angles. The dynamic range of SPR can readily be extended to be lower or higher, using different prism materials having various dielectric constants²⁷. However, the change of prism materials is not convenient in real-time monitoring. The dynamic range of SPR may be restricted, when a fixed prism is used in refractive index measurements²⁸. Therefore, the GRIS provides a reliable platform for measuring the refractive index of more complicated micro-fluids with a larger dynamic refractive index range. Figure 2d illustrates the results for tests in which the PDMS micro-fluid channel was directly bonded to the prism without a graphene sensor layer between them. Under the same conditions detailed above for the GRIS, this control was successively placed in the aforementioned fluids, producing a voltage signal that was always close to 0 V for each different liquid input. The lack of a distinctive pattern of alteration between the liquids demonstrates that the novel properties of graphene play a key role in the GRIS's detection ability.

As a sensing layer, graphene offers good, stable real-time performance. Fig. 2c shows that the voltage signal changes quite predictably and rapidly upon the inflow of each different fluid into the microfluid channel. During the injection of the 10% NaCl solution, the voltage signal exhibited a transitory decrease caused by air bubbles in the solution²⁹. Nevertheless, the evident advantages of using graphene as a sensing layer are manifold. First, with its perfect 2d

structure, graphene possesses desirable mechanical properties and chemical stability, which means that a graphene sensing layer is difficult to damage. Second, the nanometer-order thickness of graphene greatly increases the propagation distance of evanescent waves in liquid, thereby producing a more accurate detection result. The velocity distribution of the fluid in a micro-fluid channel is known to be uneven because the fluid flows more slowly as it approaches the sensing layer; thus, if the propagation distance (in the *z* direction) of the evanescent waves in the fluid is short, the detected result would be subject to larger time-delay errors, resulting in poor real-time performance. For these reasons, graphene sensors provide longer service life, better real-time performance and greater versatility in fluid measurements.

The rapid response of the GRIS makes it possible to measure a fluid using a faster flow rate and to quickly reflect the changes in refractive indexes during a process of rapid fluid flow. In the experiment, we simultaneously detect the two values by using a balanced detector. The GRIS's response speed is dependent on the response time of the detector and data acquisition equipment. To illustrate more accurate measurement using high collecting frequency, we combined rapid peristalsis (300 μ L/s) and data collection (100 kHz). The data were initially collected at a frequency of 10 kHz with an interval of 100 μ s. As shown in Fig. 3a, during successive injections of air and deionized water at different flow rates, the voltage changed by nearly 10 V is both nearly identical for different fluids and quite reproducible for different flow rates. At different flow rates, the voltage changed continuously at lower speeds and quite discontinuously at higher speeds. In particular, speeds approaching 300 μ L/s led to a large voltage interval. These changes indicate that the refractive index change of micro-fluids at higher speeds cannot be measured with good integrity at the collecting frequency of 10 kHz, which made it difficult for the sensor to conduct real-time measurements at high speeds. For this reason, we changed the frequency of data collection to 100 kHz with an interval of 10 μ s and repeated the above experiments under the same conditions. The experimental data generated after this modification indicated that minor changes in the refractive index were clearly evident at both a low speed of 5 μ L/s and a higher speed of 300 μ L/s (Fig. 3b). To better demonstrate the significance of a higher response speed in real-time refractive index measurements, we compared the curves obtained at the two different collecting frequencies at the speed of 300 μ L/s (Fig. 3c). The comparison shows that the two curves are almost identical; thus, this experiment exhibits high stability. Most importantly, the refractive index change at an interval of 10 μ s can be better measured at the collecting frequency of 100 kHz, which produces a continuous curve. In contrast, the data points measured at a frequency of 10 kHz are rather discontinuous and can only indicate rough trends. Therefore, a higher response speed facilitates the more accurate measurement of tiny changes in the refractive index; this property is particularly important for measuring refractive indexes during rapid-response processes, which are common in many biological and chemical interactions. In fact, the GRIS's response speed is theoretically dependent on the response time of the balanced detector and data acquisition equipment; the equipment used in this experiment can reach 10 ns and 340 kHz. However, the response speed of a traditional refractive index sensor, including SPR refractive index sensors, is generally on the order of milliseconds.

Moreover, the GRIS has high resolution and sensitivity. To experimentally demonstrate this property, we generated a curve (see Fig. 4a) representing the voltage changes associated with injecting deionized water, a solution of 0.1% NaCl and a solution of 20% NaCl successively in the microfluid channel by shining a 13.03 mW light at the GRIS. Under the same conditions, the refractive indexes of deionized water and 0.1% NaCl solution were determined to be 1.33091 and 1.33139, respectively (see Table S1), which differ by 0.00048. The inset of Fig. 4A shows that the corresponding voltage difference

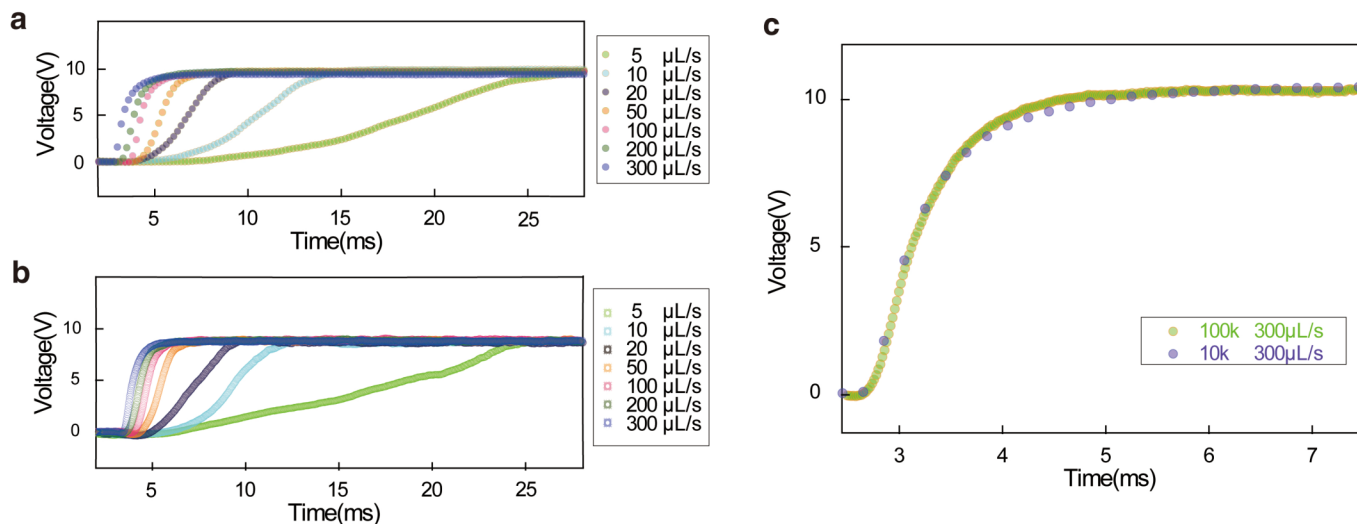


Figure 3 | An evaluation of the response speed performance of the GRIS. (a and b) The real-time voltage curve at collection frequencies of 10 kHz and 100 kHz obtained by successively injecting air and deionized water at different flow rates. The flow rate ranges from 5 $\mu\text{L/s}$ to 300 $\mu\text{L/s}$. (c) The purple dots represent the real-time voltage curve at a collection frequency of 10 kHz and a flow rate of 300 $\mu\text{L/s}$. The light-green dots represent the real-time voltage curve at a collection frequency of 100 kHz and a flow rate of 300 $\mu\text{L/s}$.

between the deionized water and the 0.1% NaCl solution is ~ 245 mV and the size of the voice signal is ~ 45 mV. Hence, the resolution which can be measured in the experiment is 1×10^{-4} . We defined sensitivity for the refractive index to be a slope of the straight line, dv/dn , where v is the voltage signal and n is the refractive index. Because the relationship between the change in the refractive index and the change in voltage is considered to be roughly linear within a

small range, the dv/dn obtained by the experiment was 5.1×10^5 mV/UIR. This result is comparable to the sensitivity of an SPR refractive index sensor (10^4 – 10^6 /UIR)^{30,31}.

In fact, both the resolution and sensitivity of the GRIS are strongly correlated with the power of the incident light (Fig. 4b), and both of them can be further improved. On one hand, under a given incident power, the voltage signal in measurements is higher for thicker NaCl

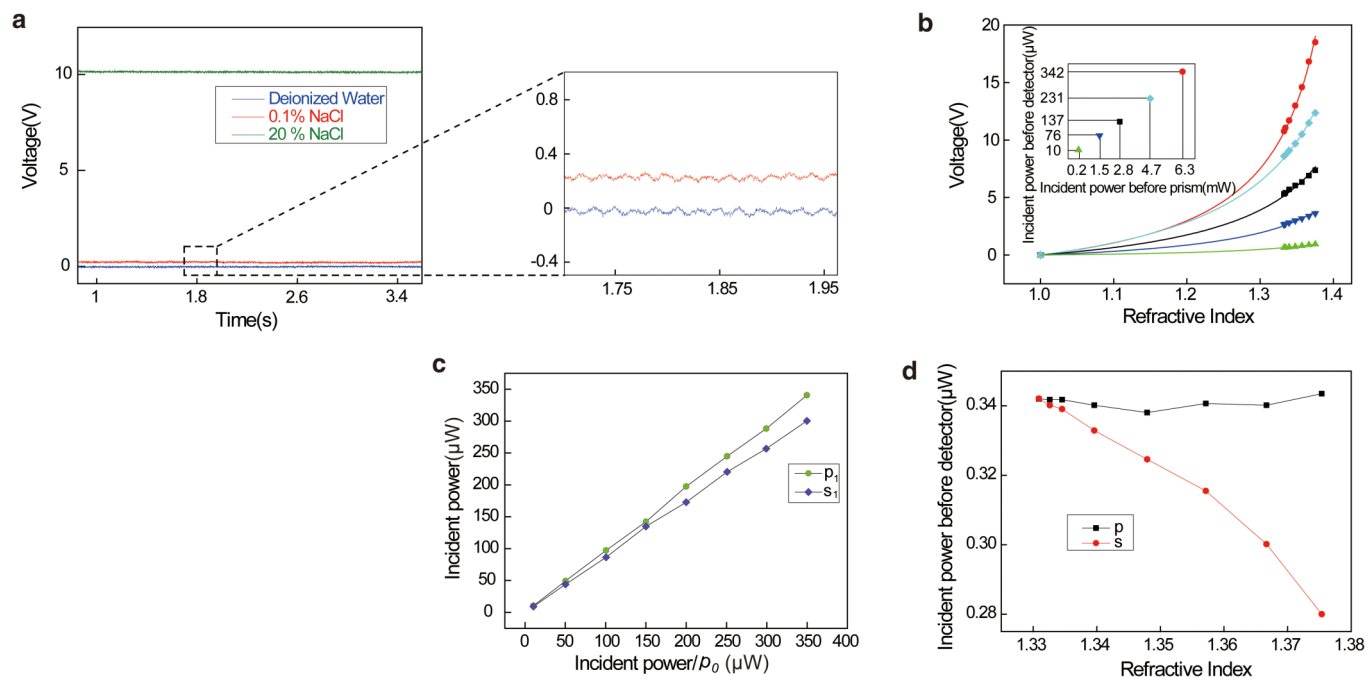


Figure 4 | The resolution performance and incident power dependence of the GRIS. (a) A curve representing the change in voltage after injecting deionized water, a solution of 0.1% NaCl and a solution of 20% NaCl into the micro-fluid channel, respectively. The incident light power is 13.03 mW before the prism. The inset shows that the corresponding voltage difference between deionized water and a solution of 0.1% NaCl is 245 mV and the size of voice signal is ~ 45 mV. (b) The incident power before the prism is, from bottom to top, 0.2, 1.5, 2.8, 4.7, and 6.3 mW. The inset indicates the correspondence between the incident power before the prism and incident power before the detector. Each point corresponds to a different concentration of the sodium chloride solution: from left to right, 1, 2, 5, 10, 15, 20, and 25%. (c) Using the p -polarized light power P_0 of deionized water as calibration, a solution of 20% NaCl was injected into the GRIS to determine the changes in polarization status S_1 and P_1 for this solution under different incident powers P_0 . (d) The power of s - and p -polarized light before the detector after injecting NaCl solutions with different concentrations into the microfluid channel.



solutions, which has a higher refractive index. How the voltage changes with the refractive index of substrates can be theoretically (solid lines in Fig. 4b) modeled well based on the boundary conditions and Snell's law (see Supplementary theory). Over a large range, the change in the refractive index with voltage is nonlinear. If the refractive index of the liquid is close to that of prism, the voltage signal from measurements is increased and the sensitivity should increase too. On the other hand, as shown in Fig. 4b, if we use this method to measure the refractive index of two solutions with different refractive index at identical incident power, the voltage signal is different for them and the signal difference increases with the incident power used.

Thus, enhancing the incident power could be a way of improving resolution and sensitivity of the GRIS (as the red line and green line), but the incident power should be lower than the damage thresholds of the graphene and the detector. The maximum incident power adopted in our experiment is 13.03 mW, which is much lower than the damage threshold ($>W$) of graphene.

To verify the influence of incident powers on the sensitivity, we measured the incident power before detector at different incident powers for *s*- and *p*- polarized light. In our measurements, we used deionized water to calibrate the GRIS, then a 20% NaCl solution was injected into the GRIS and the intensity change (see Fig. 4c) of *s*- and *p*- polarized light under different incident powers applied to the detector was measured. Then, we changed the incident power and repeat the calibration and measurements. The results are shown in Fig. 4c. In the figure, P_0 represents the calibrated power of deionized water and P_i and S_i are defined as the powers of the *p*- and *s*-polarization, respectively, upon the injection of a solution of 20% NaCl. As shown in Fig. 4c, the injection of a 20% NaCl solution only slightly changes the *p*-polarization power relative to the *p*-polarization power calibrated using deionized water. The larger the calibrated power (50, 100, 150, 200, 250, 300, and 350 mW), the larger the difference is between the powers of *s*- and *p*-polarization. Figure 4d illustrates the changes in the status of *s*-polarization and *p*-polarization that are obtained by injecting NaCl solutions of different concentrations into the microfluidic channel when the incident power is fixed at 6.73 mW and deionized water is used to calibrate the GRIS. As shown in Fig. 4d, the *p*-polarized light intensity changes only slightly (remaining at approximately 0.34 mW) when NaCl solutions with different concentrations was injected, whereas the *s*-polarized light intensity changes from 0.34 mW to 0.28 mW, which is consistent with the relationship observed between changes in the refractive index and changes in the measured voltage values (Fig. 4b).

To evaluate the potential of the GRIS under real conditions, real-time monitoring of the concentrations of glucose and NaCl solutions was attempted and the performance of the sensor was analyzed. In production processes, it is often necessary to conduct real-time measurements of the concentration of a liquid, such as a solution of glucose or NaCl. In this study, we illustrate the real-time measurement curves for a NaCl solution and a glucose solution in Fig. 5a and Fig. 5b, respectively. In these curves, the incident power is 6.73 mW, the reference power is that of the *p*-polarization, 342 μ W, and air is used to calibrate the GRIS. NaCl or glucose solutions of different concentrations are injected into the channel, proceeding from lower to higher densities. The figure clearly shows that the voltage values of NaCl and glucose solutions of different concentrations at any time correspond to the refractive index (see Tabs. S1 and S2); thus, this sensor can achieve a high response within a broad range and is able to measure the change in the refractive index of a liquid in a simple fashion.

We have demonstrated that graphene sandwiched between two dielectric layers has a stronger absorption for *s*-polarized light than for *p*-polarized light under TIR. These different absorption behaviors for *s*- and *p*-polarized light make graphene suitable for use as an optical detector of refractive indexes. The sensitive and real-time

monitoring of the refractive index was shown using a graphene-based optical sensor that has a broad dynamic refractive index range from 1.0 to 1.438, a fast response time of ~ 10 μ s, a high sensitivity of 10^5 RIU $^{-1}$, and excellent stability; these qualities are all essential for a versatile refractive index sensor. The flexibility and ease of functionalization of graphene sheets could also enable radically different refractive index sensors to be designed. For example, graphene could be integrated with flexible substrates and plastic materials. Alternatively, it could be used in novel geometries, e.g., as a flexible sensor. The recent development of large-scale graphene synthesis and transfer techniques³², as well as the structural modification of graphene by chemical or biological molecules, ensures that graphene will become the basis for powerful label-free monitoring methods for chemical or biomolecular interactions.

Methods

Preparation for graphene/prism structure. As a mature method of producing graphene devices, the transfer method of using thermal release tape can instantly etch Ni layers and easily produce large scale graphene devices. The polymer supports thermal release tape (TRT) was attached to the CVD-made, Ni-based graphene to form a structure of TRT/graphene (G)/Ni/SiO₂/Si. The multilayer structure was then soaked in deionized water. For ultrasonic processing in a few minutes, the TRT/G/Ni layers are detached from SiO₂. Then, putting the TRT/G/Ni layers into an aqueous iron (III) chloride (FeCl₃) solution (1 M) to remove the nickel layers. After that, process the prism surface with plasma oxygen cleaning for a few minutes, and then cover the TRT/G layers on the prism surface and press them tightly to some extent.

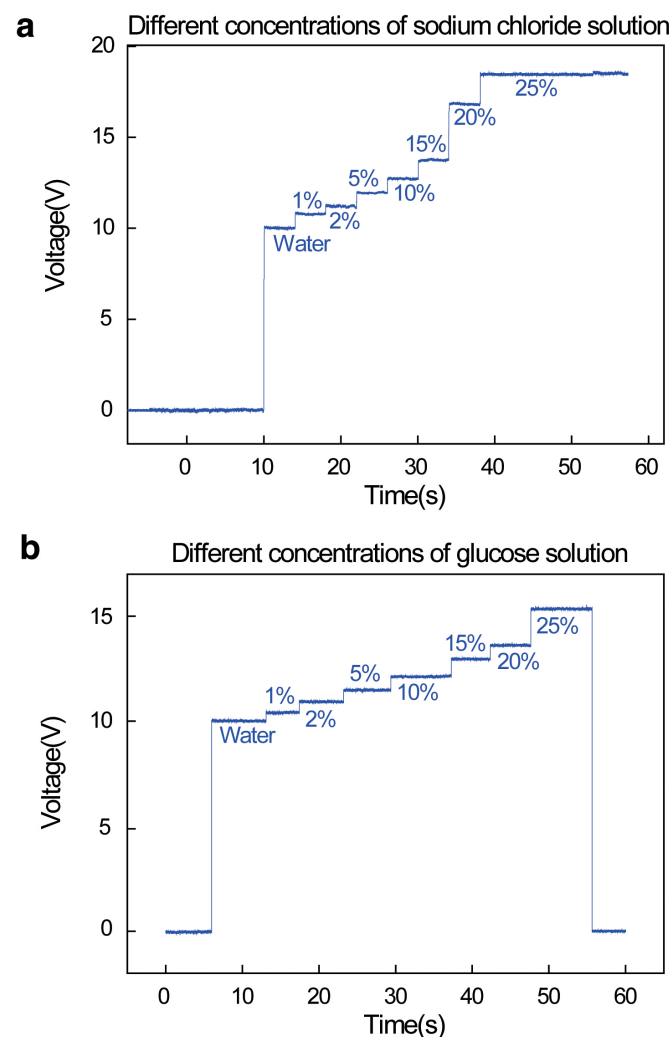


Figure 5 | The real-time measured voltage curves. (a) Different concentrations of sodium chloride solutions. (b) Different concentrations of glucose solutions.



Then, put the TRT/G/Prism layers into a vacuum drying oven for heating till 100°C, so as to detach graphene layers with TRT completely. At last, putting the G/Prism layers into an acetone solution to wash off the residual glue, and then store it in the vacuum line of the fume hood. Raman spectroscopy was carried out using RENISHAW RM2000 Raman system equipped with a 514 nm laser source and 50× objective lens (Fig. S5).

A derivative total reflection method. Light at wavelength of 632.8 nm from a He-Ne laser is split into incident and reference beams by a beam splitter M. After passing through a half-wave plate H and a polarizer P, the incident beam reached an equilateral prism fixed on a rotation stage (M-038, PI). PD1 and PD2 are the two detectors of a Dual-channel power meter (PM320E, Thorlabs). PD1 is used for monitoring the instantaneous fluctuations of the laser energy. PD2 is used to measure the final light reflected by the prism. D is an aperture diaphragm to block the scattering light. The experiment setup was first calibrated by deionized water. Reflectance curves as a function of incident angle were recorded. At 632.8 nm, the refractive index of prism is 1.61656. The refractive index of substrate can be changed by using different solvents of water (1.33174), alcohol (1.36169), butyl alcohol (1.39466), N,N-Dimethylformamide (1.47497), dimethylamine (1.43697), chloroform (1.44176).

Preparation for microfluid channel. Poly(dimethylsiloxane) (PDMS) has been shown to be biocompatible and it is also chemically stable. So it is noble material for fabrication of microfluid channel. Use computer-aided design (CAD) software programs to design a pattern. The photoresist mask was etched with electron beam lithography. Spin coat negative photoresist (SU-8) to the Si base at a speed of 1,100 r/min in 50 s and then dry it at 110°C. Then, cover the photoresist mask on the negative photoresist (SU-8)/Si layers and expose them to ultraviolet light and then photographic develops to get the master. Use a balance to weigh 70 g of Sylgard 184 silicone elastomer base and 7 g of Sylgard 184 elastomer curing agent fully (10:1 ratio) and mix them fully. Then, lay the liquid mixture into vacuum line of the fume hood to trapped bubbles for one hour. After that, pour the liquid mixture on the master, place the dish containing both the master and PDMS prepolymer in an oven set to 70°C and cure it for 3 h. Then, with a plier peel the solidified PDMS microfluid channel off the master.

Preparation for GRIS with microfluid channel. Process the prior prepared G/Prism structure and PDMS microfluid channel in a plasma oxygen cleaning with 150 W in power for 30 s, then, irreversibly adhered G/Prism structure with PDMS microfluid channel to get the GRIS with microfluid channel.

- Geim, A. K. Graphene: Status and Prospects. *Science* **324**, 1530–1534 (2009).
- Schedin, F., Geim, A. K., Morozov, S. V., Hill, E. W., Blake, P. *et al.* Detection of Individual Gas Molecules Adsorbed on Graphene. *Nat. Mater.* **6**, 652–655 (2007).
- Chen, C. W., Hung, S. C., Yang, M. D., Yeh, C. W., Wu, C. H. *et al.* Oxygen sensors made by monolayer graphene under room temperature. *Appl. Phys. Lett.* **99**, 243502 (2011).
- He, R. X., Lin, P., Liu, Z. K., Zhu, H. W., Zhao, X. Z. *et al.* Solution-Gated Graphene Field Effect Transistors Integrated in Microfluidic Systems and Used for Flow Velocity Detection. *Nano Lett.* **12**, 1404–1409 (2012).
- Newaz, A. K. M., Markov, D. A., Prasai, D. & Bolotin, K. I. Graphene Transistor as a Probe for Streaming Potential. *Nano Lett.* **12**, 2931–2935 (2012).
- Shao, Y., Wang, J., Wu, H., Liu, J., Aksay, Ilhan A. & Lin, Y. Graphene Based Electrochemical Sensors and Biosensors: A Review. *Electroanalysis* **22**, 1027–1036 (2010).
- Liu, Y., Dong, X. & Chen, P. Biological and chemical sensors based on graphene materials. *Chem. Soc. Rev.* **41**, 2283–2307 (2012).
- Stine, R., Robinson, J. T., Sheehan, P. E. & Tamanaha, C. R. Real-Time DNA Detection Using Reduced Graphene Oxide Field Effect Transistors. *Adv. Mater.* **22**, 5297–5300 (2010).
- Bonaccorso, F., Sun, Z., Hasan, T. & Ferrari, A. C. Graphene photonics and optoelectronics. *Nat. Photonics* **4**, 611–622 (2010).
- Bao, Q. & Loh, K. P. Graphene Photonics, Plasmonics, and Broadband Optoelectronic Devices. *ACS Nano* **6**, 3677–3694 (2012).
- Mikhailov, S. A. & Ziegler, K. New electromagnetic mode in graphene. *Phys. Rev. Lett.* **99**, 016803 (2007).
- Bao, Q., Zhang, H., Wang, B., Ni Candy, Z., Lim, H. Y. X. *et al.* Broadband graphene polarizer. *Nat. Photonics* **5**, 411–415 (2011).
- Vakil, A. & Engheta, N. Transformation Optics Using Graphene. *Science* **332**, 1291–1294 (2011).
- Kim, J. T. & Choi, S. Y. Graphene-based plasmonic waveguides for photonic integrated circuits. *Opt. Express* **19**, 24557–24562 (2011).
- Stanley, G. F. *Refractometers: Basic Principles* (Bellingham & Stanley Ltd. 1989).
- Homola, J. *Surface Plasmon Resonance Based Sensors* (Springer Berlin Heidelberg, 2006).
- Nair, R. R., Blake, P., Grigorenko, A. N., Novoselov, K. S., Booth, T. J. *et al.* Fine structure constant defines visual transparency of graphene. *Science* **320**, 1308–1308 (2008).
- Axelrod, D., Burghardt, T. P. & Thompson, N. L. Total internal reflection fluorescence. *Annu. Rev. biophys. Bioeng.* **13**, 247–268 (1984).
- Graf, D., Molitor, F., Ensslin, K., Stampfer, C., Jungen, A., Hierold, C. & Wirtz, L. Spatially Resolved Raman Spectroscopy of Single- and Few-layer Graphene. *Nano Lett.* **7**, 238–242 (2007).
- Sosan Cheon, Kenneth David Kihm, Jae Sung Park, Joon Sik Lee, Byeong Jun Lee, Hyeoungkeun Kim & Byung Hee Hong. How to optically count graphene layers. *Opt. Lett.* **37**, 3765–3767 (2012).
- Thongrattanasiri, S., Koppens, F. H. L. & Javier Garcia de Abajo, F. Complete Optical Absorption in Periodically Patterned Graphene. *Phys. Rev. Lett.* **108**, 047401 (2012).
- Born, M. & Wolf, E. *Principles of optics.* (Cambridge University Press, 1999).
- Bruna, M. & Borini, S. Optical constants of graphene layers in the visible range. *Appl. Phys. Lett.* **94**, 031901 (2009).
- Weber, J. W., Calado, V. E. & van de Sanden, M. C. M. Optical constants of graphene measured by spectroscopic ellipsometry. *Appl. Phys. Lett.* **97**, 091904 (2010).
- Blake, P., Hill, E. W., Castro Neto, A. H., Novoselov, K. S., Jiang, D. *et al.* Making graphene visible. *Appl. Phys. Lett.* **91**, 063124 (2007).
- Philipp Kukura, Michele Celebrano, Alois Renn & Vahid Sandoghdar. Single-Molecule Sensitivity in Optical Absorption at Room Temperature. *J. Phys. Chem. Lett.* **1**(23), 3323–3327 (2010).
- Kenneth D. Kihm. Surface plasmon resonance reflectance imaging technique for near-field (~100 nm) fluidic characterization. *Experiments in Fluids* **48**(4), 547–564 (2010).
- Antonino Parisi, Alfonso C. Cino, Alessandro C. Busacca, Matteo, Cherchi & Stefano Riva-Sanseverino. Integrated Optic Surface Plasmon Resonance Measurements in a Borosilicate Glass Substrate. *Sensors* **8**, 7113–7124 (2008).
- Ledesma-Aguilar, R., Nistal, R., Hernández-Machado, A. & Pagonabarraga, I. Controlled drop emission by wetting properties in driven liquid filaments. *Nat. Mater.* **10**, 367–371 (2011).
- Ludovic, S. Live, Jean-Francois Masson, High Sensitivity of Plasmonic Microstructures near the Transition from Short-Range to Propagating Surface Plasmon. *J. Phys. Chem. C* **113**, 10052–10060 (2009).
- Im, H., Sutherland, J. N., Maynard, J. A. & Oh, S. H. Nanohole-Based Surface Plasmon Resonance Instruments with Improved Spectral Resolution Quantify a Broad Range of Antibody-Ligand Binding Kinetics. *Anal. Chem.* **84**, 1941–1947 (2012).
- Kim, K. S. *et al.* Large-Scale Pattern Growth of Graphene Films for Stretchable Transparent Electrodes. *Nature* **457**, 706 (2009).

Acknowledgments

The authors thank the Chinese National Key Basic Research Special Fund (grant 2011CB922003), the Natural Science Foundation of China (grant 10974103, 11174159), the Program for New Century Excellent Talents in University (NCET-09-0484).

Author contributions

The experiments were conceived, designed and carried out by X.F., Z.B.L. and Z.C.D., X.D.C. and X.Q.Y. performed graphene and transfer. X.T.K. and Z.B.L. contributed to the interpretation of the data and developed analytical and computational theoretical tools. J.G.T., Q.Y., C.P.Z. and Y.S.C. analysed and interpreted the data. Z.B.L., X.F. and J.G.T. wrote the manuscript with the assistance of all other co-authors.

Additional information

Supplementary information accompanies this paper at <http://www.nature.com/scientificreports>

Competing financial interests: The authors declare no competing financial interests.

License: This work is licensed under a Creative Commons Attribution-NonCommercial-NoDerivs 3.0 Unported License. To view a copy of this license, visit <http://creativecommons.org/licenses/by-nc-nd/3.0/>

How to cite this article: Xing, F. *et al.* Sensitive Real-Time Monitoring of Refractive Indexes Using a Novel Graphene-Based Optical Sensor. *Sci. Rep.* **2**, 908; DOI:10.1038/srep00908 (2012).

Journal of Biomedical Optics

SPIEDigitalLibrary.org/jbo

Effect of tissue fluid on accurate determination of the complex refractive index of animal tissue

Jin Wang
Qing Ye
Zhi-Chao Deng
Wen-Yuan Zhou
Teng-Qian Sun
Chun-Ping Zhang
Jian-Guo Tian

Effect of tissue fluid on accurate determination of the complex refractive index of animal tissue

Jin Wang, Qing Ye, Zhi-Chao Deng, Wen-Yuan Zhou, Teng-Qian Sun, Chun-Ping Zhang, and Jian-Guo Tian

Nankai University, The Key Laboratory of Weak-Light Nonlinear Photonics, Ministry of Education, School of Physics and TEDA Applied Physics School, Tianjin 300071, China

Abstract. We investigate the effect of tissue fluid on the measurement of complex refractive index (RI) of animal tissue. A new model is proposed and verified through experimental results of simulation samples made of glycerol and methyl-red-doped poly(methyl methacrylate). Coupled with polarized optical reflectance measurements performed on several kinds of animal muscle tissues, RIs were resolved using the new model. We find that the tissue fluid existing at the prism-sample interface is unavoidable. We also find that with a change of proportion of the tissue fluid, the RI of muscle tissue can still be measured using the new model. © 2012 Society of Photo-Optical Instrumentation Engineers (SPIE). [DOI: 10.1117/1.JBO.17.7.075011]

Keywords: complex refractive index; extinction coefficient; tissue fluid.

Paper 11741 received Dec. 12, 2011; revised manuscript received Jun. 20, 2012; accepted for publication Jun. 21, 2012; published online Jul. 17, 2012.

1 Introduction

The complex refractive index (RI) can be defined in terms of a real part and an imaginary part as $n = n_r + i\kappa$, where κ means the extinction coefficient. In the field of near-infrared tomography, fluorescence diagnosis, laser surgery, and photodynamic therapy (PDT), it is vital to know the precise value of RI.¹⁻³ It has been proven that the RI value affects average diffuse intensity solved by the radiative transfer equation and the calculation of other optical parameters of biotissue, namely the absorption coefficient μ_a , the scattering coefficient μ_s , and the anisotropy factor g .⁴⁻⁶

The total internal reflection (TIR) method is recommended to have the highest precision for RI measurements of animal tissue and has been investigated by different groups worldwide.⁷⁻¹¹ The excellent work of Ding et al. first introduced the dual-parameter fitting method to obtain n_r and κ of skin tissue by nonlinear fitting simultaneously.¹² The modified version of the TIR method, named the extended derivative total reflection method (EDTRM),¹³ has recently been applied to the measurement of biotissue and a series of tissue-mimicking phantoms. Using EDTRM, n_r is directly determined by the derivative of the reflectance curve and κ is obtained from nonlinear fitting.

In the former research, RI is usually treated as the 'average value' of tissue fluid and muscle tissue. Bolin et al. resorted to homogenization by a blender and believed that the liquid expressed from homogenate has a similar RI with the overall tissue.⁷ Most of the other researchers applied pressures on the tissue sample to eliminate the air gap and tissue fluid between the prism and the tissue,⁹⁻¹³ while neglecting the role of tissue fluid. Actually, a close relationship between the increase of tissue fluid and the reduction of the local chromophore concentration as well as the scattering coefficient has been

proven by a prior study.¹⁴ Is there any method to obtain more accurate RI of muscle tissue in the presence of tissue fluid.

In this paper, we discover that the existence of the tissue fluid at the prism-sample interface is unavoidable in the measurement and has an important effect on the determination of RI of animal muscle tissue. The contacting area of the tissue sample consists of tissue fluid and muscle tissue. A new model based on EDTRM is proposed to explain the significant information revealed by the measured results. In order to verify the new model, a simulation sample made of glycerol and methyl-red-doped poly(methyl methacrylate) (MR-PMMA) is measured. Then we applied the new model for the measurement of fresh porcine, chicken breast, and ovine muscle tissues. During the laborious preparation and measurement of tissue samples, we find that a compromised pressure that is between eliminating partial tissue fluid and avoiding damage to the intrinsic properties of the tissue sample is needed in sample preparation. We also find that with a change of the proportion parameter of the tissue fluid, the RI of muscle tissue can still be measured using the new model.

2 Material and Method

The experimental setup for reflectance measuring is schematically shown in Fig. 1, which is similar to that of Ref. 13. A He-Ne laser (632.8 nm) is used. M is a beam splitter. H is a half-wave plate. P is the polarizer. PD1 and PD2 are the two detectors of a dual-channel power meter (PM320E, Thorlabs, New Jersey). The aperture size of the photodiode sensor (S130C, Thorlabs, New Jersey) is 9.5 mm, so we used an aperture diaphragm D with diameter of about 5 mm to eliminate the scattering light and parasitic light. An equilateral triangular prism is fixed on a rotation stage (M-038, Physik Instrumente, Karlsruhe, Germany).

According to the schematic diagram in Fig. 1, n_r can be solved by

Address all correspondence to: Qing Ye, Nankai University, The Key Laboratory of Weak-Light Nonlinear Photonics, Ministry of Education, School of Physics and TEDA Applied Physics School, Tianjin 300071, China; Tel.: 86-22-23503697; E-mail: yeqing@nankai.edu.cn

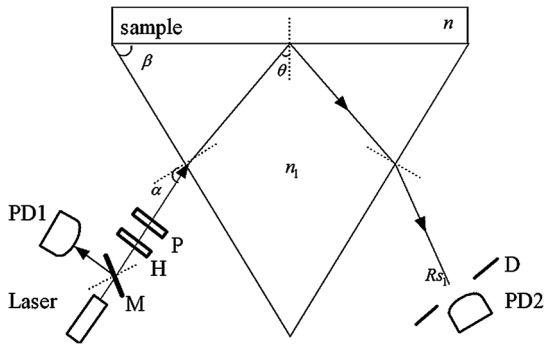


Fig. 1 Schematic diagram of the experimental setup for reflectance measuring.

$$n_r = n_1 \sin[\beta \pm \text{asin}(\sin \alpha_c / n_1)], \quad (1)$$

where α_c is the critical incident angle when TIR occurs at the prism-sample interface. According to the Fresnel formula,¹⁵ the reflectance at the prism-sample interface for a transverse electric (TE) wave $R_{1,2}$ can be expressed as

$$R_{1,2} = \frac{(n_1 \cos \theta - u_2)^2 + v_2^2}{(n_1 \cos \theta + u_2)^2 + v_2^2}, \quad (2)$$

$$2u_2^2 = n_r^2(1 - \kappa^2) - n_1^2 \sin^2 \theta + \sqrt{[n_r^2(1 - \kappa^2) - n_1^2 \sin^2 \theta]^2 + 4n_r^4 \kappa^2}, \quad (3)$$

and

$$2v_2^2 = -[n_r^2(1 - \kappa^2) - n_1^2 \sin^2 \theta + \sqrt{[n_r^2(1 - \kappa^2) - n_1^2 \sin^2 \theta]^2 + 4n_r^4 \kappa^2}], \quad (4)$$

where parameters v_2 and u_2 are the intermediate variables. The reflectance at the air-prism interface $R_{2,3}$ can be expressed as

$$R_{2,3} = \left\{ \frac{\cos \alpha - n_1 \cos[\text{asin}(\sin \alpha / n_1)]}{\cos \alpha + n_1 \cos[\text{asin}(\sin \alpha / n_1)]} \right\}^2. \quad (5)$$

When emergent light leaves the prism and enters into air, the reflection loss is approximately equal to the loss at the incident air-prism interface. The final measured reflectance R_s detected by PD2 should include the loss between the two interfaces mentioned above, which is

$$R_s = R_{1,2} * (1 - R_{2,3})^2. \quad (6)$$

By measuring the reflectance curves of the sample, α_c is obtained at the angular position of the derivative maximum of reflectance curve.¹³ n_r is calculated by Eq. (1). There are similar equations for a transverse magnetic (TM) wave.

Using Eq. (6), we found a large distortion between experimental data of animal tissues and theoretical fitting. Taking into account of the tissue fluid, Eq. (6) is modified by a new model as

$$R_s^+ = b_1 R_{s1} + b_2 R_{s2}, \quad (7)$$

where R_{s1} and R_{s2} are the reflectance from tissue fluid and muscle tissue surface, respectively; b_1 and b_2 are the proportion parameters of the tissue fluid and the muscle tissue at the

illuminated areas, $b_1 + b_2 = 1$. n_r of the muscle tissue is determined by the second angular position of the derivative maximum of the reflectance curve. Using Eq. (7) and a nonlinear fitting program based on the Nelder-Mead simplex algorithm, κ , b_1 , and b_2 can be resolved by minimizing the sum

$$S(N) = \sum_{i=1}^N (R_{m,i} - R_{s,i}^+)^2, \quad (8)$$

where $R_{m,i}$ is the i 'th measured reflectance. $R_{s,i}^+$ is the i 'th calculated reflectance obtained by Eq. (7).

The reliability of fitting are described by E_s^2 , defined as

$$E_s^2 = 1 - \frac{\sum_{i=1}^N (R_{m,i} - R_{s,i}^+)^2}{\sum_{i=1}^N (R_{m,i} - \bar{R})^2}, \quad (9)$$

where \bar{R} is the mean value of the measured reflectance over N values of incident angle. The value of E_s^2 ranges from 0 to 1 and it's closer to 1 when we obtain a reliable fitting.

According to the normal sample preparation procedure of animal tissue for RI measurement, fresh porcine tissue was frozen for 30 min first and then sliced to a thin section of about 5 mm thickness. After 15 min, the surface of tissue was cleaned with alcohol to reduce the influence of condensation. The sample was pressed on the surface of the prism to make sure no air gap exists and some tissue fluid exudates at the interface. Fresh chicken breast and ovine muscle tissue were prepared the same way as the porcine sample. Each sample was continuously measured five times to calculate the standard deviation. In order to get the RI of pure tissue fluid, we picked up some tissue fluid by pressing heavily on the fresh porcine tissue and measured it.

Since the proportions of tissue fluid and muscle tissue at the prism-sample interface are variable for different types of tissues and conditions, we made a simulation sample to simulate the reflection of tissue and verify the new model. The simulation sample is made of two materials with known n_r and κ : the glycerol ($1.4709 + 0.000014i$) and MR-PMMA ($1.5205 + 0.00057i$). The choice of these two materials is according to the difference between their RIs, which is close to the difference between the tissue fluid and the muscle tissue. The front and right side views of the cross section of the simulation sample are schematically shown in Fig. 2(a) and 2(b). For the simulation sample fabrication, methyl-red and PMMA (with a weight ratio of about 3%) were first dissolved in cyclohexanone separately and then mixed together. After stirring for 30 min, the mixture was poured carefully on the one surface of the prism. After 24 h

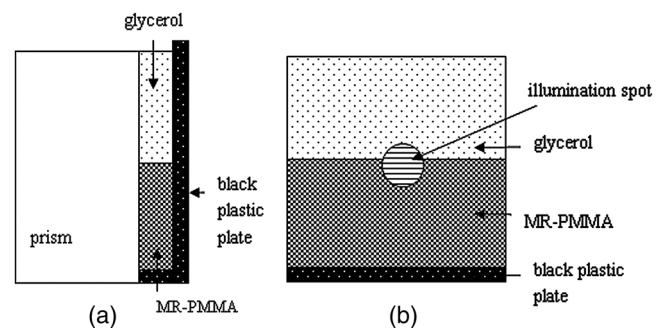


Fig. 2 Schematic of the cross section of the simulation sample. (a) Front view. (b) Right-side view.

for the volatilization of cyclohexanone and the hardening of the mixture, deposited thick MR-PMMA film was obtained with a thickness of about 5 mm. Then a small groove made of a black plastic plate is fixed on the prism. Glycerol was added into the groove. The interface of the glycerol and MR-PMMA is almost parallel to the horizontal plane. As seen in Fig. 2(b), the illuminated area inside a circle of radius about 3 mm was divided into two parts by the interface, while the upper white area is the glycerol and the lower shadow area is the MR-PMMA. The proportions of glycerol in the illuminated area can be adjusted by moving the prism vertically. Here, the subscript '1' and '2' in Eq. (7) denote the glycerol and the MR-PMMA, respectively. n_r and κ of the MR-PMMA, and b_1 and b_2 can be resolved using the method depicted above.

3 Results and Discussion

Measurements for three proportions of glycerol in the illuminated area were taken, with b_1 equal to 38.83%, 14.39%, and 10.48%, respectively. Figure 3 shows the measured reflectance data, fitting curves, and the derivative of reflectance curves for the simulation samples. The calculated n_r of glycerol is about 1.4698 and has a shift of 0.0011 compared with the pure glycerol sample. n_r of MR-PMMA are 1.5205, 1.5217, and 1.5218, respectively, which have shifts of less than 0.002. κ of MR-PMMA are 0.00030, 0.00040, and 0.00032, respectively. The values of E_s^2 are larger than 0.9920. The results have proved the reliability of the new model described by Eq. (7). In Fig. 4, it's distinct that the amplitude of the first peak increases with the proportion of glycerol b_1 , while the positions of two derivative maxima are not sensitive to b_1 . The result implies that the proportion of glycerol has no impact on the measured RI of glycerol and MR-PMMA.

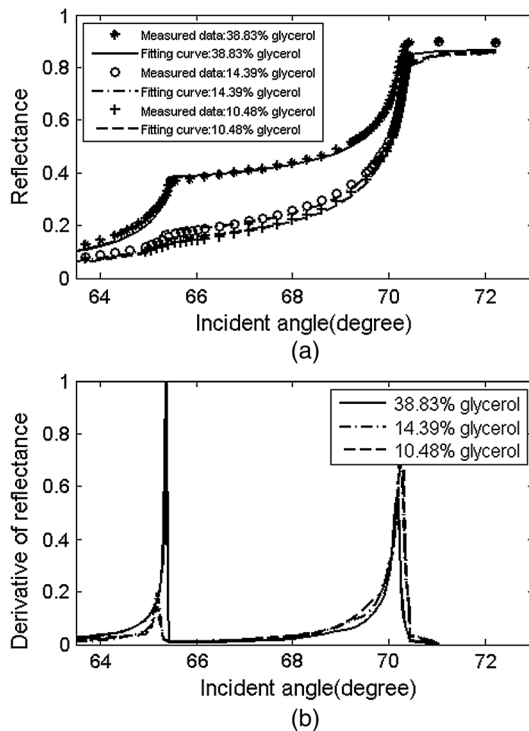


Fig. 3 (a) Measured reflectance data and fitting curves of the simulation sample with three different proportions of glycerol (TE wave). (b) The derivative of the reflectance curves.

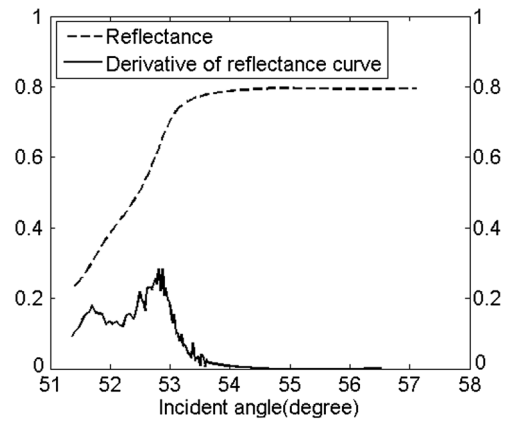


Fig. 4 Measured reflectance curve of porcine tissue and the derivative of the reflectance curve (TM wave).

We compared the values of n_r and κ of MR-PMMA determined using the new model, the dual-parameter fitting method,¹² and EDTRM.¹³ Results are listed in Table 1. Clearly we can see that using EDTRM, only the right n_r can be obtained and k is much smaller compared with the real values. The dual-parameter fitting method achieves a better fitting than EDTRM while both n_r and κ have a large shift from the real value, for example, the shift of n_r is about 0.05 when b_1 equals to 38.83%. b_1 has an obvious impact on the misleading results and a smaller b_1 will lead to a much smaller error. Results have indicated that when the sample has two components, a new model is required to achieve accurate RI of each component. Glycerol in the liquid state has close contact with the MR-PMMA. There is no air gap between the two materials, so the effect of diffraction is subtle and was not observed in the experiment. Though the interface in the illumination spot has variable proportion, it is almost an ideal line and parallel to the horizontal plane, which occupies a rather small part and the effect of the interface can be neglected.

Measured reflectance and the derivative of the reflectance curves for porcine chicken breast and ovine muscle tissues are shown in Figs. 4 and 5. In Fig. 4, b_1 equals 31.29%. We found that double peaks appear on the derivative curves. From the first peak position of the derivative curve, the calculated n_r is 1.3565, which is similar to the measured value of pure tissue fluid ($n_r = 1.3552$). The result has proved that the first smaller 'hump' on the reflectance curve should originate from the tissue fluid. From the second peak, the calculated n_r of 1.3861 is similar to the reported values of porcine tissue.^{9,12,16} Significant information is revealed that the contacting area of the sample consists of the tissue fluid and muscle tissue.

In Fig. 5, the proportion parameters of tissue fluid b_1 equals 20.79% for chicken breast and 12.17% for ovine tissue. The n_r of chicken breast tissue is about 1.3907, which is almost equal to the result of 1.399 measured using low-coherence interferometry.¹⁷ For ovine tissue, $n_r = 1.3958$, which is similar to the reported results of 1.402 and 1.389 (Refs. 12 and 16, respectively). The standard deviation of n_r is smaller than 0.001 for tissue samples. Fitting reflectance curves of ovine tissue obtained using EDTRM, dual-parameter fitting, and the new model are shown in Fig. 6. Comparisons of the three methods are listed in Table 2. The new model reveals a more superior fitting than the other two methods. Take ovine muscle tissue, for example. Similar to the analysis of the simulation sample, both the dual-parameter fitting method and EDTRM have

Table 1 Comparison of n_r and k of MR-PMMA using three methods (TE wave).

b_1	New model			Dual-parameter fitting			EDTRM		
	n_r	k	E_s^2	n_r	k	E_s^2	n_r	k	E_s^2
38.83%	1.5205	0.00030	0.9929	1.4785	0.00915	0.8309	1.5205	0.00015	0.2889
14.39%	1.5217	0.00040	0.9960	1.5210	0.00057	0.9346	1.5217	0.00029	0.9269
10.48%	1.5218	0.00032	0.9983	1.5214	0.00042	0.9694	1.5218	0.00024	0.9644

caused errors to n_r and k . E_s^2 is 0.9905 for dual-parameter fitting method and 0.9680 for EDTRM, which was usually thought to get a satisfactory fitting. The new model obtains the best fitting with E_s^2 larger than 0.9960. The subtle hump on the measured reflectance curve was enlarged in the inset of Fig. 6.

Actually, the similar small 'hump' was also recorded by Fig. 2 of Ref. 10 and Fig. 7 of Ref. 12 in the RI measurement of porcine kidney and epidermis, but it was not discussed. As seen in Fig. 2, the incident light at the surface of the sample has a beam diameter of about 3 mm. There is a random distribution of tissue fluid and muscle tissue at the prism-tissue interface. Either the fluid or the muscle tissue part can be simplified as homogenous and shows an average RI value. The first peak on the derivative curves of Figs. 4 and 5(a) originates from the reflectance of the tissue fluid, while the real n_r of the muscle tissue should be calculated from the second peak. The measured reflectance curve is the summation of the reflectance from the two kinds of contacting areas. It was commonly believed that the main differences among published results should be

ascribed to sample-to-sample variance and sample preparation conditions, so the existence of tissue fluid didn't receive much attention. A strong positive relationship was shown between the value of b_1 and the difference using the three methods. For porcine and chicken breast tissues, the values of E_s^2 vary a lot using the three methods because a larger amount of tissue fluid exists. For ovine tissue, the difference is much smaller with b_1 equal to 12.17%.

The knowledge of the optical properties of biological tissue is of fundamental importance for RI measurement. Tissue fluid usually consists of extracellular fluid ($n_r \approx 1.335$) and intracellular fluid ($n_r \approx 1.354$).¹⁸ In our experiment, most of the capillaries of the tissue samples run predominantly parallel with the muscle fibers. The main component of the tissue fluid should be the intracellular fluid, because the incisions were made perpendicular to the long axis of muscle fibers. From the optical point of view at the cells, structures with different RIs in the surroundings and in the interior of the cells contribute to the average RI of tissue. The aqueous solution of salts and proteins consisted in the cells lead to a mean RI of approximately 1.38. In membrane structures, there are about 5% of lipids having a higher RI of about 1.48.¹⁹ The measured n_r of tissue fluid or muscle tissue should be the average RI in the illumination spot. According to the electromagnetic theory, when TIR occurs, the energy of the incident light decays rapidly and some light penetrates into the less dense medium over relatively short distances. The penetration depth is usually on the order of wavelength or smaller.²⁰ If large amounts of tissue fluid or water exists and forms a thin layer between the prism and the muscle tissue, the RI of muscle tissue cannot be

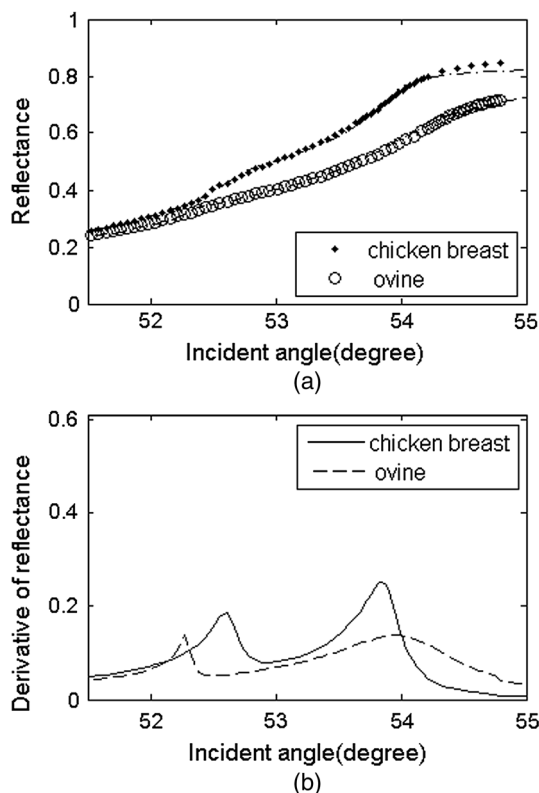


Fig. 5 (a) Measured reflectance data and fitting curves of chicken breast and ovine tissue (TM wave). (b) The derivative of the reflectance curves.

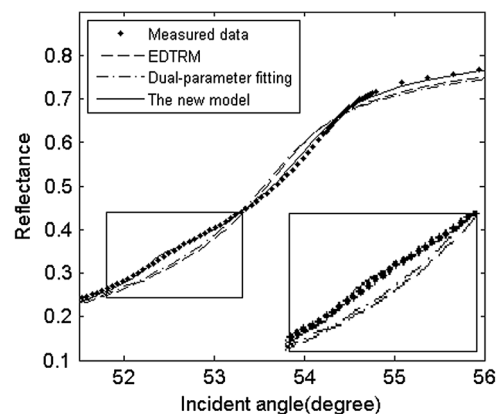


Fig. 6 Measured reflectance data and fitting curves of ovine tissue using EDTRM, dual-parameter fitting, and the new model (TM wave). An enlargement of the rectangular area on the reflectance curves is shown in the inset.

Table 2 RIs of porcine, chicken breast, and ovine tissue (TM wave).

Sample	New model			Dual-parameter fitting			EDTRM		
	n_r	k	E_s^2	n_r	k	E_s^2	n_r	k	E_s^2
Porcine	1.3861	0.0022	0.9961	1.3770	0.0041	0.9522	1.3861	0.0014	0.6808
Chicken	1.3907	0.0022	0.9960	1.3840	0.0035	0.9829	1.3907	0.0015	0.9421
Ovine	1.3958	0.0057	0.9985	1.3898	0.0067	0.9905	1.3958	0.0045	0.9680

measured because the total reflection will only occur at the fluid-prism surface. The RI value depends much on the conditions of sample preparation and storage; fresh or frozen tissue samples are needed. For frozen samples, the water brought by surface condensation should be removed by surface cleaning.

Pressure is often added on the surface of the sample for the measurement. In the former research, damage to the samples and the significant change of n_r values were observed when the pressure was higher than 0.4 Mpa,¹² so high pressure is forbidden. Similar to the tissue-machine interface concerns brought up by Chaiken et al. in their in vivo apparatus setup,²¹ pressure registration on the surface of these in vitro tissues is of essential importance in this study. They provided an appropriate apparatus for applying and maintaining pressure on the tissue surface and discussed the effects of pressure in detail. The applied pressure needs to be maintained in a reasonable range that should avoid a discernible change of the intrinsic properties of the tissue, while also guaranteeing no air gap exists at the sample-prism interface.

Cancer progression obviously alters the tissue organization, as exhibited by consistently higher RI variance in tumors versus normal regions.²² For other types of tissue, the composition of protein, lipid, and polysaccharide may lead to RI change. Studies have shown that membrane RI values can be estimated from composition studies.²³ Further studies of RI are needed for more types of tissues carried with pathological indication and composition information, which may enable more accurate diagnosis and earlier disease detection.

4 Conclusion

In conclusion, we proposed a new model based on EDTRM for accurately extracting the RI of animal tissue samples. In the simulation sample study, the theoretical results calculated by the new model show good agreement with the measured reflectance data. This work also aims to emphasize the unavoidable influence of tissue fluid on the RI measurement of animal tissue. At the prism-tissue interface, part of the contacting area is filled with tissue fluid and part is muscle tissue. Misleading results calculated using the dual-parameter fitting method and EDTRM can be attributable to neglecting the tissue fluid. The amount of tissue fluid leads to the amplitude change of the first peak of the derivative curve and the RI of animal tissue can still be measured. The new model also provides a means for novel biological sensing in the biomedical field and identification of the constituents of mixture in the industry.

Acknowledgments

This research is supported by the Chinese National Key Basic Research Special Fund (Grant No. 2011CB922003),

Fundamental Research Funds for the Central Universities (Grant No. 65010931), Science and Technology Program of Tianjin (Grant Nos. 11ZCKFSY00500 and 10ZCGHHZ01100), Basic Research and Advanced Technology Program of Tianjin (Grant No. 11JCZDJC16800), and the Natural Science Foundation of Zhejiang (Grant No. Y1100088).

References

- H. Dehghani et al., "The effects of internal refractive index variation in near-infrared optical tomography: a finite element modelling approach," *Phys. Med. Biol.* **48**(16), 2713–2727 (2003).
- D. Y. Churmakov, I. V. Meglinski, and D. A. Greenhalgh, "Amending of fluorescence sensor signal localization in human skin by matching of the refractive index," *J. Biomed. Opt.* **9**(2), 339–346 (2004).
- W. M. Star and J. P. A. Marijnissen, "Calculating the response of isotropic light dosimetry probes as a function of the tissue refractive index," *Appl. Opt.* **28**(12), 2288–2291 (1989).
- Y. Domankevitz et al., "Selective delivery of laser energy to biological tissue based on refractive-index differences," *Opt. Lett.* **25**(15), 1104–1106 (2000).
- M. A. Bartlett and H. Jiang, "Effect of refractive index on the measurement of optical properties in turbid media," *Appl. Opt.* **40**(10), 1735–1741 (2001).
- J. Tualle and E. Tinet, "Derivation of the radiative transfer equation for scattering media with a spatially varying refractive index," *Opt. Commun.* **228**, 33–38 (2003).
- F. Bolin et al., "Refractive index of some mammalian tissues using a fiber optic cladding method," *Appl. Opt.* **28**(12), 2297–2303 (1989).
- Q. W. Song et al., "Modified critical angle method for measuring the refractive index of bio-optical materials and its application to bacteriorhodopsin," *J. Opt. Soc. Am. B* **12**(5), 797–803 (1995).
- H. Li and S. S. Xie, "Measurement method of the refractive index of biotissue by total internal reflection," *Appl. Opt.* **35**(10), 1793–1795 (1996).
- J. Lai et al., "Experimental measurement of the refractive index of biological tissues by total internal reflection," *Appl. Opt.* **44**(10), 1845–1849 (2005).
- P. Sun and Y. Wang, "Measurements of optical parameters of phantom solution and bulk animal tissues in vitro at 650 nm," *Opt. Laser Technol.* **42**(1), 1–7 (2010).
- H. F. Ding et al., "Refractive indices of human skin tissues at eight wavelengths and estimated dispersion relations between 300 and 1600 nm," *Phys. Med. Biol.* **51**(6), 1479–1489 (2006).
- Q. Ye et al., "Measurement of the complex refractive index of tissue-mimicking phantoms and biotissue by extended differential total reflection method," *J. Biomed. Opt.* **16**(9), 097001 (2011).
- E. K. Chan et al., "Effects of compression on soft tissue optical properties," *IEEE J. Sel. Topics Quantum Electron.* **2**(4), 943–950 (1996).
- M. Born and E. Wolf, *Principles of Optics*, Pergamon, New York (1959).
- S. Cheng et al., "Measurement of the refractive index of biotissue at four laser wavelengths," *Proc. SPIE* **4916**, 172–176 (2002).

17. A. M. Zysk et al., "Needle-based refractive index measurement using low-coherence interferometry," *Opt. Lett.* **32**(4), 385–387 (2007).
18. M. Kohl et al., "Influence of glucose concentration on light scattering in tissue-simulating phantoms," *Opt. Lett.* **19**(24), 2170–2172 (1994).
19. J. Beuthan et al., "The spatial variation of the refractive index in biological cells," *Phys. Med. Biol.* **41**(3), 369–382 (1996).
20. D. Axelrod, "Cell substrate contacts illuminated by total internal reflection fluorescence," *J. Cell. Biol.* **89**(1), 141–145 (1981).
21. J. Chaiken et al., "Instrument for near infrared emission spectroscopic probing of human fingertips in vivo," *Rev. Sci. Instrum.* **81**(3), 034301 (2010).
22. Z. Wang et al., "Tissue refractive index as marker of disease," *J. Biomed. Opt.* **16**(11), 116017 (2011).
23. R. A. Meyer, "Light scattering from biological cells: dependence of backscatter radiation on membrane thickness and refractive index," *Appl. Opt.* **18**(5), 585–588 (1979).